Experimental and numerical description of rapid granular flows and some baseline constraints for simulating 3-dimensional granular flow dynamics

DISSERTATION
zur
Erlangung des Doktorgrades (Dr. rer. nat.)
der
Mathematisch-Naturwissenschaftlichen Fakultät
der
Rheinischen Friedrich-Wilhelms-Universität Bonn

vorgelegt von
Christian Kröner
aus Remscheid

Bonn, 2013

Angefertigt mit Genehmigung der Mathematisch-Naturwissenschaftlichen Fakultät
der Rheinischen Friedrich-Wilhelms-Universität Bonn

1. Referent:	Prof. Dr. Stephen A. Miller
2. Referent:	Prof. Dr. Nikolaus Froitzheim
Tag der Promotion:	16.07.2014
Erscheinungsjahr:	2014

Abstract

Accurate prediction of rapid granular flow behavior is essential to optimize protection measures from hazardous natural granular flows like snow avalanches and landslides and to design efficient production facilities for granulate processing industries.

So far, most successful models for rapid granular flow descriptions employ depth-averaging, assuming an essentially constant velocity over depth. This assumption greatly reduces calculation power but can lead to incorrect predictions in regions of strong velocity shearing in the flow depth direction, e.g., during the impact on an obstacle. To overcome these limitations, this study introduces a novel type of non-depth-averaged fluid dynamics simulations for rapid granular flows of cohesionless material. A series of small scale experiments with industrial (polyvinyl chloride (PVC)) and natural (sand) granular material was performed (i) to select and refine the appropriate rheological model, (ii) to yield a better insight into velocity profiles and (iii) to obtain parameters for comparison with numerical simulations. Based on these experiments, Coulomb-type friction was selected as rheological model. A Poly(methyl methacrylate) channel set-up with variable inclination angle in combination with high-speed image recording and an open source particle image velocimetry (PIV) software developed in this study allowed detailed observation of velocity profiles during flow inception, undisturbed flows, flows encountering obstacles, and shock scenarios. The PIV measurements revealed considerable changes in velocity between layers of the granular flow and thus underpin the necessity to perform non-depth-averaged simulations in order to accurately describe the flow behavior in all aspects. Comparison of the depth-averaged simulation model of the Savage-Hutter type and the non-depth-averaged simulation method introduced here with the experiments revealed that certain quantities, like the flow height and shape could only be accurately predicted using the non-depth-averaged simulations. Furthermore, the non-depth-averaged simulations were well capable of predicting the observed velocity profiles and produce accurate predictions of associated quantities like strain rates and slip velocities for both materials in most experiments. Nevertheless, this study also revealed cases where both depth-averaged and non-depth-averaged methods generate similar predictions, e.g., the height of an undisturbed flow and deposition shapes. A detailed summary of parameters and dynamic variables in different experiments, and their predictability by both methods is provided. This serves as a guideline to decide when to employ the reduced but faster depth-averaged methods and when more calculation power intensive, but more accurate, non-depth-averaged methods must be employed.

The non-depth-averaged method developed in this study was further validated to measure its predictive power in three dimensional experiments with obstacles. Also here, accurate predictions were observed. Furthermore, a method for the introduction of complex topographies into the simulation process was developed, allowing the direct integration of real mountain topographies. As pilot tests, simulations of granular flows on a complex experimental topography and a real case snow avalanche described in the literature were performed. The results demonstrated that the new method can be transferred to complex topographies and yields good predictions. These findings can serve as a basis for further refinement of the model and its expansions to describe more complex events, e.g., the entrainment of snow mass.

Taken together, the novel, non-depth-averaged model and simulation technique build in this study based on the experimental observation are a suitable tool to predict important flow dynamical quantities in non-cohesive granular flows of both natural and industrial origins. Furthermore, it can serve as a basis for the development of a non-depth-averaged predictive model for real scale hazardous granular flows and is thus an important step towards the correct prediction of granular flow behavior for risk assessment in endangered regions.

Zusammenfassung

Exakte Vorhersagen des Fließverhaltens von granularen Materialien sind essentiell für die Optimierung von Schutzmaßnahmen gegen natürlich vorkommende, gefährliche granulare Flüsse wie Schneelawinen und Erdrutsche und für die Entwicklung effektiver Produktionsprozesse in der granulatverarbeitenden Industrie.

Die meisten bisher eingesetzten Modelle zur Beschreibung granularer Flüsse sind tiefenintergriert und nehmen daher eine im Wesentlichen konstante Geschwindigkeit über die Flusstiefe an. Diese Annahme verringert die benötigte Rechenleistung erheblich, kann jedoch auch zu ungenauen Vorhersagen in Bereichen mit starken Scherkräften und schnellen Geschwindigkeitsänderungen, wie beim Auftreffen auf ein Hindernis, führen. Um diese Einschränkungen zu überwinden, wird in dieser Arbeit eine neue Art von nicht tiefenintegrierten Fluid Dynamik Simulationen für schnelle granulare Flüsse aus nicht kohäsiven Materialien eingeführt. Es wurde eine Serie von kleinmaßstäblichen Experimenten mit industriellem (Polyvinyl Chlorid (PVC)) und natürlichem Granulat (Sand) durchgeführt um ein geeignetes rheologisches Modell auszuwählen, bessere Einsicht in Geschwindigkeitsprofile zu erlangen und Parameter für einen Vergleich mit nummerischen Simulationen zu ermöglichen. Auf der Basis der Experimente wurde Coulomb-artige Reibung als rheologisches Modell ausgewählt. Ein experimenteller Aufbau bestehend aus einem Acrylglaskannal mit variabler Steigung und einer Hochgeschwindigkeitskamera gekoppelt an eine frei verfügbare, in dieser Arbeit implementierte Software zur Bestimmung von Geschwindigkeitsfeldern (Particle Image Velocimetry (PIV)) erlaubte eine detaillierte Betrachtung von Geschwindigkeitsprofilen zu Beginn von granularen Flüsse, in ungestörten Flüssen, beim Auftreffen eines Flusses auf ein Hindernis und in Schockszenarien. Die PIV Messungen zeigten erhebliche Geschwindingkeitsunterschiede zwischen den einzelnen Lagen eines granularen Flusses und bekräftigten damit die Notwendigkeit von nicht tiefenintegrierten Simulation zur akkuraten Beschreibung aller Aspekte eines granularen Flusses. Vergleiche des tiefenintegrierten Simulationsmodells der Savage-Hutter Art und der hier eingeführten, nicht tiefenintegrierten Simulationsmethode mit den Experimenten zeigten, dass Größen wie die Flußhöhe und die Form des Flusses nur von den nicht tiefenintegrierten Simulation akkurat vorhergesagt werden. Außerdem zeigte sich, dass die nicht tiefenintergrierten Simulationsmethode die beobachteten Geschwindigkeitprofile gut vorhersagen kann und, damit zusammenhängend, in den meisten Experimenten und für beide betrachteten Materialien gute Vorhersagen für die Deformationsgeschwindigkeit und Rutschgeschwindigkeiten liefert. Die Arbeit zeigt jedoch auch Fälle auf in denen beide Simulationsmethoden vergleichbar gute Ergebnisse liefern, z.B. für die Höhe der ungestörten Flusses und die Form von Ablagerungen. Daher wurde eine detaillierte Zusammenfassung der Vorhersagbarkeit der beobachteten Parameter durch die beiden Methoden erstellt, welche als Orientierungshilfe bei der Frage verwendet werden kann, wann die schnelleren, tiefenintegrierten Methoden verwendet werden können und wann die rechenleistungsintensiveren, jedoch genaueren, nicht tiefenintegrierten Simulationen einzusetzen sind.

Weitergehend wurde die in dieser Arbeit entwickelte, nicht tiefenintegrierte Simulationsmethode auf ihre Vorhersagekraft in dreidimensionalen Experimenten mit Hindernissen getested. Auch hier wurden akkurate Vorhersagen erzielt.

Außerdem wurde eine Methode zur Einbringung komplexer Topographien in den Simulationsprozess entwickelt, die ein direktes Einlesen der Topographien echter Fallbeispiele ermöglicht. Als erste Tests für diese Methode wurden Simulationen zu einer in der Literatur beschriebenen, komplexen experimentellen Topographie und einer in der Literatur dokumentierten echten Schneelawine durchgeführt. Die Ergebnisse zeigen, dass die hier eingeführte Simulationsmethode auf komplexe Topographien übertragbar ist und auch dort gute Vorhersagen liefert. Diese Resultate können

nun als Grundlage für weitere Verfeinerungen und Erweiterungen (z.B. Aufnahme von Material während des Flusses) des hier vorgeschlagenen Modells dienen.

Zusammenfassend sind das neuartige, nicht tiefenintegrierte Modell und die Simulationsmethodik, die in dieser Arbeit basierend auf den experimentellen Ergebnissen entwickelt wurden, ein geeignetes Werkzeug um wichtige Größen von granularen Flüssen, sowohl natürlichen als auch industriellen Ursprungs, vorherzusagen. Darüber hinaus kann das Modell als Grundlage für ein nicht tiefenintergriertes Vorhersagemodell für gefährliche granulare Flüsse in realem Maßstab dienen und stellt damit einen wichtige Schritt hin zur korrekten Vorhersage vom Verhalten granularer Flüsse zur Risikoabschätzung in gefährdeten Regionen dar.

Contents

Greek letters

α_1	indicator function, see equation (4.47), page 59
β	constant, see equation (1.10), page 23
Δt	time step, page 43
δ	bottom friction angle, page 15
$\delta(x)$	delta function, page 58
ϵ	aspect ratio, page 23
Φ	general tensorial property, page 45
Φ	intensive quantity, page 32
ϕ	internal friction angle, page 16
ϕ_i^x	ratio of consecutive gradients, see equation (4.70), page 65
Φ_f	interpolated face value, page 46
$\dot{\gamma}$	shear-rate, page 16
Γ	diffusivity, page 45
γ	blending factor, page 47
η	viscosity, page 15
η_E	effective viscosity, page 17
$\kappa(x)$	curvature, page 39
λ	characteristic curvature, page 39
$\lambda_{1,2}$	Eigenvalues, see equation (4.88), page 68
μ	constant of proportionality, see equation (1.0), page 16
μ_2	limiting value the friction constant converges to for high I, page 42
μ_b	Coulomb friction coefficient, see equation (1.0), page 15

Roman letters

$[D]$ diagonal coefficients of $[A]$, page 53

$[N]$ off-diagonal coefficients of $[A]$, page 53

$[R]$ source vector, page 53

∂V surface of control volume, page 32

1 Introduction

1.1 Granular material

The term "granulate" originates from the Latin word "granulum" (small grain). According to the encyclopedia Brockhaus [1999], a granulate is a pourable, fine grain mixture with uniform grain size and shape. Scientifically, the term is used in a wider context, referring to a conglomerate of discrete, solid macroscopic particles which dissipate energy at each interaction. The particles need to be of a size where Brownian motion is deniable. Therefore, the lower cutoff for a granulates diameter is in range of 1 μm (Jaeger et al., 1996; Duran, 2000; Mitarai and Nakanishi, 2012). There is no upper diameter limit as for example the rings of Saturn and the particles of rock avalanches with their particle diameters of several meters can be described as granular materials (Cuzzi et al., 2009; Hermanns and Strecker, 1999).

1.1.1 Characteristics of granular materials

Although a granular material is composed of solid particles, it also displays characteristics of fluids and gases (Jaeger et al., 1996). The characteristics depend on the kinetic energy of the material, which in turn is influenced by the density and structure of the material. A resting granular material, like a pile of sand, can be fluidized by addition of kinetic energy (e.g., from the boundary by agitation or by release of potential energy like during the draining of a silo). Since the added energy dissipates during particle interactions (through collisions and friction), the material quickly comes to rest again (Mitarai and Nakanishi, 2012). Therefore, in contrast to a drained fluid, the material does not uniformly spread on a surface when drained. It rather forms a hill with a characteristic slope, the angle of repose of the respective material. By addition of higher amounts of energy, granular matter can also reach a gas-like state (Goldhirsch et al., 2005; Krengel et al., 2013).

Due to the high impact of the kinetic energy on the behavior of a granular material, the understanding of dynamic processes is of special importance for the understanding of granular materials.

The following paragraphs summarize the most important phenomena resulting from granulate specific characteristics. Detailed reviews on characteristic properties of granular materials can be found in Jaeger et al. (1996), Duran (2000), Pudasaini and Hutter (2007).

1.1.1.1 Dilatancy

Dilatancy, due to its first mention by Reynolds in 1885 (Reynolds, 1885) also termed Reynold's dilatancy, refers to the increase in volume of a granular material upon shearing. Reynolds explained this phenomenon by kinematic restriction: prior to stress application the densely packed particles fill the spaces between them in the best way possible. Application of stress causes the particles to move relatively to each other, resulting in a less optimal packing. As a consequence, the volume increases and leads to uptake of surrounding gas or fluid (Pudasaini and Hutter, 2007).

1.1.1.2 Cohesion

Granular materials can be distinguished as cohesive and non-cohesive according to the forces applied between particles. Cohesive materials can be stressed by tension, which does not only influence the particles to which the tension is applied but also adjacent layers (Pudasaini and Hutter, 2007). An example for a cohesive material is wet sand: when picking up a hand full of wet sand, not only the directly touched particles are lifted but also several layers of the neighboring material. Cohesiveness can either be caused by interactions between the particles (e.g., electrostatic forces) or by the surrounding material (e.g., water). In contrast to that, no tension can be applied to non-cohesive materials. When lifting a fraction of dry sand, only the directly touched particles will be lifted, while the surrounding particles remain unaffected.

1.1.1.3 Segregation

Mixtures of granular materials with differences in particle diameter and density display some intuitively unexpected effects: shaking of the mixture results rather in a segregation of the particle types than mingling (Ottino and Khakhar, 2000). A famous example is the so-called Brazil nut effect, which occurs when a package of cereals is oscillated vertically. Larger and less dense particles like nuts segregate to the surface of the mixture and are found at the top of the package (Rosato et al., 1987).

1.1.2 Applications of granular flow dynamics

Granular dynamics have an impact on many areas of daily life in private households as well as industries. Many food components like cereals, coffee, flour, sugar and cleaning agent are granular materials. A wide application field for granular flow dynamics are industrial production processes. Many basic components are supplied as granulates and need to be transported. Here, fluidization is widely applied to transport material (e.g., when discharging a shipload or transporting plastic granulate by vibration convey-

ors). Although these applications appear to be easy and self-evident, they are subject to complex physical phenomena. One example is the effect that the direction of transport of a vibration conveyor belt might be reversed upon changes in the vibration frequency (Grochowski et al., 2004).

Beside this, many geological processes are influenced by granular dynamics. The most abundant granular material in nature is sand, which is responsible for formation of landscape in many areas like deserts and coasts. The multiple shapes of sand dunes are one example where slow granular morpho-dynamics strongly influences landscape formation.

Apart from these rather slow structure formation processes, some of the most dangerous natural hazards, landslides and avalanches, are composed of granular materials and thus are rapid granular flows.

1.2 Hazardous rapid granular movements in nature

Hazardous rapid granular movements in nature can be subdivided according to their material composition and their origin into landslides, volcanic flows and snow avalanches.

1.2.1 Zones of a granular flow in nature

In general, hazardous granular movements in nature can be divided into three zones: a starting zone, the track and a deposition or run-out zone (Pudasaini and Hutter, 2007). The starting zone contains the granular material which is subsequently mobilized and enters the track. Mobilization can be triggered by various events like heavy snow or rainfall and temperature differences (in the case of snow avalanches and landslides) or seismic activity (volcanoes and earthquakes). From the starting zone, the granular material enters the track zone. Since mountains usually become less steep towards the bottom, the flow is gradually slowed down. Small flows with a small inertia might stop in this region, creating a deposit on the slope. In contrast, large flows only stop when they have traveled a considerable distance in the valley or encounter obstacles. Such avalanches create long shallow run-out zones and can super-elevate in the opposite mountain sites (Pudasaini and Hutter, 2007; Molina et al., 2004; Pudasaini and Miller, 2013). Especially in the case of landslides, the track is also often called failure, while the initiation and run-out situation are called pre- and post-failure, respectively.

1.2.2 Landslides

The term “Landslides” refers to all movements of soil and rocks with variable water content and grain size. A first classification was proposed by Varnes (1978) according to the

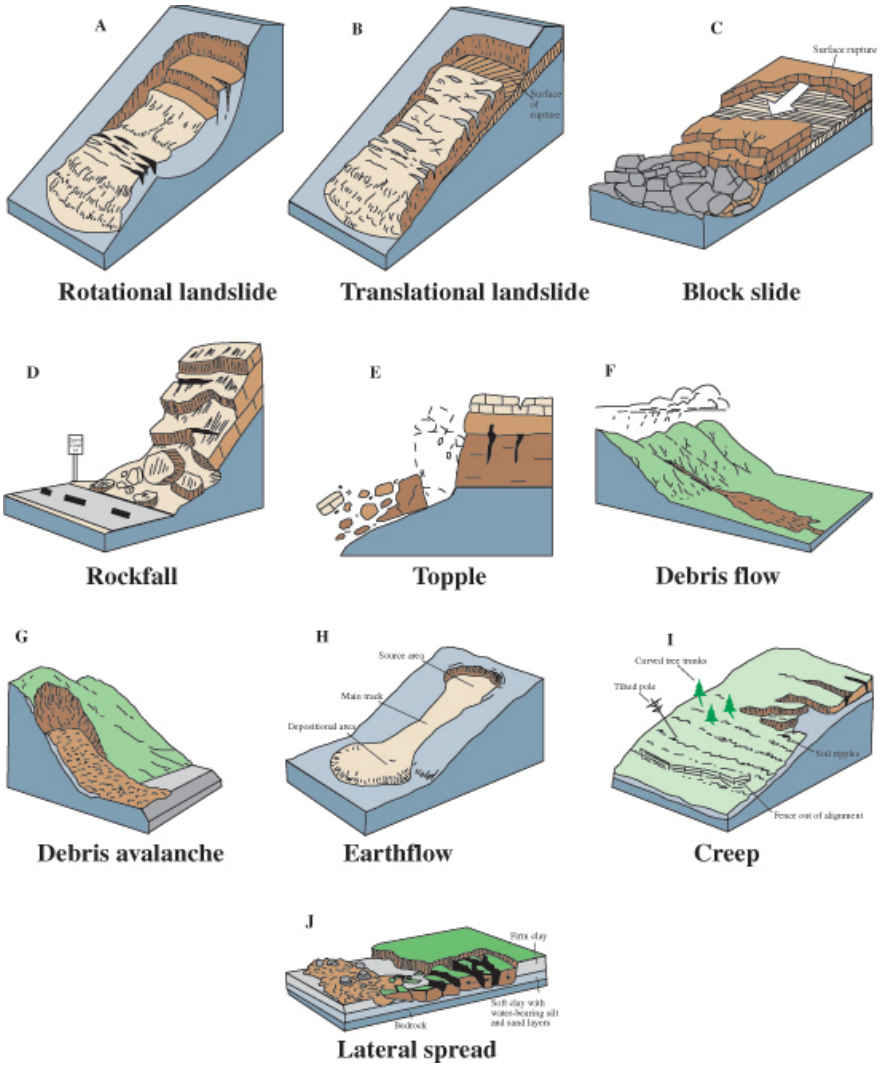

Figure 1.1 – Sketches of the different types of landslides (Highland and Bobrowsky (2008)). For details see text.

type of movement. Varnes distinguishes slides, flows, falls, topples and lateral spreads (Fig. 1.1). Of these five, falls and topples are non granular movements where either one piece of rock (fall) or a hole mountain site (topples) falls down, whereas lateral spreads (e.g., induced by an earthquake) are granular flows but non rapid ones. In this work, only the rapid granular types of landslides, slides and flows, are considered. Depending on the type of movement and the involved material (rock or soil), these types can further be subdivided and classified in more detail as summarized in the following paragraphs (for a detailed description of all landslides types see Varnes (1978), Highland and Bobrowsky (2008)).

1.2.2.1 Slides

Slides are movements along only one sliding surface, meaning that the material slides down as a block. Because of this cohesive behavior, the internal parameters of the mate-

rial can be neglected and the sliding friction between the material and the ground dominates the movement (Highland and Bobrowsky, 2008). The movement performed by the block of material can be either a rotational or a translational one. Rotational slides with several parallel curved planes of movement are also termed slumps, while translational movements are classified as slides (Highland and Bobrowsky, 2008). Despite the block-like sliding behavior, there can be huge differences in the damages caused by the slide depending on the material density, slide depth and velocity. Therefore, slumps and slides can be further subdivided in soil (earth (predominantly fine) or debris (predominantly coarse)) slumps/slides and rock slumps/slides (Varnes, 1978).

1.2.2.2 Flows

Flows are rapid granular movements where the granular material is fluidized. In this case, the material characteristics are of critical importance for the description of the movement. Like slides, flows can be subdivided according to the involved material into rock and soil flows (Varnes, 1978).

Rock flow

Rock flows are composed of fragmented rock of any kind. Very rapid rock flows (0.05 m/s or faster) are also termed "rock avalanches". Rock avalanches are defined as very rapid rock flows that involve the breakdown of the rock particles (Hungr et al., 2001).

Soil flows

Because of the importance of the material parameters, flows of soil-like material can be further subdivided according to the degree of cohesion between the particles, their exact material composition including water content and the velocity of the flow. These factors, together with the multitude of possible granular soil components results in a complex classification of soil type flows suggested by Hungr et al. (2001) which is shortly resumed in the following paragraph:

Non-cohesive flows

Debris: The term debris flow refers to rather coarse (< 80% sand and finer, (Varnes, 1978)) unsorted material, often a mixture of stones and organic material (Highland and Bobrowsky, 2008). According to Hungr et al. (2001) and Highland and Bobrowsky (2008), debris flows are rapid ($5 \cdot 10^{-4}$ m/s and faster) to extremely rapid (up to 100 m/s) flows and can be classified according to their water content and the way they take down the slope: debris flows are saturated with water and rapidly flow down a pre-established channel over a large part of the path, while debris

avalanches are extremely rapid, not necessarily saturated with water and usually occur in the absence of established flow channels (Hungr et al., 2001; Highland and Bobrowsky, 2008). Established channels are often associated with free running water, wherefore the water content of a debris flow increases during the flow by water uptake. Additionally, the established channel prevents spreading of the flow, which results in increased flow heights compared to debris avalanches (Hungr et al., 2001). A special case is a debris flood, which occurs when free water is present between the debris particles (Hungr et al., 2001).

Sorted Material: Other non-cohesive flows can be composed of rather uniform material with small variations in particle size like sand, silt or gravel (Hungr et al., 2001). These sorted material flows can reach from completely dry to water saturated flows. Saturated flows are similar to debris flows and as those extremely rapid and dangerous, while dry sand slides can for example also be slow like flows occurring on sand dunes (Hungr et al., 2001).

Cohesive flows

Clay, mud and material mixtures with > 80% sand and finer usually are cohesive soils. Depending on their water content and degree of cohesion, the flow behavior can either be plastic, meaning that deformation without breakage is possible but no liquid behavior occurs (water content > plastic limit and < liquid limit) or liquid (water content > liquid limit) (Hungr et al., 2001).

Earth flows: Rather moderate to slow (below $5 \cdot 10^{-4}$ m/s), plastic movements of clay or fine soil are termed earth flows. These slow flows consist of dry or wet material below the liquid limit (Hungr et al., 2001).

Mud flows: Extremely rapid flows of clay and soil (5 m/s and above) occur when surface water is mixed into the soil matrix so that the liquid limit is reached (Hungr et al., 2001). Because of their rapid behavior, mud flows are sometimes considered as cohesive debris flows (Scott et al., 1992).

1.2.3 Volcanic flows

The eruption of a volcano and the associated seismic activity can trigger various hazardous rapid granular movements. One the one hand, landslides of the above mentioned kinds can be induced when the edifice of the volcano becomes unstable and parts of it collapse and form for example a debris avalanche (McGuire, 1996). One the other hand, there are also volcano specific flows, pyroclastic flows and lahars, which are among the

most hazardous granular flows in nature and can cause more damage than the actual lava eruption.

1.2.3.1 Pyroclastic flows

Recent experiences with volcanoes in Iceland that cause flights to be stopped all over Europe impressively demonstrated once again that the danger of a volcano is not only its eruption of lava but can also be caused by clouds of ashes, stones and gases erupted from it (Schumann et al., 2011). When these clouds become to heavy to keep rising into the air, they sink to the ground and flow down the flank of the volcano. Such flows are called pyroclastic flows and can reach extreme velocities of 200 m/s and can reach for distances up to 200 km from the erupting volcano. Additionally they are, as their name indicates, usually very hot, up to around 1000° C, which causes organic material like trees or bushes but also houses to burn immediately when hit by a pyroclastic flow (Bryant, 1991; Francis, 1993; Pudasaini and Hutter, 2007).

1.2.3.2 Lahars

When a pyroclastic flow is entrained with water, a so-called lahar is formed, a mudflow of volcanic origin. Sources of water to produce a lahar can be steam from the eruption produced from snow or ice covering the volcano or from rivers the pyroclastic flow overruns on its way. Another possibility to create a lahar is the eruption of a crater lake (Bryant, 1991; Janda et al., 1996).

1.2.4 Snow avalanches

It has become a convention to classify avalanches first according to the material density and air content into powder snow avalanches and dense flow avalanches. Dynamics of powder snow avalanches mostly depend on the movement of the air phase between the particles, the entrainment of snow particles into the air and the mixing of the two phases. In contrast, the dynamics of dense flow avalanches is dominated by the solid particles.

1.2.4.1 Powder snow avalanches

Powder snow avalanches consist of clouds of snow, which rapidly flow down a mountain site. Due to their airborne character, the major part of these avalanches does not follow ground structures but take the steepest possible pass down the mountain slope. These avalanches can reach great flow heights of up to 100 m (Hopfinger, 1983) and velocities of 50-100 m/s (Ancey, 2001b), which indicates their huge impact force and destructive power. The avalanche usually behaves like a turbulent two-phase flow, which causes further uptake of material from the snow cover during the flowing process and results in

sometimes hazardous winds (Pudasaini and Hutter, 2007). Powder snow avalanches can only form from dry snow, where no cohesion is present and are therefore typical for dry climates. Usually large clouds of snow are also caused by the traveling of dry dense snow avalanches through air entrainment (Turnbull and McElwaine, 2007). In these cases, the powder snow can often travel faster and thus overtake the dense snow avalanche, resulting in a cloud traveling ahead of the dense snow (Hopfinger, 1983; Pudasaini and Hutter, 2007).

1.2.4.2 Dense flow avalanches

In contrast to the turbulent powder avalanches, dense flow avalanches are laminar flows following a track guided by the topography. As a consequence, dense flow avalanches can be channelized just as debris flows, depending on the topography of the mountain. Free running dense snow avalanches usually develop a wedge-like shape and the greatest height (up to a few meters) is observed at the front of the avalanche (Hopfinger, 1983). A very intuitive way of classifying snow is its humidity: wet snow is cohesive and can be easily formed to balls, whereas dry snow is a non-cohesive granular material. Thus wet and dry snow avalanches can be distinguished. The cohesive wet snow avalanches are two-phase flows as the dry snow avalanches and display similar behavior as debris flows, while dry dense snow avalanches form cohesionless one-phase flows (Hopfinger, 1983; Iverson and Denlinger, 2001). The cohesion influences the initiation mechanisms (see below) as well as the flow behavior: due to the cohesive forces between the particles of a wet snow avalanche (usually snowballs of up to several dm in diameter or ice particles in water) that have to be overcome to move the avalanche forward, some of the avalanche's energy is consumed. This results in a lower average velocity for wet snow avalanches (10-30 m/s) compared to the more mobile, cohesionless dry snow avalanches (30-60 m/s) (Issler, 2003). Additionally, wet snow avalanches are more dense then dry snow avalanches (300-400 kg/m^3 compared to 50-300 kg/m^3) (Hopfinger, 1983). As a consequence, they cannot override the snow cover as easily as dry snow avalanches do and sometimes even plow down through it into the ground. These so-called ground avalanches are often observed in spring time, when the snow cover is wet throughout all layers as a result of higher temperatures, solar irradiation and rainfall (Hopfinger, 1983; Pudasaini and Hutter, 2007). When huge amounts of snow are warmed up they can also transform into small ice particles, especially when night temperatures are still freezing. When warmed up again, such ice particles can built an ice-water slurry that literally flows down the slope and behaves more like a viscous fluid than a granular material (Hopfinger, 1983; Pudasaini and Hutter, 2007).

Release mechanisms

Dense flow avalanches can also be classified according to their rupture mechanism. An avalanche can either be initiated by a point failure or by a line fracture. Point failures are loose snow phenomena and can start with little material at one point of the slope. They can entrain further snow on their way but mostly result in rather small avalanches, which usually occur on slopes steeper than 45° (Hopfinger, 1983) and often stop before they reach the end of the slope. The deposit of such avalanches is often tongue-shaped. Often the snow cover is not loose but gained some cohesion due to slight transformation induced either by the weight of heavy snow fall or by temperature differences. These conditions lead to the formation of layers in the snow cover. If so-called weak layers (planes where the layers do not stick together very well) are formed and new snow load, storms or artificial triggers like skiers cause the snow cover to break vertically, the upper layers start sliding down the slope over the lower layers (Schweizer et al., 2003). During the first meters of the track, the whole snow mass moves as an elastic block, which subsequently breaks apart, forming the granular matrix of the avalanche (Hopfinger, 1983). Such avalanches are termed slab avalanches (German:"Schneebrettlawine") and usually result in larger masses of snow being mobilized than in the case of point failures. They mostly occur in slopes between 30° and 45° (Margreth, 2007). The initial cohesion inside the sliding block should not be confused with the cohesion between the avalanche particles. Depending on the water content of the initial slab, dry and wet slab avalanches can occur. Especially dry snow is very prone of forming large slab avalanches. In this case, the resulting fragments of the slab form a cohesionless granular matrix, which can also develop a powder component (Pudasaini and Hutter, 2007).

1.2.5 Damages

Hazardous granular flows cause plenty of damages and loss of lives each year all over the world. Especially in mountainous countries such as Switzerland and Austria, hazardous granular movements are among the most common and dangerous natural hazards. In both countries, seven of the ten worst events in terms of fatal accidents caused by natural hazards from 1900 to 2012 were caused by landslides and avalanches (source: EM-DAT: The OFDA/CRED International Disaster Database www.emdat.be Université Catholique de Louvain Brussels Belgium). Since the occurrence of landslides and volcanic flows does not necessary follow a seasonal pattern, the destructive forces of these events are illustrated in the following paragraphs by single events and their consequences. In the case of avalanches, which occur each year in alpine regions, also yearly statistics are provided.

1.2.5.1 Landslides

Landslides are not as limited in terms of amount of material that can be mobilized as avalanches. The amount of snow in combination with the topography provides a natural upper limit to the volume an avalanche flow can acquire. In the case of landslides, whole mountain sides can be mobilized. Examples for such extreme landslides are several earthquake induced landslides in loess material in China in 1920. All together these hazardous events killed about 180,000 people. One of the blocks that were mobilized had dimensions of about 520 m to 2000 m and traveled for more than 3 km, together with another block of similar size it had a volume of $1.5 \cdot 10^7 m^3$ (Zhang and Wang, 2007). Beyond the fatal accidents, landslides also cause enormous economic damage due to demolition of homes and infrastructure. The worst landslide in terms of economic loss was a landslide in Peru in 1983, which caused damage of nearly one Billion US $ (source: EM-DAT: The OFDA/CRED International Disaster Database www.emdat.be Université Catholique de Louvain Brussels Belgium). Landslide may reach volumes up to $10^{12} m^3$, which results in extreme mobility due to a correlation between mobility and flow volume (Legros, 2002; Pudasaini and Miller, 2013)

1.2.5.2 Volcanic flows

The special danger of volcanic flows lies on the one hand in their height temperature but also in their long range. One of the deadliest lahar events in history, caused by the eruption of the ice-capped Nevado del Ruiz in Peru, impressively demonstrates these characteristics: the event killed about 23,000 people, of which many were living in villages more than 70 km away from the volcano. The lahar traveled 104 km in total and destroyed more than 5000 homes (Pierson et al., 1990; Legros, 2002; De Blasio, 2011).

1.2.5.3 Snow avalanches

Snow avalanches are frequent, seasonally reoccurring hazard in mountainous regions. In Europe, up to 300 people have been killed by avalanches in a single winter season (Ancey, 2001b). In addition to this, the economic loss due to avalanche damages is enormous. Most victims of huge, often unexpected wide ranging avalanches are caught inside of houses. The force of an avalanche can cut buildings in two, transport complete house away from their foundation and uproot complete forest areas (Voellmy, 1955; Bebi et al., 2009).

Although avalanches occur each year, there is great variation in the intensity and number of events. Unfavorable weather conditions like unusually strong precipitation, cold temperatures and strong winds can lead to accumulation of unusual amounts of snow and can trigger so-called avalanche winters (German: “Lawinenwinter”) and events that are

observed in this intensity only once in a century (German: "Jahrhundertlawine", meaning avalanche of the century) (Wilhelm et al., 2001). Such conditions were present in the February 1999, when two of the deadliest avalanches in the century happened within three days in Evoléne (Switzerland) and Galtür (Austria) and killed 12 and 31 people, respectively (Wilhelm et al., 2001; Barbolini et al., 2004; Schweizer and Seiler, 2007). Both avalanches were initially dry dense flow slab avalanches which developed a powder component and in the case of Evolène also involved wet snow in the lower slope parts (Barbolini et al., 2004; Schweizer and Seiler, 2007). Beyond these fatal accidents, the avalanche winter of 1999 caused an economic loss of more than 300 million SFR due to direct damage on houses and infrastructure (Nöthiger et al., 2002).

But the year 1999 also demonstrated that so far employed avalanche protection means were greatly successful: in the only winter with similar snow amounts in the 20th century, 1951, 98 people where killed by avalanches in Switzerland, while 17 were killed in 1999, despite the ever-growing alpine population and exploitation for winter sports (Wilhelm et al., 2001).

1.2.6 Protection against hazardous granular flows

There are various possibilities to prevent fatal incidents and infrastructure damage by hazardous granular flows. The simplest method is to avoid civil constructions and human activities in regions which are prone to such events. This is of course only possible for newly build houses and infrastructure. However, due to the wide spread occurrence of hazardous granular flows, avoidance is impossible in most cases. Nevertheless, it is probably the only method to protect human lives from volcanic lava and pyroclastic flows. Due to their enormous heat, no defense structures can be built against such flows. On the other hand, these events are the hazardous granular flows which are best predictable because of the seismic and volcanic activity associated with them. Therefore, evacuation is often possible. Landslides and snow avalanches often do not provide such warnings but can be to some extent predicted by empirical means when considering the snow/rainfall, temperature and soil/snow conditions. However, landslides can sometimes be predicted because of some slow creeping of the soil before the slide and by associated cracks in the soil. Although extremely important for evacuation and protection of human live, a warning can only help to protect mobile goods. Infrastructure can not be protected this way. The next intuitive way of protection would be to prevent the granular flow itself. Roads are for example protected from landslides by large nets spanned over the adjacent slopes. The nets aim to keep the rock/soil structure intact and prevent it from sliding onto the road. The flow of snow cannot be completely prevented, but many defense structures in alpine regions aim to prevent their acceleration and thus the formation of avalanches. Such defense structures are often found in alpine regions as protections from

snow avalanches, although some are also used for prevention of rock slides (Pudasaini and Hutter, 2007). They consists of snow fences, grids or nets arranged approximately normal to the slope and are placed in areas where avalanches may initiate. Thus, they are intended to anchor the snow in its place and prevent the formation of large avalanches by stopping creeping snow early on the track. The creeping snow forms a deposit in front of the defense structure, which leads to decrease of the flow velocity before reaching the structure (Margreth, 2007).

Two other ways of protection are widely employed for landslide and avalanche protection so far: the establishment of defense structures that either slow down, stop or redirect the granular flow and the controlled, intended release of a granular flow before a hazardous flow can be built. The second mostly applies to snow avalanches which are often triggered by explosions initiated from helicopters or special pipes installed on mountain tops. The avalanches are released before huge amounts of snow can accumulate and form hazardous avalanches and at times of day when skiing areas are closed.

The flow of a fully developed large avalanche can only be stopped by solid structures like walls. One example for such a wall are protection structure built to protect the village of Neskaupstaður (Iceland): here, two rows of so-called breaking mounds of 10 m height were built to first slow down avalanches and behind them a 17 m catching dam was built to finally stop the movement (Jóhannesson and Hákonardóttir, 2003). A natural defense structure to slow down or stop the movement of avalanches are forests, which should for that reason be especially conserved or re-planted in avalanche prone areas (Bebi et al., 2009).

The most common structure to redirect the flow are so-called galleries built over roadways (Pudasaini and Hutter, 2007). Instead of entering a road or railway passage, avalanches or landslides are caused to flow over the gallery and continue to flow downslope afterwards. The advantage of such structures is that they do not need to stop the complete flow, which would require great pressure resistance almost impossible to built, but only slightly redirect the flow without loosing much of its kinetic energy.

Another way to redirect the flow is to cause it to split into two parts with slightly different direction. This can be done by solid structures of a triangular/pyramidal shape with one edge facing the expected direction of the flow (Tai et al., 1999b; Pudasaini and Hutter, 2007). One example for such a defense structure are the dams built to protect the coastal village of Flateyri, Iceland. The village encountered a devastating avalanches in 1996 and afterwards three dams where built in a triangular, A-like shape, with two of them meeting at the point where further impacts where expected. In subsequent years, indeed avalanches were observed and were caught and channelized away from the village into the sea (Jóhannesson, 2001). Smaller examples are stones piled up as a pyramid at the slope facing side of houses that are found in Switzerland (`thomasmayerarchive.de/`

details.php?image_id=89108&l=english, 20.05.2013) and V-shaped wall built in front of houses in Austria (mearsandwilbur.com/structural_defenses.html, 20.05.2013).

A recently developed and more and more popular personal protection system is the so-called Avalanche Airbag System, a backpack that is inflated upon impact (abs-airbag.de, 03.06.2012). It lowers the density and increases the volume of a person and thus prevents the person from being buried in the avalanche because of the phenomenon of segregation (see section 1.1.1.3).

A maximum of protection can be achieved by combining several or all methods described above. To properly understand and to optimize such a combination, it is necessary to know and predict the behavior of the granular flow during initiation, flow in track and run-out phase as well as the exact time of flow occurrence. For these purposes, empirical observations over many years and simulations of granular flows are combined.

1.3 Predictions and modeling on granular flows

Empirical predictions and model-based simulation of granular flows are employed to answer various questions for protective purposes. The most important questions are: when will a hazardous event take place, where exactly will it take place, how much material will be involved, how far will the flow move into the valley and what velocities and heights will it reach. From the answers to these questions, it will be possible to create evacuation plans as well as to calculate the forces resulting from the flow onto infrastructure and defense structures. Predictions and simulations of granular flow are therefore divided in approaches dealing with the initiation of the hazardous event and approaches describing the actual flow of the granular material.

1.3.1 Initiation of a hazardous granular flow

There are two main components associated with the prediction of granular flow events: the time and the place. In most cases it is extremely hard to predict the exact time point of a landslide or avalanche in order to evacuate endangered areas, although some advances are made in this field recently (Sornette et al., 2004). In the case of landslides, this is even more difficult, since landslides can occur basically everywhere, while snow avalanches are at least restricted to snow covered mountains with a certain inclination. It is therefore easier to monitor avalanche endangered regions and predict avalanche events. Snow avalanche recording, prediction and warning has a long history and is therefore well developed, especially in the field of statistical risk predictions derived from empirical data. In the alpine regions of Europe, snow avalanche events have been reported since the middle ages and organized avalanche research has been started in the 19th century

(Pudasaini and Hutter, 2007). For this reason, the methods of snow avalanche prediction are presented as an example in the following paragraphs.

1.3.1.1 Permanent risk maps

Many avalanche prone regions are comprised in risk maps, which do at least display the probability of an avalanche event. To obtain risk maps for the safety oriented building of new infrastructure, it is necessary to predict the occurrence of hazardous granular flows in the region of interest for the next decades. Such risk maps are usually based on empirical data (for an example see www.planat.ch/en/authorities/hazard-maps, 20.05.2013), statistical models based on observed events (Eckert et al., 2008) or on combinations of empirical data with either analytically or numerically solved model equations and simulations (Jamieson et al., 2008). For single spots, for instance in the case of a house that is built inside an endangered area, simulations can be employed to design defense structures and to calculate the necessary strength of the walls (http://www.slf.ch/forschung_entwicklung/lawinen/lawinenschutz/index_EN, 20.05.2013). Such simulations rely more on the flow behavior than on the initiation and are described in detail in section 1.3.5.

1.3.1.2 Avalanche warning stages

During the winter season, avalanche research centers in alpine countries provide the inhabitants with daily (or even more frequently) updated avalanche risk assessments. These assessments are comprised in frequently updated hazard maps. For this purpose, the region of interest is divided in danger levels and these levels are indicated to mountaineers in the form of flags of different color and pattern. Hazard maps are for example provided by the Institute for Snow and Avalanche Research (SLF) (for Swiss) and meteo france (France). It is extremely hard to exactly predict time and place of avalanche formation, especially for hazardous deep slab avalanches (Jamieson et al., 2001), even if the snow cover height and snow quality is know at a given time point. Therefore, current avalanche risk maps and danger levels usually rely on empirical observations from former years. For this purpose, meteorologic observations like temperature, snowfall, humidity, solar radiation and wind as well as snow cover information like snow heights, snow quality, layer formation and water content are correlated with terrain information and risks are calculated according to empirical knowledge on the influence of the above mentioned factors (http://www.slf.ch/lawineninfo/zusatzinfos/howto/entstehung_bulletin_gross_d.jpg; 20.05.2013).

1.3.2 On-track behavior and run-out events in granular flows

To built defense structures of the right strength and dimensions, it is not only necessary to know where granular flows as avalanches are likely to occur but also to know which forces will affect the structures. A central parameter in designing defense structures is the so-called impact pressure, meaning the pressure that is applied on the structure when it is hit by the flow. This pressure has to be measured inside the flow and cannot, as the events themselves or the dimensions of the run-out zone and deposition, be observed and recorded from previous events. It can to some extent be estimated from the observed deposition and track, but such estimates are usually inaccurate since the actual flow height and involved mass of an avalanche is rarely recorded in detail. In addition to that, events like the European avalanche winter of 1999 demonstrate that empirical data are not sufficient to provide a realistic risk calculation. It is well possible, that extreme events not taken into account in the empirical risk assessment can occur also in future and this possibility needs to be taken into account for safety assessments (Ancey, 2012). For these reasons, modeling and simulations of granular flow dynamics are of extreme importance for the prediction of parameters like the impact pressure, flow heights and possible run-out distances. Thus, model-based predictions are an important mean for the construction of effective defense structures and the generation of hazard and risk maps.

1.3.3 The concept of modeling

Predictions of complex events like granular flows require simplification of the process in the form of physical and mathematical models. Models are simplified, abstract mirrors of reality, which allow to draw conclusions about the real world but may at the same time be handled by human measures or machines. Models can either be small scale experiments with controlled conditions or systems of equations which describe a certain situation. Often a combination of both is used in an iterative process, where experiments are used to establish simulation models, which in turn are tested with experiments and optimized to describe the observed phenomena. Usually, new models are combinations of already existing models, which were built during the history of physics over the last thousands of years. The challenge in building a new model is to decide which of the existing models and natural laws can be employed to describe the matter of interest in the most precise, effective and applicable way.

1.3.4 General models for down slope mass movement

To describe the movement of a granular mass down a slope, the most important feature to understand is the dissipation of energy. The material starts at an elevated location with

a certain potential energy that needs to be completely dissipated during the movement in order to make the mass stop again. Energy can be dissipated through interaction with the ground on which the material is sliding (the bottom friction) or through shearing resulting from the bottom friction, which causes interactions inside the material (internal friction). The flow behavior and the processes inside a flowing material are considered in rheological science. Therefore, an appropriate rheological model needs to be chosen or developed to describe the granular flow. The following paragraphs introduce the bottom sliding friction and the rheological models that have been employed to model granular flows so far.

1.3.4.1 Bottom friction models

Coulomb friction

When two solid bodies in contact move relative to each other, the Coulomb-type friction is the rate independent force effective in the opposite direction of the movement. The friction is only proportional to the normal force N acting on the sliding surface with a constant $\mu_b = \tan\delta$, where δ is the bottom friction angle between the two materials. The bottom friction angle is defined as the inclination angle at which a body resting on an inclined plane starts to slide down (Coulomb, 1773; Jaeger et al., 1989; Hutter and Koch, 1991; Savage and Hutter, 1991). The Coulomb friction force can be written as $F_C = -\frac{u}{|u|}\tan\delta N$, where u is the velocity of the flow.

Turbulent boundary layer

Some avalanche models consider (see section 1.3.5) the granular material as a fluid streaming over the ground and developing a turbulent boundary layer when high velocities are reached. The transition from laminar to turbulent flow can be estimated by the Reynolds number (Re) of a fluid in a given topography (Reynolds, 1883). Above a critical Reynolds number ($\mathrm{Re}_{\mathrm{crit}}$), the flow will display a turbulent behavior. The Reynolds number of a fluid depends on the density ρ , the viscosity η and the velocity u of the fluid as well as on the typical traveling length of the considered flow l and is defined as: $\mathrm{Re} = \frac{\rho \cdot u \cdot l}{\eta}$.

For a turbulent flow, the force causing energy dissipation due to friction is termed the friction loss F_f , which is the analog to the Coulomb-friction force in a fluid. It is proportional to the square mean of the flow velocity (Ludwieg and Tillmann, 1950; Landau and Lifšic, 1975).

1.3.4.2 Rheological models

The retraction of the granular material, which is caused by the bottom friction, may lead to shearing and thus additional stress generation inside the material. The employed rhe-

ological model should describe how the material reacts to the applied stress and which forces are active inside the material. This characteristic can be described by the shear-stress τ, which represents the force being effective on a plane in the material. As mentioned in section 1.1.1), a granular material can, depending on the applied kinetic energy, display characteristics of both a solid body and a fluid. Therefore, the models employed to describe the shear-stress of a granular material describe elastic behavior, which is applicable for a rigid body that can be deformed but returns to its original state upon stress removal, plastic behavior, which describes a rigid body that remains permanently deformed after stress removal and fluids, which display viscous behavior. Often these concepts are combined in models describing flow behavior of granular materials.

Coulomb-type intergranular interaction

Like the interaction with the ground, also the interaction between particles in a non-cohesive material can be described by Coulomb-type friction. The Coulomb friction is in this case proportional to the internal friction angle ϕ (constant of proportionality $\mu = \tan\phi$). The Coulomb friction force can then be written as $F_C = -\frac{\mathbf{u}}{|\mathbf{u}|}\tan\phi N$. From this force, τ can be calculated for any given plane, given the normal force and the internal friction angle are known.

Newtonian fluid

As a granular material in motion displays many characteristics of a fluid, several early models employed fluid mechanics to describe granular flows. The basic model of a fluid is a so-called Newtonian fluid, in which τ is linear proportional to the velocity gradient in the fluid, the shear-rate ($\dot{\gamma}$). The proportional constant is the viscosity η of the fluid: $\tau = \eta\dot{\gamma}$.

Non-Newtonian fluid

In a Non-Newtonian fluid, the viscosity is not constant but depends on other variable sizes like the shear-rate, the shear-rate history or time (a detailed review on Non-Newtonian fluids can be found in Nguyen and Nguyen (2012)). For the time-independent cases, the resulting viscosity is termed effective viscosity η_E.

Power law dependent viscosity

In power law dependent fluids, η_E depends on the shear-rate: $\eta_E = k\dot{\gamma}^{n-1}$. τ is therefore proportional to $\dot{\gamma}^n$: $\tau = (k\dot{\gamma}^{n-1})\dot{\gamma}$, where n denotes a number different from 1 for Non-Newtonian fluids and k is the flow consistency index. The flow consistency index ensures that the term $k\dot{\gamma}^{n-1}$ has the unit of a viscosity, therefore the unit of k is $\mathrm{Pa}\cdot\mathrm{s}^n$. In the case

of $n = 1$, k is equal to η and the fluid would display Newtonian behavior. For $n < 1$, the effective viscosity decreases with the shear-rate. Thus, the fluid flows faster upon shearing, the fluid appears to be "thinner". Such fluids are therefore termed shear-thinning fluids. Pseudo-plasticity is a synonym for shear thinning, as the the fluid behaves almost plastic at low shear rates. For $n > 1$, the effective viscosity increases with the shear-rate. Thus, the fluid appears to be"thicker" and is termed a shear-thickening fluid.

The Bingham model

A special case of a Non-Newtonian fluid is a Bingham plastic. Bingham performed experiments with suspensions of fine material (clay) in water at various concentrations (Bingham, 1917). Below a certain concentration of clay, the suspension behaves like a Newtonian fluid. Above a critical concentration, the clay behaves like a rigid body when low stress is applied. In contrast to that, it can regain a certain fluidity, when shear-stresses higher than a critical shear-stress τ_0, also termed yield stress, are applied. For $\tau > \tau_0$, τ is proportional to $\dot{\gamma}$ with an effective viscosity $\eta_E = \eta + \frac{\tau_0}{|\dot{\gamma}|}$. At shear-stresses slightly above τ_0, a Bingham material displays pseudo-plastic behavior. This is caused by very low values of $\dot{\gamma}$ and a resulting high effective viscosity. Upon increasing shear-rate, the effective viscosity becomes lower and approximates η, resulting in viscosity dominated behavior. A Bingham material thus displays viscoplastic behavior above τ_0 with elastic parts below τ_0 and is an example of a shear thinning Non-Newtonian fluid.

The Herschel-Bulkley relationship

Non-Newtonian fluids with a critical shear-stress τ_0 and a higher order relationship between $\dot{\gamma}$ and the viscosity can be described by the Herschel-Bulkley relationship (Herschel and Bulkley, 1926): $\tau = \tau_0 + k\dot{\gamma}^n$. In this case, $\eta_E = k\dot{\gamma}^{n-1} + \frac{\tau_0}{|\dot{\gamma}|}$. The Herschel-Bulkley relationship can also be interpreted as a general description of Newtonian and Non-Newtonian fluids, as for $n = 1$ and $\tau_0 = 0$ it describes a Newtonian fluid, while deviating values of n describe the Non-Newtonian behavior mentioned above. In the special case of $n = 1$ and $\tau_0 \neq 0$ it describes a Bingham material.

Time-dependent rheology

Certain materials are capable of memorizing their previous state when stress is applied. These materials will allow deformation upon stress exposure but will return to their previous shape after the stress has been released. In the case of fluids, which seem to flow during the application of stress (viscous behavior) but afterwards return to their previous form the term viscoelastic fluid is used. Examples for viscoelastic fluid models are

Oldroyd-B, Maxwell-A/B and UCM (upper connective Maxwell), for a detailed description see Bird et al. (1987), Fang et al. (2008).

The Bagnold model

A first granulate specific model for the shear behavior of granular material was established by Bagnold (1954): He performed experiments in which he exposed mixtures of spherical wax particles in viscous fluids with varying volume fractions of the solid particles to controlled shear stress. The particle diameter was constant and the density was chosen to equal the density of the surrounding fluid (water and a more viscous glycerol-water-alcohol mixture) in order to achieve neutral buoyancy. Bagnold characterized the relationship between τ and $\dot{\gamma}$ for this material in a drum with rotating side-walls. He found two different orders in the relationship, depending on the speed of the side wall:

At low speed, τ is proportional to $\dot{\gamma}^2$. He called this situation a grain-inertia regime. This is analogous to a shear-thickening Non-Newtonian fluid.

Above a certain speed, the material can be considered as a macro-viscous fluid. In this case τ is proportional to $\dot{\gamma}$ and the proportional constant is the viscosity η as for Newtonian fluids.

1.3.4.3 Continuum mechanics models

Once a bottom friction model and a rheology have been chosen, the next step is to calculate how the forces influence the movement of the granular material. To calculate the velocity field of a continuous and deformable mass, continuum mechanics models are employed. The continuum mechanics model for momentum is the Cauchy momentum equation, which describes the conservation of momentum at a given point inside the continuous material:

$$\rho \frac{D\mathbf{u}}{Dt} = \nabla \cdot \boldsymbol{\sigma} + \mathbf{f} \tag{1.1}$$

In this equation, ρ is the bulk density of the material, $\boldsymbol{\sigma}$ denotes the Cauchy stress tensor, which includes the pressure inside the material and the shear-stress, and $\mathbf{f}$ denotes the body forces (in the case of a granular material sliding down a slope this is only gravity). The solution of this equation yields the velocity field of the material. The specialization of the Cauchy momentum equation for Newtonian fluids is described in the Navier-Stokes equations. In this case, for σ the shear-stress of a Newtonian fluid is chosen (Hutter and Jöhnk, 2004).

A simplification of the Navier-Stokes equations can be achieved by depth-integration. Depth-integration means, that the velocity profile through the depth of a flow is ne-

glected, the velocity (u) of the flow at a given point is averaged over the whole depth of the flow ($\bar{u}$). This simplification can be made if the flow height (h) is very small compared to the flow length (s). Since it was first introduced in hydrodynamics for water models, the resulting equations for a gravity (g) flow are termed Shallow-Water equations (de Saint-Venant, 1871; Stoker, 1948):

$$\frac{\partial h}{\partial t} + \frac{\partial}{\partial s}(\bar{u}h) = 0 \tag{1.2}$$

$$\frac{\partial h\bar{u}}{\partial t} + \frac{\partial (h\bar{u}^2)}{\partial s} = -\frac{\partial}{\partial s}\left(\frac{1}{2}gh^2\right) \tag{1.3}$$

However, in these equations, viscous stresses are neglected and the flow is only driven by a pressure gradient.

1.3.5 Models for granular flows

This section provides a short overview on some models that have been employed to describe hazardous rapid granular flows in the past. Since the first models were developed for snow avalanche dynamics, we will focus mainly on this field. Another specialty to snow avalanches is that several test sides were established in alpine regions to measure important parameters like impact pressure, run-out distance and overall flow movements on real scale avalanches. For this purpose, pressure and velocity sensors as well as laser-scanning devices were installed at selected places which are prone for avalanches. Avalanches observed at these sites can then either be of natural origin or artificially triggered by explosions. Such experimental sites are for example found in the Swiss "Vallée de la Sionne", at the French "Col du Lautaret", at Ryggfonn, Norway and at "Seehore" in the Aosta Valley, Italy (Barbolini and Issler, 2006; Maggioni et al., 2012). Results from these natural test sites are employed on the one hand to test existing models and on the other hand to continuously improve them (Sovilla and Bartelt, 2002; Meunier et al., 2004). Nevertheless, the model developed for snow avalanches can also be applied to rockslides and other hazardous granular flows e.g. pyroclastic flows and debris avalanches (Körner, 1976; Crosta et al., 2004; Pudasaini and Hutter, 2007; Christen et al., 2012; Deubelbeiss and Graf, 2013). The different models differ in the rheological model and in the amount of empiric data or physical deduction used to built the model.

1.3.5.1 Voellmy model

After several strong winters in the early 1950s, in which avalanches reached onto places where no avalanches had been observed since the beginning of recording at the beginning of the 20th century, the need for predictions and physical descriptions of avalanches

became obvious. One of the first scientist replying to this need was Voellmy (Voellmy, 1955), who collected data about the damages caused by several of the most destructive avalanches in Switzerland at this time and used this data to estimate the velocities and forces that were effective during the avalanche flow. He then made use of this data to establish the first mathematical model to describe the movement of an avalanche as a flow and thus according to hydrodynamics.

From his observations, Voellmy came to the following conclusions: at the beginning of the flow, the complete slab is moving in a slow laminar way. With increasing velocities, the flow becomes turbulent. In the case of a slab avalanche Voellmy considers the point when the slab is breaking up into several granular particles as the transition point from laminar to turbulent flow. The flow of the avalanche over most parts of the track is thus characterized by turbulent flow according to Voellmy. He therefore suggested a combined turbulent and Coulomb friction force F_r affecting a particle in a flow with the height h on a slope with an inclination angle ζ which can be described as:

$$F_r = -\rho \cdot g \cdot h \cdot \cos\zeta \cdot \mu - \frac{\rho}{\xi} \cdot u^2 \tag{1.4}$$

Voellmy used the model of turbulent flow to explain the appearance of a term proportional to the square of the flow velocity (u). In this model he introduced the two fit parameters μ (proportional constant of the Coulomb friction, see above) and the sliding coefficient ξ, which have to be estimated from observed avalanches. Since Voellmy treated the granular material at the initial phase as a rigid block, μ was not calculated from the internal friction angle but estimated from observations and ξ was estimated from values observed in hydraulics.

By using estimates of these two parameters, Voellmy was able to calculate the estimated maximal velocity and pressure effective in an avalanche at one point. Further investigations were later on performed to yield better estimates from large avalanche events (Buser and Frutiger, 1980).

1.3.5.2 Extensions to the Voellmy model

The first attempt to describe the movement of avalanches as a granular material was introduced by Salm (1966). He considered the material of the avalanche as a cohesionless granular material with internal friction and modified Voellmys model (Voellmy-Salm (VS) model).

One crucial difference between a fluid and a granular material is the pressure distribution inside the material. Inside a fluid, the pressure is constant at a given height inside the fluid and independent of direction. The same pressure effecting the bottom of a fluid cell also effects the walls. This is not the case for a granular material. Due to interac-

tions between the particles, the pressure can be distributed over long distances and in an asymmetric way. This fact is long known for soil mechanics, where the pressure caused by a soil that is held back by a wall is of great importance. The theory describing such phenomena is termed earth-pressure theory. Three different kinds of earth-pressures are considered: the earth-pressure at rest, the active earth-pressure (the minimum pressure a wall needs to withstand to prevent adjacent soil from failure) and the passive earth-pressure (the maximum pressure that can be applied to a soil before a failure occurs). According to Rankine (1857), the earth-pressure depends on the internal friction angle (ϕ) and is defined as

$$k_{act/pass} = \tan^2\left(45° \pm \frac{\phi}{2}\right), \tag{1.5}$$

where +,- indicated passive and active earth pressure, respectively. Salm implemented this term in Voellmy's model and received the following equations for the conservation of mass and momentum to describe the full evolution of the avalanche movement:

$$\frac{\partial h}{\partial t} + \frac{\partial (uh)}{\partial s} = 0 \tag{1.6}$$

$$\frac{\partial u}{\partial t} + u\frac{\partial (u)}{\partial s} = g\sin\zeta - \mu g\cos\zeta - \frac{gu^2}{h\xi} - \frac{\partial}{\partial s}\left[k_{act/pass} g\cos\zeta \frac{h^2}{2}\right] \tag{1.7}$$

where s is the coordinate along the slope, g is the gravity constant and all other parameters are employed as described above (Salm et al., 1990; Salm, 2004).

These model equations and numerical simulations based on them have been used for many years to predict avalanche flows for the construction and improvement of risk maps in Switzerland (Sovilla and Bartelt, 2002). Further improvement of the numerical simulations and generation of detailed tables for μ and ξ at different elevations, topographies and return periods have led to the development of the software packages AVAL-1D and RAMMS, which are currently in used for hazard map generation and flow simulations (Christen et al., 2002; Jamieson et al., 2008; Christen et al., 2010a). Current research focuses on improvements of the Voellmy-Salm model implemented in RAMMS for application to complicated topographies and on improvement of the physical significance by reducing the parts which require fit parameters (Fischer et al., 2012).

North American hazard maps are often based on another modification of Voellmy's model, the Perla, Cheng and McClung (PCM) model (Perla et al., 1980; Jamieson et al., 2008). The PCM model is, as the VS model based on Coulomb friction, but the fit parameters μ and ξ are replaced by the mass-to-drag ratio M/D. M/D has to be calibrated from previous events and is thus a fit parameter as well (Jamieson et al., 2008).

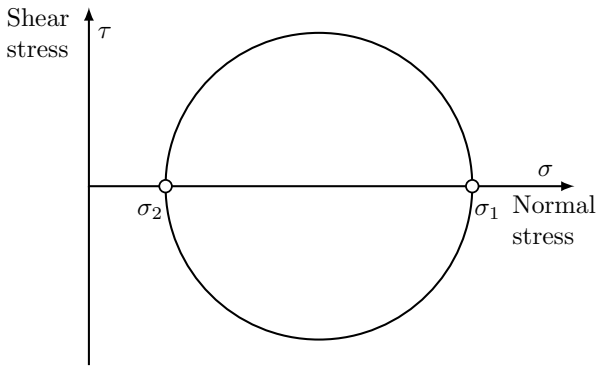

Figure 1.2 – Example of a Mohr-circle spanned by the two maximal and minimal stresses that are effective in the two perpendicular planes in which no shearing stress is effective (σ_1 and σ_2). All possible combinations of τ and σ that can be observed in the considered object have to be on this circle.

Nevertheless, all these models still contain the fit parameters μ and ξ (VS) or M/D (PCM) which cannot be determined exactly for a given event but are usually fitted according to previously observed events.

1.3.5.3 Savage-Hutter

In 1989, Savage and Hutter suggested a model in which the earth pressure was determined by a so-called Mohr-Coulomb criterion (Savage and Hutter, 1989). For this criterion, Coulomb's friction law is combined with a Mohr circle (Jung, 1947). A Mohr circle is a graphical way of displaying all combinations of shear and normal stresses (τ and σ) associated with different cutting planes of a body. In a diagram where the y-axis denotes the shear stress and the x-axis denotes the normal stress, the circle is spanned by the two maximal and minimal stresses that are effective in the two perpendicular planes in which no shearing stress is effective (σ_1 and σ_2, where $\sigma_1 > \sigma_2$) (Fig. 1.2).

For their avalanche model, Savage and Hutter considered a square element of granular material sliding down an inclined plane. As described above, Coulomb's law applied to a granular material yields two minimum forces, above which movements will occur. These are associated with the bottom friction and the internal friction. According to the relations described in section 1.3.4, the block will start to slide down the plane when forces higher than $F_C = -\frac{\mathbf{u}}{|\mathbf{u}|}\tan\delta N$ are applied, while the block will shear internally due to the overcome of internal friction, when higher forces than $F_C = -\frac{\mathbf{u}}{|\mathbf{u}|}\tan\phi N$ are applied. These two yield criteria can be displayed in the Mohr circle by two lines with the slope $\mu_b = \tan\delta$ and $\tan\phi$ respectively (Fig. 3.2). Savage and Hutter assumed that the normal pressure that is effective on a plane at the bottom of the square (that is not a plane parallel to the inclined plane) is given by the hydrostatic pressure $\sigma = \rho \cdot g \cdot h\cos\zeta$. The stress combination, at which sliding starts is thus the point on the $\tan\delta$ line at which this value

of sigma is reached. This point characterizes one point that has to be on the Mohr cycle for the considered block. If now additionally also the yield criterion for an internal failure should be reached, the respective cycle needs to be drawn in a way that the $\tan\phi$ line is a tangent. There are exactly two cycles possible that will fulfill this criterion (Fig. 3.2). From this construct, the active and passive earth pressure ($k_{act/pass}$) effective in the granular material can be determined in a geometric way as functions of ϕ and δ. With this assumption, Savage and Hutter formulated the following set of partial differential equations for conservation of mass and momentum:

$$\frac{\partial h}{\partial t} + \frac{\partial}{\partial s}(uh) = 0 \tag{1.8}$$

$$\frac{\partial u}{\partial t} + u\frac{\partial (u)}{\partial s} = \left(\sin\zeta - \mu_b \frac{u}{|u|}\cos\zeta\right) - \beta\frac{\partial h}{\partial s} \tag{1.9}$$

The earth pressure (see section 3.36) is integrated into the model via β as follows:

$$\beta = \epsilon k_{act/pass}\cos\zeta \tag{1.10}$$

Here, the aspect ratio ϵ is defined by a typical span or spread of the slight (L) and a typical depth (H): $\epsilon = \frac{H}{L}$.

Note that here, in contrast to Salm's model, the bottom friction angle δ in μ_b is used to describe the Coulomb part of the movement and not the internal friction. Due to the determination of the earth pressure by using both ϕ and δ, the Savage-Hutter model is the first to include both characteristic friction angles of a granular material in an avalanche model. In this model, the flow is determined when these two material parameters are known. Since ϕ and δ can be determined in experiments, the model offers a complete physical description of a granular flow without any fit parameters.

In the following years, the Savage-Hutter (SH) model was extended to more complicated flow situations, by both the establishment of new mathematical model components and laboratory experiments employed to achieve a realistic description of a granular flow. This process is described in detail in section 3.2.

1.3.5.4 Other models

A Norwegian model, suggested by Norem, Irgens and Schieldrop (NIS-model), describes the flow of an avalanche by a Criminale-Ericksen-Filbey-rheology, assuming that the mass does not slight down as a block but generates a velocity profile in depth (Bartelt et al., 1999). For this purpose, a shear viscosity and viscoelastic elements are included in the model (Norem et al., 1987). This model was shown to yield good results in predicting

entrainment of snow during avalanche flow Sovilla and Bartelt (2002).

Another suggestion for the simulation of snow entrainment during avalanche motion was made by Bovet et al. (2010): they employ a non-Newtonian fluid model with shear thinning as suggested by Bingham. The model is an example of a non-depth-integrated model and thus has a potential to be extended three dimensions. However, the authors state that the model requires long calculation time and can therefore not directly be conveniently employed for hazard map generation.

The Austrian avalanche dynamics software SAMOS-AT employes an extended, depth-averaged Voellmy model in combination with a mixture model describing the behavior of ice and air fractions to model dense flow avalanches with powder components (Sauermoser, 2006; Sampl, 2007). A previous version (SAMOS99) employed a SH-type description for the dense flow part, but was revised in the SAMOS-AT version since the SAMOS99 software overestimated the lateral and longitudinal spread of the avalanche (Granig and Oberndorfer, 2008).

1.3.5.5 Common features, differences and limitations of currently available models

Since the beginning of avalanche modeling in the 1950's, more than 30 models for the description of avalanche flows have been developed (Harbitz, 1998). Detailed reviews on existing models for avalanche dynamics can be found in Harbitz (1998), Jamieson et al. (2008). Although different rheologies are employed in these models, a clear dominance of Coulomb-type friction descriptions is visible in the field, especially since all models employed for hazard mapping are based on Coulomb-type friction assumptions. As described above, huge differences are found in the required input parameters. Commonly used and well established simulation methods like RAMMS require fit parameters, while the Savage-Hutter model for example only requires the material parameters ϕ and δ, which enables the model to be transferred to other materials like debris (Pudasaini, 2012). One common feature of all models employed for hazard assessment of dense flow avalanches so far is their depth-averaged character, meaning that velocity profiles in the flow depth are neglected, although they have been demonstrated to exist at least in experiments (Kern et al., 2004; Barbolini et al., 2005). Thus, no true three-dimensional simulations are possible (Jamieson et al., 2008) and important parameters like the impact pressure can only be estimated from the averaged velocities in the depth. So far developed non-depth-averaged models were mostly tested on laboratory experiments and their applicability to real three-dimensional topographies remains to be demonstrated (e.g. Jop et al. (2006) and Ancey et al. (2012)). However, a great advantage of the depth-averaged simulations is their limited requirement for calculation power compared non-depth-averaged simulations.

1.3.6 Nummerical methods to solve model equations

The final goal of modeling the flow of a granular material is to describe the complete flow for given initial and boundary conditions. The partial differential model equations mentioned above describe the continuous flow of a granular material in time and space. In contrast to Voellmy's considerations for one point (the moment and space where the maximum velocity is reached), equations (1.6) to (1.9) cannot be solved in an analytic way. A way to nevertheless solve the problem is a numerical solution. For this purpose, time, space and equations are discretized and the flow evolution is calculated step by step using algebraic equations which approximate the partial differential model equations. Several methods for the discretization were established so far and employed to solve flow behavior problems. The most important among those are the finite differences method (FDM), the finite element method (FEM) and the finite volume method (FVM). A common feature of all methods is the discretization of space and time in a grid. In the following paragraph, first the possible grids are described and then the different discretization methods are shortly introduced and their advantages and disadvantages for the modeling of granular flows are discussed. In principle, all methods should result in the same solution for very fine grids, but such a fine grid can usually not be achieved due to limits in calculation power. Therefore, the most suitable discretization method for the problem of interest has to be selected (Ferziger and Peri, 1999).

1.3.6.1 Grid

Structured (regular) grid

A structured regular grid would be a Cartesian grid, where all axis of a Cartesian coordinate system are divided into discrete parts by drawing orthogonal lines. These lines do not necessarily have the same distance from each other but are all parallel. In such a grid, every cell has a defined number of neighboring cells (four in 2D and six in 3D). By giving indexes to the cells, the next and second next neighbor of each cell in one direction is defined as the index plus one or two respectively. Thus, the grid has a neighbor connectivity, which is important for some numerical processes. A structured grid can be also skewed in a way that the angles are no longer 90° but the neighbor connectivity has to be conserved. The cell in such grids always have the shape of tetragons or cuboids. These properties make it hard and complicated to model for example obstacles, since they require a fine grid structure. Because of the structure restrictions, a finer grid at the place of an obstacle would also cause all other parts of the grid to became finer and thus elevate the calculation power required (Ferziger and Peri, 1999).

Unstructured grid

In an unstructured grid, the cells can be of any shape and the shape does not have to be the same for all cells. This allows subdivision of cells in the place of an obstacle and modeling of complex geometries as for example needed for the simulation of an avalanche encountering a defense structure. On the other hand, the neighbor connectivity does no longer exist in this type of grid, since one cell can have several neighbors in one direction if the neighboring cell was split (Ferziger and Peri, 1999).

1.3.6.2 Discretization methods

FDM

The FDM makes use of the Taylor approximation of the partial derivatives in the conservation equation to obtain algebraic equations. Thus, the single partial derivatives are displayed as local differences between neighboring cells, making the method very simple and intuitive. On the other hand, all partial derivatives (for example the velocity down slope and perpendicular to the slope) are considered separately and thus the method is not conservative per se. Additionally, because of this consideration of neighboring cells, the FDM has so far only been used for structured grids and thus has a limitation for complex flows (Ferziger and Peri, 1999). However, older types of avalanche simulations often employ this method because of its simplicity (Norem et al., 1987; Christen et al., 2002; Jamieson et al., 2008).

FVM

This method considers volumes instead of the single points in the grid considered in the FDM method. The variables are calculated for the center of the volume and the conservation equations are used to calculate integrals that denote the flow through the boundary planes of the volumes. For this purpose, the velocities at the boundaries need to be interpolation from the centers of the volume. In contrast to the FDM, the FVM can be applied to complex geometries described by unstructured grids and is conservative, since the flow through all boundary planes is considered at the same time. A disadvantage of the FVM is that higher order terms are hard to cope with, since they would require information about the second or higher next neighbor for the interpolation and as mentioned above, these neighbors are not uniquely defined in complex grids (Ferziger and Peri, 1999). FVM is for example employed in the RAMMS software and thus widely used for hazard mapping purposes (Christen et al., 2010a).

FEM

The FEM is very similar to the FVM but additionally makes use of weighting base functions inside the cell, which allows to account for the distribution of parameters in the cell by weighting of the equations before the integration. This allows the method to be applied to more complex geometries, since the interpolation is no longer necessary (Ferziger and Peri, 1999).

The two methods employed in this work (FDM and FVM) are described in detail in chapter 4.

The ultimate goal of granular flow dynamics simulations is to accurately predict the flow shape and velocities at any given point during the motion. Furthermore, these simulations should ideally yield exact information about the spatial and temporal pressure and velocity distribution in the granular flow. These parameters are of special importance for the calculation of the impact pressure, which is directly related to the hazardous power of a natural granular flow. Ideally, the simulations should require a minimum of input parameters and those parameters should be easy to determine for a given material.
To contribute to this goal, the present study aims to address the following tasks:

1. Design of a small scale experimental model for a rapid granular flow

The designed small scale experiments should, on the one hand, help to gain more insight into the actual velocity profiles occurring during a granular flow, and, on the other hand serve as a validating experiments for existing and developed simulations. The design of the experiments has to allow measurements of the flow shape and velocities. For this purpose, a goal of this study is to introduce experimental set-ups which allow capturing of the flow with a high-speed camera system. This image recording system is coupled to a particle image velocimetry image analysis software established in this study. The resulting information is used to select the underlying rheological model for simulations of the experimental flows.

2. Simulation of the performed experiments with existing depth-averaged models for granular flows

To test the predictive power of state-of-the-art granular dynamics numerical simulations and to elucidate their range of applicability and limitations, the widely used depth-averaged Savage-Hutter model is employed to simulated the experimentally observed flows.

3. Developing a novel, non-depth-averaged type of simulations for granular flows

Taking together the information obtained from the two first tasks, the third part aims to develop a new kind of numerical simulation for rapid granular flows. The rheological information obtained from the experiments is implemented in a simulation software usually used for fluid dynamics. This should enable more precise and complete prediction of the granular flow in situations where classical depth-averaged simulations fail to predict the flow behavior. Especially, the spatial velocity distribution in the flow depth direction should be predictable with these simulations.

In this work, two types of numerical simulations are employed to simulate rapid granular flows. As a state-of-the-art model for depth-averaged simulations, the Savage-Hutter model was chosen. This model has been widely used for the simulation of laboratory experiments on rapid granular flows with good agreements (e.g. in Koch et al. (1994), Greve et al. (1994), Pudasaini and Kröner (2008), Cui and Gray (2013)). Implied by the depth integration, the Savage-Hutter type simulations are always limited to two dimensions, even when three-dimensional topographies are considered. Thus, shearing inside the material and velocity profiles in depth are neglected, which results in a less accurate description of the flow. This can lead to inaccurate predictions of the flow behavior especially in situations with strong internal shearing as it is the case when the flow encounters an obstacle or when deposition occurs (Pudasaini et al. (2007) and this work, chapter 6). For these reasons, the accurate description and prediction of such events requires a non-depth-averaged description. This is realized in this work by employing a simple Coulomb friction assumption in a hydrodynamic approach. This chapter first describes the basic conservation equations for continuum mechanics used in both the depth-averaged and the non-depth-averaged approach, then presents the essential model equations for the non-depth-averaged approach (section 3.1.2) and finally describes the deduction of the essential model equations of the Savage-Hutter model as well as experiments which were performed to further develop the model (section 3.2). Additionally, previous considerations for the generation of a non-depth-averaged description for granular flows, which have influenced this work, are mentioned in section 3.3.

3.1 Governing equations of continuum mechanics

An ideal continuum is a material, whose infinitesimal small parts would still display the same behavior as the complete material. Although all materials are discontinuous distributions at a certain scale (e.g. a mass of particles with air filling the space in-between them or atoms with empty space between them), they often display continuous behavior at macroscopic scales, as if their whole space of occupancy was completely filled with the material. A fluid (or granular material) can be considered as continuum when the observed length-scales are significantly larger than the scale of the material components (the molecules of the fluid or the individual particles). Additionally, the intensive (scale invariant) quantities density, pressure and velocity field have to be differentiable. If these criteria are met, the motion of the material can be described by continuum mechanics.

There are two general ways of observing the motion of a fluid: an external and an

internal observation. From an external observer position, a certain position in space is observed and the evolution of the fields of interest is observed for this position. In the case of an internal observation, a certain volume of the fluid is observed and the evolution of the fields in this volume is considered. The derivative of a field is termed Eulerian derivative in the case of an external observation and convective, Lagrangian or material derivative in the case of internal observation.

3.1.1 Basic conservation equations

Given an Eulerian derivative $\frac{\partial}{\partial t}(\star)$ of a quantity $(\star)$, the material derivative is defined as the operator:

$$\frac{D}{Dt}(\star) := \frac{\partial}{\partial t}(\star) + \mathbf{u} \cdot \nabla(\star), \tag{3.1}$$

where the second term on the right represents changes of the quantity with respect to position, while the quantity moves with the velocity $\mathbf{u}$ of the fluid.

According to Reynolds' transport theorem (Reynolds, 1903), the change of an intensive quantity Φ in a continuum with a density of ρ integrated over a control volume V has to equal the amount transported (in and out) through boundaries of the control volume plus the amount created or consumed by sources or sinks ($\mathbf{Q}$) (Aris, 1989; Hutter and Jöhnk, 2004; Jasak, 1996):

$$\frac{d}{dt}\int_V \rho\Phi(\mathbf{x},t)dV = \frac{\partial}{\partial t}\int_V \rho\Phi dV + \oint_{\partial V} d\mathbf{S}\cdot(\rho\Phi\mathbf{u}) = \int_V Q_V(\Phi)dV + \oint_{\partial V} d\mathbf{S}\cdot\mathbf{Q}_S(\Phi), \tag{3.2}$$

where $\mathbf{Q}_S$ and Q_V are the surface and volume sources, respectively.

This fact can be also denoted in differential form:

$$\frac{\partial\rho\Phi}{\partial t} + \nabla\cdot(\rho\Phi\mathbf{u}) = Q_V(\Phi) + \nabla\cdot\mathbf{Q}_S(\Phi). \tag{3.3}$$

The governing equations of continuum mechanics can be written in the form of (3.3) (Aris, 1989; Jasak, 1996), where the conservation of linear momentum equates the Cauchy momentum equation (see section 1.3.4.3):

- Conservation of mass ($\Phi = 1$, no internal sources or sinks of mass)

$$\frac{\partial\rho}{\partial t} + \nabla\cdot(\rho\mathbf{u}) = 0 \tag{3.4}$$

- Conservation of linear momentum ($\Phi = \mathbf{u}$, $Q_V(\Phi) = \rho\mathbf{g}$ and $\mathbf{Q}_S(\Phi) = \boldsymbol{\sigma}$)

$$\frac{\partial \rho \mathbf{u}}{\partial t} + \nabla \cdot (\rho \mathbf{u}\mathbf{u}) = \rho \mathbf{g} + \nabla \cdot \boldsymbol{\sigma} \tag{3.5}$$

- Conservation of angular momentum[1] ($\Phi = \mathbf{x} \times \mathbf{u}$, $Q_V(\Phi) = \rho(\mathbf{x} \times \mathbf{g})$ and $\nabla \cdot \mathbf{Q}_S(\Phi) = \mathbf{x} \times (\nabla \cdot \boldsymbol{\sigma})$)

$$\frac{\partial \rho(\mathbf{x} \times \mathbf{u})}{\partial t} + \nabla \cdot (\rho \mathbf{u}(\mathbf{x} \times \mathbf{u})) = \rho(\mathbf{x} \times \mathbf{g}) + \mathbf{x} \times (\nabla \cdot \boldsymbol{\sigma}) \tag{3.6}$$

with the position vector $\mathbf{x}$.

These conservative laws are valid for any continuum but the number of unknown quantities is larger than the number of equations. The next paragraphs will explain how σ can be expressed, leaving an equal number of equations and unknown quantities. To achieve a lower number of unknown quantities than equations, the pressure field has to be determined, which will be described in chapter 4.

3.1.2 Newtonian fluids

As described in paragraph 1.3.4, the stress tensor σ of a fluid can be determined using rheological models. For Newtonian fluids with the generalized form of the Newton's law of viscosity σ is defined as:

$$\boldsymbol{\sigma} = -\left(p + \frac{2}{3}\mu \nabla \cdot \mathbf{u}\right)\mathbf{I} + \mu\left[\nabla \mathbf{u} + (\nabla \mathbf{u})^T\right]. \tag{3.7}$$

Introducing this σ (3.7) into the above mentioned system of equations yields the Navier-Stokes equations (see also section 1.3.4.3):

$$\frac{\partial \rho}{\partial t} + \nabla \cdot (\rho \mathbf{u}) = 0 \tag{3.8}$$

$$\frac{\partial \rho \mathbf{u}}{\partial t} + \nabla \cdot (\rho \mathbf{u}\mathbf{u}) = \rho \mathbf{g} - \nabla\left(p + \frac{2}{3}\eta \nabla \cdot \mathbf{u}\right) + \nabla \cdot \left[\eta\left(\nabla \mathbf{u} + (\nabla \mathbf{u})^T\right)\right]. \tag{3.9}$$

The system can be further simplified by assuming incompressible fluids ($\rho = const.$):

$$\nabla \cdot (\mathbf{u}) = 0 \tag{3.10}$$

$$\frac{\partial \mathbf{u}}{\partial t} + \nabla \cdot (\mathbf{u}\mathbf{u}) = \mathbf{g} - \nabla p_{kin} + \nabla \cdot (\nu \nabla \mathbf{u}) \tag{3.11}$$

with a kinetic viscosity $\nu = \frac{\eta}{\rho}$ and a kinematic pressure of $p_{kin} = \frac{p}{\rho}$.

[1] Combining (3.5) and (3.6) states that $\boldsymbol{\sigma}$ is a symmetric tensor: $\boldsymbol{\sigma} = \boldsymbol{\sigma}^T$

In these equations, different rheological models can be employed for ν and η.

3.2 Savage-Hutter Model

In this section, the derivation of the Savage-Hutter (SH)-equations denoted in section 1.3.5.3 is described for slopes with low variance in inclination angle following Savage and Hutter (1989).

3.2.1 Governing equations

The Savage Hutter Model assumes an incompressible nonviscous solid with the negative Cauchy stress tensor $\sigma = -\mathbf{p}$.

Therefore, (3.4) and (3.5) can be written as:

$$\nabla \mathbf{u} = 0 \tag{3.12}$$

$$\frac{\partial \mathbf{u}}{\partial t} + \nabla \cdot (\mathbf{u}\mathbf{u}) = -\frac{1}{\rho}\nabla \cdot \mathbf{p} + \mathbf{g}. \tag{3.13}$$

In these equations, $\mathbf{u}$ denotes the velocity vector, ρ the constant density, $\mathbf{p}$ the pressure tensor and $\mathbf{g}$ the vector of gravitational acceleration.

To specify the equations for the considered problem, boundary conditions are needed. Describing the free surface by the function $F_S(\mathbf{x}, t) = 0$ firstly facilitates defining the kinematic statement that the free surface is material and secondly expresses the stress-free conditions:

$$\left.\begin{aligned} \tfrac{\partial F_S}{\partial t} + \nabla F_S \cdot \mathbf{u} &= 0 \\ \mathbf{p} \cdot \mathbf{n} &= 0 \end{aligned}\right\} \text{ at } F_S(\mathbf{x}, t) = 0 \tag{3.14}$$

Analogously, the bottom surface can be described as $F_B(\mathbf{x}) = 0$. With a solid friction law, the local friction angle δ, the shear traction $\mathbf{S}$ and the normal stress $\mathbf{N}$ can be expressed by $\mathbf{S} = \mathbf{n}\cdot\mathbf{p} - \mathbf{n}(\mathbf{n}\cdot\mathbf{p}\cdot\mathbf{n})$ and $\mathbf{N} = \mathbf{n}\cdot\mathbf{p}\cdot\mathbf{n}$. With these assumptions, the two boundary conditions of the bottom surface can be written as:

$$\left.\begin{aligned} \mathbf{u} \cdot \mathbf{n} &= 0 \\ \mathbf{n}\cdot\mathbf{p} - \mathbf{n}(\mathbf{n}\cdot\mathbf{p}\cdot\mathbf{n}) &= -\left(\tfrac{\mathbf{u}_s}{|\mathbf{u}_s|}\right)(\mathbf{n}\cdot\mathbf{p}\cdot\mathbf{n})\tan\delta \end{aligned}\right\} \text{ at } F_B(\mathbf{x}) = 0 \tag{3.15}$$

Savage and Hutter chose a plane Cartesian coordinate system (Fig. 3.1).

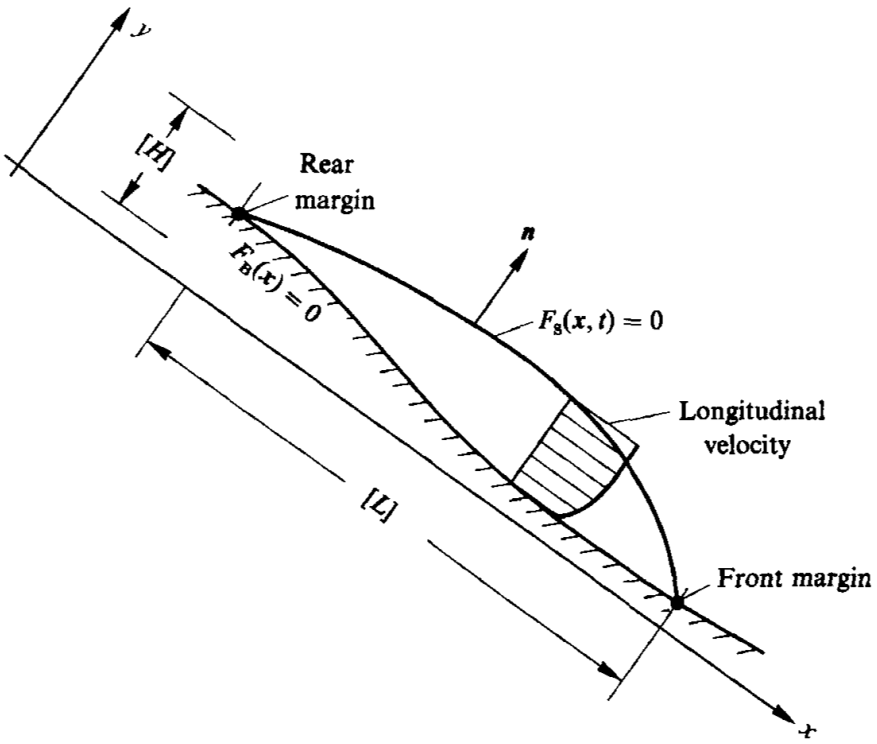

Figure 3.1 – Sketch of the geometry assumed by Savage and Hutter (1989). Picture taken from Savage and Hutter (1989).

Equations (3.12)-(3.13) in this frame of reference are

$$\frac{\partial u}{\partial x} + \frac{\partial v}{\partial y} = 0, \tag{3.16}$$

$$\rho\left\{\frac{\partial u}{\partial t} + u\frac{\partial u}{\partial x} + v\frac{\partial u}{\partial y}\right\} = \rho g \sin\zeta - \frac{\partial p_{xx}}{\partial x} - \frac{\partial p_{xy}}{\partial y}, \tag{3.17}$$

$$\rho\left\{\frac{\partial v}{\partial t} + u\frac{\partial v}{\partial x} + v\frac{\partial v}{\partial y}\right\} = -\rho g \cos\zeta - \frac{\partial p_{xy}}{\partial x} - \frac{\partial p_{yy}}{\partial y}. \tag{3.18}$$

The mean inclination angle ζ is constant.

The equations can be non-dimensionalized by scaling variables accordingly (Savage and Hutter, 1989):

$$(x, y) = ([L]x^*, [H]y^*), \tag{3.19}$$

$$(u, v, t) = \left([(gL)^{\frac{1}{2}}]u^*, \left[\frac{H}{L}(gL)^{\frac{1}{2}}\right]v^*, \left[\left(\frac{L}{g}\right)^{\frac{1}{2}}\right]t^*\right), \tag{3.20}$$

$$(p_{xx}, p_{yy}, p_{xy}) = [\rho g \cos\zeta H](p^*_{xx}, p^*_{yy}, \tan\zeta p^*_{xy}). \tag{3.21}$$

where the aspect ratio or shallowness parameter $\epsilon = \frac{H}{L}$ is small.

With this the equations (3.16)-(3.18) become

$$\frac{\partial u}{\partial x} + \frac{\partial v}{\partial y} = 0 \tag{3.22}$$

$$\frac{\partial u}{\partial t} + u\frac{\partial u}{\partial x} + v\frac{\partial u}{\partial y} = \sin\zeta\left(1 - \frac{\partial p_{xy}}{\partial y}\right) - \epsilon\cos\zeta\frac{\partial p_{xx}}{\partial x} \tag{3.23}$$

$$\epsilon\left\{\frac{\partial v}{\partial t} + u\frac{\partial v}{\partial x} + v\frac{\partial v}{\partial y}\right\} = -\cos\zeta\left(1 + \frac{\partial p_{yy}}{\partial y}\right) - \epsilon\sin\zeta\frac{\partial p_{xy}}{\partial x} \tag{3.24}$$

in which for brevity asterisks have been omitted, and will be omitted from here on.

The limit of (3.24) for $\epsilon \to 0$ reduces it to the hydrostatic equilibrium. Integration yields

$$p_{yy}(x, y, t) = h(x, t) - y \tag{3.25}$$

when taking into account the zero pressure condition at the free surface ($h(x,t)$). To describe slight changes in the bottom topography, deviations form the slope line defined by ζ are included employing the base parameter $b(x)$.

Depth-integration of (3.23) results in

$$\frac{\partial}{\partial t}\int_b^h u\,dy + \frac{\partial}{\partial x}\int_b^h u^2\,dy - \left[u\left(\frac{\partial h}{\partial t} + u\frac{\partial h}{\partial x} - v\right)\right]_{\text{free surface}} + \left[u\left(u\frac{\mathrm{d}b}{\mathrm{d}x} - v\right)\right]_{\text{base}} =$$
$$\sin\zeta\Big[(h-b) - p_{xy}(h) + p_{xy}(b))\Big] - \epsilon\cos\zeta\left[\frac{\partial}{\partial x}\int_b^h p_{xx}\,dy - p_{xx}(h)\frac{\partial h}{\partial x} + p_{xx}(b)\frac{\mathrm{d}b}{\mathrm{d}x}\right]. \tag{3.26}$$

Several terms in this expression vanish in view of the boundary conditions which are imposed at the free surface and the bed. The kinematic conditions can be expressed as:

$$\left.\begin{array}{ll} \frac{\partial h}{\partial t} + u\frac{\partial h}{\partial x} - v = 0 & \text{at } y = h(x,t), \\ u\frac{\partial b}{\partial x} - v = 0 & \text{at } y = b(x). \end{array}\right\} \tag{3.27}$$

The stress condition at the free surface in dimensionless coordinates reads as follows:

$$-\epsilon\cos\zeta p_{xx}\frac{\partial h}{\partial x} + \sin\zeta p_{xy} = 0,\ -\epsilon\sin\zeta p_{xy}\frac{\partial h}{\partial x} + \cos\zeta p_{yy} = 0 \ \text{ at } \ y = h(x,t). \tag{3.28}$$

Considering $p_{xx} = k_{\text{act/pass}}p_{yy}$ and the constitutive relationship for the pressure tensor as described below ((3.34) and (3.35)), equation (3.28) implies

$$p_{xy} = p_{yy} = 0 \Rightarrow p_{xx} = 0 \text{ at } y = h(x,t) \tag{3.29}$$

and (3.26) becomes

$$\frac{\partial}{\partial t}\int_b^h u\,dy + \frac{\partial}{\partial x}\int_b^h u^2\,dy = \sin\zeta(h-b) + \sin\zeta\, p_{xy}\Big|_{\text{base}} - \epsilon\cos\zeta\left[\frac{\partial}{\partial x}\int_b^h p_{xx}\,dy + p_{xx}(b)\frac{\mathrm{d}b}{\mathrm{d}x}\right]. \tag{3.30}$$

By defining the following transversal averages

$$\overline{u}\hat{h} = \int_b^h u\,dy, \overline{p}_{xx}\hat{h} = \int_b^h p_{xx}\,dy, \overline{p}_{yy}\hat{h} = \int_b^h p_{yy}\,dy, \tag{3.31}$$

$$\overline{u^2}\hat{h} = \int_b^h u^2\,dy = \chi\overline{u}^2\hat{h}, \tag{3.32}$$

with $\hat{h} = h - b$ and χ being a parameter describing the velocity profile. At this point, Savage and Hutter introduce the simplification $\chi = 1$, which corresponds to a sliding block without internal deformation neglecting the putative existence of a velocity profile.

With the shallowness assumption the non-dimensional form of the Coulomb sliding law (3.15) becomes

$$p_{xy} = -sgn(\overline{u})p_{yy}\cot\zeta\tan\delta + O(\epsilon^2) \text{ at } y = b(x). \tag{3.33}$$

As mentioned above, a constitutive relationship for the pressure tensor is needed. Using a cohesionless Mohr-Coulomb type material (see section 1.3.5.3) with a constant internal friction angle ϕ, yielding will occur if

$$|S| = N\tan\phi, \tag{3.34}$$

where S and N are the shear and the normal stress acting on a considered element.

There are two possible yielding Mohr-Coulomb circles crossing the critical bottom yielding $(p_{yy}, \tau)_{bed}$, these two possible circles correspond to an active and passive stress state. Therefore, the pressure p_{xx} can be expressed as proportional to p_{yy} using the earth pressure coefficient:

$$p_{xx} = k_{\text{act/pass}}p_{yy}. \tag{3.35}$$

The value of $k_{\text{act/pass}}$ can therefore be directly obtained from the Mohr-Coulomb dia-

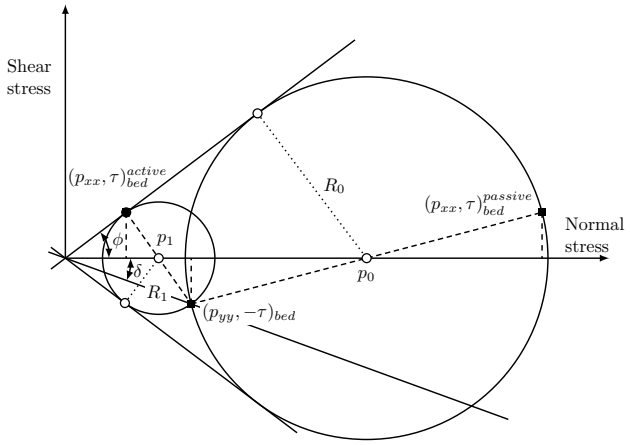

Figure 3.2 – Example of the two possible yielding Mohr-Coulomb circles crossing the critical bottom yielding $(p_{yy},\tau)_{bed}$. The smaller circle corresponds to the active stress state, while the larger circle corresponds to the passive stress state.

gram (Fig. 3.2) (Savage and Hutter, 1989):

$$\left.\begin{matrix} k_{\text{act}} \\ k_{\text{pass}} \end{matrix}\right\} = 2\Big[1 \mp (1-(1+\tan^2\delta)\cos^2\phi)^{\frac{1}{2}}\Big]/\cos^2\phi - 1 \;\text{ for }\; \frac{\partial \overline{u}}{\partial x} \gtrless 0. \tag{3.36}$$

Using these findings (3.31)-(3.35) in (3.30) yields

$$\begin{aligned}\frac{\partial}{\partial t}(\hat{h}\overline{u}) + \frac{\partial}{\partial x}(\chi\hat{h}\overline{u}^2) =& sin\zeta\hat{h} - \epsilon\cos\zeta k_{\text{actpass}}\left[\frac{\partial}{\partial x}(\hat{h}\overline{p}_{yy}) + p_{yy}(x,b)\frac{\mathrm{d}b}{\mathrm{d}x}\right] \\ & - \cos\zeta\,\text{sgn}(\overline{u}p_{yy}(x,b)\tan\delta.\end{aligned} \tag{3.37}$$

With the overburden pressure

$$p_{yy}(x,b) = h(x,t) - b(x) = \hat{h}(x,t), \tag{3.38}$$

$$\hat{h}\overline{p}_{yy}(x,t) = \frac{1}{2}(h(x,t)-b(x))^2 = \frac{1}{2}\hat{h}^2(x,t), \tag{3.39}$$

(3.37) becomes

$$\frac{\partial}{\partial t}(\hat{h}\overline{u}) + \frac{\partial}{\partial x}(\chi\hat{h}\overline{u}^2) = \sin\zeta\hat{h} - \cos\zeta\,\text{sgn}(\overline{u})\tan\delta\hat{h} - \epsilon\cos\zeta k_{\text{act/pass}}\left[\frac{\partial}{\partial x}\left(\frac{\hat{h}^2}{2}\right) + \hat{h}\frac{\mathrm{d}b}{\mathrm{d}x}\right]. \tag{3.40}$$

Integrating the continuity equation (3.16) over the depth and using the kinematic boundary condition (3.27) yields

$$\frac{\partial \hat{h}}{\partial t} + \frac{\partial}{\partial x}(\hat{h}\overline{u}) = 0. \tag{3.41}$$

This simplifies the momentum equation (3.40) to

$$\frac{\partial \overline{u}}{\partial t} + \overline{u}\frac{\partial \overline{u}}{\partial x} = \sin\zeta - \epsilon\cos\zeta k_{\text{act/pass}}\left[\frac{\partial \hat{h}}{\partial x} + \frac{\mathrm{d}b}{\mathrm{d}x}\right] - \operatorname{sgn}(\overline{u})\cos\zeta\tan\delta. \tag{3.42}$$

For simple channel flows $b(x) = 0$, the system of equations can be finally written as introduced in section 1.3.5.3, equations (1.8) and (1.9)

$$\frac{\partial h}{\partial t} + \frac{\partial}{\partial x}(hu) = 0, \tag{3.43}$$

$$\frac{\partial u}{\partial t} + u\frac{\partial u}{\partial x} = (\sin\zeta - \tan\delta\operatorname{sgn}(u)\cos\zeta) - \beta\frac{\partial h}{\partial x} \tag{3.44}$$

with $\beta = \epsilon k_{\text{act/pass}}\cos\zeta$. From here on overbars are omitted for simplicity following the notation convention of Savage and Hutter (1989).

3.2.2 Model extensions

Savage and Hutter (1991) extended the Model to curvilinear coordinates. This extension creates the possibility to analyze the granular flow from its initialization to the run-out including changes in inclination angle. The derivation of the new system of equation is very similar to the above described one mentioned in Savage and Hutter (1989). Therefore, only the differences are mentioned here. The previous constant inclination angle is now a function of arc-length. The coordinate is chosen to follow the bottom boundary profile. By including a change in the inclination angle a new quantity, the curvature $\kappa(x)$ is added and needs to be considered for the dimensional-analysis. The non-dimensionalized curvature is calculated with $\kappa = \frac{H}{R}$. The characteristic curvature is also given by $\lambda = \frac{L}{R}$, where R denotes a scale for the radius of the bed profile.

The depth integration results in similar equations as describe above:

$$(1 - \epsilon\eta\kappa h)\frac{\partial h}{\partial t} + \frac{\partial hu}{\partial x} = 0, \tag{3.45}$$

$$\left(1 - \frac{\epsilon\eta\kappa h}{2}\right)\frac{\partial u}{\partial t} + \left(1 + \frac{\epsilon\eta\kappa h}{2}\right)u\frac{\partial u}{\partial x} = \left(1 - \frac{\epsilon\eta\kappa h}{2}\right)\sin\zeta - \frac{\epsilon h}{2}\frac{\partial}{\partial x}\left(k(\cos\zeta + \eta\kappa u^2)\right) - (\cos\zeta + \eta\kappa u^2) \cdot\left[\left(1 + \frac{\epsilon\eta\kappa h}{2}\operatorname{sgn}(u)\tan\delta + \epsilon k_{\text{act/pass}}\frac{\partial h}{\partial x}\right)\right]. \tag{3.46}$$

These equation deliver different systems if different order of $\tan\delta$ and λ are chosen. For example, for $\tan\delta = O(\epsilon)$ and $\lambda = O(\epsilon)$ the final system of equations has the same form as that used by Savage and Hutter (1989) for the flow down rough channels with a constant inclination angle ζ. But if the order is $\tan\delta = O(\epsilon^{1/2})$ and $\lambda = O(\epsilon^{1/2})$ the final

set of equations is

$$\frac{\partial h}{\partial t} + \frac{\partial (hu)}{\partial \xi} = 0, \tag{3.47}$$

$$\frac{du}{dt} = \frac{\partial u}{\partial t} + u\frac{\partial u}{\partial \xi} = \sin\zeta - \tan\delta\,\mathrm{sgn}(u)(\cos\zeta + \lambda\kappa u^2) - \epsilon_{act/pass}\cos\zeta\frac{\partial h}{\partial \xi}. \tag{3.48}$$

(3.48) contains an additional centrifugal force term ($\lambda\kappa u^2$), which enhances the normal load.

Savage and Hutter (1991) compare their newly developed equations with an experiment consisting of two straight parts joint together with a short curved transition. The influence of the curved part is small, because the curvature only deviates from zero for a very short distance. Therefore, Hutter and Koch (1991) constructed a channel with a changing curvature down the entire track with exponentially decaying inclination. To analyze an even stronger influence, Greve and Hutter (1993) build a convex and concave channel and compared it to their model. In this experiment, the curvature even varies in sign and thus gains a strong influence. All these experiments displayed quite good agreement with the proposed model. An even better agreement was achieved by modifying the very simple model of Coulomb friction which accounts for the influence of the sidewall friction and including a velocity dependence on the bottom friction law. Nevertheless, the results do not change drastically. The overall geometry and the dynamic of the flow is well captured with the simple approach of a constant rate independent bottom friction angle.

Because of their wide successful applications and the good agreements with experimental data, (3.47) and (3.48) are used in this work for comparison with experimental data and simulations.

3.2.3 Extension to 3D, erosion and deposition

In the past two decades, several extensions have been added to the Savage-Hutter model in order to extend the 2D model to describe three-dimensional granular flows and to allow the prediction of erosion and deposition behavior. Although not employed in this work, these extensions are mentioned briefly in the following paragraph to complete the picture of application possibilities of the Savage-Hutter type models. A detailed review of the extensions can be found in Pudasaini and Hutter (2007).

The extension to 3D is realized by accommodating the model to the description of twisted and curved channels. In this set-up, a "master-curve" is introduced for the description of the channel surface. This curve is not only described by the curvature κ but also by the torsion τ, which denotes bending away from the plane in which variations

of κ occur. To adopt such complex topographies to the Savage-Hutter model equations, a curvilinear coordinate system following the master-curve is employed. This extension was developed in various steps and arose from the work of Hutter et al. (1993), Hutter and Greve (1993), Greve et al. (1994), Gray et al. (1999), Pudasaini et al. (2005c,b,c).

Several comparisons with the different evolved models have been performed and a good agreement could be shown for 3D flow with run-out zone (Koch et al., 1994), 2D flow with run-out (Hutter et al., 1995), 3D slightly curved and twisted modeled with b(x,y) (Gray and Hutter, 1998), 3D flow with run-out zone and slightly curved cross section (Gray et al., 1999), deflection and shocks of granular flow down planes (Tai et al., 1999a; Gray et al., 2003; Gray and Cui, 2007), 3D slightly curved and twisted modeled with b(x,y) (Wieland et al., 1999; Tai et al., 2001), numerical simulation of Savage and Hutter (1991), Hutter and Koch (1991) and Greve and Hutter (1993), flow height and velocity measurements as well as comparison of a longitudinal curved, lateral flat 3D channel (Pudasaini et al., 2005a,c) with twisted and curved channels (Pudasaini et al., 2008). Nevertheless, it should be noted here that these extensions still rely on depth-averaging and are thus only quasi-3D descriptions which cannot capture velocity profiles along the flow depth.

In the original derivation of the Savage-Hutter-Model, the closure for the pressure tensor assumes all material to be in a yielding state, and, therefore, no material is allowed to settle. In reality, the mobile and resting parts are sharply divided by a solid-liquid interface. The solid-liquid interface is time dependent, and can be modeled by assuming a time varying bottom profile $b(\mathbf{x}, t)$ or by changing the curvilinear coordinate system with time. The resting material can be mobilized and become a part of the flowing part, this process is called erosion, or the flowing material can come to rest (deposition). These processes need to be included in the bottom and free surface boundary condition and, therefore, will enter not only the continuum equation but will also influence the momentum equations (Gray, 2001; Pitman and Le, 2005; Lê and Pitman, 2009; Tai and Kuo, 2008; Tai et al., 2012; Bouchut et al., 2008), namely as mass and momentum production terms.

3.3 Work of other groups relevant to this work

Pouliquen (1999) analyzed granular flows down rough inclined planes. For rough beds, a steady, uniform flow can develop for a range of inclination angles and flow heights. For high inclination angles, no steady flow can develop since the gravitational force is bigger than the friction force and the flow is accelerated down the channel. For small inclination angles, the friction force dominates the gravitational force and the flow will deposit. Within the range of possible inclination angles for flow behavior, a steady, uni-

form flow only occurs if the flow height is above a certain threshold height, $h_{stop}(\zeta)$ (Daerr and Douady, 1999), and below an upper limit, where accelerating flows will be present. Pouliquen (1999) measured these uniform velocity for several values of ζ and flow heights h and different wall roughnesses and grain diameters.

Plotting normalized height with respect to $h_{stop}(\zeta)$ against the dimensionless velocity $\frac{u}{\sqrt{gh}}$, he found a scaling law with the scale factor Fr, which is the Froude number. With his measurements he provides an empirical way to predict velocities, with

$$\frac{u}{\sqrt{gh}} = c\frac{h}{h_{stop}(\zeta)}, \tag{3.49}$$

where $c = 0.136$ represents a constant, which depends neither on the inclination nor on the particle size of granular material considered (glass beads in this case) nor on the roughness of the bed.

These findings were subsequently used to model the friction coefficient μ which now is a function of velocity and flow height. The friction angle can be expressed as

$$\tan\delta = \tan\zeta_1 + (\tan\zeta_2 - \tan\zeta_1)\exp\left(-\frac{h_{stop}}{Ld}\right). \tag{3.50}$$

ζ_1 corresponds to the lower angle where the function h_{stop} diverges, ζ_2 is the upper angle where $h_{stop}(\zeta)$ vanishes. d denotes the particle diameter and L is a characteristic dimensionless thickness over which $\zeta_{stop}(h)$ varies.

This modified friction law was compared with experiments (Pouliquen and Forterre (2002)), where the release of a cup shaped initial mass sliding down an inclined plane was analyzed. In contrast to Savage and Hutter, they claim the earth pressure coefficient to be one because of the fluid like behavior of their granular flow.

The simple scaling law for inclined channels and inclined chutes was later extended to a simple empirical rheological model by Jop et al. (2005), Jop et al. (2006), Pouliquen et al. (2006), Forterre and Pouliquen (2008) and GDR MIDI (2004). With the observation of a series of different slow moving granular surface flows they constructed the friction coefficient $\mu(I)$ as a function of the inertia number $I = \dot{\gamma}d/(p/\rho_s)^{0.5}$, where d is the diameter of the grain, ρ_s is the particle density and p is the pressure. The proposed friction law is

$$\mu(I) = \mu_s + (\mu_2 - \mu_s)(I_0/I + 1), \tag{3.51}$$

where I_0 is a constant, μ_s is the friction constant at zero shear-rate and μ_2 is the limiting value the friction constant converges to for high I.

This work employes, on the one hand, classical depth-averaged simulations of the Savage-Hutter type and, on the other hand, a novel type of non-depth-averaged simulations developed during this study. As mentioned in section 1.3.6, the model equations described in the previous chapter can, in general, not be solved in an analytical way, but need to be implemented in a numerical scheme to describe the flow of a granular material. Here, OpenFOAM® is employed to implement a FVM numerical scheme for the simulation of rapid granular flows in a non-depth-averaged manner to facilitate full three-dimensional simulation of the flow. OpenFOAM® is an open source computational fluid dynamics (CFD) software package that is widely used to simulate fluid dynamics problems. OpenFOAM® was initially developed by Weller et al. as later summarized in Weller et al. (1998) and was brought to its current formate with various adaptation methods by Jasak (1996). Rusche (2002) further extended the method for two-phase flows. As described in section 6.1, the rheological model employed for the non-depth-averaged simulations in this study is a simple Coulomb frictional viscosity model. The resulting viscosity is introduced into the Navier-Stokes equations to describe the dynamics of the granular material. This chapter will first describe the theory underlying the discretization of the basic continuum mechanics equations by the FVM as introduced in OpenFOAM® by Jasak (1996) and Rusche (2002) and afterwards describe the differences between the FVM and the FDM which is used in the SH-model discretization for comparisons.

4.1 Navier-Stokes equations

4.1.1 Finite volume

The FVM is a widely used discretization method (Ferziger and Peri, 1999; Denlinger and Iverson, 2001; Huilin et al., 2003; García Nieto et al., 2010) that is especially suitable for complex flow geometries due to its flexible grid structure (see section 1.3.6.2). The discretization of time, space and the model equations is performed as described in the following paragraphs according to Jasak (1996) and Rusche (2002).

4.1.1.1 Discretization of the physical domain

As described in section 1.3.6.1, the space domain is discretized into a grid, while the time domain is split into steps (Δt). Depending on the observed dynamics (e.g. a changing flow velocity), the size of Δt can be varied. The cells of the grid are non-overlapping and completely fill the space domain. Therefore, a single cell is delimited by a number of

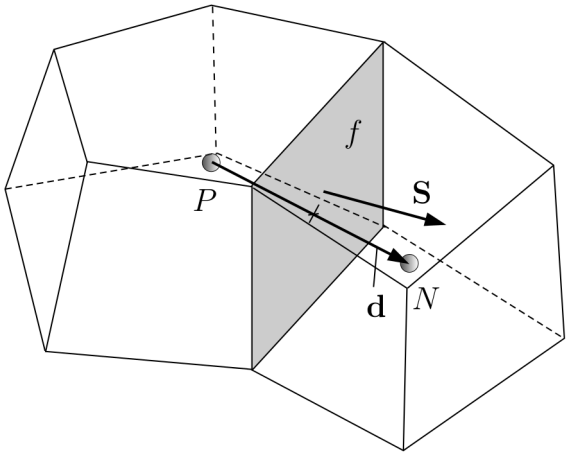

Figure 4.1 – Parameter notation for the finite volume discretization as utilized in (Nabla Ltd. (2001), Rusche (2002)) (figure from Nabla Ltd. (2001), Rusche (2002)).

faces, which can be either the faces of neighboring cells (internal faces) or the boundary of the space domain (boundary faces). This study only considers flat faces, without any concave or convex bending. The position vector of the center $\mathbf{x}_f$ of a flat face (f) is defined by the following integral:

$$\int_s \left(\mathbf{x} - \mathbf{x}_f\right) dS = 0. \tag{4.1}$$

The variables and properties of the flow in a cell P are deposited in the cell center, whose position vector $\mathbf{x}_P$ is defined to match

$$\int_{V_P} (\mathbf{x} - \mathbf{x}_P)\, dV = 0. \tag{4.2}$$

Furthermore, a face area vector $\mathbf{S}$ normal to the respective face is defined for each boundary of a cell. $\mathbf{S}$ has a magnitude representing the face's area and a direction pointing out of the cell into the neighboring cell (N). Thus, the normal unit vector of the face is defined as $\mathbf{n} = \frac{\mathbf{S}}{|\mathbf{S}|}$. Another vector describing the orientation of the cells to one another is $\mathbf{d}$, which is the vector pointing from the center of P to the center of N: $\mathbf{d} = \mathbf{x}_N - \mathbf{x}_P$. In the case of an orthogonal grid, $\mathbf{d}$ would be parallel to $\mathbf{S}$ for all faces in the grid. Figure 4.1 depicts two cells with the respective vectors.

4.1.1.2 Storage of the variables in the grid

When using the FVM, the variables for the whole cell have to be stored at one point of the cell. Two kinds of variables can be distinguished in a numerical scheme: dependent variables, which are determined in the numerical process by solving the governing equations for them and independent variables which specify the observed domain, meaning time and space in our case.

Two scenarios are possible for the storage: at the center of the cells ("volume field") or at the centers of the boundary faces ("face field"). When all variables are stored at the cell centers, the respective arrangement is termed a "collocated" arrangement, while a "staggered" arrangement is employed when the velocities are stored in a face field and the other variables are stored in the centers (Harlow and Welch, 1965; Hirt et al., 1974; Patankar, 1980).

Especially for non-orthogonal, complex grids as used in this study, the collocated arrangement has been proven to be superior to the staggered arrangement (Peric et al., 1988). Advantages are the minimized number of coefficients that need to be calculated (since there are far less centers than faces) and the better suitability for complex boundary condition (Ferziger and Peri, 1999).

As Rusche (2002) points out, the collocated arrangement remained, despite its many advantages, hard to implement for many years due to problems with the pressure-velocity coupling and oscillations in the pressure field caused by 2nd order terms in the pressure equation. Two different solutions have been suggested for this problem by Chorin (1968) and Rhie and Chow (1982). The method of Rhie and Chow (1982) is adopted in OpenFOAM® and thus used in this study. Nevertheless, Rusche (2002) reports some difficulties with the complete collocated variable arrangement in the solution of the two-fluid and interface-capturing models where sharp density gradients occur. As a solution he suggested a procedure which "mimics the operation of a solution procedure devised for a staggered variable arrangement, but keeping the collocated variable arrangement" (Rusche, 2002). This procedure was included into OpenFOAM® and is also used in this study (for details on the procedure see below, paragraph 4.1.1.6).

4.1.1.3 Equation discretization

This paragraph describes, in a generalized form, the transformation of the governing equations into a system of algebraic equations as included in the numerical scheme of OpenFOAM® by Rusche (2002). Most dependent variables require a gradient-diffusion term of the following form $-\nabla\cdot(\Gamma\nabla\Phi)$, where Γ is the diffusivity. This term will therefore be included in (3.3) for a general tensorial property Φ, yielding a standard transport equation:

$$\underbrace{\frac{\partial\rho\Phi}{\partial t}}_{\text{time derivative}} + \underbrace{\nabla\cdot(\rho\mathbf{u}\Phi)}_{\text{convection term}} = \underbrace{\nabla\cdot(\Gamma\nabla\Phi)}_{\text{diffusion term}} + \underbrace{S_\Phi(\Phi)}_{\text{source term}} , \tag{4.3}$$

where $S_\Phi(\Phi)$ contains all terms that cannot be fitted to the other terms (source term). The single expressions in (4.3) describe the change over time (time derivative), the efflux by convection (convection term), the rate of transport caused by diffusion (diffusion term)

and the rate of generation/destruction (source term) for a given unit volume.

This standard transport equation will be used as an example to describe the discretization of governing equations but at some points also other terms, which are important for the numerical scheme employed here by using OpenFOAM® are described. Discretization of (4.3) for finite volumes is achieved by integration over a control volume V_P and time:

$$\int_t^{t+\delta t}\left[\int_{V_P}\frac{\partial\rho\Phi}{\partial t}dV+\int_{V_P}\nabla\cdot(\rho\mathbf{u}\Phi)dV\right]dt=\int_t^{t+\delta t}\left[\int_{V_P}\nabla\cdot\Gamma\nabla\Phi dV+\int_{V_P}S_\Phi(\Phi)dV\right]dt. \tag{4.4}$$

According to Gauss' theorem, spatial derivatives over a volume can be converted to integrals by integration over the boundary surface of the respective volume (here represented by the surface area vector **S**):

$$\int_V\nabla\otimes\Phi\,dV=\int_S d\mathbf{S}\otimes\Phi. \tag{4.5}$$

Here, $\otimes$ represents any tensor product (inner, outer or cross) and with this the respective derivatives are (in case the particular derivative is defined): divergence $\nabla\cdot\Phi$, gradient $\nabla\Phi$ and curl $\nabla\times\Phi$.

In OpenFOAM®, this generalized form of Gauss' theorem is employed to transform most spatial derivative into integrals. Afterwards, the volume and surface integrals are approximated by appropriate schemes.

Face interpolation

As mentioned above, a collocated arrangement will be employed in this study and the variables will be stored at the cell centers. Nevertheless, as seen in the last paragraph, the Gauss integrals require the values of the variables on the cell surface. Therefore, the cell centered values have to be interpolated to the face centers. Several schemes have been introduced for this interpolation (reviewed in Patankar (1980), Peric et al. (1988), Muzaferija (1994), Jasak (1996) and Ferziger and Peri (1999)). Here, first some general considerations common to all schemes are presented and then the three most frequently used schemes (central differencing, upwind differencing and blended differencing) are introduced. These schemes differ in the bounding of the solution (meaning that bounded solutions only allow physically realistic values for the variables, while unbounded solutions also allow unrealistic ones) and the order of accuracy.

Discretization schemes are employed to interpolate the face value $\Phi_{f(F,S,\gamma)}$ from the

neighboring cells, which can depend on the flux F through the face f and other parameters γ. F is defined by the governing equations and the numerical procedure to solve those. The resolution flux field is a face field and its exact calculation process will be described below. To describe the interpolation procedure, the mass flow $F = \mathbf{S} \cdot (\rho \mathbf{u})_f$ is taken as an example.

Central Differencing (CD)

The CD scheme simply calculates the mean values between two cells for the variables:

$$\Phi_{f(\mathrm{CD})} = f_x \Phi_P + (1 - f_x)\Phi_N, \tag{4.6}$$

where $f_x \equiv \frac{|\mathbf{x}_f - \mathbf{x}_N|}{|\mathbf{x}_f - \mathbf{x}_N| + |\mathbf{x}_f - \mathbf{x}_P|}$.

An advantage of CD is its second-order accuracy (Ferziger and Peri, 1999), but the solution can be unbounded (Jasak, 1996; Ferziger and Peri, 1999).

Upwind Differencing (UD)

UD considers the direction of the flow to determine Φ_f (Courant et al., 1952; Barakat and Clark, 1966; Gentry et al., 1966):

$$\Phi_{f(F,\mathrm{UD})} = \begin{cases} \Phi_P & \text{for } F \geq 0 \\ \Phi_N & \text{for } F < 0 \end{cases} \tag{4.7}$$

In contrast to CD, UD guaranties the solution to be bounded but the accuracy is only of first order. As a consequence, a diffusive term is contained in the scheme (numerical diffusion), which can led to distortions in the case of coarse meshes (Ferziger and Peri, 1999).

Blended Differencing (BD)

BD schemes are linear combinations of UD and CD and were designed to enable a weighting between boundedness and accuracy:

$$\Phi_{f(F,\mathrm{BD},\gamma)} = (1 - \gamma)\Phi_{f(F,\mathrm{UD})} + \gamma \Phi_{f(\mathrm{CD})}. \tag{4.8}$$

A blending factor γ, which can be varied from 0 to 1, determines the amount of numerical diffusion which will be introduced. γ can be expressed in several ways (reviewed in Patankar (1980), Peric et al. (1988), Muzaferija (1994) and Ferziger and Peri (1999)).

In this study, all three schemes are employed (see appendix A.1.2).

Gradient

Several ways exist to evaluate the gradient term $\nabla\Phi$ of the standard transport equation. OpenFOAM® offers Gauss integration and a face normal gradient for this purpose.

Gauss integration

Here, Gauss' theorem is applied as described above to receive the cell centered gradient of Φ:

$$\int_V \nabla\Phi dV = \int_S d\mathbf{S}\Phi \approx \sum_f \mathbf{S}\Phi_f, \tag{4.9}$$

where Φ_f can be evaluated by any face interpolating scheme.

Face normal gradient

If gradients at faces are to be considered, the face normal gradient $\nabla_f^\perp\Phi$ is employed. It is given by the inner product of the face gradient $\nabla_f\Phi$ and the normal unit vector n. $\nabla_f^\perp\Phi$ is approximated in OpenFOAM® by:

$$\nabla_f^\perp\Phi = \frac{\Phi_N - \Phi_P}{|\mathbf{d}|}. \tag{4.10}$$

In an orthogonal grid, this approximation is second order accurate, while for non-orthogonal grids this is not the case but a correction can be employed. This correction term can be obtained from cell centered gradients received by Gauss integration (Jasak, 1996).

Time derivative

A time derivative $\frac{\partial\rho\Phi}{\partial t}$ can be discretized by integration over a control volume. This study uses the Euler implicit time differencing scheme in OpenFOAM®. This scheme is unconditionally stable, meaning that no restriction to the lengths of time steps has to be given. It is only first order accurate but thus also not prone to oscillations. For a static grid (as employed in this study) and an assumed linear variation of Φ within a time step the scheme yields:

$$\int_V \frac{\partial\rho\Phi}{\partial t} dV \approx \frac{\rho_P^n\Phi_P^n - \rho_P^0\Phi_P^0}{\Delta t} V_P, \tag{4.11}$$

where $\Phi^n \equiv \Phi(t+\Delta t)$ denotes the new value at the currently considered time step and $\Phi^0 \equiv \Phi(t)$ denotes the previous value.

Convection term

A convection term $\nabla \cdot (\rho \mathbf{u} \Phi)$ can be discretized by integration over a control volume followed by application of Gauss' theorem to yield a surface integral:

$$\int_V \nabla \cdot (\rho \mathbf{u} \Phi) dV = \int_S d\mathbf{S} \cdot (\rho \mathbf{u} \Phi) \approx \sum_f \mathbf{S} \cdot (\rho \mathbf{u})_f \Phi_{f(F.S)} = \sum_f F \Phi_{f(F,S)}, \tag{4.12}$$

with F being the mass flux through the face f: $F = \mathbf{S} \cdot (\rho \mathbf{u})_f$.

Diffusion term

A diffusion term $\nabla \cdot (\Gamma \nabla \Phi)$ can be discretized analogous to a convective term by integration over a control volume followed by application of Gauss' theorem to yield a surface integral. In contrast to the convective term, the surface integral here still contains a gradient, which is then approximated by a face normal gradient:

$$\int_V \nabla \cdot (\Gamma \nabla \Phi) dV = \int_S d\mathbf{S} \cdot (\gamma \nabla \Phi) \approx \sum_f \Gamma_f (\mathbf{S} \cdot \nabla_f \Phi). \tag{4.13}$$

However, this approximation is only valid if Γ is a scalar. As pointed out in paragraph 4.1.1.3, the face normal gradient approximation is only second order accurate for orthogonal grids. For non-orthogonal grids, the following correction is introduced:

$$\mathbf{S} \cdot \nabla_f \Phi = \underbrace{|\Delta| \nabla_f^{\perp} \Phi}_{\text{orthogonal contribution}} + \underbrace{\mathbf{k} \cdot (\nabla \Phi)_f}_{\text{non-orthogonal correction}} . \tag{4.14}$$

Δ and $\mathbf{k}$ are vectors which are determined by a non-orthogonality treatment. This study uses the over-relaxed non-orthogonality approach implemented in OpenFOAM® by Jasak (1996).

Source term

Prior to discretization, a source term $S_\Phi(\Phi)$ has to be linearized, where explicit (S_I) and implicit (S_E) source terms are constructed separately (Patankar, 1980):

$$S_\Phi(\Phi) = \Phi S_I + S_E. \tag{4.15}$$

S_E and S_I can be dependent on Φ. Integration over a control volume then yields

$$\int_V S_\Phi(\Phi) dV = S_I V_P \Phi_P + S_E V_P. \tag{4.16}$$

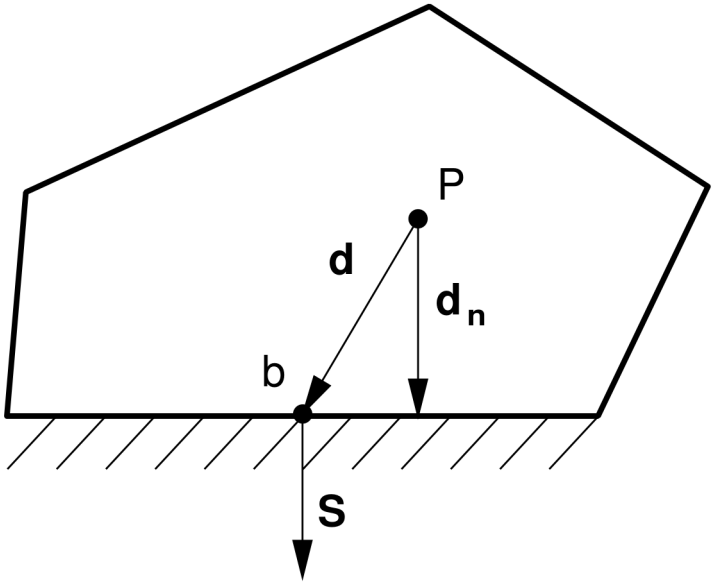

Figure 4.2 – Parameters in finite volume discretization for cells with a boundary face as denoted in (Rusche, 2002). Picture taken from Rusche (2002).

4.1.1.4 Boundary conditions

So far only the variables in cell surrounded by other cell in the continuum have been considered. It is for sure of similar importance to consider the events in cell at the boundary of a continuum. Since some of the discretization procedures described above approximate values by summation over faces, also the boundary faces need to carry values for all dependent variables. These values are specified in so-called boundary conditions. Two main forms of boundary conditions can be distinguished: "Dirichlet" boundary conditions assign fixed values to the dependent variable on the boundary, while "von Neumann" boundary conditions only prescribe a fixed gradient for the respective variable in normal direction to the boundary.

To describe the situation at the boundary, additional parameters are introduced into the numerical scheme (Fig. 4.2): if a cell P is a boundary cell, the boundary face is denoted by b. Furthermore, a vector d is specified, being the vector between the cell center and the center of the boundary face, with a boundary normal component d_n. OpenFOAM® assumes that for a given face a boundary condition is constant over the whole face.

Fixed value

In a fixed value scheme, values required for a face are substituted by the fixed boundary value for boundary faces: $\Phi_f = \Phi_B$. When a gradient is required it is calculated between

the boundary face and the cell center:

$$\mathbf{S} \cdot \nabla_f \Phi = |\mathbf{S}| \frac{\Phi_b - \Phi_P}{|\mathbf{d}_n|}. \tag{4.17}$$

This is only second order accurate if Φ_B is constant at the complete face and the grid is orthogonal. For non-orthogonal grids a correction as described above for the diffusion term can be employed.

Fixed gradient

In a fixed gradient scheme, the face normal gradient $g_B = \nabla_f^{\perp} \Phi$ is predefined at the boundary and gradients required at the boundary are directly substituted with this value. If values are needed for the boundary face, the value of the cell center is extrapolated to the boundary:

$$\Phi_f = \Phi_P + \mathbf{d}_n \cdot \nabla_f \Phi = \Phi_P + |\mathbf{d}_n| g_B. \tag{4.18}$$

Again, the scheme is second order accurate if g_B is constant along one face. In the case of varying Φ_B and non-orthogonal grids it is only first order accurate, but it has been shown that the error can be neglected as described in Jasak (1996).

Zero gradient

A zero gradient boundary condition is a special case in which $g_B = 0$. The discretization is performed as above.

4.1.1.5 Temporal discretization

As described above, the integral form of the standard transport equation is denoted as follows:

$$\int_t^{t+\delta t} \left[\int_{V_P} \frac{\partial \rho \Phi}{\partial t} dV + \int_{V_P} \nabla \cdot (\rho \mathbf{u} \Phi) dV \right] dt = \int_t^{t+\delta t} \left[\int_{V_P} \nabla \cdot \Gamma \nabla \Phi dV + \int_{V_P} S_\Phi(\Phi) dV \right] dt. \tag{4.4}$$

With the dircretizations described above in (4.11), (4.12), (4.13) and (4.16), (4.4) can

be written as:

$$\int_t^{t+\delta t}\left[\rho_P\frac{\Phi^n-\Phi^0}{\Delta t}+\sum_f F\Phi_{f(F,S)}\right]dt=\int_t^{t+\delta t}\left[\sum_f \Gamma_f\mathbf{S}\cdot\nabla_f\Phi+S_I V_P\Phi_P+S_E V_P\right]dt. \quad (4.19)$$

Here and throughout this whole work, it is assumed that the control volume does not change in time.

(4.4) is only discretized in space for a control volume and the time integrals of (4.4) were not considered so far. Therefore, (4.19) is termed the "semi-discretized" form of the standard transport equation. Several ways have been proposed to express these integrals in a discretized form (Jasak, 1996; Ferziger and Peri, 1999; Hirsch, 2007). To solve the time integral, the temporal variation of Φ_P at the cell center, the face values and gradients need to be expressed. It is a common practice to neglect the temporal variation of these spatial terms during a time step and assume their changes to happen between time steps (Patankar, 1980; Rusche, 2002). There are two common ways to evaluate their new and old values, the explicit and the implicit method:

Explicit

In an explicit method, the value of the present step (Φ) is initially assumed to be equal to the values at the previous time step Φ^0 and the actual value of Φ is calculated the following way and included in (4.19):

$$\Phi_P=\Phi_P^0, \quad (4.20)$$

$$\Phi_f=\Phi_f^0, \quad (4.21)$$

$$\mathbf{S}\cdot\nabla_f\Phi=\mathbf{S}\cdot\nabla_f\Phi^0=|\Delta|\nabla_f^{\perp}\Phi^0+\mathbf{k}\cdot(\nabla\Phi^0)_f. \quad (4.22)$$

This method is only first order accurate in time and might cause instability. The criterion for stability is defined by the Courant number Co:

$$Co=\frac{\mathbf{u}_f\cdot\mathbf{S}}{\mathbf{d}\cdot\mathbf{S}}\Delta t, \quad (4.23)$$

here, $\mathbf{u}_f$ is a characteristic velocity of the considered flow. For stability, Co has to be smaller than one.

Euler implicit

The Euler implicit method uses the values of the next time step Φ^n to calculate the values for the next time step Φ^n. Thus the following values are included in (4.19):

$$\Phi_P = \Phi_P^n, \tag{4.24}$$

$$\Phi_f = \Phi_f^n, \tag{4.25}$$

$$\mathbf{S} \cdot \nabla_f \Phi = \mathbf{S} \cdot \nabla_f \Phi^n = |\Delta| \nabla_f^{\perp} \Phi^n + \mathbf{k} \cdot (\nabla \Phi^0)_f. \tag{4.26}$$

With this method, Φ^n cannot be calculated directly but by solving the standard transport equation (see section 4.1.1.6), which has the following form:

$$\rho_P \frac{\Phi^n - \Phi^0}{\Delta t} V_P + \sum_f F \Phi^n_{f(F,S)} = \sum_f \Gamma_f \mathbf{S} \cdot \nabla_f \Phi^n + S_I V_P \Phi_p^n + S_E V_P. \tag{4.27}$$

The Euler implicit method is also only first order accurate in time but the solution is bounded and unconditionally stable. However, this is only true for orthogonal grids, while for non-orthogonal an explicit correction is necessary (see below, section 4.1.1.6).

4.1.1.6 Solution technique for system of linear algebraic equations

Discretization and linearization of the governing equations yields linear algebraic equations for each control volume (e.g. (4.27). These equations now need to be solved. A more general expression of such an equation, independent of the discretization, is:

$$a_P \Phi_P^n + \sum_N a_N \Phi_N^n = R_P. \tag{4.28}$$

In this equation, Φ_P is dependent on the values of the neighbor cells. For all cells in the grid an equation system for each variable is generated that way, which can be expressed as the following matrix:

$$[A][\Phi] = [R]. \tag{4.29}$$

$[A]$ in this case is a sparse (i.e., most of the coefficients are zero) square matrix with coefficients a_P on the diagonal and a_N off the diagonal, $[\Phi]$ is the column vector of the dependent variable and $[R]$ is the source vector. According to Rusche (2002) it should be noted here that $[\Phi]$ and $[R]$ are not vectors in strict sense but rather a list of values stored at the centers of the control volumes. Decomposition of the matrix $[A]$ into two matrices

containing the diagonal $[D]$ and off-diagonal $[N]$ coefficients yields:

$$[A] = [D] + [N]. \tag{4.30}$$

Each term in a governing equation contributes either to the matrix coefficient $[A]$ or to the source vector $[R]$ or to both. Implicit treatment results in contribution to $[A]$ and eventually to $[R]$, while explicit treatment results in sole contribution to $[R]$.

Several different numeric techniques can be employed to solve the linear algebraic equation system (4.29) and to obtain values for Φ (Theodoropoulos, 1990; Golub and Van Loan, 1996; Ferziger and Peri, 1999). Two general methods can be distinguished: direct and iterative ones. Direct methods solve the equations by a limited number of arithmetic operations while iterative methods guess a first solution and improve it during subsequent refinements until a certain quality of the guess is achieved. The number of necessary operations in a direct method is scaled with a cubic function of the number of equations, thus making them time and cost intensive for large equation systems (Theodoropoulos, 1990; Muzaferija, 1994; Ferziger and Peri, 1999; Versteeg and Malalasekera, 2007). Because of this, iterative methods are the more economic way to solve large equation systems but require certain matrix formates like diagonal dominance (see below). Another advantage of the iterative method is its preservation of the sparseness of the matrix, which results in a lower memory requirement. Together with the fact that the accuracy of an iterative method is usually much larger than the accuracy implied by the discretization error, these advantages let the founders of OpenFOAM® decided for an iterative solver, the Conjugate Gradient (CG) method (Hestenes and Stiefel, 1952). This method guarantees to reach a solution in a number of iterations smaller than the number of equations. To achieve an improved convergence rate (which is dependent on the dispersion of the eigenvalues of the matrix), OpenFOAM® makes use of preconditioned solver: the Incomplete Cholesky Conjugate Gradient (ICCG) solver for symmetric matrices (Jacobs, 1980) and the Bi-CGSTAB for asymmetric matrices (Van der Vorst, 1992).

As mentioned above, these iterative solvers require the matrix to be diagonally dominant. This is the case when at least one diagonal coefficient $|a_p|$ is larger in magnitude than the sum of the off-diagonal coefficients in the respective row $|a_p| > \Sigma_N |a_n|$. Analyzing the structure of the matrix has further advantages: according to Hirsch (2007), diagonally equal systems of equations with positive coefficients will ensure the boundedness of the solution. Thus, the diagonal dominance of the matrices can help to evaluate the boundedness of the discretization scheme.

Analysis of matrix structure

Jasak (1996) and Rusche (2002) give a detailed view on the contribution of the single

terms of discretized standard transport equation (4.19) to the matrix and the boundedness of the solution. These contributions are summarized in the following paragraph.

The temporal derivative in (4.11) contributes to the diagonal coefficient and a source term. It first increases diagonal dominance, while the source term is not taken into account for the boundedness but its influence should be small due to its inertial nature. For the convective term in (4.12), the formulation of the boundedness criterion is more complex. A transport equation without sources and diffusion is considered:

$$\frac{\partial \rho \Phi}{\partial t} + \nabla \cdot (\rho \mathbf{u} \Phi) = 0, \tag{4.31}$$

which can be rewritten as:

$$\rho \left(\frac{\partial \Phi}{\partial t} + (\mathbf{u} \cdot \nabla) \Phi \right) + \Phi \left(\frac{\partial \rho}{\partial t} + \nabla \cdot (\rho \mathbf{u}) \right) = 0. \tag{4.32}$$

Since the first two terms contain the substantive derivative Φ, the solution of the simplified transport equation is bounded when the second part is zero, i.e.,

$$\frac{\partial \rho}{\partial t} + \nabla \cdot (\rho \mathbf{u}) = 0. \tag{4.33}$$

This is true for example for an incompressible flow (as considered in this study), where $\rho = const$. With this, the transport equation can be written as:

$$\frac{\partial \Phi}{\partial t} + \nabla \cdot (\mathbf{u} \Phi) = 0. \tag{4.34}$$

From this equation, a simple criterion for boundedness can be derived:

$$\nabla \cdot \mathbf{u} = 0. \tag{4.35}$$

To examine the contributions of a diffusion term in (4.13), a transport equation without convection and additional sources is considered:

$$\frac{\partial \Phi}{\partial t} = \nabla \cdot (\Gamma \nabla \Phi). \tag{4.36}$$

This equation is bounded for positive diffusion coefficients (Γ), which means that a solution forward in time is considered. In the case of an orthogonal mesh, the diffusion term contributes a diagonally equal matrix. As pointed out before, a non-orthogonal correction term is needed for non-orthogonal grids (4.14). This correction term can, in contrast to the face normal gradient in OpenFOAM®, not be treated implicitly because it would create an unbounded solution because of negative coefficients for the second next neighbors of the cells considered (described in detail in Jasak (1996)). Therefore, the correction term is treated explicitly in OpenFOAM®.

The linear part of a source term of a transport equation (4.16) only contributes to the diagonal coefficients of the matrix. It increases the diagonal dominance if $S_I < 0$ and decreases diagonal dominance when $S_I > 0$. Thus OpenFOAM® only includes S_I into the diagonal coefficient when it is negative. Positive S_I are included into the source and updated during the solution process as described in Patankar (1980) and Ferziger and Peri (1999).

Under-relaxation

Under-Relaxation is a method implemented in OpenFOAM® to enhance diagonal dominance in steady-state calculations. It is necessary because the positive contribution of the temporal derivative to diagonal dominance is omitted in this case and only negative linear source terms can cause diagonal dominance. Thus, steady-state calculations with positive S_I could not be treated with iterative solvers.

In order to generate diagonal dominance in a generalized transport equation for a control volume (eq. 4.28), an artificial term is added on both sides:

$$a_P \Phi_P^n + \frac{1-\psi}{\psi} a_P \Phi_P^n + \sum_N a_N \Phi_N^n = R_P + \frac{1-\psi}{\psi} a_P \Phi_P^0. \tag{4.37}$$

This can be simplified to

$$\frac{a_P}{\psi} \Phi_P^n + \sum_N a_N \Phi_N^n = R_P + \frac{1-\psi}{\psi} a_P \Phi_P^0, \tag{4.38}$$

where Φ^0 and Φ^n are values of the considered variable in two consecutive iterations, while ψ is a newly introduced under-relaxation factor, which can have positive values up to 1. As a result, all diagonal coefficients a_P are divided by ψ which yields larger values and thus increases diagonal dominance. The addition on the right part of the equation causes the source term to increase, which also only contributes to the diagonal part. At the convergence of the solution, when Φ^0 and Φ^n are equal, the additional terms are canceled out.

4.1.1.7 Finite volume notation

Weller (2002) introduced an unambiguous notation for the terms described above (Tab. 4.1). Beside the already mentioned terms of the standard transport equation (4.3), governing equations may contain additional terms. Governing equations containing such terms are non-standard forms of equations that are used in this study as in Rusche (2002) for the phase fraction continuity equation in the two-fluid methodology. The fact that these additional terms are often treated in a different way than the “standard” terms

let Weller (2002) to his code independent notation. He suggested to describe the discretized term from an implicit operator ($\mathcal{L}$, a spatial or temporal derivative or a source term) by $[\![\mathcal{L}[\Phi]]\!]$). The double brackets indicate am implicit treatment, while explicitly treated terms are denoted without brackets. Such a notation of a linear equation system ($\mathcal{A}$) resulting from the discretized standard transport equation reads as follows

$$\mathcal{A} := \left[\!\!\left[\frac{\partial \rho[\Phi]}{\partial t} \right]\!\!\right] + \left[\!\!\left[\nabla \cdot \left(\rho \mathbf{u} [\Phi]_{f(\rho\mathbf{u},S)} \right) \right]\!\!\right] = [\![\nabla \cdot (\Gamma \nabla[\mathbf{u}])]\!] + [\![S_I[\Phi]]\!] + S_E. \tag{4.39}$$

As described in Rusche (2002), special operators can be employed to extract the matrix coefficients and the source vector of systems of linear algebraic equations: $\mathcal{A}_A \equiv [A]$ and $\mathcal{A}_S \equiv [R]$. The diagonal and off-diagonal coefficient matrices are $\mathcal{A}_D \equiv [D]$ and $\mathcal{A}_N \equiv [N]$.

Table 4.1 – Finite volume notation according to Weller (2002).

Term	Term in Finite Volume Notation	Discretized Term
Time Derivative	$\left[\!\!\left[\frac{\partial \rho[\Phi]}{\partial t} \right]\!\!\right]$	$\frac{\rho_P^n \Phi_P^n - \rho_P^0 \Phi_P^0}{\Delta t} V_P$
Convection Term	$\left[\!\!\left[\nabla \cdot \left(F[\Phi]_{f(F,S)} \right) \right]\!\!\right]$	$\sum_f F \Phi^n_{f(F,S)}$
Diffusion Term	$[\![\nabla \cdot (\Gamma \nabla[\Phi])]\!]$	$\sum_f \Gamma_f \mathbf{S} \cdot \nabla_f \Phi^n$
Divergence Term	$\nabla \cdot \Phi$	$\sum_f \mathbf{S} \cdot \Phi_f^0$
Cell Gradient Term	$\nabla \Phi$	$\sum_f \mathbf{S} \Phi_f^0$
Curl	$\nabla \times \Phi$	$2(\text{skew} \nabla \Phi^0)$
Implicit Source Term	$[\![S_I[\Phi]]\!]$	$S_I V_P \Phi^n$
Explicit Source Term	S_E	$S_E V_P$
Cell Avarage	$\langle \Phi \rangle_\square$	$\frac{1}{N} \sum_{P=\square} \Phi_P^0$

As further specified in Rusche (2002), in OpenFOAM®, another operator $\mathcal{A}_H$ is widely used, which is defined as

$$\mathcal{A}_H \equiv \mathcal{A}_S - \mathcal{A}_N \Phi, \tag{4.40}$$

and is termed the "H" operator. It is used in a so-called Jacobi iteration scheme, which

is employed to obtain a first approximation of Φ:

$$\Phi \approx \mathcal{A}_D^{-1}\mathcal{A}_H = \frac{\mathcal{A}_H}{\mathcal{A}_D}. \tag{4.41}$$

The exact usage of this approximation is described in the next section, which will explain the concrete discretization for the Navier-Stokes equations.

4.1.2 Discretization of the Navier-Stokes equations

In this study, granular flows are simulated as a two-phase flow. One phase contains the granular material, which is described as a continuum (no difference made between space occupied by particles and inter-particle air) and the other phase contains the air above free surfaces. Analogous to Rusche (2002), both fluids are assumed to be immiscible and incompressible without any mass transfer between them. Rusche (2002) suggested a model, where both fluids are described by one set of conservation equations. In a mathematical representation, the two fluids (1 and 2) are distinguished by a step (Heaviside) function $H(x,t)$, whose value is 1 for the granular fluid and 0 for the surrounding air. With this, any material property at any place in the two fluids can be described as a combination of the two properties, provided the Heaviside function value is known. With this, the density can be for example written as:

$$\rho(x,t) = \rho_1 H(x,t) + \rho_2(1 - H(x,t)). \tag{4.42}$$

In this case, 1 would be the granular fluid and 2 the air. The interface between the two fluids is characterized as the point of a non-zero gradient of $\rho(x,t)$. To describe interface phenomena such as surface tension, interface terms can be added to the governing equations in OpenFOAM®. These terms are represented by a three-dimensional δ function, which is a repeated multiplication of the one-dimensional δ function Rusche (2002):

$$\delta(\mathbf{x}) = \delta(x)\delta(y)\delta(z). \tag{4.43}$$

As in Rusche (2002), the model to describe the granular flow in this study are the Navier-Stokes equations for an incompressible fluid. However, in contrast to Rusche (2002), the rheological model employed for the granular material is a simple Coulomb frictional viscosity. For a single-field formulations as mentioned above, OpenFOAM® employs the following mass continuity and momentum equation (Unverdi and Tryggvason, 1992; Tryggvason et al., 1998):

$$\nabla \cdot \mathbf{u} = 0 \tag{4.44}$$

$$\frac{\partial \rho \mathbf{u}}{\partial t} + \nabla \cdot (\rho \mathbf{u}\mathbf{u}) = -\nabla p + \nabla \cdot \boldsymbol{\tau} + \rho f + \int_{S(t)} \sigma_S \kappa' \mathbf{n}' \delta(\mathbf{x} - \mathbf{x}') dS \tag{4.45}$$

In this equation, f denotes all body forces, however, gravity is the only considered body force in the procedure of this study.

The integral on the right hand site of (4.45) represents the momentum contributed by the surface tension. By integrating over the three-dimensional δ-function, a momentum only acting on the interface of the two fluids is created, where σ_S is the surface tension coefficient, κ' is the curvature of the surface and n is the normal vector of the interface. In the case of water, surface tension may not be neglected and the term has to be taken into consideration. In the case of a granular material, the surface tension is of minor importance and is therefore neglected in this study. For this purpose σ_S is set to zero here.

As mentioned above, the granular material is treated a non-Newtonian fluid with Coulomb frictional viscosity. The air, however, is treated as Newtonian fluid. The stress tensor τ of (4.45) is defined as

$$\boldsymbol{\tau} = \mu(\nabla \mathbf{u} + \nabla \mathbf{u}^T) \tag{4.46}$$

in OpenFOAM®, where μ denotes the kinematic viscosity of the respective fluid.

4.1.2.1 VOF method

The representation of the interface between the two fluids by a Heaviside function is a precise mathematical description for two immiscible fluids, but creates problems for the numerical solution. In this case, the boundary between the two fluids would be forced to boundaries between cells. In order to circumvent this problem and still be able to describe the flow in a single-field formulation, OpenFOAM® makes use of the volume of fluid method (VOF) (Hirt and Nichols, 1981). In this system, the border between the two fluids is not considered discontinuous but consists of cells, which contain fractions of both fluids, thus a mixture of the two. The fraction of the respective fluid in a cell is given by an indicator function α_1:

$$\alpha_1 = \begin{cases} 1 & \text{for a point inside fluid 1} \\ 0 < \alpha_1 < 1 & \text{for a point in the transitional region} \\ 0 & \text{for a point inside fluid 2} \end{cases} \tag{4.47}$$

α_1 is propagated with the respective fluid as a Lagrangian invariant (Hirt and Nichols, 1981) and follows a transport equation of the form:

$$\frac{\partial \alpha_1}{\partial t} + (\mathbf{u} \cdot \nabla)\alpha_1 = 0. \tag{4.48}$$

With α_1, the local viscosity and density in a flow of the fluids 1 and 2 are described by

$$\rho = \alpha_1 \rho_1 + (1 - \alpha_1)\rho_2, \tag{4.49}$$

$$\mu = \alpha_1 \mu_1 + (1 - \alpha_1)\mu_2. \tag{4.50}$$

These expressions for ρ and μ are now included in (4.45) and (4.46) to describe the flow behavior of the two phases together.

4.1.2.2 Solution procedure of the Navier-Stokes equations including the interface terms

In this section, the solution procedure for the governing equations described above underlying the implementation of OpenFOAM® is denoted. This procedure has gradually evolved during the development of OpenFOAM® and is described in detail in Rusche (2002). Here, the important steps for this study are summarized.

Bounded compression of the interface

The definition of the boundary by an indicator function contains the potential to create a confused boundary with a width of several cells. This is undesirable and avoided in OpenFOAM® by an artificial compression term in the transport equation for α_1:

$$\frac{\partial \alpha_1}{\partial t} + \nabla \cdot (\mathbf{u}\alpha_1) + \nabla \cdot (\mathbf{u}_r \alpha_1 (1 - \alpha_1)) = 0. \tag{4.51}$$

$\mathbf{u}_r$ denotes a velocity field, which is chosen to compress the interface. The procedure of determining a suitable $\mathbf{u}_r$ is described below. The artificial term (third term in (4.51) cancels out in all cells containing exclusively one fluid and thus only influences the boundary region.

According to Rusche (2002), (4.51) can be discretized as:

$$\left[\!\left[\frac{\partial [\alpha_1]}{\partial t}\right]\!\right] + \left[\!\left[\nabla \cdot (\Phi [\alpha_1]_{f(\Phi,S)}\right]\!\right] + \left[\!\left[\nabla \cdot \left(\Phi_{r_b} [\alpha_1]_{f(\Phi_r,S)}\right)\right]\!\right] = 0, \tag{4.52}$$

with $\Phi_{r_b} = (1 - \alpha_1)_{f(-\Phi r,S)} \Phi_r$ and $\Phi = \mathbf{S} \cdot \mathbf{u}_f$, where Φ denotes the volumetric flux. As will be described below, Φ cannot be calculated from the face-interpolate of $\mathbf{u}$ but will be calculated from the pressure.

In OpenFOAM®, the compression velocity $\mathbf{u}_r$ is calculated from the maximum velocity magnitude in the transition region. In order to achieve a compression acting perpendicular to the interface between the two fluids, the maximum velocity magnitude is multiplied by the normal vector of the interface:

$$\Phi_r = K_c \mathbf{n}^* \max \frac{|\mathbf{n}^* \Phi|}{|\mathbf{S}|^2}. \tag{4.53}$$

Here, K_c is a coefficient determining the strength of the compression. It is set to 1.5 based on empirical optimization (Rusche, 2002).

4.1.2.3 Final momentum equation

To facilitate a more stable numerical solution, two terms of (4.45) need to be reformulated, namely the pressure and the viscous stress. The motion of the flow does not depend on the absolute values of the pressure but on its gradient. Therefore, it is legitimate to remove the hydrostatic pressure component at a position $\mathbf{x}$ of the flow from the pressure. This yields a modified pressure p^*:

$$p^* = p - \rho \mathbf{g} \cdot \mathbf{x}. \tag{4.54}$$

To include p^* in the momentum equation, its gradient is required:

$$\begin{aligned} \nabla p^* &= \nabla p - \nabla(\rho \mathbf{g} \cdot \mathbf{x}) \\ &= \nabla p - \rho \mathbf{g} - \mathbf{g} \cdot \mathbf{x} \nabla \rho. \end{aligned} \tag{4.55}$$

To achieve a more effective numerical treatment of the viscous stress term, it is reformulated as

$$\begin{aligned} \nabla \boldsymbol{\tau} &= \nabla \cdot \left(\mu \left(\nabla \mathbf{u} + (\nabla \mathbf{u})^T \right) \right) \\ &= \nabla \cdot (\mu \nabla \mathbf{u}) + \nabla \cdot \left(\mu (\nabla \mathbf{u})^T \right) \\ &= \nabla \cdot (\mu \nabla \mathbf{u}) + (\nabla \mathbf{u}) \cdot \nabla \mu + \mu \nabla (\nabla \mathbf{u}) \\ &= \nabla \cdot (\mu \nabla \mathbf{u}) + (\nabla \mathbf{u}) \cdot \nabla \mu. \end{aligned} \tag{4.56}$$

With this, the momentum equation (4.45) reads as follows:

$$\begin{aligned} &\frac{\partial \rho \mathbf{u}}{\partial t} + \nabla \cdot (\rho \mathbf{u} \mathbf{u}) \\ &\quad = -\nabla p^* + \nabla \cdot (\mu \nabla \mathbf{u}) + (\nabla \mathbf{u}) \cdot \nabla \mu - \mathbf{g} \cdot \mathbf{x} \nabla \rho + \sigma_S \kappa \nabla \alpha_1. \end{aligned} \tag{4.57}$$

4.1.2.4 PISO

The Pressure-Implicit Split-Operator (PISO) method is employed in OpenFOAM® to avoid the pressure-velocity coupling problems in the collocated arrangement discussed in paragraph 4.1.1.2 (Issa, 1986). It is one of the great advantages of the OpenFOAM® implementation by Rusche (2002) that the interface capturing method can be used with a collocated variable arrangement. In addition to the solution of the pressure-velocity coupling problems, the case of two fluids also requires the sharpness of the boundary to be preserved. For the PISO method, corrections of the momentum and the pressure equation are derived from the semi-discretized momentum-equation:

$$\mathcal{A}_D \mathbf{u} = \mathcal{A}_H - \nabla p^* - \mathbf{f} \cdot \mathbf{x} \nabla \rho + \sigma_S \kappa \nabla \alpha_1. \tag{4.58}$$

$\mathcal{A}$ denotes the equation system resulting from the discretization of the phase momentum equations without surface tension and buoyancy terms:

$$\mathcal{A} := \left[\!\!\left[\frac{\partial \rho[\mathbf{u}]}{\partial t} \right]\!\!\right] + \left[\!\!\left[\nabla \cdot \left(\rho_f \Phi [\mathbf{u}]_{f(\rho_f \Phi, S)} \right) \right]\!\!\right] = \left[\!\!\left[\nabla \cdot (\mu_f \nabla [\mathbf{u}]) \right]\!\!\right] + (\nabla \mathbf{u}) \cdot \nabla \mu_f. \tag{4.59}$$

Decomposition of (4.59) into diagonal and "H" parts yields

$$\mathbf{u} = \frac{\mathcal{A}_H}{\mathcal{A}_D} - \frac{\nabla p^*}{\mathcal{A}_D} - \frac{\mathbf{f} \cdot \mathbf{x} \nabla \rho}{\mathcal{A}_D} + \frac{\sigma_S \kappa \nabla \alpha_1}{\mathcal{A}_D}. \tag{4.60}$$

In the PISO scheme, the flux is first predicted neglecting the pressure (flux predictor Φ^*) and then corrected (flux corrector Φ). Φ^* and Φ are obtained from interpolation of the momentum correction equation by central differencing:

$$\Phi^* = \left(\frac{\mathcal{A}_H}{\mathcal{A}_D} \right)_f \cdot \mathbf{S} - \left(\frac{1}{\mathcal{A}_D} \right)_f (\mathbf{f} \cdot \mathbf{x})_f |\mathbf{S}| \nabla_f^\perp \rho + \left(\frac{1}{\mathcal{A}_D} \right)_f (\sigma_S \kappa)_f |\mathbf{S}| \nabla_f^\perp \alpha_1 \tag{4.61}$$

$$\Phi = \Phi^* - \left(\frac{1}{\mathcal{A}_D} \right)_f |\mathbf{S}| \nabla_f^\perp p^* \tag{4.62}$$

With this, the final continuity equation at the cell faces including the flux corrector reads:

$$\left[\!\!\left[\nabla \cdot \left(\left(\frac{1}{\mathcal{A}_D} \right)_f \nabla [p^*] \right) \right]\!\!\right] = \nabla \cdot \Phi^*. \tag{4.63}$$

Solving this equation enables updating of fluxes and velocities with corrected values to ensure continuity.

4.1.2.5 Timestep control

To ensure numerical stability, time steps have to be sufficiently small. Thus, OpenFOAM® adjusts the time step at the beginning of each iteration using a maximum Courant number (see paragraph 4.1.1.5) as restriction. In general, OpenFOAM® favors a smooth adjustment to ensure the stability of the procedure, which is achieved by keeping Co close to a predefined target value Co_t using under-relaxation. Nevertheless, there are moments in which Co is much smaller than Co_t, like during the initialization with a small time step. Here, the length of the next time step is limited to an appropriate multiple of the first time step. This limit has to be predefined as well. In the other extreme case, when the maximum Co is larger than Co_t, the length of the time-step is set to the value for Co_t. This is represented by the following constrain:

$$\Delta t^n = \begin{cases} \min(\Delta t^0 + \psi_t(\Delta t_t - \Delta t^0), 2\Delta t^0) & \text{for } Co^0 \leq K_l Co_t \\ \Delta t_t & \text{for } Co^0 > K_l Co_t \end{cases} \tag{4.64}$$

where ψ_t is the under-relaxation factor, K_l is the maximum multiple of the next time-step and Co^0 is the maximum Courant number of the last time-step. Δt_t is the time-step defined by Co_t:

$$\Delta t_t = \frac{Co_t}{Co^0}\Delta t^0. \tag{4.65}$$

Empirical studies displayed good stability for Courant numbers smaller than 0.5 (Rusche, 2002), wherefore this value is used in this study. The under-relaxation factor ψ_t is fixed to 0.1 in OpenFOAM® and K_l is fixed to 1.2 in the OpenFOAM® version employed in this study.

4.1.3 Sequence of numerical solution procedure

The numerical solution procedure in OpenFOAM® using the PISO scheme is depicted in Tab. 4.2. The procedure used in this study is adopted from Rusche (2002) but modified because of the neglect of surface tension and the usage of a non moving reference frame. First, the time-step is adjusted (steps 1). Then the boundary conditions are updated (step 2) followed by solving and smoothening of the transport equation for the indicator function (step 3). Afterwards the unit normal vector and the curvature are calculated (step 4) and the discretized momentum equation is constructed (step 5). The pressure-velocity algorithm is corrected in the PISO correction loop, where after solving the pressure equation the momentum is corrected based on the change in pressure (step 6).

Table 4.2 – Numerical solution procedure, modified from Rusche (2002). For detailed explanation see text.

1. Adjust time step (4.64)
2. Adjust boundary conditions
3. Solve the α_1-equation (4.52)
4. Calculate curvature
5. Construct $\mathcal{A}$ (4.59)
6. PISO-Loop:
   (a) Predict fluxes using (4.61)
   (b) Construct and solve the pressure equation (4.63)
   (c) Correct fluxes (4.62)
   (d) Reconstruct velocities

4.2 Numerical solutions for the Savage-Hutter equations

As mentioned in section 3.2.2, the Savage-Hutter model is used in this study for comparison with the numerical simulations obtained by using OpenFOAM®. Comparisons are only made for simulations of flows in a 10 cm wide Poly(methyl methacrylate) (PMMA) channel (see section 5.2.2), which represents a quasi two-dimensional set-up. Due to the depth-averaged character of the Savage-Hutter type simulations, this situation is reduced to a one-dimensional problem. For this reason, only one dimensional flows down an inclined plane are described here. The numerical scheme employed is the one described in Tai et al. (2001) and Wang et al. (2004), which is a non-oscillatory central (NOC) scheme using total variation diminishing (TVD) limiters.

In this section, the numerical procedure to solve the Savage-Hutter model equations using a standard technique for non-linear hyperbolic conservation equations for a one-dimensional case will be presented analogous to the description for a two-dimensional case by Wang et al. (2004). A hyperbolic system of partial differential equations can be written as

$$\frac{\partial}{\partial t}\mathbf{w} + \frac{\partial}{\partial x}\mathbf{f}(\mathbf{w}) = \mathbf{s}(\mathbf{w}). \tag{4.66}$$

Introducing the unknown vector $\mathbf{w} = (h, m_x)^T$ with the new variable $m_x = hu$, the

Savage-Hutter model equations (3.47) and (3.48) become

$$\frac{\partial}{\partial t}\begin{pmatrix} h \\ m_x \end{pmatrix} + \frac{\partial}{\partial x}\begin{pmatrix} m_x \\ m_x^2/h + 1/2\beta h^2 \end{pmatrix} = \begin{pmatrix} 0 \\ hs_x \end{pmatrix}, \tag{4.67}$$

with parameter $\beta = \epsilon k_{act/pass}\cos\zeta$ and $s_x = \sin\zeta - \tan\delta\,\mathrm{sign}(u)\cos\zeta$.

For the numerical solution, the physical domain is split into cells, a single cell C_i is defined as

$$C_i = \left\{(x)\middle| |x - x_i| \leq \frac{\Delta x}{2}\right\}. \tag{4.68}$$

In each cell, the variables are stored as cell averaged values. The local value inside this cell can be reconstructed assuming a linear interpolation function. To keep the slope of this interpolation function at moderate values, a TVD slope limiter is introduced. The piecewise linear reconstruction of $\mathbf{w}(x, t^n)$ is

$$\mathbf{w}(x, t^n) = \mathbf{w}_i^n + (x - x_i)\left(\frac{\partial \mathbf{w}}{\partial x}\right)_i^n = \mathbf{w}_i^n + (x - x_i)\boldsymbol{\sigma}^x. \tag{4.69}$$

For a scalar physical variable w, i.e. a component of $\mathbf{w}$, the slope limiter σ_i^x can be expressed as $\sigma_i^x = \phi_i^x(w_{i+1} - w_i)/\Delta x$ and $\phi_i^x$is defined as the ratio of consecutive gradients θ_i^x,

$$\phi_i^x = \phi(\theta_i^x),\ \theta_i^x = \frac{w_i - w_{i-1}}{w_{i+1} - w_i}. \tag{4.70}$$

Several slope limiters can be employed in the non-oscillatory TVD scheme to ensure second-order accurate cell reconstruction. These limiters are introduced as constrains which must be met by $\phi(\theta)$.

In this work, only the Minmod limiter (Harten, 1983)

$$\phi_{Minmod}(\theta) = \max(0, \min(1, \theta)) \tag{4.71}$$

is used, which is defined by the lower boundary of the second-order TVD region. This limiter is the most diffusive of all acceptable limiters.

The NOC scheme is a predictor-corrector method, meaning that two calculation steps are performed to solve the next time step. First, the cell averages are evaluated at the boundaries between cells. Therefore, the half time-step variables are stored at the old cell boundaries (staggered grid). The piecewise linear reconstruction (4.70) at time-step t^n is smooth and remains smooth for $t < t^{n+1}$ if an appropriate time-step is chosen. The restriction of the time-step will be described below.

The fluxes across boundaries can be evaluated by Taylor extrapolations using differential equation and standard quadrature rules. The midpoint rule in time is employed to

archive temporally second-order accuracy.

The staggered averages at time t^{n+1} is determined by integrating (4.66), this yields

$$\begin{aligned}\mathbf{w}_{i+1/2}^{n+1} =& \frac{1}{\Delta x}\int_{x_i}^{x_i+1}\mathbf{w}(x,t^{n+1})dx \qquad (4.72)\\ =& \frac{1}{\Delta x}\int_{x_i}^{x_i+1}\mathbf{w}(x,t^{n})dx\\ &-\frac{1}{\Delta x}\int_{t^n}^{t^{n+1}}(\mathbf{f}(x_{i+1},t)-\mathbf{f}(x_i,t))dt\\ &+\frac{1}{\Delta x}\int_{t^n}^{t^{n+1}}\int_{x_i}^{x_i+1}\mathbf{s}(x,t)dxdt. \qquad (4.73)\end{aligned}$$

Each term of (4.73) is now analysed in detail. Starting with the first term, the average of $w(x,t^n)$ can be evaluated by the midpoint rule in each half cell segment

$$\begin{aligned}\frac{1}{\Delta x}\int_{x_i}^{x_{i+1}}\mathbf{w}(x,t^n)dx =& \frac{1}{\Delta x}\left\{\int_{x_i}^{x_{i+1/2}}\mathbf{w}(x,t^n)dx+\int_{x_i}^{x_{i+1/2}}\mathbf{w}(x,t^n)dx\right\}\\ =& \frac{1}{2}\left\{\mathbf{w}_{i+1/4}^n+\mathbf{w}_{i+3/4}^n\right\}. \qquad (4.74)\end{aligned}$$

The half way values at $i+1/4$ and $i+3/4$ are calculated by (4.70) as

$$\mathbf{w}_{i+1/4}^n = \mathbf{w}_i^n + \frac{\Delta x}{4}\sigma_i^x, \qquad (4.75)$$

$$\mathbf{w}_{i+3/4}^n = \mathbf{w}_{i+1}^n - \frac{\Delta x}{4}\sigma_{i+1}^x. \qquad (4.76)$$

The second term in (4.73),which represents the flux, is approximated by second-order rectangular rule for the spatial integral and by midpoint quadrature rule for second-order accuracy of the temporal integral. Thus,

$$\begin{aligned}&\frac{1}{\Delta x}\int_{t^n}^{t^{n+1}}(\mathbf{f}(x_{i+1},t)-\mathbf{f}(x_i,t))dt\\ &\quad=\frac{\Delta t}{2\Delta x}\left\{\mathbf{f}(x_{i+1},t^{n+1/2})-\mathbf{f}(x_i,t^{n+1/2})\right\}\\ &\quad=\frac{\Delta t}{2\Delta x}\left\{\mathbf{f}(\mathbf{w}_{i+1}^{n+1/2})-\mathbf{f}(\mathbf{w}_i^{n+1/2})\right\}. \qquad (4.77)\end{aligned}$$

The values for the half time-step $t^{n+1/2}$ are approximated by first-order Taylor series

expansion in time. With (4.66), this yields the predictor step of the NOC-scheme:

$$\begin{aligned}\mathbf{w}_i^{n+1/2} &= \mathbf{w}_i^n + \frac{\Delta t}{2}\left(\frac{\partial \mathbf{w}}{\partial t}\right)_i^n \\ &= \mathbf{w}_i^n - \frac{\Delta t}{2}\left(\frac{\partial \mathbf{f}(\mathbf{w})}{\partial t}\right)_i^n + \frac{\Delta t}{2}\mathbf{s}(\mathbf{w}_i^n) \\ &= \mathbf{w}_i^n - \frac{\Delta t}{2}\sigma_i^f + \frac{\Delta t}{2}\mathbf{s}(\mathbf{w}_i^n),\end{aligned} \tag{4.78}$$

where σ_i^f is the flux limiter for the flux f. This can be expressed by the corresponding Jacobian as follows:

$$\sigma_i^f = \left(\frac{\partial \mathbf{f}(\mathbf{w})}{\partial \mathbf{w}}\right)_i^n \sigma_i^x. \tag{4.79}$$

To approximate the integral of the last term in (4.73), again the domain is split into the two cell segments and the midpoint quadrature rule is employed for second-order accuracy of the temporal integral, resulting in the corrector step of the NOC scheme:

$$\begin{aligned}&\frac{1}{\Delta x}\int_{t^n}^{t^{n+1}}\int_x^{x+1}\mathbf{s}(x,t)dxdt \\ &\quad= \frac{\Delta t}{4}\left\{\mathbf{s}(x_{i+1/4}, t^{n+1/2}) + \mathbf{s}(x_{i+3/4}, t^{n+1/2})\right\} \\ &\quad= \frac{\Delta t}{4}\left\{\mathbf{s}(\mathbf{w}_{i+1/4}^{n+1/2}) + \mathbf{s}(\mathbf{w}_{i+3/4}^{n+1/2})\right\}.\end{aligned} \tag{4.80}$$

Values at $t^{n+1/2}$ and $i+1/4$ and $i+3/4$ are determined by space-time Taylor extrapolation:

$$\mathbf{w}_{i+1/4}^{n+1/2} = \mathbf{w}_i^{n+1/2} + \frac{\Delta x}{4}\sigma_i^x, \tag{4.81}$$

$$\mathbf{w}_{i+3/4}^{n+1/2} = \mathbf{w}_{i+1}^{n+1/2} - \frac{\Delta x}{4}\sigma_{i+1}^x. \tag{4.82}$$

Taken together, the NOC-scheme is composed of a predictor step (4.78) and a staggered corrector step (4.73) , which is achieved by substituting (4.74) , (4.77) and (4.80). With this scheme, the cell average value is determined by

$$\mathbf{w}_{i+1/2}^{n+1} = \frac{1}{4}\left\{\mathbf{w}_{i+1/4}^n + \mathbf{w}_{i+3/4}^n\right\} - \frac{\Delta t}{2\Delta x}\left\{\mathbf{f}\left(\mathbf{w}_{i+1}^{n+1/2}\right) - \mathbf{f}\left(\mathbf{w}_i^{n+1/2}\right)\right\} \tag{4.83}$$

$$+ \frac{\Delta t}{4}\left\{\mathbf{s}\left(\mathbf{w}_{i+1/4}^{n+1/2}\right) + \mathbf{s}\left(\mathbf{w}_{i+3/4}^{n+1/2}\right)\right\}. \tag{4.84}$$

To ensure stability of the numerical solution and that no material and information can

proceed further than one cell per time step, the Courant-Friedrichs-Lewy (CFL) condition (Courant et al., 1928; Jiang and Tadmor, 1998) is employed as described by Wang et al. (2004). Therefore, the characteristic speeds have to be determined. For this purpose, (4.66) and (4.67) can be written as

$$\frac{\partial \mathbf{w}}{\partial t} + \mathbf{A_x}\left(\frac{\partial \mathbf{w}}{\partial x}\right) = \mathbf{s}, \tag{4.85}$$

where $\mathbf{A}_x$ is the Jacobian of $\mathbf{f}$:

$$\mathbf{A}_x = \frac{\partial \mathbf{f}}{\partial \mathbf{w}} = \begin{pmatrix} 0 & 1 \\ -(m_x)^2/h^2 + \beta_x h & 2m_x/h \end{pmatrix}. \tag{4.86}$$

With this, the characteristic equation is given by

$$\det(\mathbf{A}_x - \lambda \mathbf{I}_2) = 0. \tag{4.87}$$

This equation has two solution:

$$\lambda_{1,2} = m_x/h \pm \sqrt{\beta_x h}, \tag{4.88}$$

which are the Eigenvalues specifying the sub-critical and super-critical speed of the system. With (4.88), the maximum wave speed can be determined as

$$c_x^{max} = \max_{all\ i}\left(|u_i| + \sqrt{(\beta_x)_i h_i}\right),\ u_i = (m_x)_i/h_i. \tag{4.89}$$

This maximum speed is then included in the CFL condition to determine the maximal duration of a time step:

$$\Delta t\, |c_x^{max}|/\Delta x < \frac{1}{2}. \tag{4.90}$$

This restriction of the time step length ensures that the solution remains smooth, so that the Taylor expansions and midpoint quadrature rules are justified.

For brevity, the depth-averaged simulations employing the Savage-Hutter model equations and the numerical solution technique described in this section will be called Savage-Hutter simulations from here on.

5 Experimental setup and measurement techniques

Three experimental set-ups were employed in this study: a rotating box for the observation of steady-state flows, an inclined translucent channel for two-dimensional flow observation and a wide inclined channel for three-dimensional observations. As granular material for the small scale laboratory experiments performed here, sand and polyvinyl chloride (PVC) pellets were chosen. The motion of the granular flow was captured by a high speed camera to allow detailed temporal resolution in the flow observation. The different materials, experimental set-ups and the respective imaging and measurement techniques are described in this section.

5.1 Granular materials

Three different granular materials where employed:

- PVC pellets:

  $d = 4\,\mathrm{mm}$, $\phi = 32°$, $\delta = 20°$, $\rho = 1550\,\mathrm{kg/m^{-3}}$

- Quartz Sand:

  $d = 0.71 - 1.25\,\mathrm{mm}$, $\phi = 37°$, $\delta = 18°$, $\rho = 2650\,\mathrm{kg/m^{-3}}$

- Fine Quartz Sand:

  $d = 0.1 - 0.25\,\mathrm{mm}$, $\phi = 37°$, $\delta = 18°$, $\rho = 2650\,\mathrm{kg/m^{-3}}$

The bottom friction angle δ was determined by filling a cylinder (without bottom) with the respective material, placing it in the channel and measuring the inclination which is necessary to make this cylinder start to slide down the channel. Similar values were observed for both channel set-ups employed in this study. The internal friction angle ϕ was determined by assuming it to be equal to the angle of repose (Lambe and Whitman, 1969; Kutzbach and Scherer, 1977; Pudasaini et al., 2007). The angle of repose was measured as the inclination of a pile of the respective material raised to the maximal possible height.

5.2 Experimental set-ups

5.2.1 Rotating box

A slowly rotating box was used to analyze a quasi steady flow for the determination of the rheological model to describe the granular flow. The box has a square base of $h \times b =$

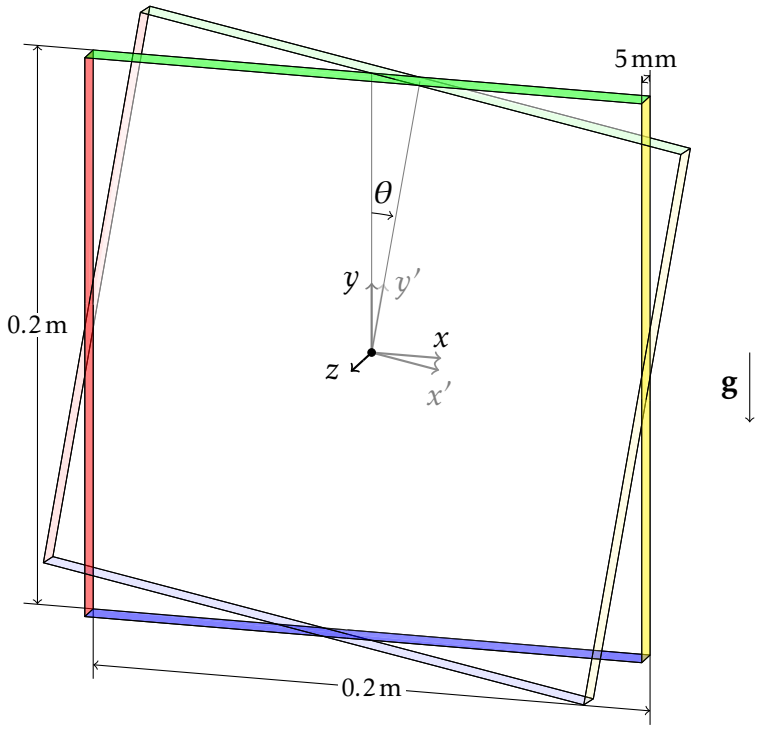

Figure 5.1 – Sketch of rotating box geometry.

20 cm × 20 cm and a depth of $d = 0.5$ cm (Fig.5.1). Front and back of the box are made of PMMA, and the other faces are made of wood. The box was filled with fine sand until the free surface of the sand reached $h_0 = 11$ cm. The volume of the bulk sand is 55% of the whole container. The container can be rotated with a constant rotating speed of a period of T_{rot}. The actual rotating speed is extracted from the captured images.

5.2.2 Inclined channel

The channel set-up employed in this study is similar to Pudasaini et al. (2007). The channel consists of a reservoir for granular material and a straight, 2 m long channel (Fig. 5.2). The reservoir can take up to 50 l of granular material. A movable wall at the interface between the reservoir and the channel defines a constant inflow height h_0 which can be adjusted between 0 cm and 30 cm. A swinging gate holds back the material in the reservoir. Both the wall and the gate can be removed, and the gate can be placed on different positions of the channel to perform studies of collapsing columns of granular materials. The wall at the end of the channel (depicted in red in Fig. 5.2) can be removed to generate an undisturbed outflow or inserted to perform impingement test with a perpendicular wall. Additionally, obstacles can be installed inside the channel. The inclination angle of the channel ζ can be varied from 0° to 50°. All walls of the channel except for the gate are made of PMMA, allowing observation of the granular flow from all directions. By capturing the flow behavior from the side of the channel, velocity profiles

can be recorded.

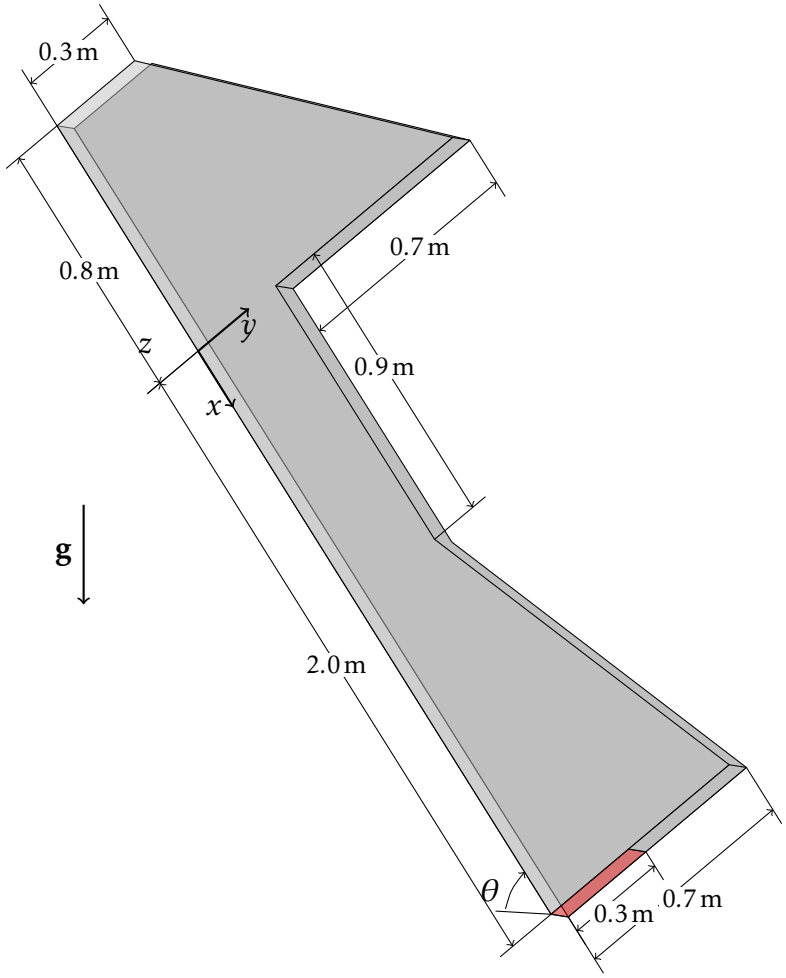

Figure 5.2 – Sketch of the channel geometry.

5.2.3 Wide channel

To analyze the flow around obstacles, a wide channel similar to the channel described in the previous paragraph was build. It has a similar reservoir for up to 7 l of granular material, a 59 cm long slope and a fixed inclination angle of $\zeta = 45°$ (Fig.5.3). The container wall facing the channel (depicted in red in Fig.5.3) is rapidly pulled up to a constant inflow height h_0. Different obstacles can be mounted on the lower part of the channel. Obstacles employed in this study were a tetrahedron with an edge-length of 12 cm and a cylinder with 3.96 cm radius and a height of 5 cm.

5.3 Image acquisition

The progressive Scan CMOS Highspeed Camera (Optronis CR600x2) used in this study captures RAW images with a color depth of 10-bits at a size of 1280 px × 1024 px with

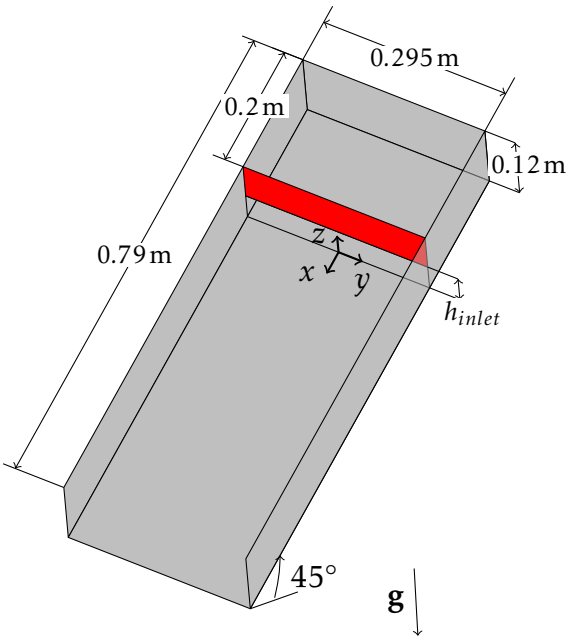

Figure 5.3 – Sketch of the wide channel geometry.

a framerate of 500 fps. Each pixel has a size of $14\,\mu\text{m} \times 14\,\mu\text{m}$. The active area of the CMOS sensor is $17.92\,\text{mm} \times 14.34\,\text{mm}$. The framerate can be increased by choosing a lower resolution. The internal storage of 4 GB can store sequences of up to 6.5 s length at full resolution and framerate. The RAW images contain the intensity of each pixel stored as a two dimensional arrays of gray values between 0 and 1024. The conversion factor between 1 px and the physical measured dimensions in m are obtained by taking an image of a calibration pattern and correlating the known positions of the pattern with their positions (in px) on the image plane.

5.4 Particle Image Velocimetry (PIV)

PIV is employed in this study to obtain highly resolved temporal and spatial velocity profiles of the granular flow. For this purpose, a set of custom made c++ programs was generated. The calculation steps performed by these programs are described here. To analyze the velocities, first the area covered by grains needs to be determined. Afterwards, the cross-correlation of an image pair is used to determine the velocity (Eckart et al., 2003).

5.4.1 Identification of Region of Interest (ROI)

To determine the region of interest (ROI), a reference frame $\mathcal{I}^0$ of the "empty" experiment was used. This empty frame was substracted from the actual frame $\mathcal{I}^n$. The new intensity

levels were binarized if the difference lay above some predefined threshold T (Fig. 5.4).

$$\mathcal{I}^n_{mask} = \begin{cases} 0 & \text{if } |\mathcal{I}^n - \mathcal{I}^0| > T \\ -1 & \text{else.} \end{cases} \tag{5.1}$$

This study only intended to observe the bulk fluid and no movements of the gate or single flying particles. Therefore, the recorded frame $\mathcal{I}^n_{mask}$ was segmented into different regions and only the region with the biggest area was taken into consideration by an algorithm performing the following steps: a counter for the number of segments S with an initial value of 1 is introduced. The segmentation is done by looping through the image data until a point is found where the value is 0, the value is set to S and now starting from this point all adjacent pixels with value 0 are set to S. Afterwards, the counter of segments is increased by one and the search for values of 0 is continued. The biggest segment can now be identified from a histogram of pixel values in $\mathcal{I}^n_{mask}$. The final mask is created by setting all values other than those belonging to the chosen segment to zero and afterwards the value in the chosen segment to 1.

The height profile $h(x)$ was determined by searching from the upper image boundary for each column for the first occurrence of a value different from zero. The bottom profile $b(x)$ was created in the same way but starting from the lower boundary of the image.

Figure 5.4 – Determination of the region of interest (ROI) and the resulting height profile.

5.4.2 Cross-correlation

To determine the velocity, two images are needed ($\mathcal{I}^n$ and $\mathcal{I}^{n+1}$) which have been acquired with a delay of Δt (Fig. 5.5). In the PIV-Method, a small area ($2n+1 \times 2m+1$) was cut out around the coordinate x_0 and y_0 of $\mathcal{I}^n$, the so-called interrogation window, and the most similar image in $\mathcal{I}^{n+1}$ was found by shifting the interrogation window over $\mathcal{I}^{n+1}$ and calculation of the cross-correlation $K_{x_0,y_0}(a,b)$ for each offset (shift in x-direction a, shift in y-direction b) (Keane and Adrian, 1992; Eckart et al., 2003). The values of a and b were limited to a specified search area:

$$K_{x_0,y_0}(a,b) = \sum_{i=x_0-n}^{x_0+n} \sum_{j=y_0-m}^{y_0+m} \left(\mathcal{I}^n(i,j) - \mathcal{I}^{n+1}(i+a, j+b)\right)^2. \tag{5.2}$$

The best fitting offset was achieved by searching for the minima of $K_{x_0,y_0}(a,b)$. The actual sub-pixel coordinate was calculated from two parabolic fits in x- and y-direction around x_0, y_0.

The offset $o = (a,b)\left[\frac{\text{px}}{\text{frame}}\right]$ was converted to a velocity by multiplying the scale $s_{\text{px}\to\text{m}}$ and dividing by Δt:

$$u(x_0,y_0)\left[\frac{\text{m}}{\text{s}}\right] = o(a,b)\left[\frac{\text{px}}{\text{frame}}\right] \cdot \frac{s_{\text{px}\to\text{m}}\left[\frac{\text{m}}{\text{px}}\right]}{\Delta t\left[\frac{\text{s}}{\text{frame}}\right]}. \tag{5.3}$$

Figure 5.5 – Cross-correlation in PIV. The red outline marks the interrogation area, while the pink outline marks the search area in two consecutive images $\mathcal{I}^n$ and $\mathcal{I}^{n+1}$. The panel on the right displays the correlation between the two frames as a heat-map. The arrow points at the minimum value.

This procedure to find the velocity $u(x_0,y_0)$ is performed for all points of interest inside the ROI. To speed up the calculation of the cross-correlation, a 2D Fast-Fourier-Transformation is employed.

5.4.3 Special considerations for the rotating box

To determine a fixed body reference frame, the actual rotation angle of the box and the position of the container boundaries need to be determined. To capture these, a Canny edge detection algorithm was employed followed by a linear Hough transformation.

5.4.3.1 Canny-Edge-Detection

Canny edge detection (Canny, 1986) is a multi-stage algorithm used to detect multiple edges in an image. The Algorithm uses the following steps:

1. Noise reduction

   The algorithm employes gradients between direct neighboring pixels. For this reason, noise might induce very high gradients and needs to be minimized. To do so, a Gaussian filter of 5x5 is implemented. This smoothing does not relocate the edges and thus no error is introduced. It rather results in a stronger assessment of the overall structure compared to the local structure.

2. Calculate intensity gradient of the images

   The intensity gradient is calculated using the Sobel operator (Jähne, 2002). The Sobel operator consists of two 3x3 kernels which are convolved with the original image to calculate the horizontal ($\mathbf{G}_x = \mathbf{S}_x \cdot \mathcal{I}$) and vertical gradients ($\mathbf{G}_y = \mathbf{S}_y \cdot \mathcal{I}$). The Sobel operators are a convolution of a 1D-central-difference ($CD_{1D} = (-1, 0, 1)$) and a 1D-Gaussian-blur ($G_{1D} = (1, 2, 1)^T$) filter:

$$\mathbf{S}_x = \begin{bmatrix} -1 & 0 & 1 \\ -2 & 0 & 2 \\ -1 & 0 & 1 \end{bmatrix} \text{ and } \mathbf{S}_y = \begin{bmatrix} -1 & -2 & -1 \\ 0 & 0 & 0 \\ 1 & 2 & 1 \end{bmatrix}. \tag{5.4}$$

   The gradient magnitude and direction are then given by:

$$\mathbf{G} = \sqrt{\mathbf{G}_x^2 + \mathbf{G}_y^2} \text{ and } \mathbf{\Theta} = \arctan\left(\frac{\mathbf{G}_y}{\mathbf{G}_x}\right). \tag{5.5}$$

   The edge direction is now rounded to one of four angles representing the direction to the neighboring image points (0°, 45°, 90°, 135°).

3. Non-maximum suppression

   The magnitude of each point in the gradient field is now compared to the magnitude of the two neighboring points on a line spanned by the gradient of the respective point. Only if the magnitude of a point is higher than the one of both neighbors, the point is assumed to be on the edge and thus this point is set to 1 in a binary edge map **E**.

4. Tracing edges through the image and hysteresis thresholding

   The binary edge map contains all detected edges, even very weak ones, but only strong edges should be considered further. Therefore, a threshold must be applied. The main problem is that it is in most cases impossible to specify a single threshold to differentiate between strong and weak edges. If the threshold is very high to filter out all unwanted edges, many parts of the strong edges are not detected, but a complete detection of the boundary of a given object is necessary. For this reason, a second, lower threshold is defined. Points adjacent to already detected edge-points are now considered to be edge-points if their value is above the second threshold. This facilitates detection of edges without interruptions.

5.4.3.2 Linear-Hough-Transformation

The Hough Transformation (Hough, 1959; Duda and Hart, 1972) is a "brute force" algorithm to detect parameterized objects. For the linear Hough transformation a line is

described by:

$$r(\theta) = x \cdot \cos(\theta) + y \cdot \sin(\theta) \tag{5.6}$$

with the angle θ of the vector from the origin to the closest point($\theta \in [0, \pi]$) and the distance r between the origin and the line ($r \in \mathbb{R}$). The parameter plane (r,θ) is called the Hough space for straight lines in two dimensions. The Hough space is discretized into an accumulator and set initially to zero. The algorithm loops over all possible edges (extracted by the Canny edge detection) and for each possible parameter pair, whose line will pass through the coordinate (x_0, y_0), its accumulator increases by one. This corresponds to a sinusoidal curve in the (r,θ) plane. When all edge points have voted, the parameters with the highest scores are the desired lines.

With this method, the 4 strongest lines which define the boundary of the box are determined. The corners of the box can be found by analyzing the intercept of these lines. Afterwards, the ROI inside the box is determined as described above.

5.5 3D reconstruction in wide channel

The wide channel described in section 5.2.3 allows the observation of three dimensional flows around obstacles. To reconstruct the three-dimensional surface of the flow and the obstacles, the structured light method (Lanman and Taubin, 2009) was used. This method allows 3D-reconstruction with only one camera and a projector (M209X, Dell). All steps of the 3D reconstruction were performed with cvStructuredLight (Lanman and Taubin, 2009) and the openCV library (Bradski, 2000). Here, the cvStructuredLight software was adapted to work on a Linux operating system. Furthermore, the software, which is originally intended to work on static scenes recorded by conventional cameras, was extended to capture the dynamics of a set-up with the high speed camera used in this study.

The structured light method reconstructs 3D information from the recorded image by triangulation between the projected pixels and the pixels recorded by the camera. This requires first an accurate calibration of the camera and projector position relative to the observed object and second an unique identification of each projected pixel.

5.5.1 Calibration of camera and projector

First, internal camera parameters (the focal length and the radial distortion caused by the lens) are calibrated by taking a series of pictures from a checkerboard pattern with known dimensions in different orientations. From these pictures, the openCV software calculates a matrix which is later used to convert pixel coordinates to real space coordinates. Second,

the position of the camera relative to the observed area is calibrated by taking a picture of the checkerboard pattern placed in the area of interest. At the same time, intrinsic and extrinsic parameters of the projector are calibrated by projecting a checkerboard pattern of known pixel dimensions on the actual checkerboard pattern.

The calibration was performed by recording a video of a 1.5 x 1.5 cm checkerboard pattern with the high-speed camera while the projection of the checkerboard pattern was automatically switched on and off each second. This ensured that the checkerboard pattern was captured with and without the projection in each orientation.

5.5.2 Identification of projected pixels

The structured light method allows the identification of each projected pixel by a sequence of pictures which results in a unique color (or black and white) sequence for each pixel. In cvStructuredLight (Lanman and Taubin, 2009), this unique identification is performed using black and white patterns for maximal contrast on multicolored surfaces of the objects to be scanned. The position of each pixel is decoded by a so-called Gray code (Gray, 1953), which ensures a minimum number of switches from black to white during the projection of the picture series. To uniquely identify the 1024 x 768 pixel of the projector, a series of 21 patterns was employed. For enhanced accuracy, the inverse of each pattern was projected as well, resulting in a series of 42 patterns in total. This resulted in a data set containing a collection of projector/camera pixel pairs for each time step of 42 projected patterns.

5.5.3 Triangulation

To reconstruct the 3 dimensional surface, cvStructuredLight (Lanman and Taubin, 2009) correlates the calibration data with the projector/camera pixel pair sets. Through the calibration it is know in which angle the light of each pixel leaves the projector relative to a plane between the projector and the camera. The same holds true for the light which is captured by each pixel of the camera. With these two angles and the information about the distance between projector and camera (also known through the calibration) the intersection of two straight lines originating from the middle of the projector/camera pixel can be determined. This intersection point yield the coordinates of the observed object in the 3D space at the observed position. Due to the three dimensional character of this triangulation process, the two lines will not necessarily intersect. In such cases, the point of closest approximation of the two lines is taken for the 3D reconstruction.

6 Comparison between numerical simulations and experiments

This chapter describes several experiments which were conducted to yield better insight into the complex processes occurring during a granular flow. The PIV method employed in this work (see section 5.4) allows to record velocity distributions during a granular flow at particle size level and thus enables the recording of velocity profiles with fine temporal and spatial resolution. The data generated with this method is, on the one hand, used to draw conclusions about the rheology underlying the granular flow and, on the other hand, to provide detailed information of the flow parameter evolution. These results are then compared with numerical simulations to allow a detailed analysis of the precision provided by the numerical predictions and to improve the simulation process through observed deviations from the experimental data. For this purpose, first simulations of the Savage-Hutter type are performed as described in chapter 4 to test and demonstrate the predictive power of state-of-the-art simulation methods for the performed experiments. A second set of simulations is performed using the OpenFOAM® software described in chapter 4 to perform non-depth-averaged simulations and enable predictions of velocity profiles inside the granular flow.

6.1 Choice of the rheological model for non-depth-averaged simulations

In contrast to depth-averaged simulations, where shearing inside the material is neglected, the implementation of a non-depth-averaged simulation requires a model for the description of the material's response to shearing. In this work, non-depth-averaged simulations are performed using a fluid dynamics approach. As described in section 1.3.4, the choice of the rheological model is the central aspects for description of granular flows by fluid dynamics simulations. Thus, the rheological model describing the behavior of the employed material was determined in order to choose a law for the description of the materials response to stress and shearing in the non-depth-averaged simulations developed here. The granular material can be either considered as a viscous, a viscoelastic, a viscoplastic or a visco-elasto-plastic fluid (section 1.3.4).

6.1.1 Experimental findings

To determine to which of the above mentioned categories the granular materials used in this study belongs, a pilot experiment was performed using the slowly rotating box set-up described in section 5.2.1 with fine quartz sand filling. The rectangular geometry of

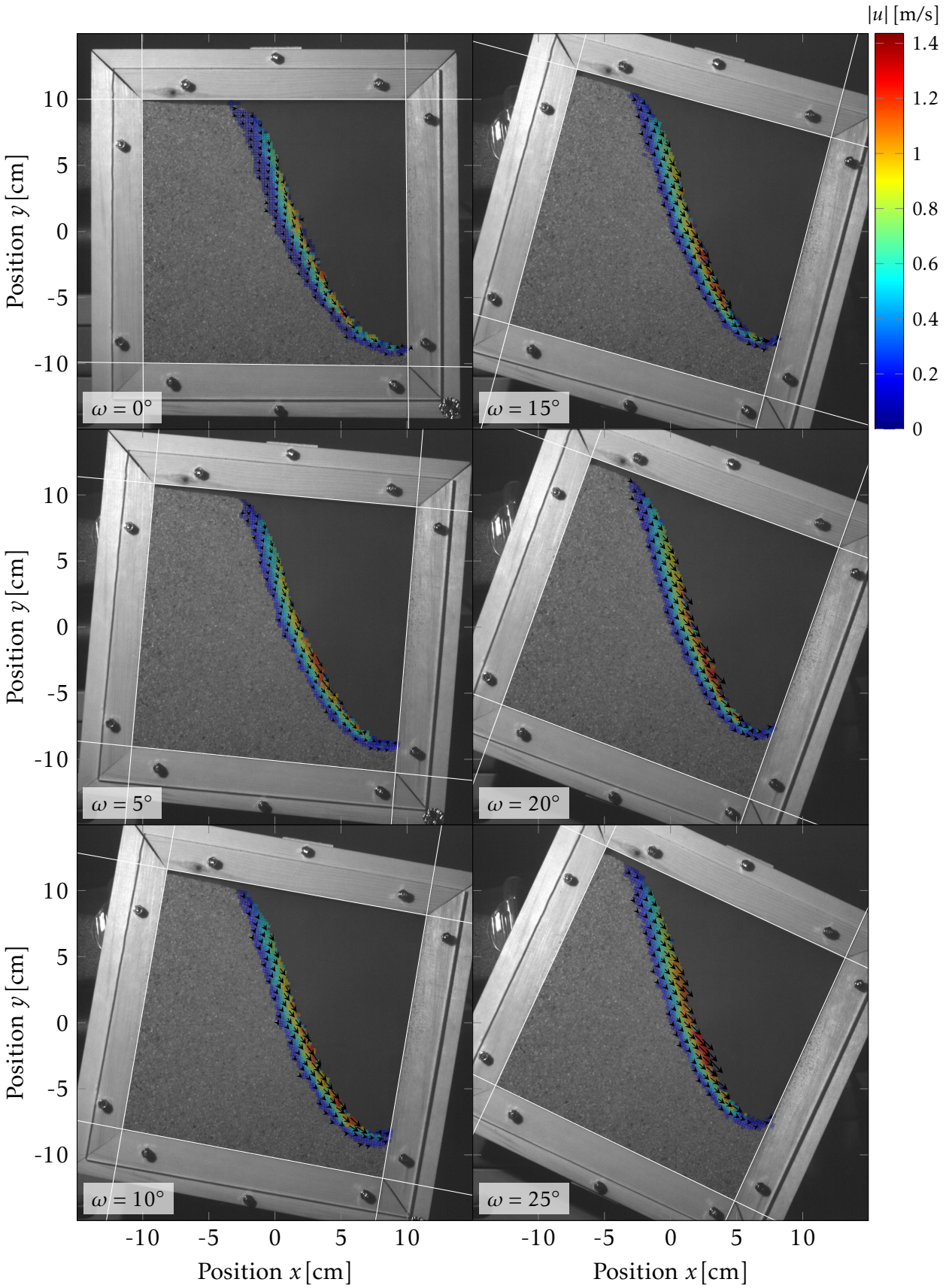

Figure 6.1 – Rotating rectangular Box: PIV measurements. Overlay of velocity fields measured by PIV with pictures of the granular flow of sand particles in a clockwise rotating box during a 90° rotation. Displayed are representative pictures for rotation angle steps of 5°. Magnitudes of mean velocities in 5 mm x 5 mm patches are represented by a heat map (reaching from blue for the minimal velocity to red for the maximal velocity). Direction of the velocities are depicted by arrows, the length of the arrows corresponds to the magnitude. For a better overview, only arrows for each third patch in x'-direction and every other patch in y'-direction are shown. Figure continued on next page.

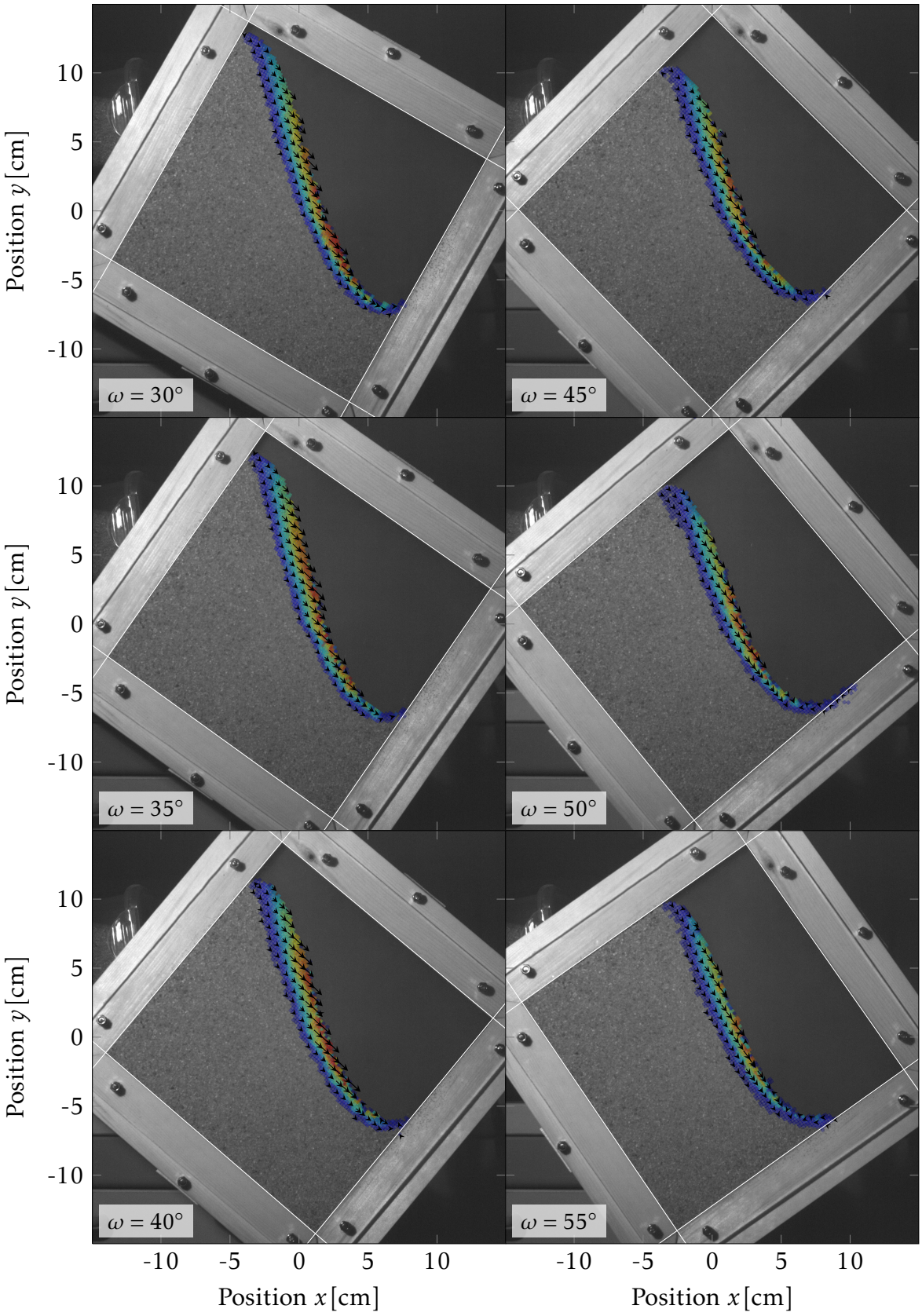

Figure 6.1 – Rotating rectangular Box: PIV measurements.(cont.)

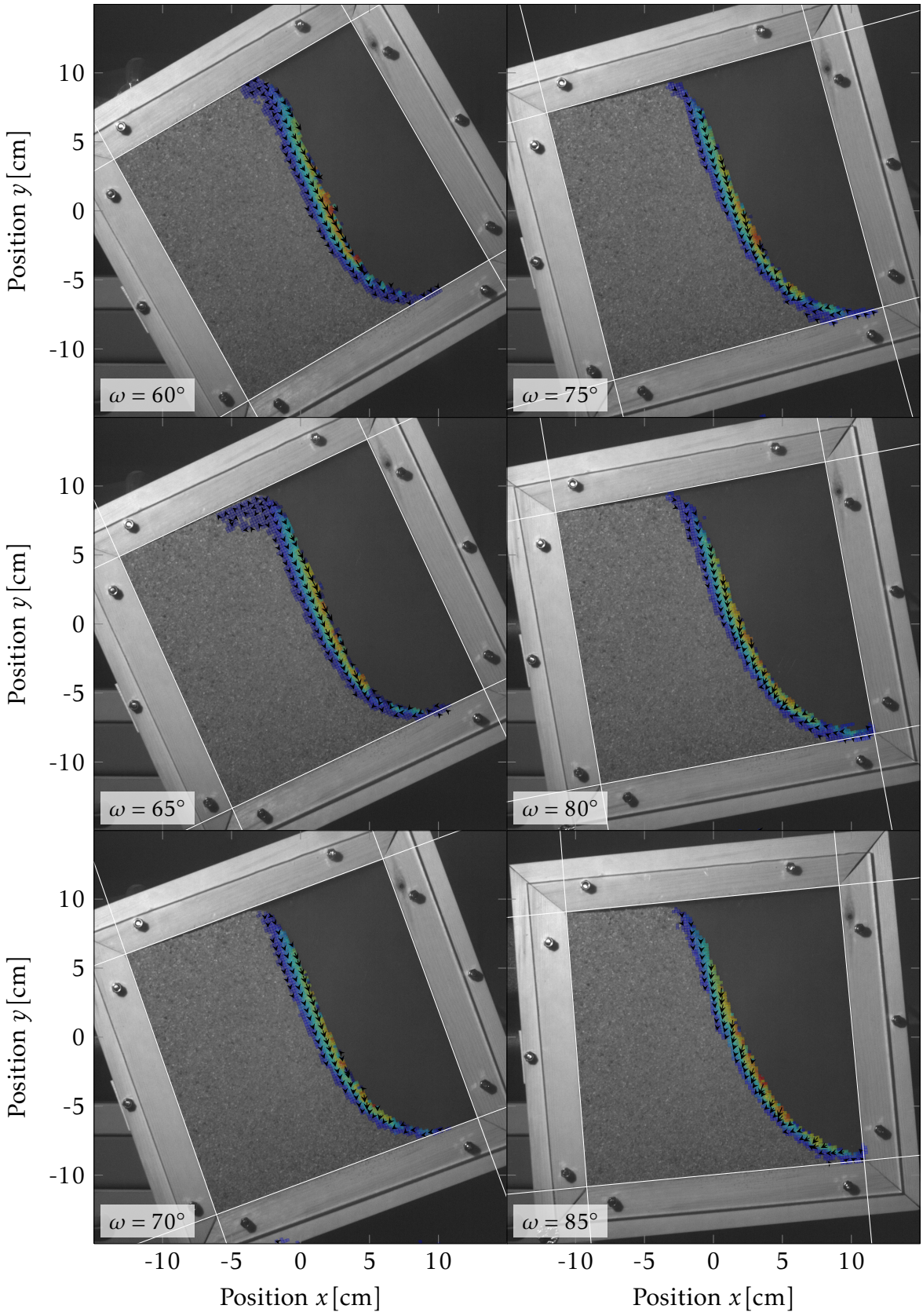

Figure 6.1 – Rotating rectangular Box: PIV measurements.(cont.)

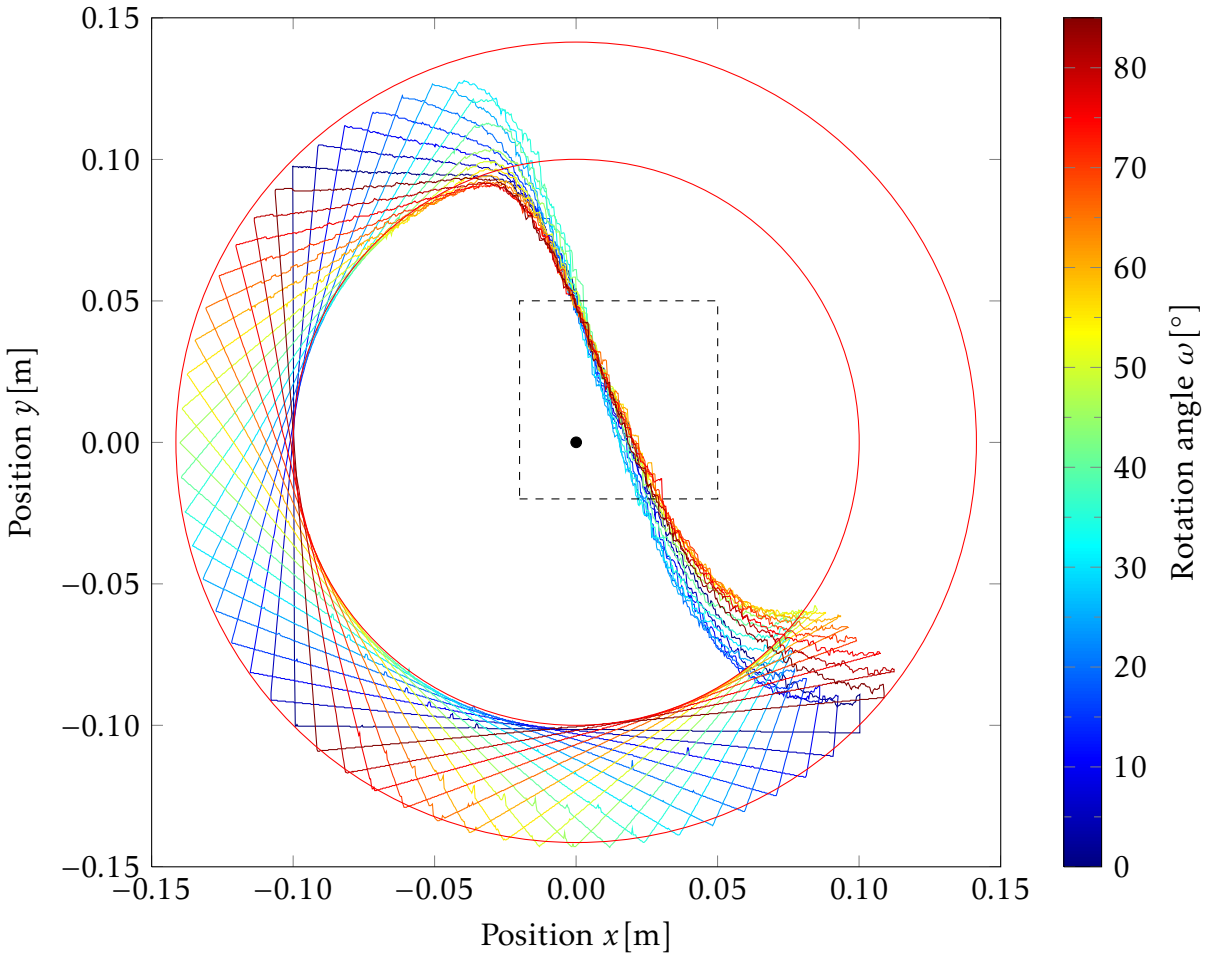

Figure 6.2 – Rotating rectangular box: Temporal evolution of free surface shape. Geometry of total granular material in the rotating box depicted for rotation angle steps of 5°. Outlines show the free surface and the surfaces facing the container walls. The black dot indicates the center of the container, the dashed square outlines the area considered for calculation in the following figures. The two red circles represent the minimal (smaller circle, diameter corresponds to edge length of the box) and maximal (larger circle, diameter corresponds to diagonal of the box) distance to the center, respectively.

the box allows observations of quasi-steady-state flows with small periodic disturbance by the boundaries. The resulting movement of the material reveals if elastic properties of the material cause a delay of response to rotation and if viscous or plastic behavior dominates the flow. Fig. 6.1 depicts the velocity evolution in the box during a 90° rotation in the steady-state flow recorded with the PIV method. It demonstrates that only a part of the material is fluidized and builds a relatively thin flow layer while the rest remains solid. From this observation it can be ruled out that the material behaves like a pure viscous fluid, which would result in a fluidization of the complete material. To obtain comparable parameters for further characterization of the evolution of the fluidized fraction, the free surface geometry is considered (Fig. 6.2) and analysed in detail in an area close to the center of the box (the dashed box indicated in Fig. 6.2). As described

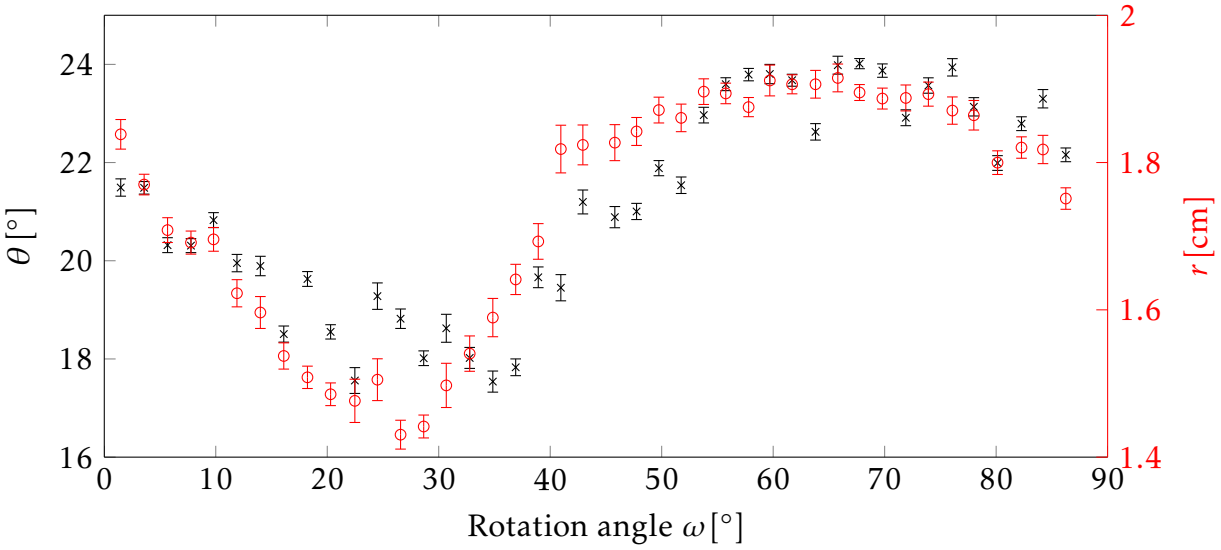

Figure 6.3 – Rotating rectangular box: Evolution of free surface relative to box center. Evolution of the free surface relative to the box center expressed by the parameter describing a fitted line to the free surface in the square indicated in Fig. 6.2 during rotation steps of 2°. Lines were fitted by linear regression using the equation $r = \cos(\theta) \cdot x + \sin(\theta) \cdot y$, where r denotes the minimum distance between the box center and the line and θ denotes the angle between the horizontal and a vector pointing from the box center to closest point on the line. Error bars represent errors of the linear regression.

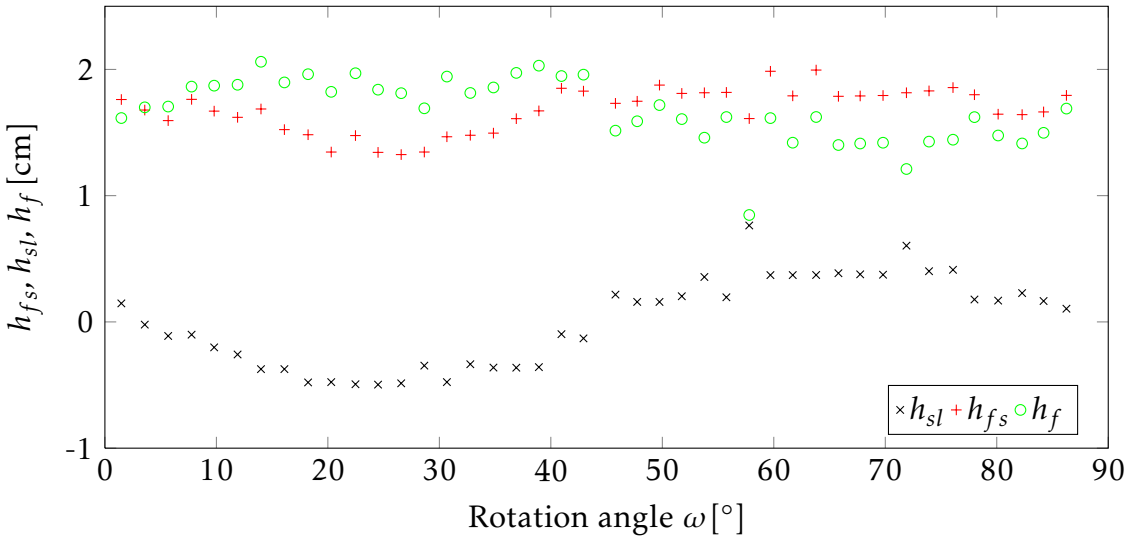

Figure 6.4 – Rotating rectangular box: Temporal evolution of flow thickness. Temporal evolution of the fluid-solid interface (h_{sl}) and free surface (h_{fs}) position relative to the center and the resulting height of the fluidized layer (h_f) during rotation steps of 2°. All values are determined on a line through the box center and the closest point on the regression line of the respective point described in Fig. 6.3.

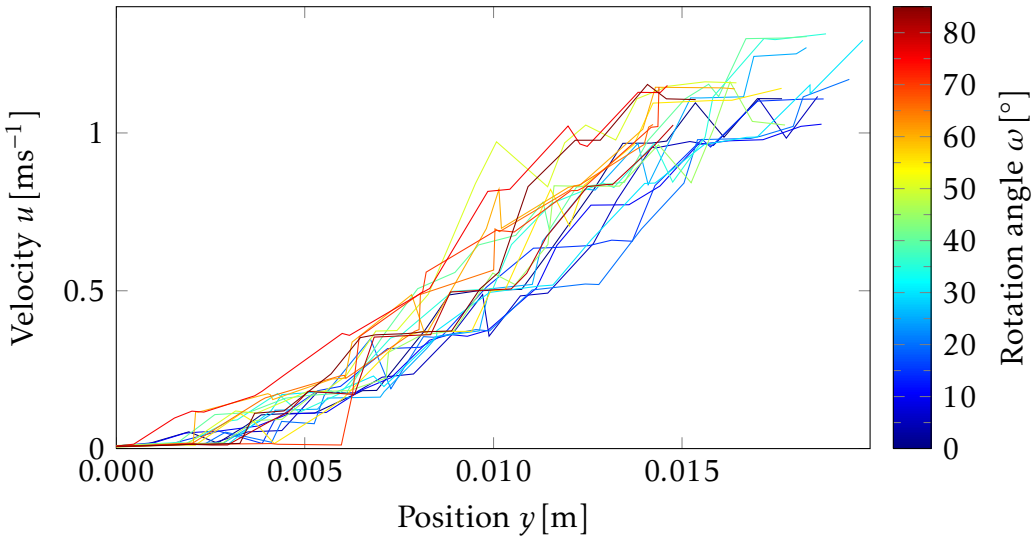

Figure 6.5 – Rotating rectangular box: Temporal evolution of velocity profile. Velocity profile inside the fluidized fraction along the line described in Fig. 6.4 (line trough the center perpendicular to the regression of the free surface at the closest distance to the center). Velocity values were extracted from the PIV measurements.

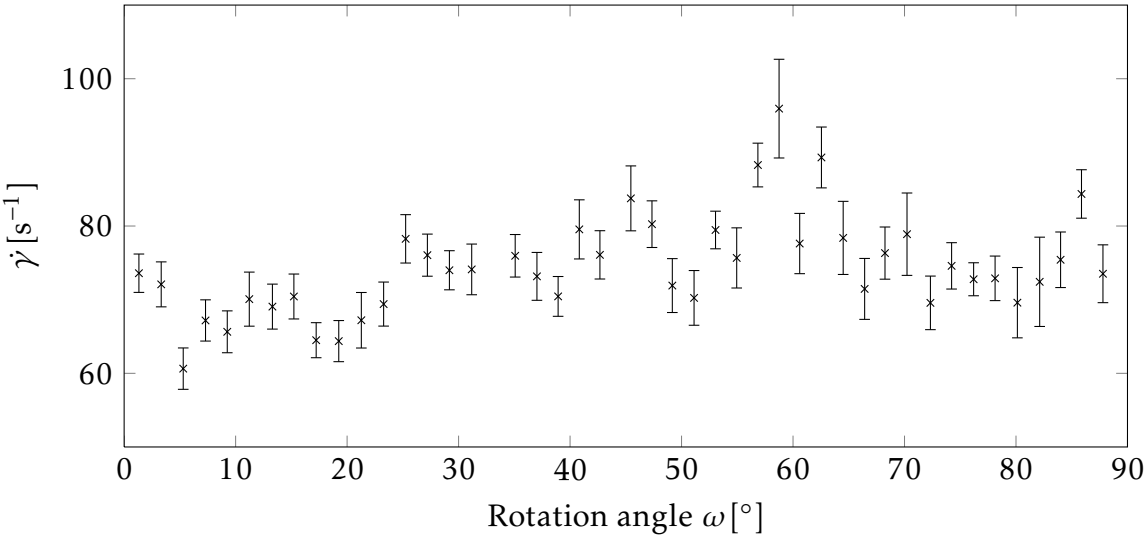

Figure 6.6 – Rotating rectangular box: Temporal evolution of strain rate. Strain rate in the fluidized fraction during rotation steps of 2°. Strain rate was determined as inclination of a linear regression line fitted to the velocity profiles of Fig.6.5. Error bars represent errors of the regression.

in section 5.4.3, the free surface in this area can be described by a fitted line with the parameters r (minimum distance between the box center and the line) and θ (angle between the horizontal and a vector pointing from the box center to closest point on the line). Both parameters display periodic alterations during the quarter rotation considered here (Fig. 6.3), with the highest alterations occurring around 0° , 45° and 90°. The system returns to its initial configuration after a 90° rotation. Thus, the behavior of the material directly corresponds to the symmetry of the box, which also reaches the same configuration after a 90° rotation. This indicates a direct response of the material to the disturbance by the boundaries without a temporal delay, which can be considered as a hint for a non-elastic behavior. A further parameter to classify the evolution of the fluidized fraction is the thickness of the fluidized fraction at the point of lowest distance to the center. The solid-fluid interface position relative to the box center (h_{sl}) slightly alters with the same periodicity as the free surface position (h_{fs}), resulting in an approximately constant flow thickness (h_f) over 45° of the rotation (Fig. 6.4). After 45° rotation, the flow thickness suddenly decreases and afterwards remains approximately constant at a lower level for the remaining 45° of the rotation. This change in flow thickness coincides with the sudden change in the inclination angle of the free surface (Fig. 6.3), further supporting the idea of an instant response of the material and a non-elastic behavior. The velocities measured in Fig. 6.1 allow to draw a velocity profile in the fluidized fraction along a line from the box center to the closest point on the free surface for each rotation step. These velocity profiles are approximately linear (taking into account that a coarse grid was employed) for all considered rotation steps (Fig. 6.5) and therefore, allow to calculate a strain rate by a linear regression. The strain rate remains approximately constant within the error range (Fig. 6.6). This observation confirms the initial assumption of a quasi-steady-state flow during the experiment and thus justifies the consideration of only one 90° rotation. Taken together, the results indicate that the material considered in this work cannot be treated as a pure viscous fluid. Furthermore, no indications for elastic behavior were observed in the performed experiments. Thus, further considerations focused on the description of the non-cohesive granular material employed here by a plastic law. To decide whether some viscous components should be included in the rheological model, theoretical considerations and pilot simulations were performed.

6.1.2 Theoretical considerations and first pilot simulations for the choice of a rheological model

Several approaches have been discussed in the literature to implement a plastic law for numerical simulations in fluid dynamics (section 1.3.4.2). Among those, a simple model introducing plastic behavior for a viscous fluid is the Bingham model assuming a constant

shear stress τ_0 to be added to the viscous parts of the shear stress. A Bingham behavior would imply that the material can resist a certain amount of stress (lower than τ_0) before it reacts and starts to flow. This would cause the motion of the material to start at the walls of the container, where highest stress is applied. Pilot simulations assuming a Bingham model displayed exactly this behavior: a rigid block of material is formed in the middle of the container and rolls over a thick flowing layer at the walls (data not shown). The failure of the Bingham model can be explained by the negligence of a pressure component since the pressure gradient might be responsible for the solid state of the lower layers observed in the experiment. Thus, a model considering the pressure inside the material would be suited best to simulate the material used in this work.

A model taking pressure components into account to simulate plastic fluid dynamics has been proposed by Jop et al. (2006) (section 3.3). An implementation of this model for the problems considered here would require the determination of five material parameter: the density of the material, the particle diameter, the Savage number, the internal friction angle and the floating angle. Several of these parameters are hard to determine for a heterogeneous mixture like sand with varying particle diameter. As a simplification of the model of Jop et al. (2006), a simple Coulomb law can be employed. For this purpose, the Coulomb friction coefficient is considered constant. This results in a model depending only on the internal friction angle (ϕ) as a material parameter and the density of the material:

To implement a simple Coulomb model for numerical simulations, the OpenFOAM® software described in chapter 4 is employed in this study. For this purpose, classes were added to OpenFOAM® allowing the calculation of the Coulomb friction related parameters viscosity and bottom friction angle (parameters for simulations of each experiment and excerpts of major functions employed can be found in appendix A and B). For brevity, the non-depth-averaged simulations with a simple Coulomb rheology performed with OpenFOAM® will be called OpenFOAM® simulations from here on.

6.1.3 Pilot simulations using a simple Coulomb law

As mentioned above, the only input parameter for the OpenFOAM® simulations in this study are the internal friction angle and the density of the material. In normal conditions, the internal friction angle closely corresponds to the angle of repose and can thus be easily determined for a given material (Lambe and Whitman, 1969; Kutzbach and Scherer, 1977; Iversen and Rasmussen, 1994; Hutter and Koch, 1991; Pudasaini et al., 2007). Simulations of the rotating box experiment with this angle resulted in too low inclination of the free surface and an intermittent flow was observed in contrast to the observed steady-state flow (data not shown). An explanation for this observation might be that in the rotating box experiment, the side walls provide a strong pressure and thus cause the an-

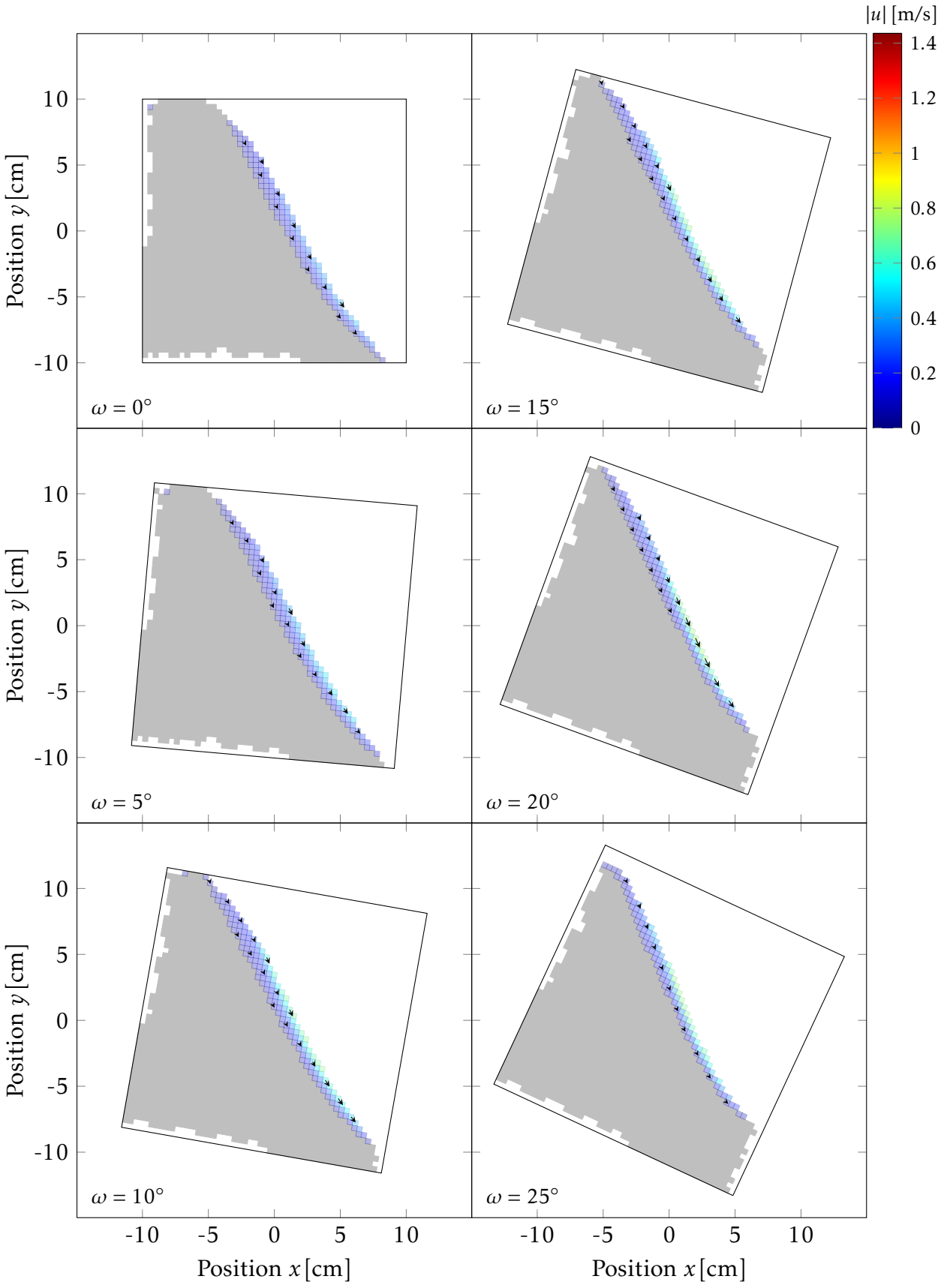

Figure 6.7 – OpenFOAM® simulations of rotating rectangular box: Overview on velocity fields. Overlay of simulated velocity fields with simulated shape during a 90° clockwise turn of the rotating box. Displayed are representative pictures for rotation angle steps of 5°. Velocities in single patches corresponding to the numerical grid are represented by a heat map (reaching from blue for the minimal velocity to red for the maximal velocity). Direction of the velocities are depicted by arrows, the length of the arrows corresponds to the magnitude. For a better overview, only arrows for each third patch in x'-direction and every other patch in y'-direction are shown. Figure continued on next page.

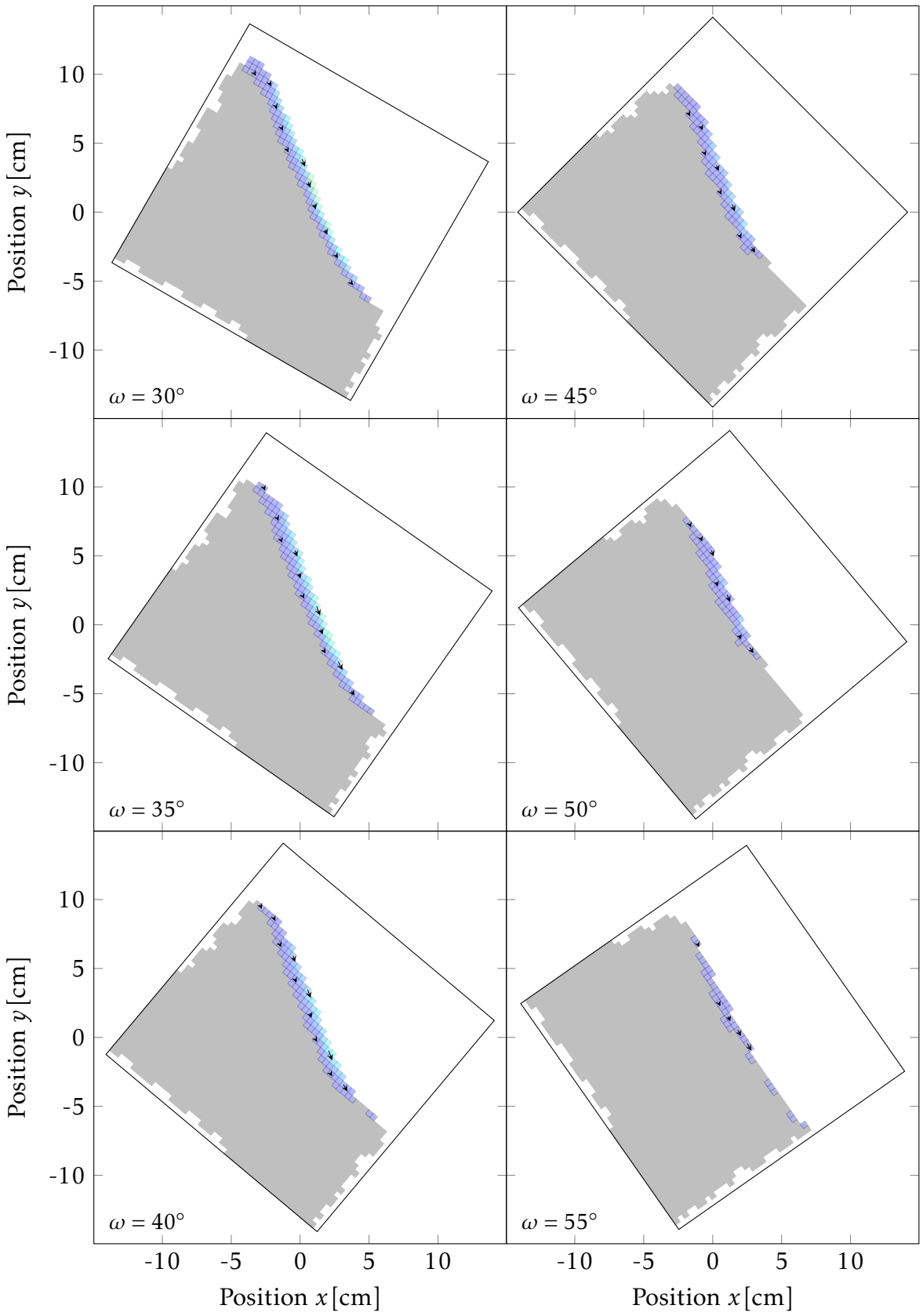

Figure 6.7 – OpenFOAM® simulations on rotating rectangular box: Overview on velocity fields.(cont.)

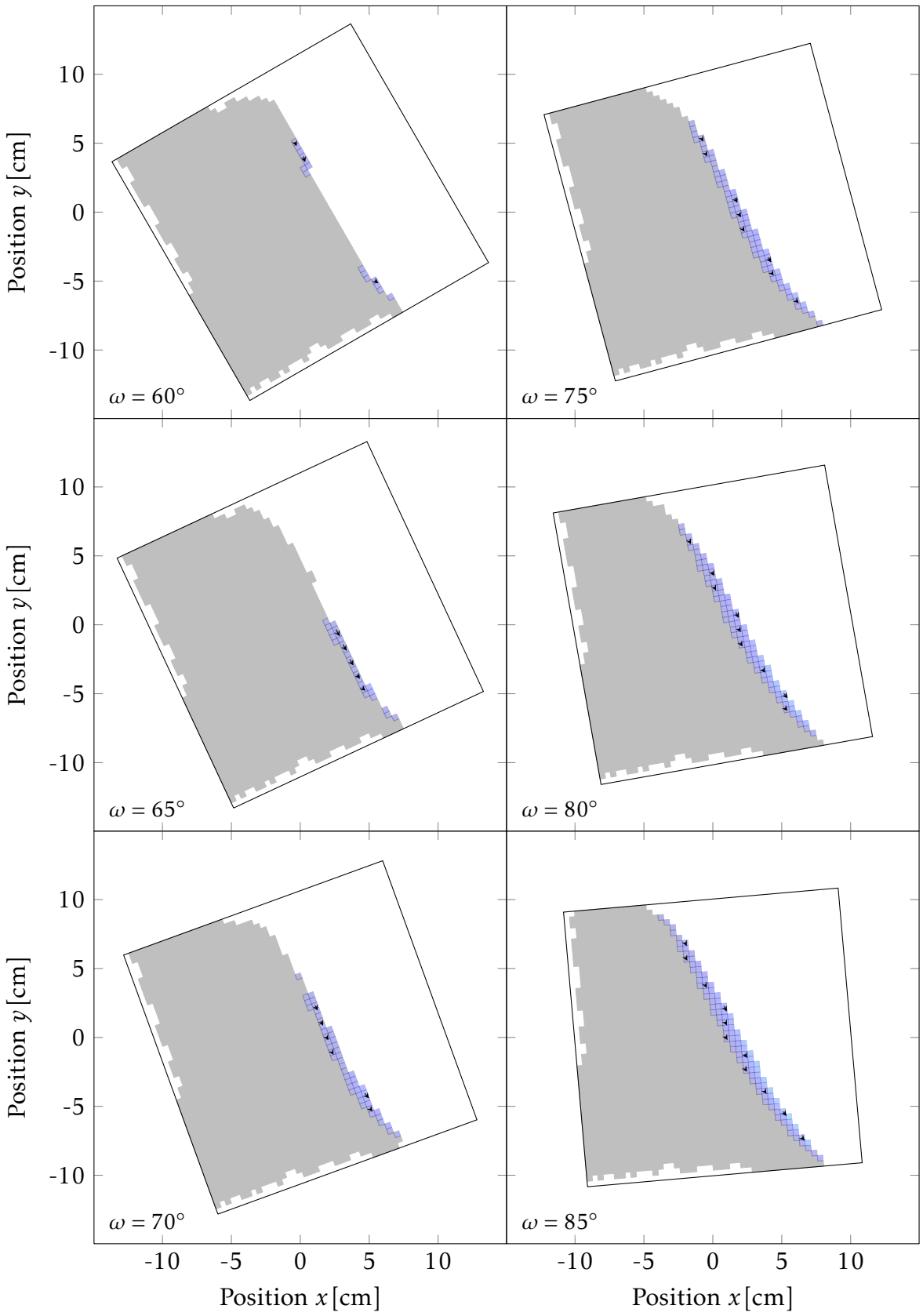

Figure 6.7 – OpenFOAM® simulations on rotating rectangular box: Overview on velocity fields.(cont.)

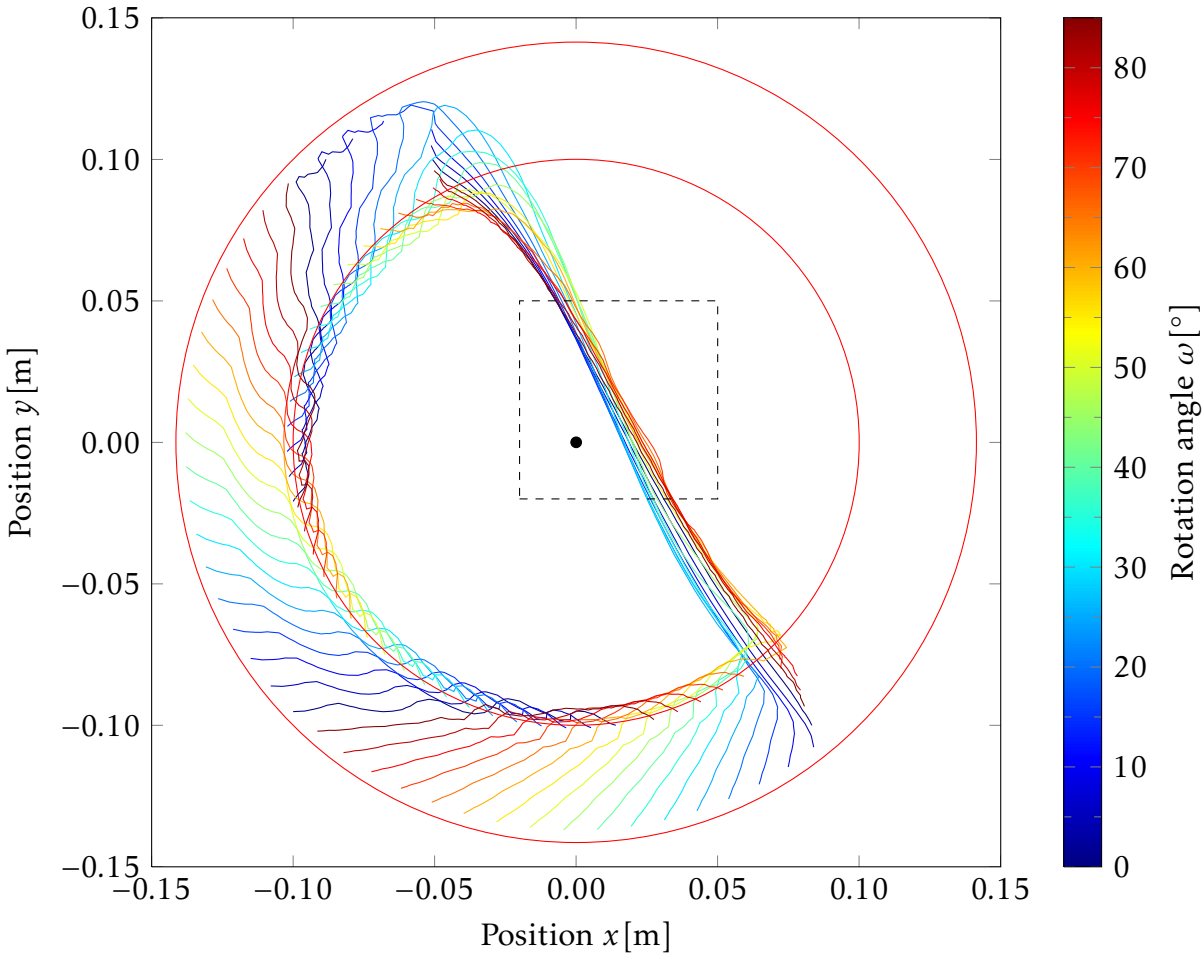

Figure 6.8 – OpenFOAM® simulations of rotating rectangular box: Temporal evolution of free surface shape. Simulated geometry of total granular material in the rotating box depicted for rotation angle steps of 5°. Outlines show the free surface. The black dot indicates the center of the container, the dashed square outlines the area considered for calculation in the following figures. The two red circles represent the minimal (smaller circle, diameter corresponds to edge length of the box) and maximal (larger circle, diameter corresponds to diagonal of the box) distance to the center, respectively.

gle of repose to raise above the normal value for the employed material (Jop et al., 2005; Hutter et al., 1995; Savage, 1979). Thus, to estimate the internal friction angle for sand in the rotating box set-up, the inclination of the free surface observed in the experiment was taken into account. Therefore, an internal friction angle of $\phi = 55°$ was used in the simulations.

As described in chapter 4, the non-depth-averaged fluid dynamics simulations by OpenFOAM® employ the VOF method in which a single mass and momentum equation is solved for both the air and the material. This method yields the following parameters for each cell during each time step of the simulation: the velocity field, the pressure, the filling parameter α_1 and the effective viscosity. Plotting of the velocity field and the filling parameter for different rotation angles of the box allows comparison to the PIV images

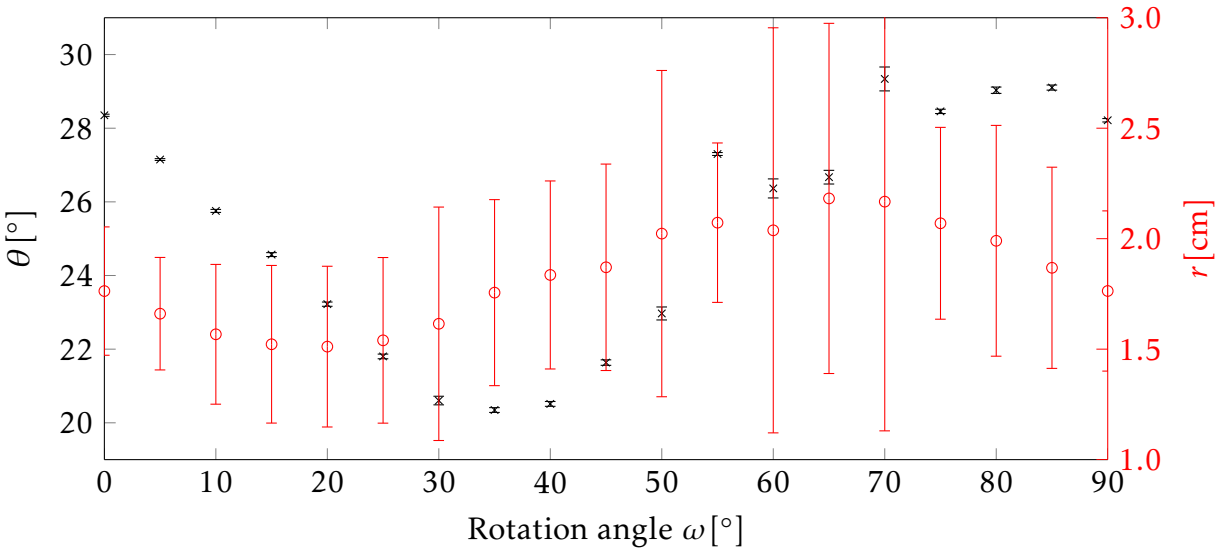

Figure 6.9 – OpenFOAM® simulations of rotating rectangular box: Evolution of free surface relative to box center. Simulated evolution of the free surface relative to the box center expressed by the parameter describing a fitted line to the measured free surfaces in the square indicated in Fig. 6.8 during rotation steps of 2°. Lines were fitted by linear regression using the equation $r = \cos(\theta) \cdot x + \sin(\theta) \cdot y$, where r denotes the minimum distance between the box center and the line and θ denotes the angle between the horizontal and a vector pointing from the box center to closest point on the line. Error bars represent errors of the linear regression.

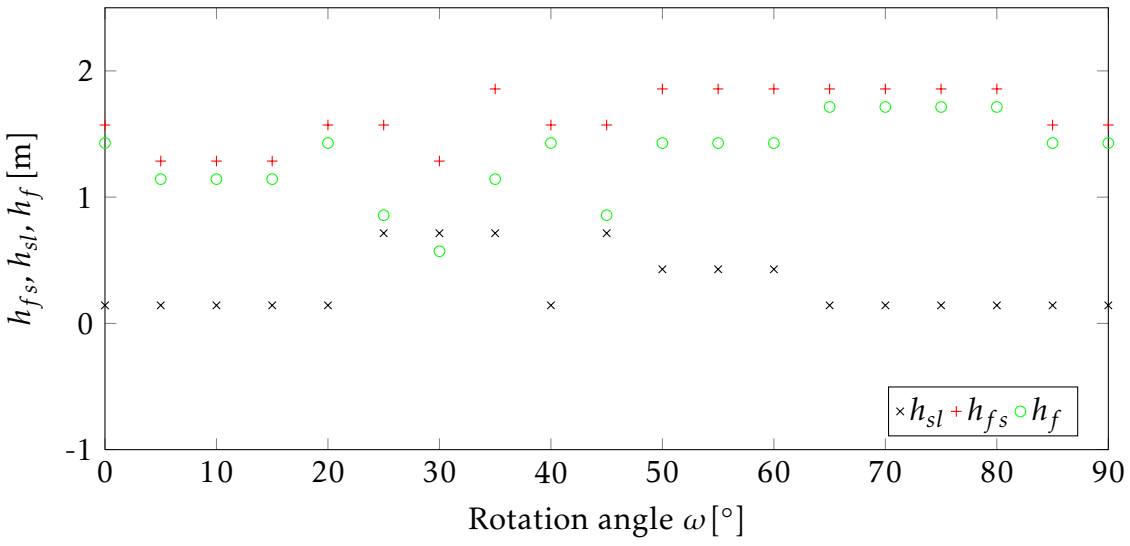

Figure 6.10 – OpenFOAM® simulations of rotating rectangular box: Temporal evolution of flow thickness. Temporal evolution of the fluid-solid interface (h_{sl}) and free surface (h_{fs}) distance to the center and the resulting height of the fluidized layer (h_f) during rotation steps of 2°. All values are determined on a straight line perpendicular to the regression line of the respective point described in Fig. 6.9.

(Fig. 6.7). These images reveal that the OpenFOAM® simulations are capable of qualitatively predicting the flow geometry in the rotating box: a thin flowing layer is formed, while the majority of the material underneath remains in a solid state. Quantitatively, the observed velocities are underestimated by the simulation, which might be caused by the size of the grid cells, which were chosen to be relatively large for this pilot simulation. The qualitative agreement of the simulated flow geometry with the experiment is also reflected in the free surface shape (Fig. 6.8). Especially in the central area, the simulated free surface display a linear shape as the experimentally observed free surfaces. For both simulated and experimentally observed free surfaces, the slope in the central area becomes gradually steeper during the first 40 seconds of the rotation and then flattens again. Some deviations from the observed free surface shape occur at the edges of the box, since here some cells are considered to be filled with air. This is caused by the fact that the two components air and granular material are considered immiscible and thus entrained air cannot exhaust. Therefore, only the free surface is considered here. The periodic evolution of the distance to the center and the angle θ are also qualitatively well captured by the simulation (Fig. 6.9). Deviations in the absolute values of the parameters might be explained by a still underestimated value of ϕ due to strong effects of the side walls. The large error bars can be explained by the low number of data points in the simulation (order of centimeters, caused by the large cell size) compared to the fine resolution of the experiment (order of millimeters, pixel size of the camera). As a consequence of this inaccuracy and due to the low number of observed points, a strong dispersion of the values of h_{sl}, h_{fs} and h_f and deviations compared to the experiment are observed (Fig. 6.10). Nevertheless, the predicted values are in the same order of magnitude as the experimental value. Due to the coarse grid, no velocity profiles and the resulting strain rates were calculated for this pilot experiment, which was only employed to validate the choice of the rheological model.

As a conclusion, the simple Coulomb model suggested here can be used to describe the fluid behavior of a granular material in the time and size scales considered in this study. To fine tune and validate this model to describe experimental findings in different situations without a strong influence of the side walls, a larger experimental set-up with a thicker particle layer of 10 cm in an inclined channel was employed using PVC and sand particles.

6.2 Initialization of a granular flow - granular collapse

To investigate the course of an undisturbed granular flow in non-steady-state conditions, dam break experiments inside the 10 cm wide inclined channel (see section 5.2.2) are considered. Dam break experiments are widely employed experiments mimicking the

situation of a sudden break of a dam or other retention structure, which was retaining material raised above its angle of repose. Experiments found in literature differ in the size of the performed experiment, the material employed, the inclination of the channel, the roughness of the sliding surface (channel bottom), the number of dimensions considered (2D vs. 3D) and in the precision of the recording system (Artoni et al., 2013; Thompson and Huppert, 2007; Rondon et al., 2011; Mériaux, 2006; de Vet et al., 2010; Chen et al., 2011; Roche et al., 2011; Maeno et al., 2013; Trepanier and Franklin, 2010; Lube et al., 2004; Lajeunesse et al., 2004; Mériaux and Triantafillou, 2008; Ancey and Cochard, 2009; Ancey, 2012). Dam break scenarios are also often used for the validation of new models and simulations on granular flows (Lagrée et al., 2011; Staron and Hinch, 2007; Larrieu et al., 2006; Lacaze and Kerswell, 2009; Kerswell, 2005; Josserand et al., 2009; Hogg and Pritchard, 2004; Ertaş and Halsey, 2002; Doyle et al., 2007). The experiments performed in this work should facilitate a deeper insight into velocity profiles of the flow and the validation of non-depth-averaged simulations of non-cohesive granular flows. Thus, non-cohesive materials with particle sizes optimal for detailed PIV measurements in combination with the employed camera were chosen. A two dimensional set-up was employed to allow recording of velocity profile through the translucent PMMA walls of the channel. The inclination angle was chosen to be variable to evaluate its influence on the flow in experiments and simulations. Although such experiments have been performed and described in the literature before (Zenit, 2005; Siavoshi and Kudrolli, 2005; Lube et al., 2005, 2007, 2011; Lajeunesse et al., 2005; Lacaze et al., 2008; Hogg, 2007; Balmforth and Kerswell, 2005), there is only a limited amount of the original data available and not all parameters of interest for this study have been recorded (e.g. the influence of the channel inclination, especially for high inclination angles). For this reason and to obtain comparable data for all situations considered here (initialization of a flow, undisturbed granular flow, encountering of an obstacle and granular shock), the dam break experiments described in the following sections were performed and recorded with the detailed PIV measurements system described in section 5.4.

6.2.1 Experimental findings

The collapse of a granular column is investigated. Two experiments were performed, first for smaller inclination angles the rectangular container filled with grains is opened on the downslope face. Second, for a high inclination ($\zeta > \phi$) a small triangular initial deposit was filled inside the channel and the collapse was observed. Because of the larger observed area compared to the previous experiment, mostly the larger PVC particles were used for the following experiments to assure the PIV measurements are working precisely. To investigate the influence of the material, the dam break with triangular initial deposit was also performed with sand.

6.2.1.1 Rectangular container

The collapse of the rectangular column was performed for inclination angles of 0°, 10°, 20° and 30° with PVC particles.

General considerations and influence of the inclination angle

The PIV measurements (Fig. 6.11 and 6.12) reveal a clear difference between 0°, 10° and 20° compared to 30°: for smaller slopes, only a fraction of the granular material is mobilized and forms a thin surface flow. In contrast to this, for 30°, all particles are mobilized and the complete material slides down the channel in a thin layer. The measured velocities indicated a gradient of the velocity distribution in the flow depth dimension (y-direction) with faster flowing particles at the surface of the flow. Considering the course of the mobilized and total volume over time, three phases can be distinguished (Fig. 6.13): an initial short phase of rapid mobilization in which the mobilized fraction increases (I), followed by a longer phase of motion of a constant volume fraction (II) and a deposition phase during which the fluidized fraction slowly decreases again (III). This evolution of the fluid volume is observed for all lower slopes but over different time scales. For 30°, the initial fast mobilization of a fraction of the granular material is followed by a steady increase of the flowing fraction until the complete material is fluidized. To further classify the flow for comparison with simulated flows, the initial area of motion, the shape of the final deposit and the maximal flow height are compared for the different slopes. Due to the complete fluidization of the material, the 30° measurement is only included for the maximum flow height. The initial area of motion for the lower slopes increases with the slope and is shaped like a triangle including the upper corner facing the gate (Fig. 6.14). This results in a final deposit shaped as a halved trapezoid, with an decreasing acute angle for increasing slopes (Fig. 6.15). The evolution of the maximal flow height is characterized by a sudden increase during the mobilization phase, followed by an exponential decay with decreasing decay constants for increasing slopes (Fig. 6.16).

Introduction of a curvilinear coordinate system using the example of 0° inclination

Determining flow heights as in Fig. 6.16 requires the localization of the free surface and the solid-fluid interface in the recorded pictures. As a showcase and for illustration of the analysis methods employed to describe this interface, the shape evolution during the dam break with no inclination (Fig. 6.17) is analyzed in detail. In this work, flow height is defined as the height of the fluidized granular fraction perpendicular to the solid-fluid interface. A curvilinear coordinate system is used to describe this interface (Fig. 6.18) and analysis of the height profile (Fig. 6.19) is performed in this coordinate system.

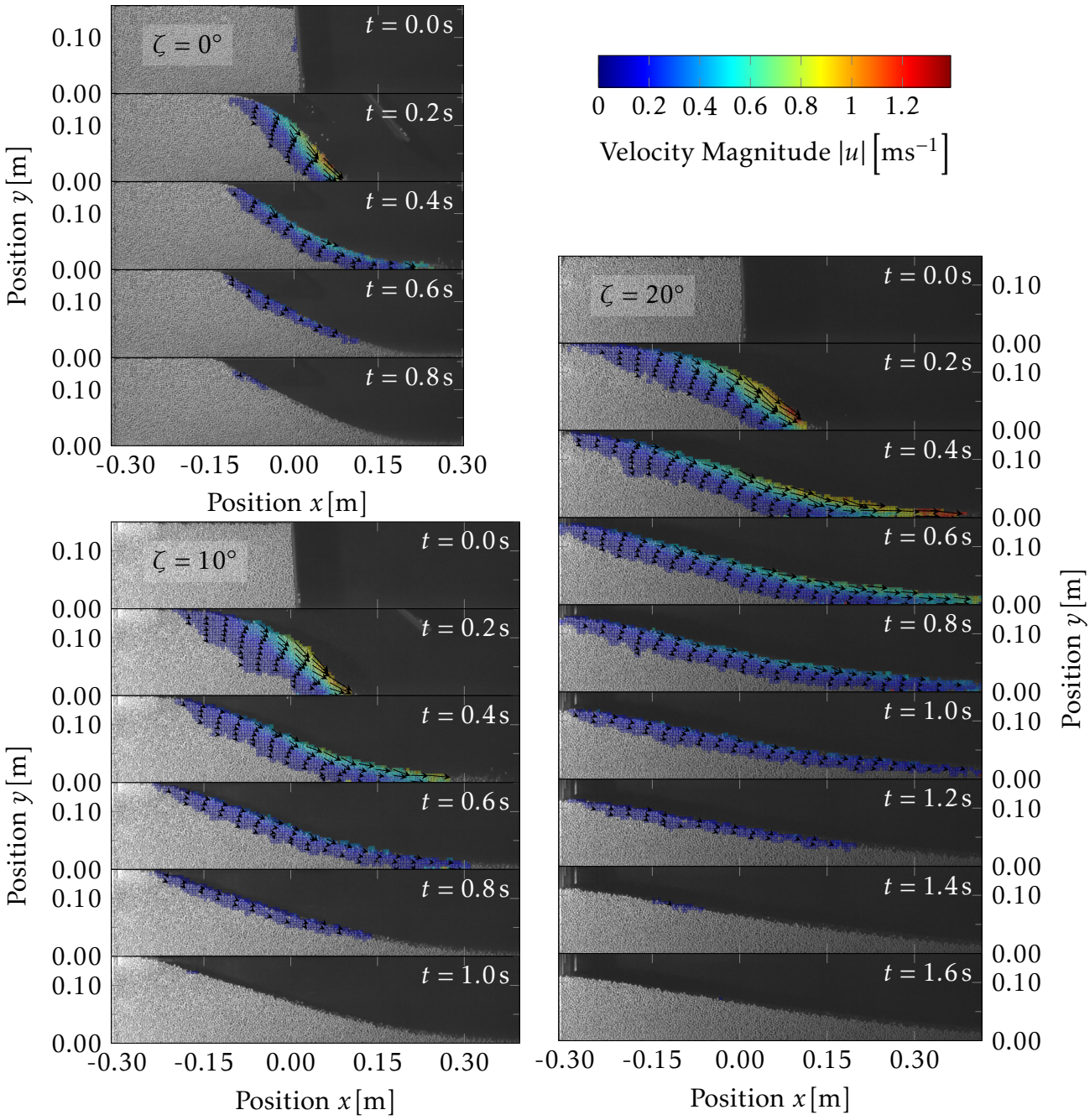

Figure 6.11 – Draining of a rectangular container: PIV measurements for small inclination angles. Overlay of velocity fields measured by PIV with pictures of the granular flow of PVC particles during the draining of a rectangular container at 0°, 10° and 20° inclination angle. Magnitudes of mean velocities in 5 mm x 5 mm patches are represented by a heat map (reaching from blue for the minimal velocity to red for the maximal velocity). Direction of the velocities are depicted by arrows, the length of the arrows corresponds to the magnitude. For a better overview, only arrows for each sixth patch in x-direction and every other patch in y-direction are shown.

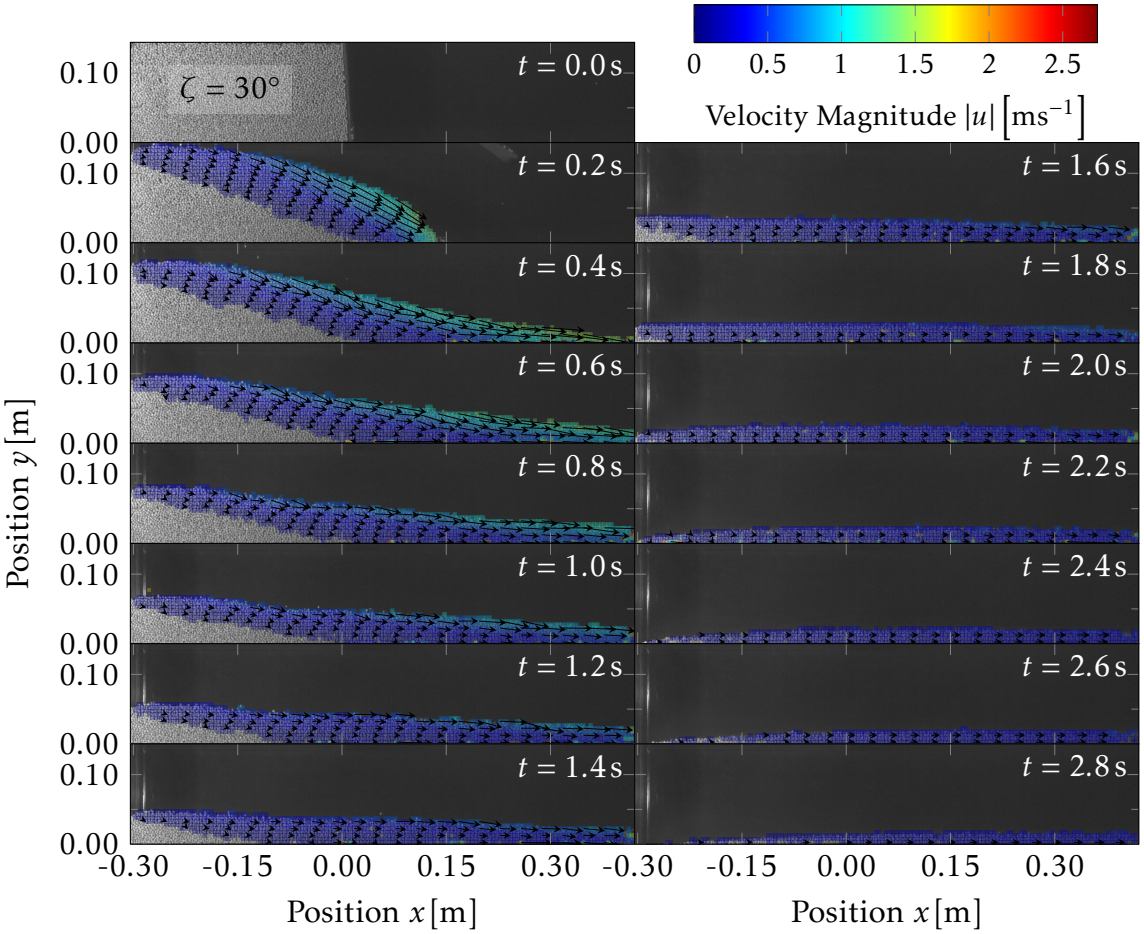

Figure 6.12 – Draining of a rectangular container: PIV measurements for 30° inclination angle. Overlay of velocity fields measured by PIV with pictures of the granular flow of PVC particles during the draining of a rectangular container at 30° inclination angle. Magnitudes of mean velocities in 5 mm x 5 mm patches are represented by a heat map (reaching from blue for the minimal velocity to red for the maximal velocity). Direction of the velocities are depicted by arrows, the length of the arrows corresponds to the magnitude. For a better overview, only arrows for each sixth patch in x-direction and every other patch in y-direction are shown.

It becomes clear that after the mobilization of the initial triangular fraction the fluidized fraction spreads into the channel and is simultaneously flattened (Fig. 6.19). Deposition starts at the most distant point from the initial abruption edge (the lowest point on the solid-fluid interface) and continues in opposite direction of the flow (Fig. 6.18).

In accordance with these observations, the front of the motion first spreads into the channel during the flow phase and is than retracted to the starting point and even beyond it during the deposition (Fig. 6.20). The rear position of the motion area is abruptly shifted backwards during the initiation of the triangular mobile zone and then remains constant during the whole flow. Therefore, the time when the rear motion line reaches it minimum value can be utilized for a precise determination of the transition point form the initialization to the sliding phase (Fig. 6.20).

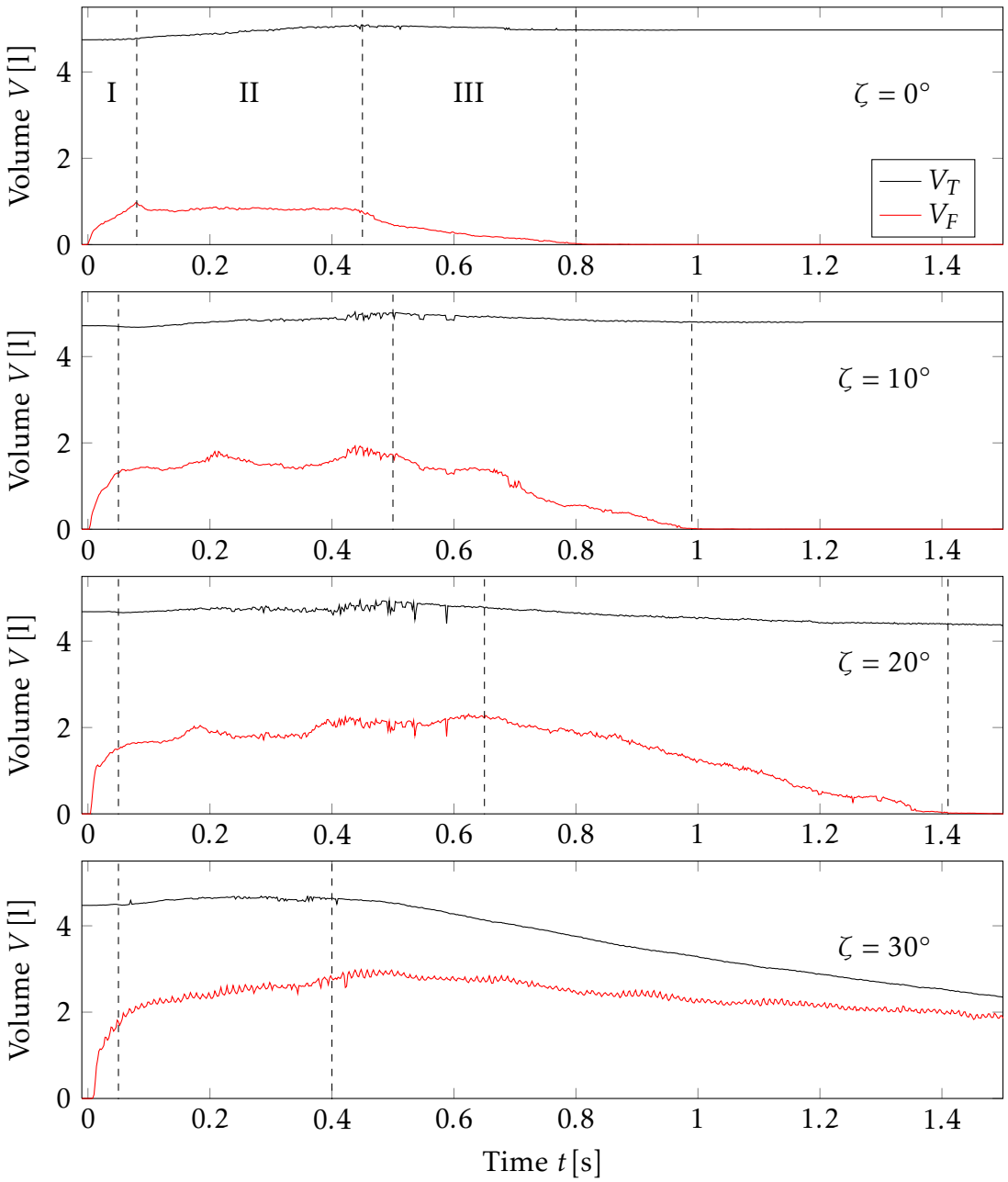

Figure 6.13 – Draining of a rectangular container: Temporal evolution of flowing volume. Temporal evolution of the flowing volume fraction (V_F) and the total volume (V_T) within the observed area during the draining of a rectangular container filled with PVC particles at 0°, 10°, 20° and 30° inclination angles. Vertical dashed lines mark (from left to right) the initial fluidization phase, the constant outflow phase and the phase in which the mass comes to rest again (0°, 10° and 20°).

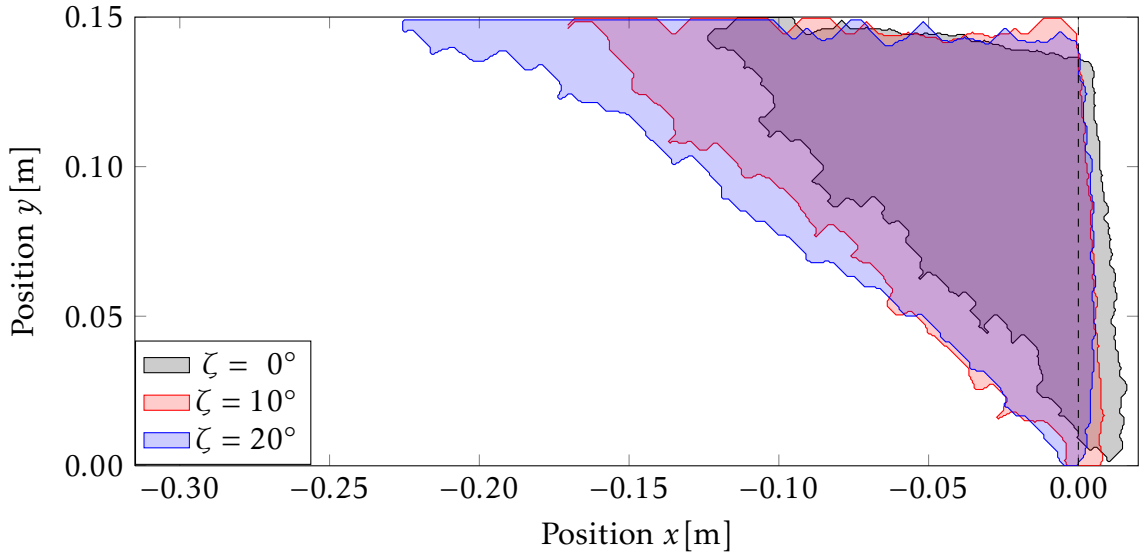

Figure 6.14 – Draining of a rectangular container: Initial area of motion. Outline of the initial mobilized fraction of PVC particles for 0°, 10° and 20° inclination angle. The vertical dashed line marks the position of the gate.

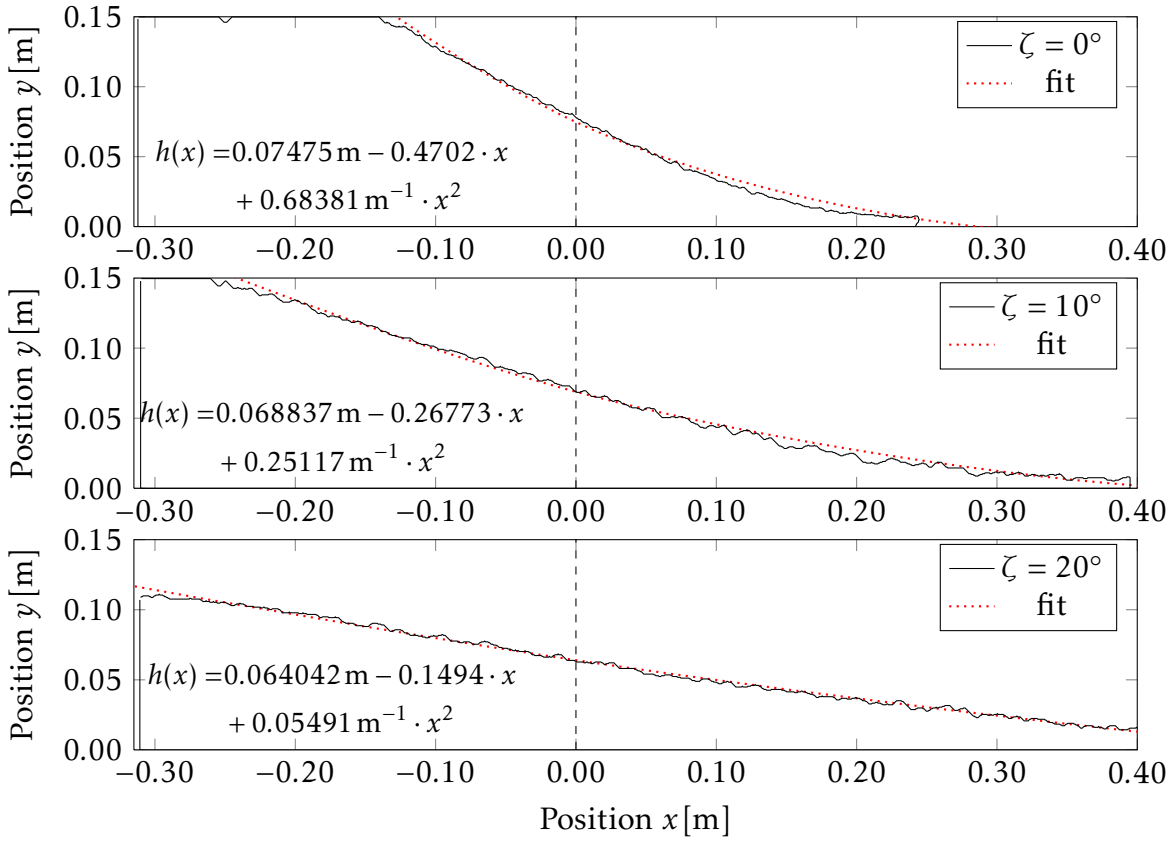

Figure 6.15 – Draining of a rectangular container: Final deposit. Shape of the final deposit in the starting zone of PVC flow for 0°, 10° and 20° inclination angle (black lines). Red doted lines depict a second order polynomial fit to the deposit surface, the respective equations are displayed for each graph. The vertical dashed black lines mark the position of the gate.

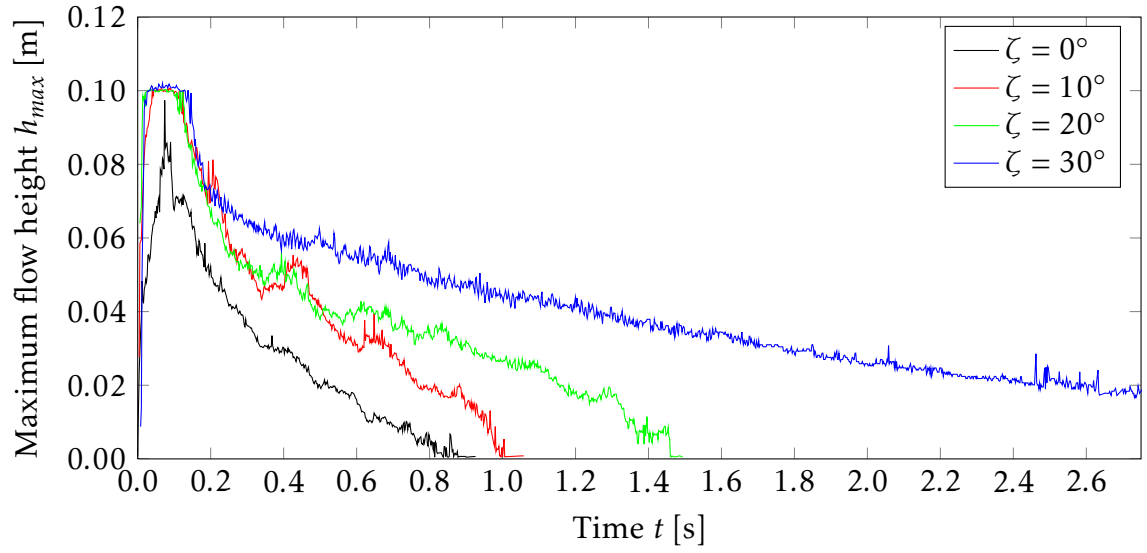

Figure 6.16 – Draining of a rectangular container: Maximal flow height in the observed area. Temporal evolution of the maximal flow height of PVC particles perpendicular to the solid-fluid interface for 0°, 10°, 20° and 30° inclination angle.

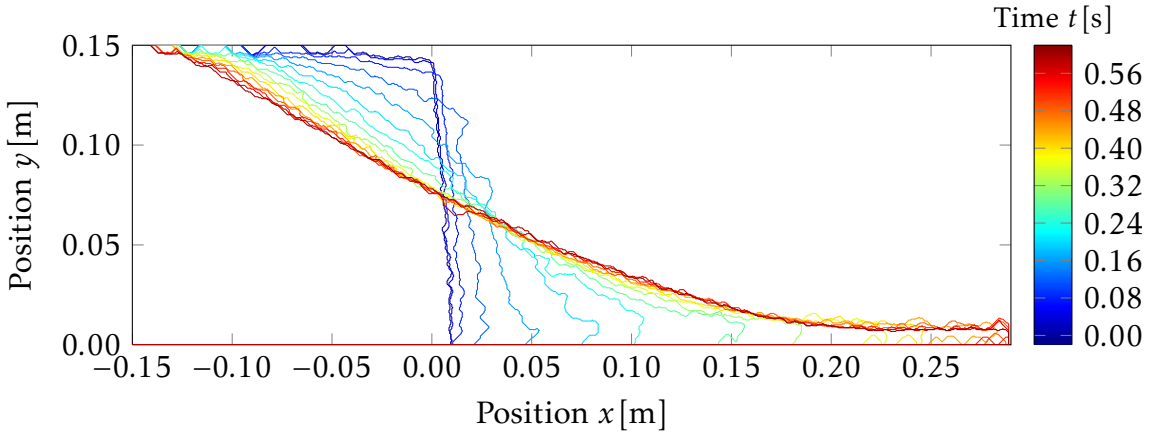

Figure 6.17 – Draining of a rectangular container: Temporal evolution of free surface shape at 0° inclination angle. Outline of the free surface during the granular flow of PVC particles at 0° inclination angle depicted for time steps of 0.04s.

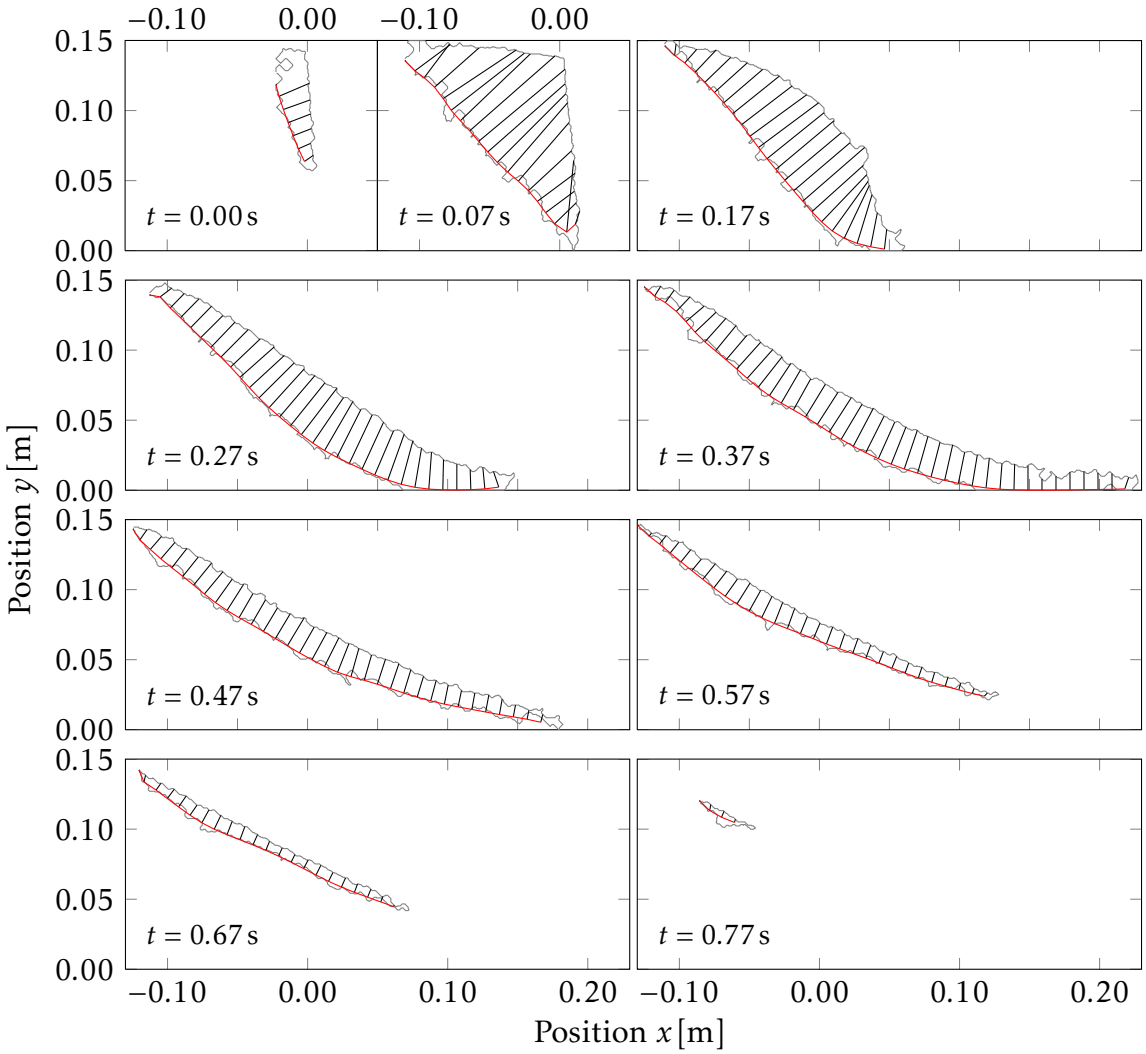

Figure 6.18 – Draining of a rectangular container: Shape of fluidized area for 0° inclination angle. The fluidized area of the PVC flow (where PIV velocities > 0 are observed) is outlined in gray. The solid-fluid interface (red line) is obtained by smoothing of the measured interface with a running average. Flow heights (black lines) are determined as lines perpendicular to local linear fits to the solid-fluid interface.

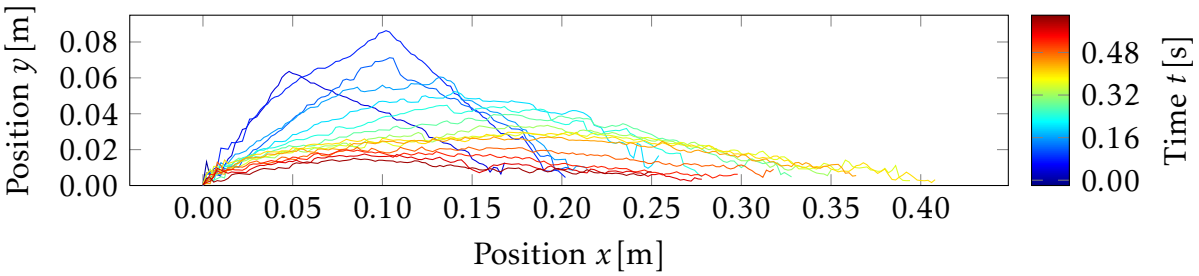

Figure 6.19 – Draining of a rectangular container: Temporal evolution of flow height. Temporal evolution of PVC flow height at 0° inclination angle perpendicular to the solid-fluid interface.

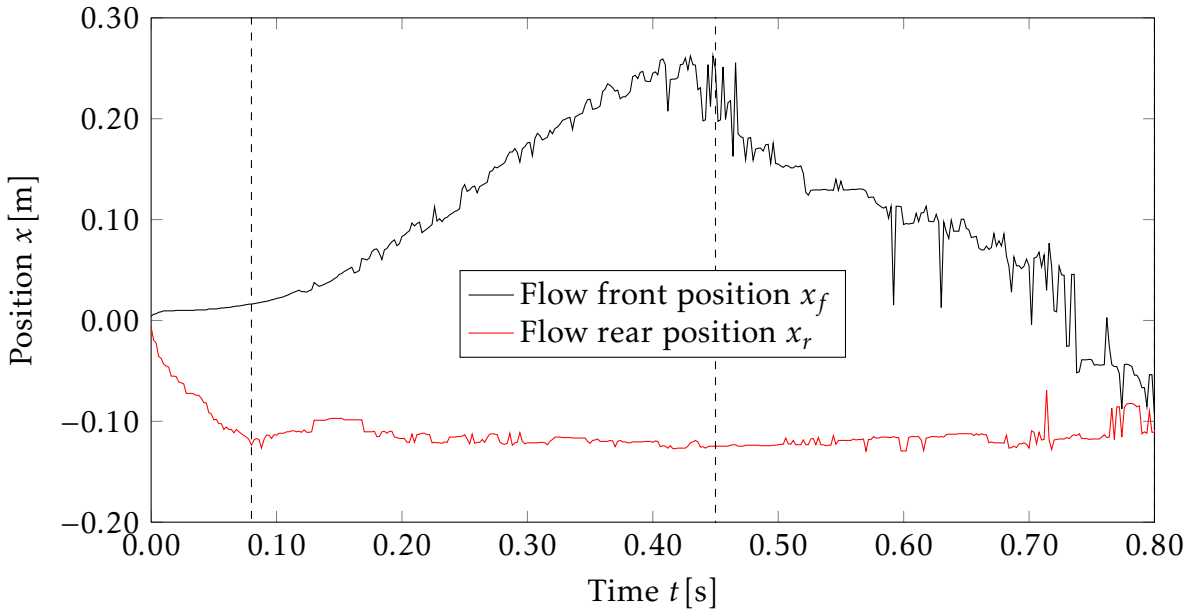

Figure 6.20 – Draining of a rectangular container: Flow front and rear position. Temporal evolution of PVC flow front and rear position for 0° inclination angle. Vertical dashed lines mark (from left to right) the initial fluidization phase, the constant outflow phase and the phase in which the mass comes to rest again.

6.2.1.2 Triangular initial deposit

At inclination angles above ϕ, the material can not be filled as a rectangular shape anymore. But nevertheless, it is important to consider higher inclination angles, since natural avalanches and rock slides usually occur at steep mountain sides. Therefore, PVC particles and sand were backfilled behind the gate to a maximum possible angle (the angle of repose with respect to a horizontal line) (Fig. 6.21). This results in the triangular shaped filling with the longest possible edge of the triangle. Both experiments were conducted with high inclination angles of 50°. The different materials were employed to allow variation in parameters such as density, friction angle and angle of repose and to test the ability of the numerical model to predict flows of different materials after optimizing the simulations with only one material. In contrast to the draining of a rectangular container, a smaller amount of material was used, resulting in a fast fluidization of the complete mass. Similar to the rectangular dam break, first a triangular shaped fraction is mobilized. The particles in this fraction are strongly accelerated creating a steep velocity gradient and strong shearing in y-direction. This results in a collapse of the initial form to a hill like structure sliding and flowing down the slope with again the highest velocities being observed at the surface of the flow (Fig. 6.21).

Considering the course of the flowing volume over time (Fig. 6.22), the fast fluidization of the complete material becomes obvious (0.07 s for PVC and 0.09 s for sand in contrast to 1.8 s for 30°, PVC rectangular). This fluidization phase is followed by an increase

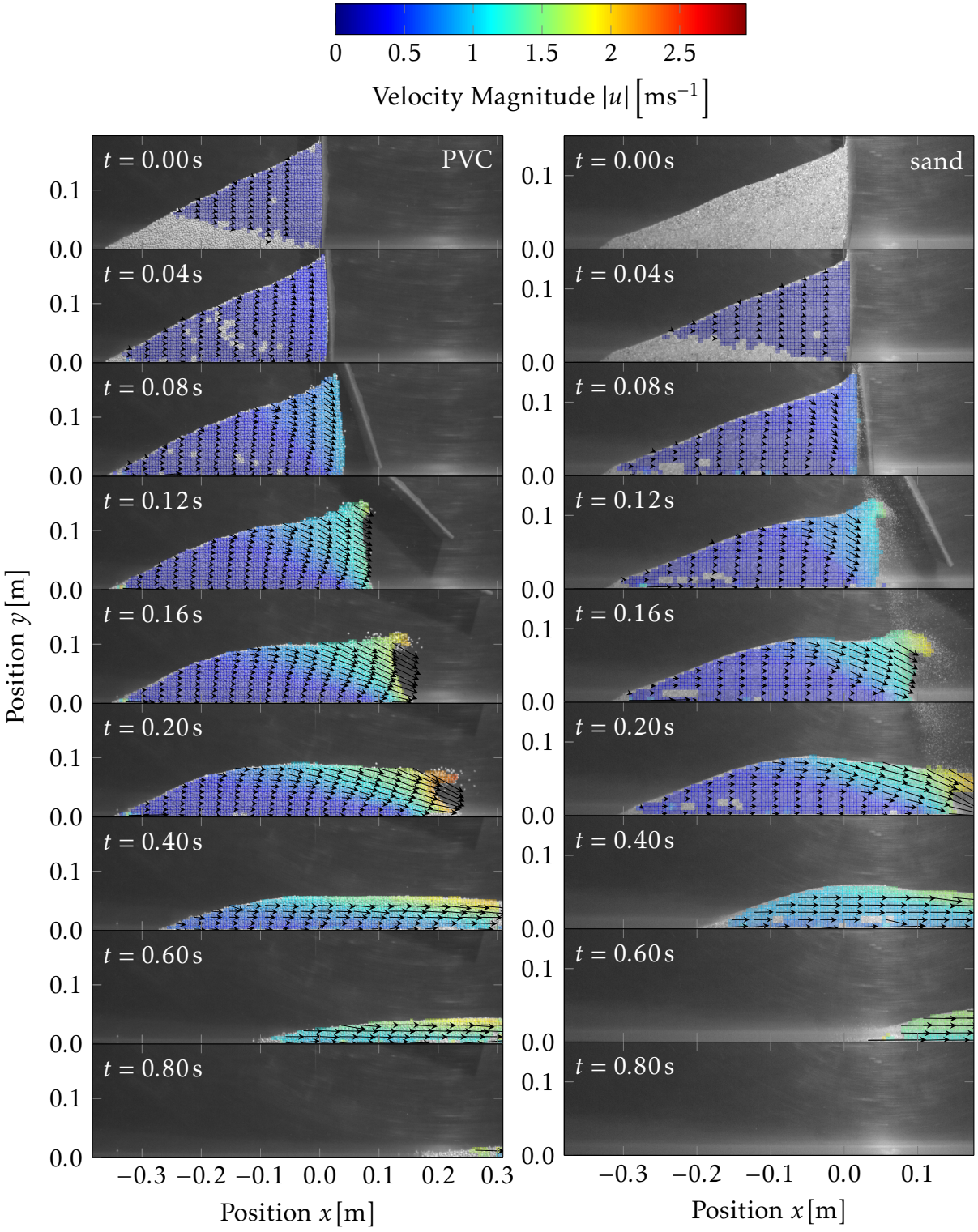

Figure 6.21 – Triangular initial deposit experiment: PIV measurements. Overlay of velocity fields measured by PIV with pictures of the granular flow of PVC (left panel) and sand (right panel) particles during the triangular initial deposit experiment experiment at 50° inclination angle. Magnitudes of mean velocities in 5 mm x 5 mm patches are represented by a heat map (reaching from blue for the minimal velocity to red for the maximal velocity). Direction of the velocities are depicted by arrows, the length of the arrows corresponds to the magnitude. For a better overview, only arrows for each tenth patch in x-direction and every fourth patch in y-direction are shown.

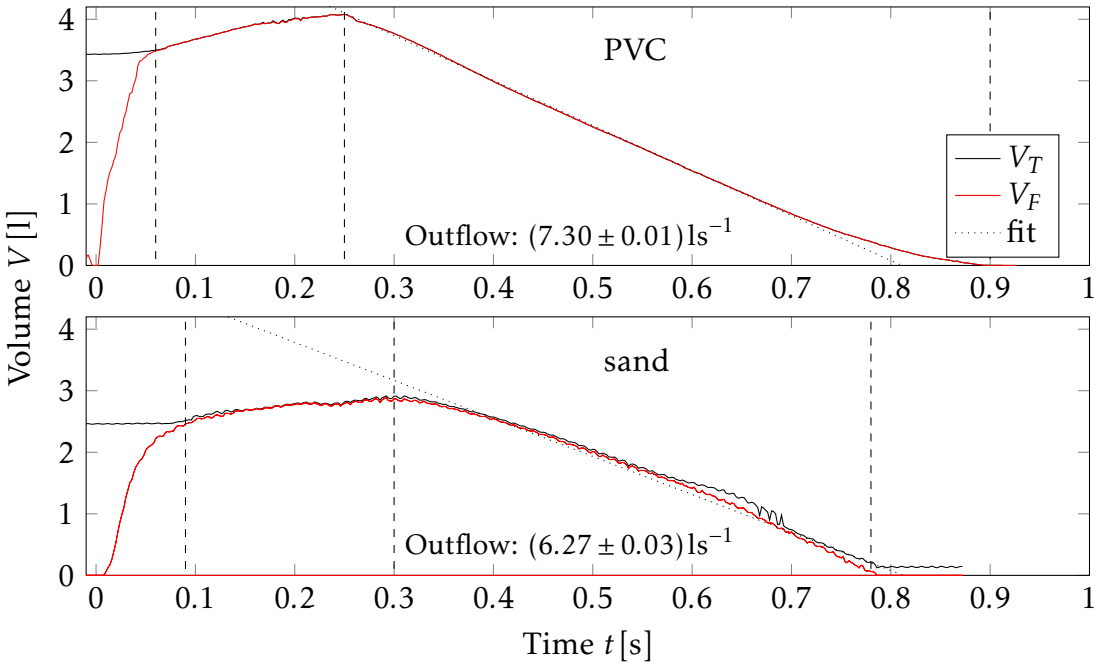

Figure 6.22 – Triangular initial deposit experiment: Temporal evolution of flowing volume. Temporal evolution of the flowing volume fraction (V_F) and the total volume (V_T) during the triangular initial deposit experiment of PVC and sand particles at 50° inclination angle. Vertical dashed lines mark (from left to right) the initial fluidization phase, the constant outflow phase and the phase in which the mass leaves the observed area. The indicated outflow rate is calculated by a linear fit to the curve in the constant outflow phase.

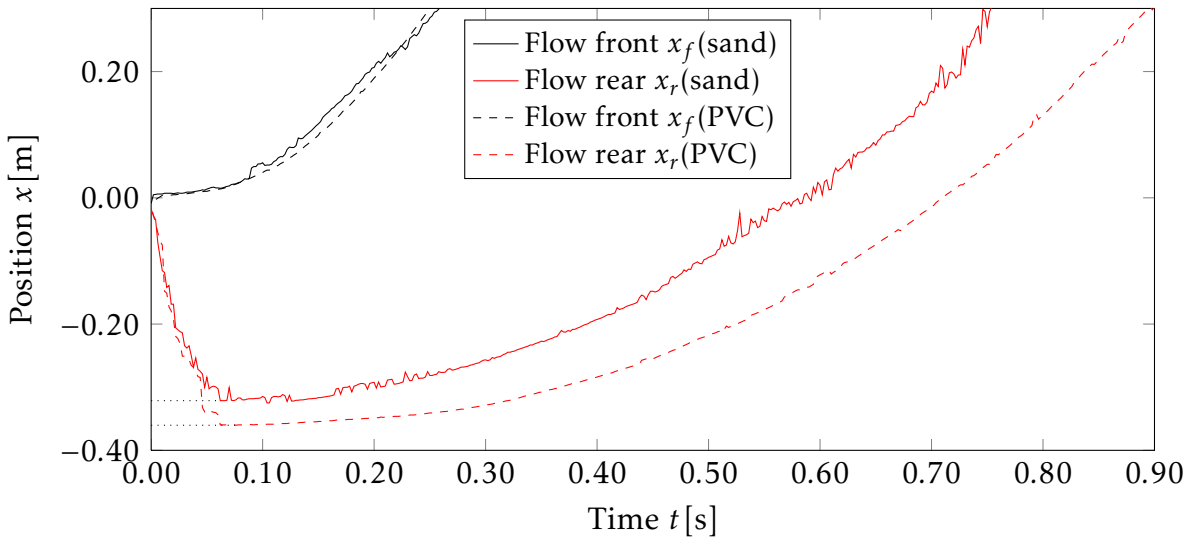

Figure 6.23 – Triangular initial deposit experiment: Flow front and rear position. Temporal evolution of PVC and sand flow front and rear position for 50° inclination angle.

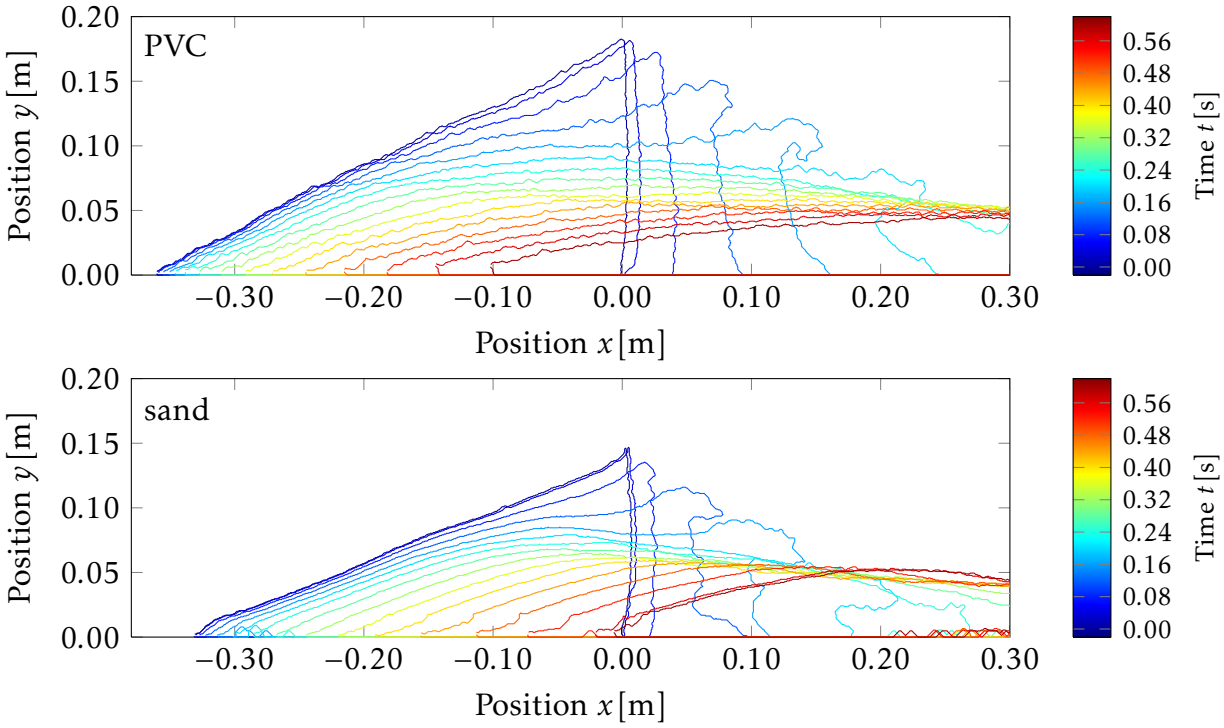

Figure 6.24 – Triangular initial deposit experiment: Temporal evolution of free surface shape. Outline of the free surface during the granular flow of PVC and sand particles at 50° inclination angle depicted for time steps of 0.04 s.

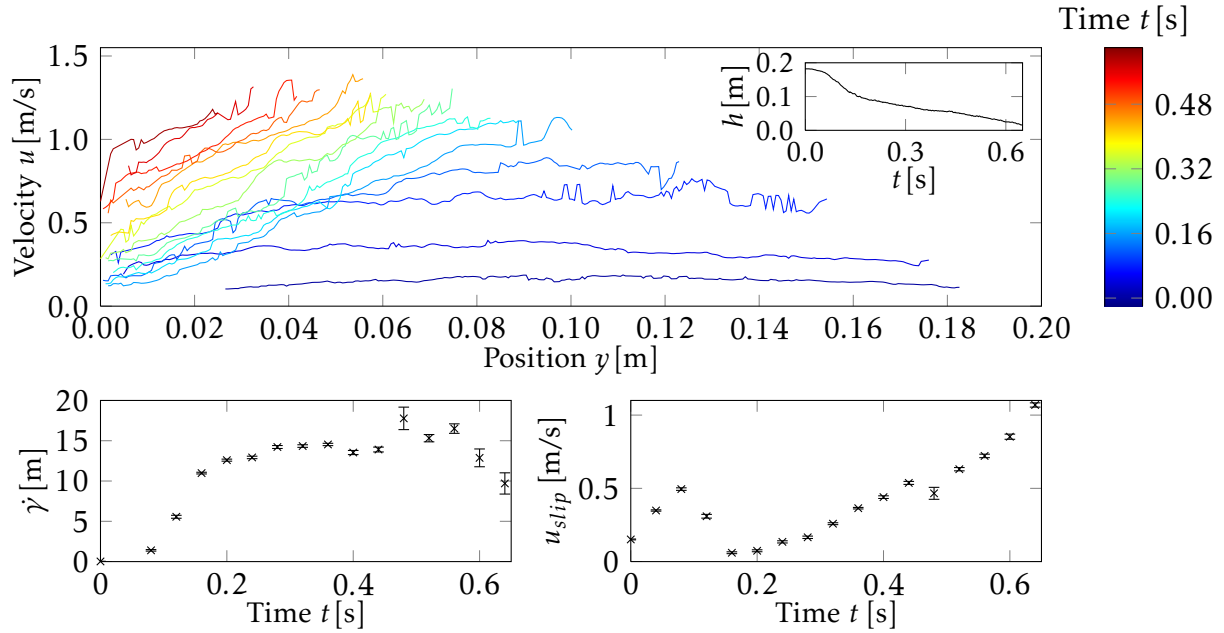

Figure 6.25 – Triangular initial deposit experiment: Velocity profiles at gate position ($x = 0$) for PVC. Upper panel: y-direction dependent velocity profiles during the triangular initial deposit experiment experiment with PVC at the position of the gate ($x = 0$). Time steps are color coded as in Fig. 6.24. The included panel in the upper left corner depicts the height evolution of the flow at the gate position. Lower left panel: Strain rate $\dot{\gamma}$ calculated from linear regression fitted to the velocity profiles. Lower right panel: Slip velocity u_{slip} calculated from linear regression fitted to the velocity profiles.

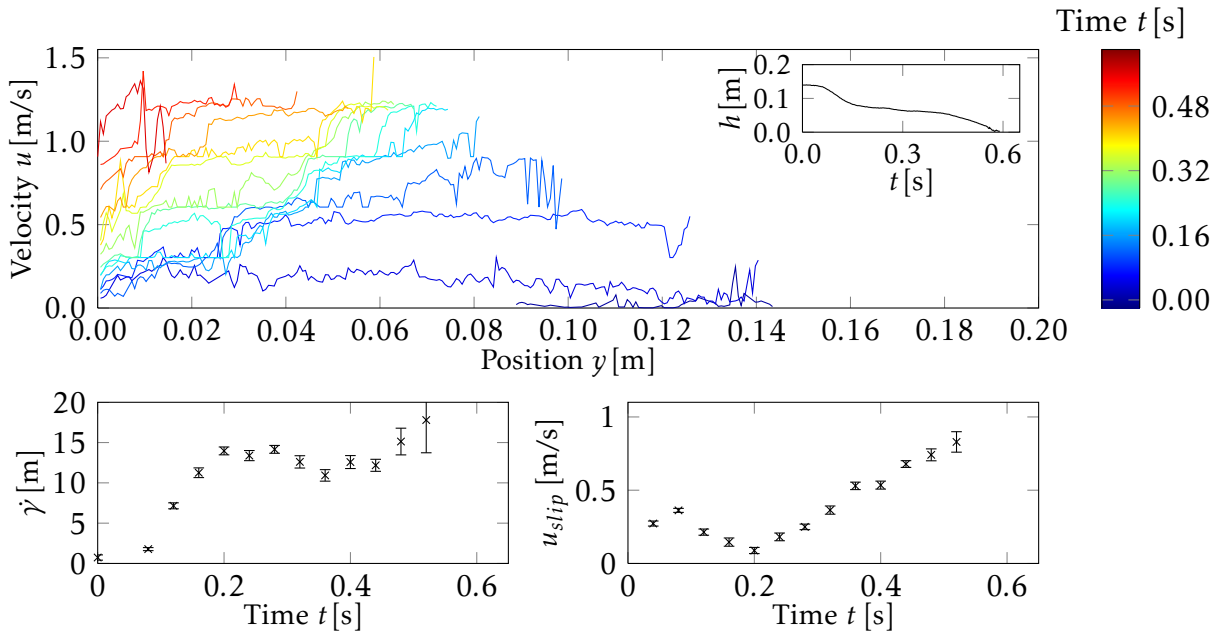

Figure 6.26 – Triangular initial deposit experiment: Velocity profiles at gate position ($x = 0$) for sand. Upper panel: y-direction dependent velocity profiles during the triangular initial deposit experiment experiment with sand at the position of the gate ($x = 0$). Time steps are color coded as in Fig. 6.24. The included panel in the upper left corner depicts the height evolution of the flow at the gate position. Lower left panel: Strain rate $\dot{\gamma}$ calculated from linear regression fitted to the velocity profiles. Lower right panel: Slip velocity u_{slip} calculated from linear regression fitted to the velocity profiles.

in volume of around 20 % due to dilatancy for both materials until a phase of constant outflow from the observed area is reached (at 0.24 s for PVC and 0.3 s for sand). The flow rate remains constant at 7.30 $\frac{\text{l}}{\text{s}}$ (PVC) and 6.27 $\frac{\text{l}}{\text{s}}$ (sand) over a remarkable long time and only decreases towards the end of the experiment. The faster mobilization of the PVC material can be explained by its lower internal friction angle in comparison to sand. As for the rectangular dam break at 0°, the front position of the moving fraction remains almost unchanged during the initiation of the triangular shape and afterwards moves down the channel with an increasing velocity (Fig. 6.23). The rear position of the motion area is, like in the rectangular case, abruptly shifted backwards during the initiation of the triangular zone, but afterwards moves forward following the front position at an increasing distance due to a slower acceleration of the the rear position. While the front positions for both materials moves with the same speed, the rear position of sand moves faster compared to the one of PVC.

The floating behavior during the two experiments of triangular initial deposits is reflected in the evolution of the free surface shape over time (Fig. 6.24). The initial shape is at least partially preserved for 0.12 s for both materials (Fig. 6.24), although the complete mass is fluidized earlier (0.07 s for PVC and 0.09 s for sand, Fig. 6.22). This indicates that the material slides down the slope as a block with little deformation during these

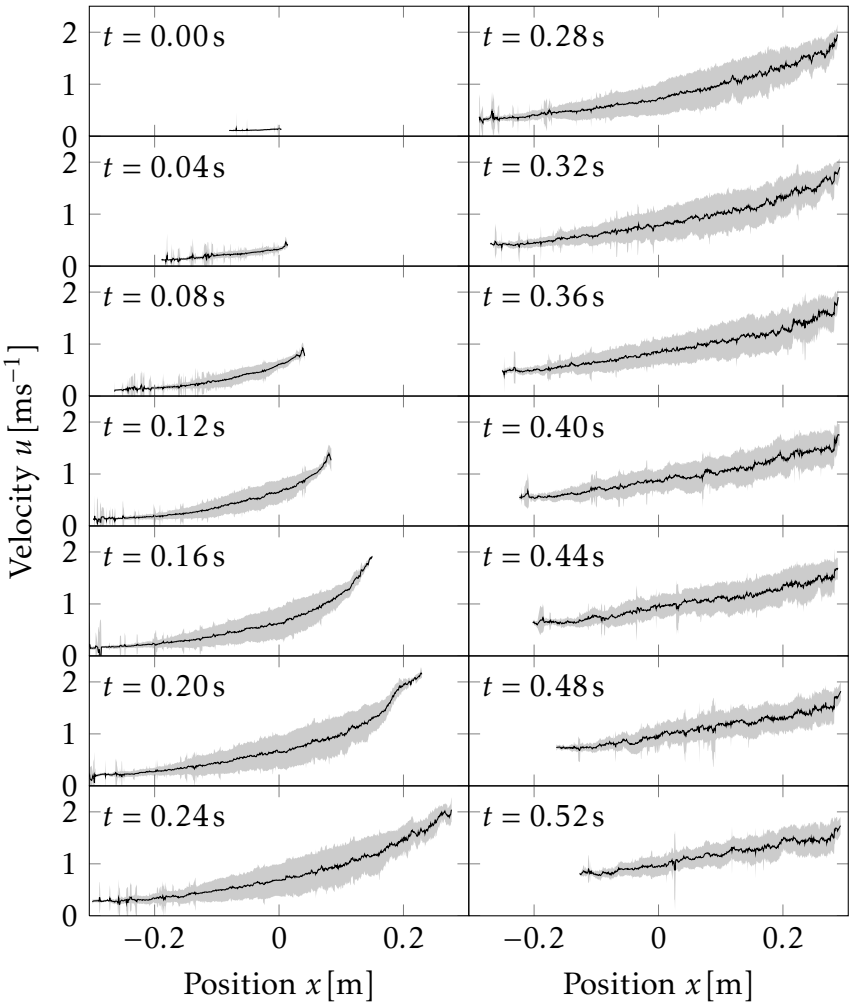

Figure 6.27 – Triangular initial deposit experiment: Temporal evolution of spatial velocity profiles(PVC). Mean velocities over the complete observed area during the triangular initial deposit experiment experiment with PVC are depicted by the black lines. The gray area displayes the variance of the mean for the single measurements.

first 0.12 s. Afterwards, massive deformations occur and the initial shape is dissolved (Fig. 6.24). The initially mobilized triangular fraction is accelerated stronger than the rest of the material, forming a projection preceding the remaining material (Fig. 6.24). As indicated by the increasing distance of the front and rear line (Fig. 6.23), the mass is afterwards stretched out and therefore flattened (Fig. 6.24). During the phase of constant outflow (starting at 0.3 s for sand and 0.25 s for PVC, Fig. 6.22), the height of the flow remains almost constant at the exit point of the observed area (Fig. 6.24), suggesting a constant overall velocity at this point as well. This shape evolution is observed for PVC and sand with only very small differences (Fig. 6.24).

Due to the fast complete fluidization, flow heights and velocities can be determined quickly without a curvilinear coordinate system here: Local velocities as a function of height inside the moving granular material are first analyzed at the initial position of the

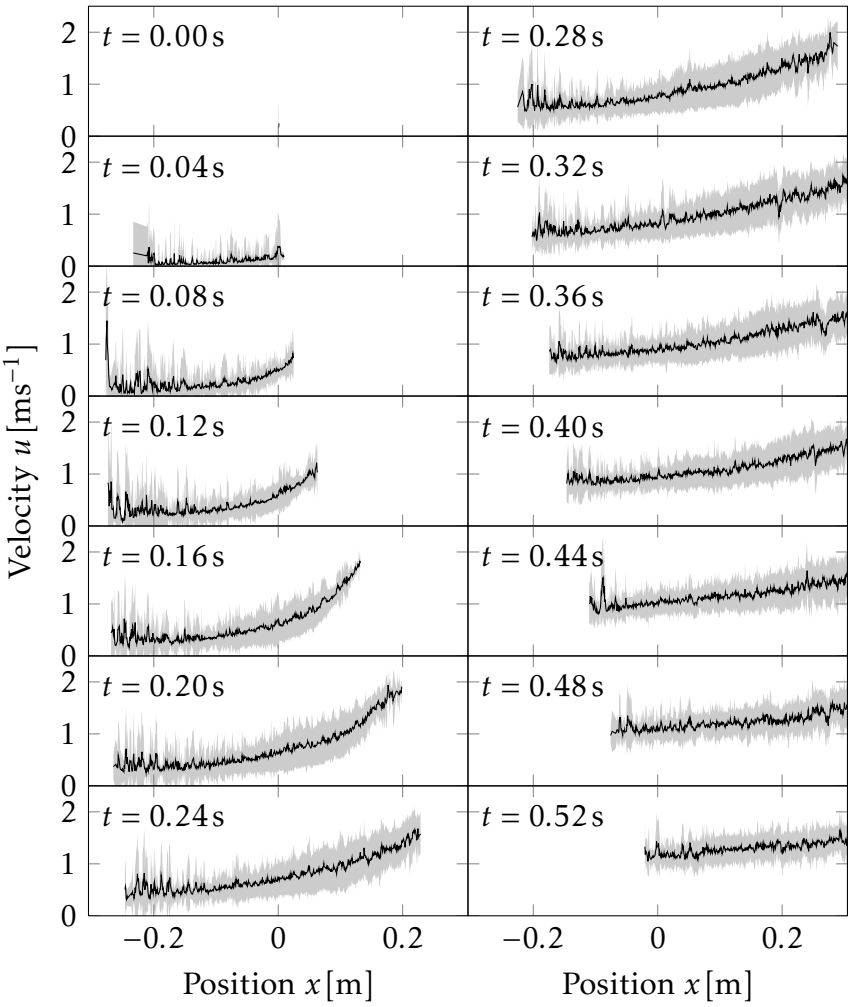

Figure 6.28 – Triangular initial deposit experiment: Temporal evolution of spatial velocity profiles(sand). Mean velocities over the complete observed area during the triangular initial deposit experiment experiment with sand are depicted by the black lines. The gray area displayes the variance of the mean for the single measurements.

gate for the different time steps (Figs. 6.25 and 6.26). By fitting a linear regression to the curves of each time point, the slope of each regression line represents the relative velocity between particles (the strain rate), while the y-axis intercept represents the velocity at the bottom of the channel (the slip velocity). During the initial mobilization of the triangular fraction characterized by low deformation, the velocity over height is nearly constant, resulting in a low strain rate. The calculated slip velocity increases rapidly during this phase, indicating block like sliding with little deformation. After the complete mobilization, the strain rate increases as the deformation increases. During this phase, the slip velocity decreases as the pressure caused by the particles behind is decreasing and friction terms become more important. Afterwards, a linear flow profile with a constant slope emerges, and the strain rate remains constant at around $14\,\frac{1}{\mathrm{s}}$ with some variation. The slip velocity increases as expected for a mass under gravity influence once static fric-

tion is overcome. Again, both materials behave similar.

To get an overview of the spatial velocity profile over the complete observed area, mean downstream velocities were calculated (Figs. 6.27 and 6.28). The variance of the respective values can be considered as an indication of the strain rate at this point. The velocity increases both spatially and temporally, indicating an accelerated flow. As suggested by the constant volume outflow (Fig. 6.22) and flow height (Fig. 6.24), the velocity remains constant at the exit point of the observed area (Figs. 6.27 and 6.28). The rather large variance of the velocity indicates a high strain rate throughout the experiment. In the range of the variance, PVC and sand display again similar behavior, except for a higher variance in the sand experiment. This variance is caused by the low contrast in between the small, rather dark sand particles.

6.2.2 Nummerical simulations with the Savage-Hutter model

The output of the depth-averaged Savage-Hutter type of simulations (section 3.2) yield the mean velocity and the height of a granular flow. The following sections describe the comparisons to the dam break experiments which are possible using these two parameters.

6.2.2.1 Rectangular container

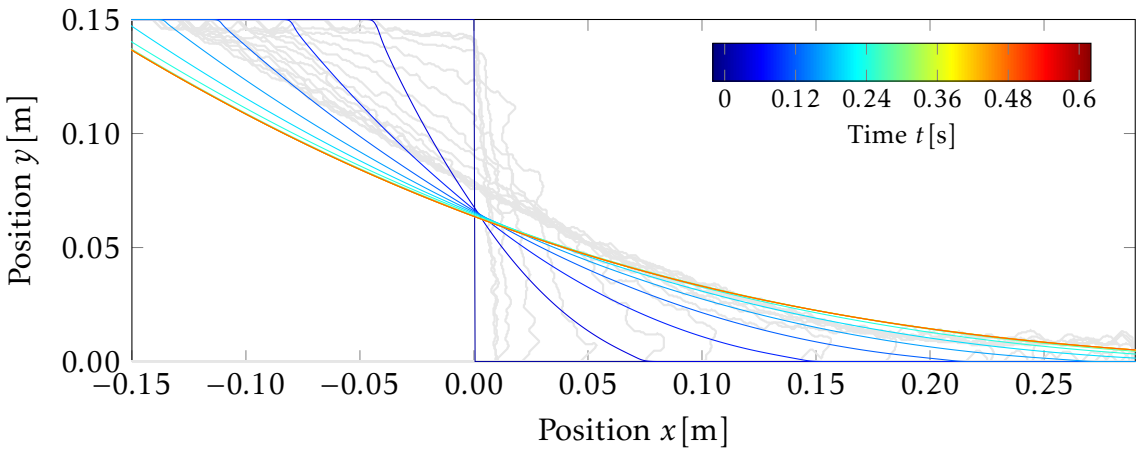

Figure 6.29 – Savage-Hutter simulations of draining of a rectangular container: Temporal evolution of free surface shape at 0° inclination angle. Simulated outline of the free surface during the granular flow of PVC particles at 0° inclination angle depicted for time steps of 0.04 s. The light gray lines are the experimentally observed shapes.

Comparing experimental and numerical results of the shape evolution during the dam break with no inclination (Fig. 6.29) reveals that the simulation fails to predict the initial formation of a triangular shaped moving area but provides good results for the flow shape once the flow has flattened. To allow a comparison of the mean velocity evolution

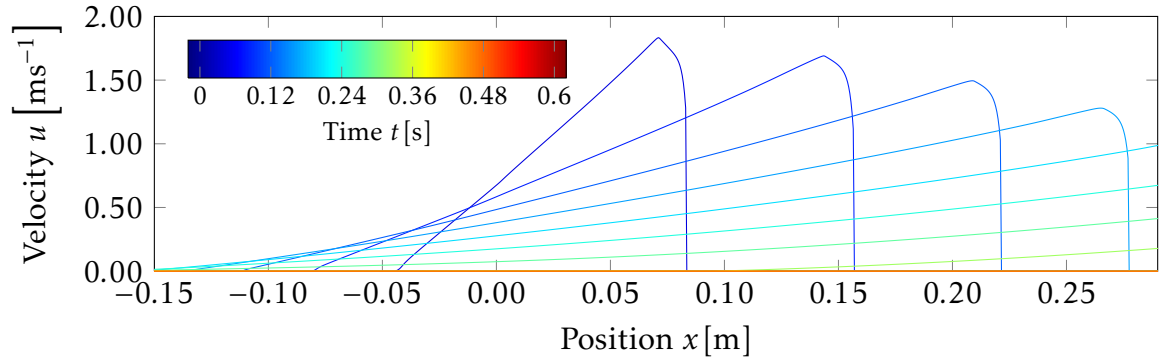

Figure 6.30 – Savage-Hutter simulations of draining of a rectangular container: Temporal evolution of mean velocities at 0° inclination angle. Simulated distribution of mean velocities over the observed are during the granular flow of PVC particles at 0° inclination angle depicted for time steps of 0.04s.

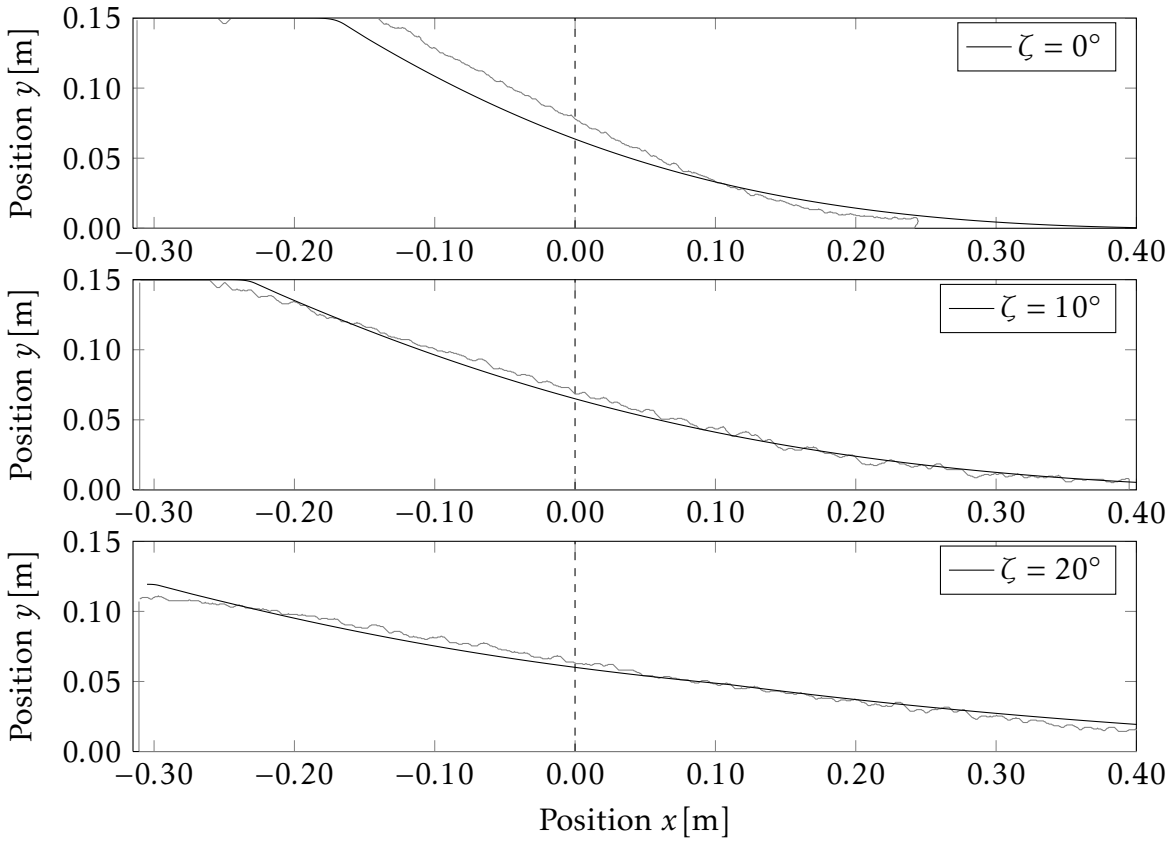

Figure 6.31 – Savage-Hutter simulations of draining of a rectangular container: Final deposit. Simulated shape of the final deposition in the starting zone of PVC flow for 0°, 10° and 20° inclination angle (black line). Gray lines represent the measured deposits. The vertical dashed black lines mark the position of the gate.

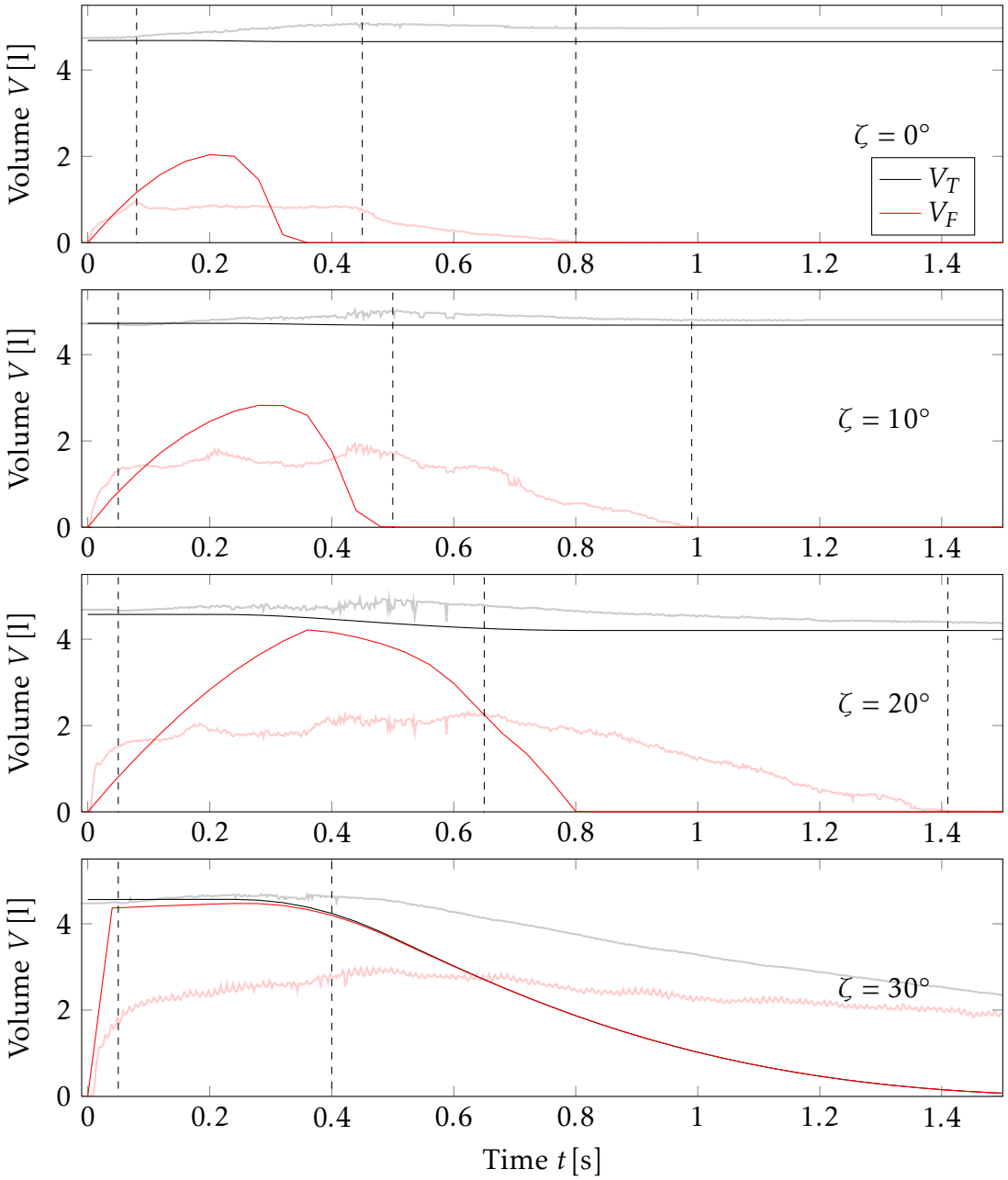

Figure 6.32 – Savage-Hutter simulations of draining of a rectangular container: Temporal evolution of flowing volume. Simulated temporal evolution of the flowing volume fraction (V_F) and the total volume (V_T) during the draining of a rectangular container filled with PVC particles at 0°, 10°, 20° and 30° inclination angle. Vertical dashed lines mark (from left to right) the initial fluidization phase, the constant outflow phase and the phase in which the mass comes to rest again (0°, 10° and 20°) or leaves the observed area (30°). The light red and gray lines represent the experimentally measured volume evolution.

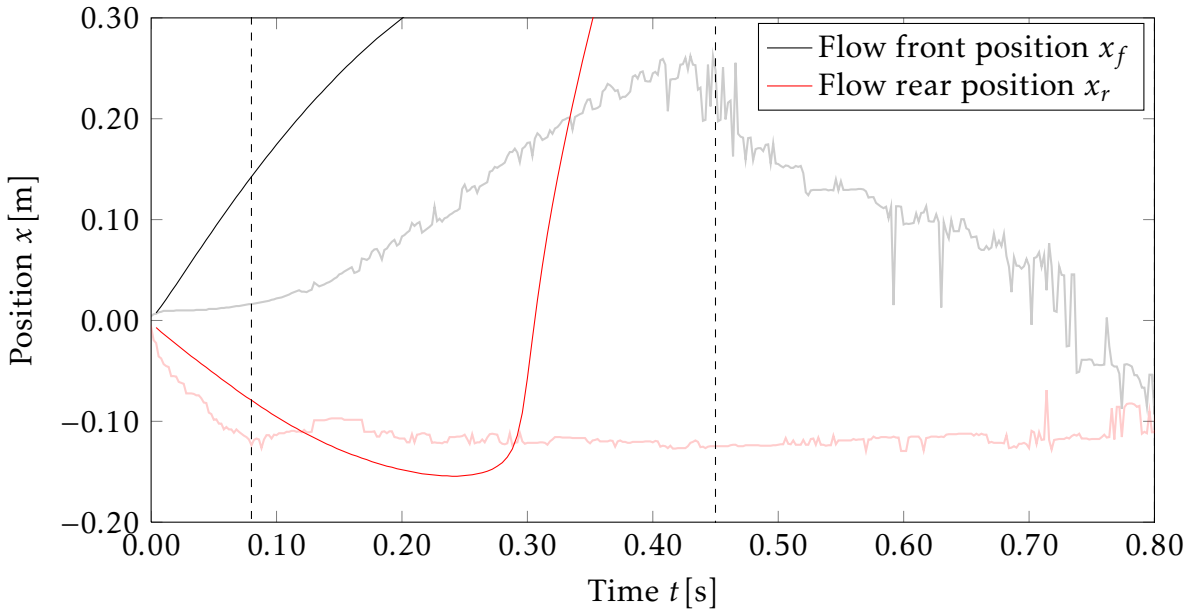

Figure 6.33 – Savage-Hutter simulations of draining of a rectangular container: Flow front and rear position. Simulated temporal evolution of PVC flow front and rear position for 0° inclination angle. Vertical dashed lines mark (from left to right) the initial fluidization phase, the constant outflow phase and the phase in which the mass comes to rest again during the experiment. Experimental data is depicted in light red and gray.

predicted by the simulations to the experimental values, combined mean velocities of the moving and resting fractions are calculated (Fig. 6.30). This is necessary because of the depth-averaging over the complete granular material in the Savage-Hutter simulations. A comparison of these combined mean velocities with the experimental PIV measurements reveals that although no resolution through the flow depth can be obtained, the simulation is capable of predicting the existence of a small fast moving fraction in the beginning of the flow which then develops into a larger fraction with lower velocities as observed during the PIV measurements (Fig. 6.11).

As suggested by the good agreement between the simulated and observed flow geometry in the later stages of the $\zeta = 0°$ experiment, also the final deposition is well predicted by the simulations (Fig. 6.31). This is also true for inclination angles of 10° and 20°, indication a good prediction of the later phases of the flow geometry at these inclination angles as well. Nevertheless, comparison of the simulation with the measured flow volume evolution over time (Fig. 6.32) reveals that the time scales of these simulations strongly differ from the experimentally observed ones. The simulated flow takes place in about half the time of the experimentally observed flow. Additionally, the depth-averaged simulations are per definition unable to distinguish between fluidized and resting fractions and thus predicts the complete volume of the parts where flow occurs ($u > 0.01\mathrm{ms}^{-1}$) to be mobilized although only a thin layer is mobilized (Fig. 6.11). The deviation of the time frame in the simulations compared to the experiment also becomes obvious when

the simulated flow front and rear positions are compared to the experiment (Fig. 6.33): the front position moves too quickly and even leaves the considered area (an area corresponding to the observed area in the experiment). The rear position does not remain constant behind the gate position as observed for the experiment but also leaves the observed area. This indicates that the deposition is simulated to start from the rear of the flow and not from the front as observed.

6.2.2.2 Triangular initial deposit

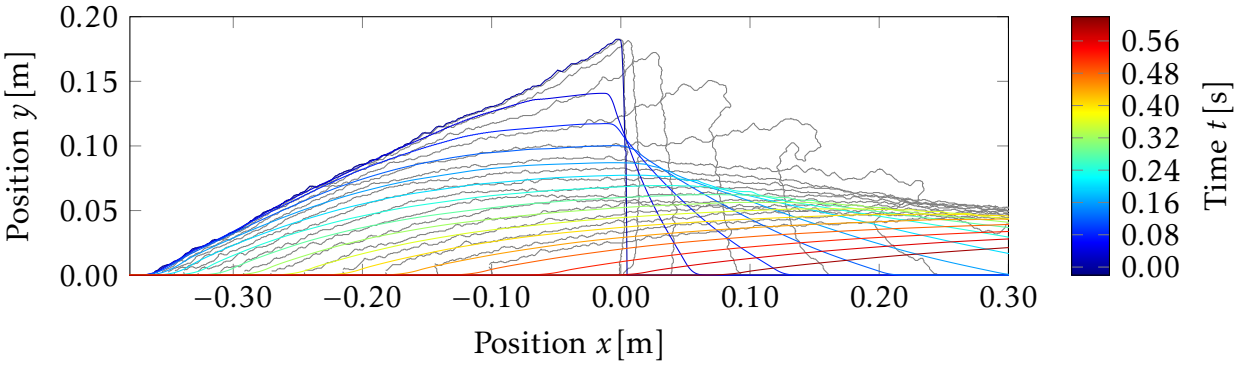

Figure 6.34 – Savage-Hutter simulations of the triangular initial deposit experiment: Temporal evolution of free surface shape(PVC). Outline of the free surface during the granular flow of PVC particles at 50° inclination angle depicted for time steps of 0.04s. Experimentally observed shapes are depicted in gray.

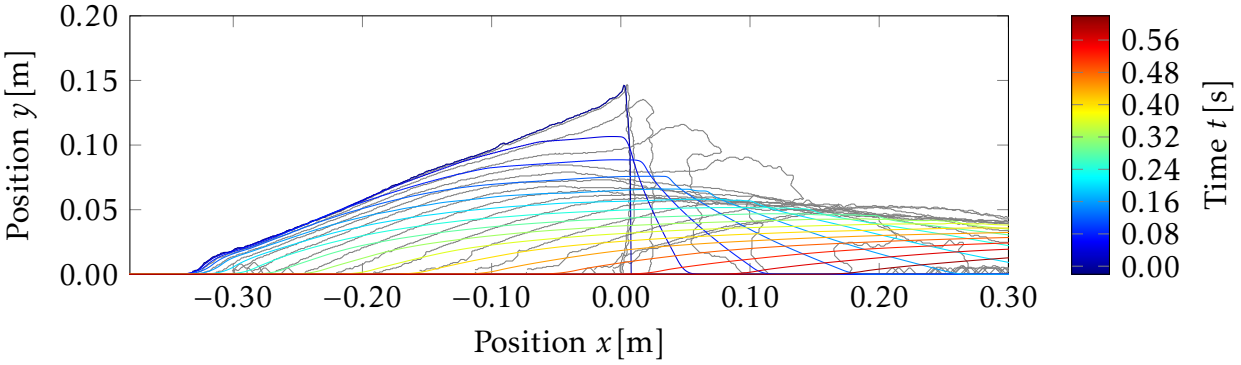

Figure 6.35 – Savage-Hutter simulations of the triangular initial deposit experiment: Temporal evolution of free surface shape(sand). Outline of the free surface during the granular flow of sand particles at 50° inclination angle depicted for time steps of 0.04s. Experimentally observed shapes are depicted in gray.

As in the rectangular case, the simulations are capable of describing the later stages of the granular flow geometry for both PVC and sand but fail to predict the initialization as the simulated flow spreads to fast (Figs. 6.34 and 6.35). The similarity between the free surface shape evolutions simulated for PVC and sand, indicated that the simulation

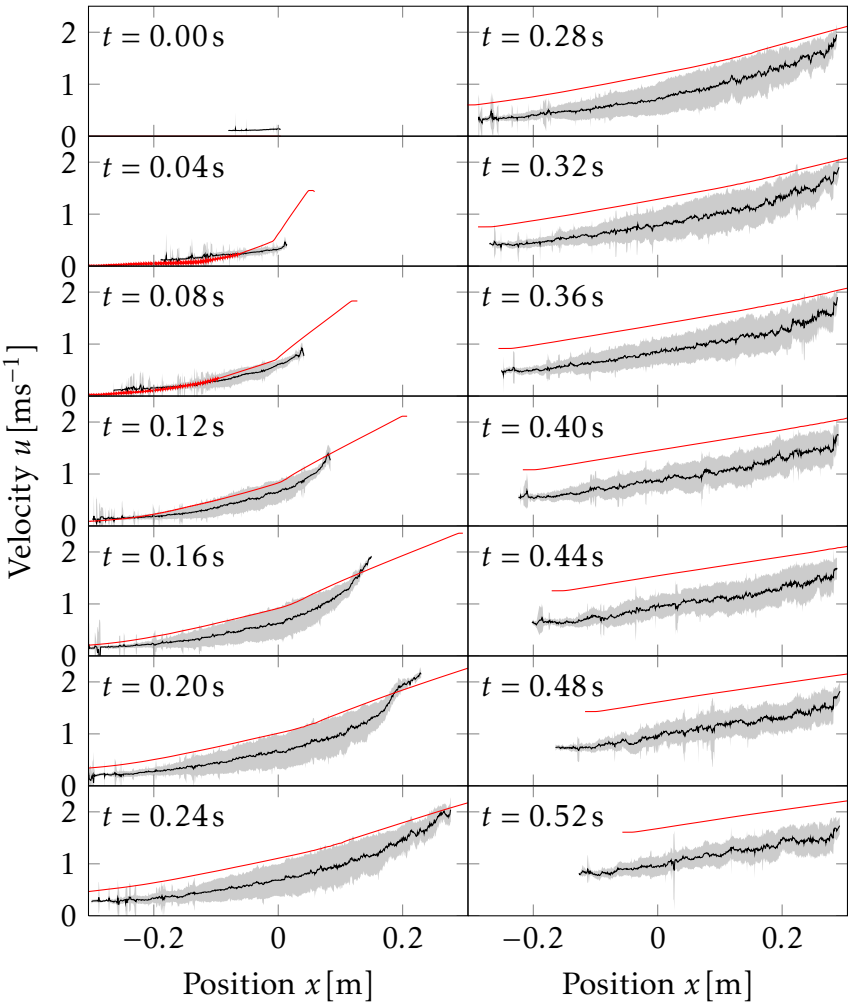

Figure 6.36 – Savage-Hutter simulations of the triangular initial deposit experiment: Temporal evolution of spatial mean velocity distribution(PVC). Simulated mean velocities over the complete observed area during the triangular initial deposit experiment experiment with PVC are displayed by a red line. Mean velocities of the experiment are depicted by the black lines, the gray area displayes the variance of the mean for the single measurements.

are almost independent of the material. Comparison of the simulated mean velocity evolution with measured velocities (Figs. 6.36 and 6.37) reveals a good agreement during the first time steps for both PVC and sand. Thereafter, the simulated velocities are too high, especially for PVC. Additionally, the front positions are moving much faster in the downstream position as expected. This can be explained by the fast spreading of the simulated flow into the channel. Nevertheless, the velocity gradient over the channel length is approximated well by the simulations. Especially for sand, the simulated velocity is in relatively good agreement with the upper boundary of the variance range. The measured velocity profiles indicate the highest velocity at the free surface of the flow (Figs. 6.25 and 6.26). Thus, it seems that the high mean velocity in the depth-averaged simulations represents rather the free surface velocity than the mean velocity. This is in contrast to

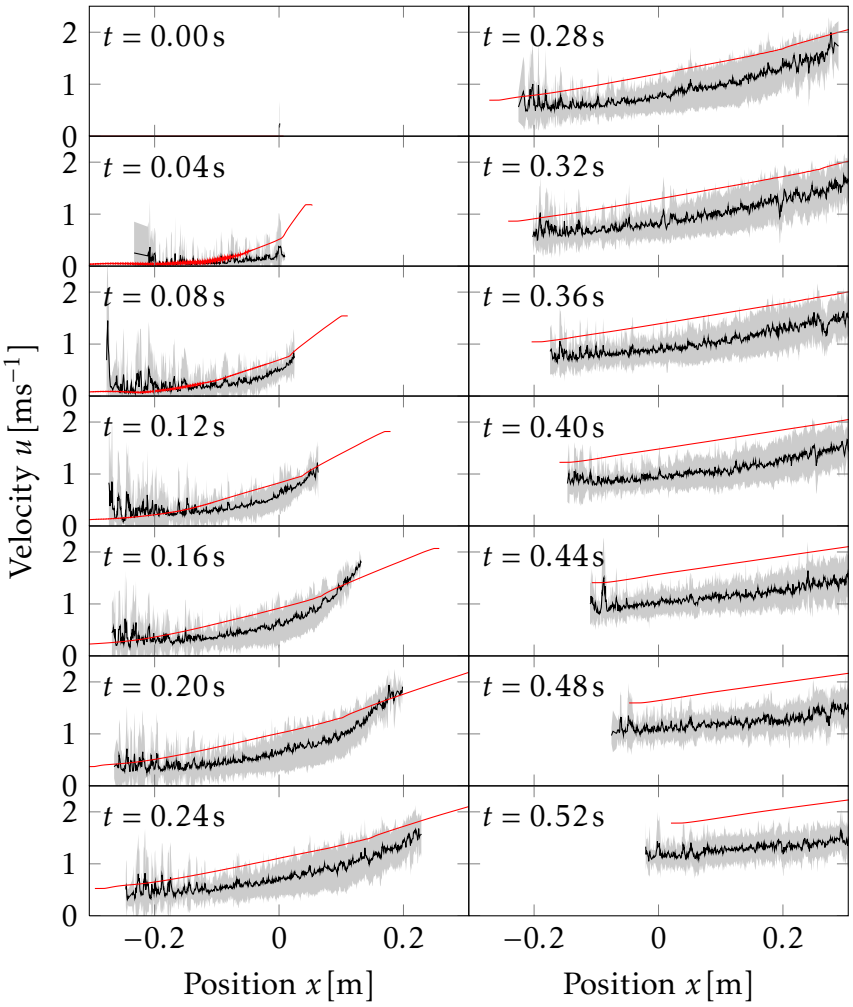

Figure 6.37 – Savage-Hutter simulations of the triangular initial deposit experiment: Temporal evolution of spatial mean velocity distribution(sand). Simulated mean velocities over the complete observed area during the triangular initial deposit experiment experiment with sand are displayed by a red line. Mean velocities of the experiment are depicted by the black lines, the gray area displayes the variance of the mean for the single measurements.

the essence of the depth-averaged models, which assume the whole material to slide with the same, basal velocity. However, velocity tendencies and orders of magnitude are well captured in both cases.

The overestimated velocity of the simulated flow is reflected in the evolution of the resting and fluidized volume fractions: for both PVC and sand higher rates of outflow are observed, resulting in a shorter flow time than observed in the experiment (Fig. 6.38). In contrast to that, the fluidization occurs slower in the simulations. This can be explained by the depth-averaged and pressure driven nature of the simulation: upon opening of the gate, a high pressure gradient exists, which causes the first columns of the material to collapse and then results in a rarefied wave being transported through the material until the end of the initial deposit is reached and finally fluidized. In the experimentally

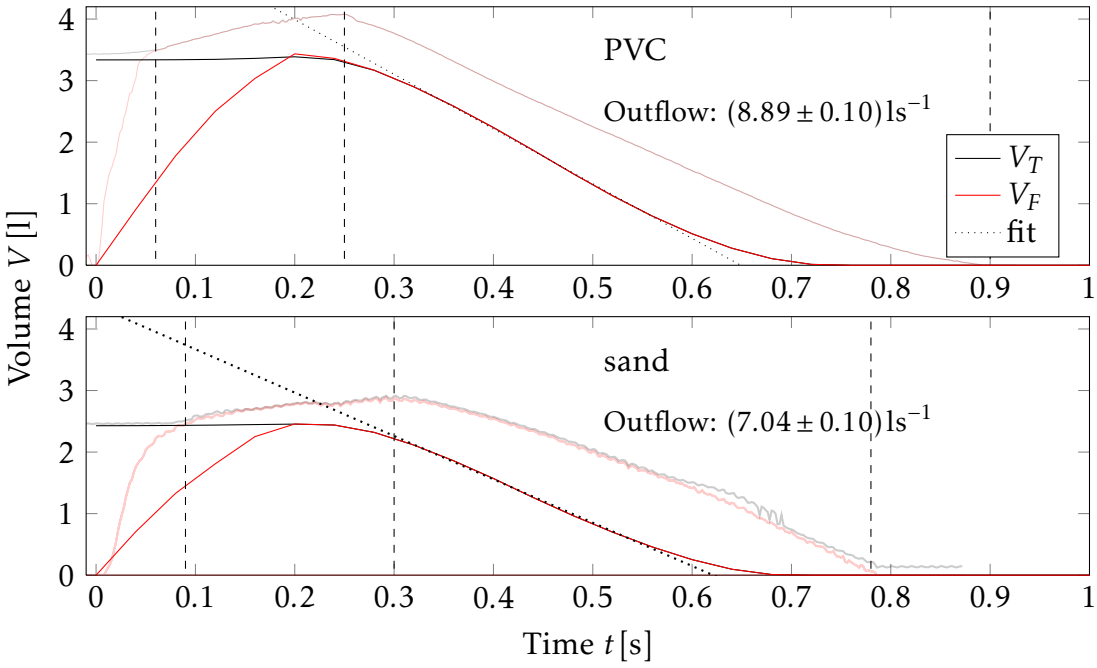

Figure 6.38 – Savage-Hutter simulations of the triangular initial deposit experiment: Temporal evolution of flowing volume. Simulated temporal evolution of the flowing volume fraction (V_F) and the total volume (V_T) during the triangular initial deposit experiment of PVC and sand particles at 50° inclination angle in comparison to the measured volume (depicted in light red and gray). Vertical dashed lines mark (from left to right) the initial fluidization phase, the constant outflow phase and the phase in which the mass leaves the observed area during the experiment. The outflow rate is calculated by a linear fit (black dotted line) to the curve in the constant outflow phase. The respective outflow rates for the simulated curves are given in the graphs.

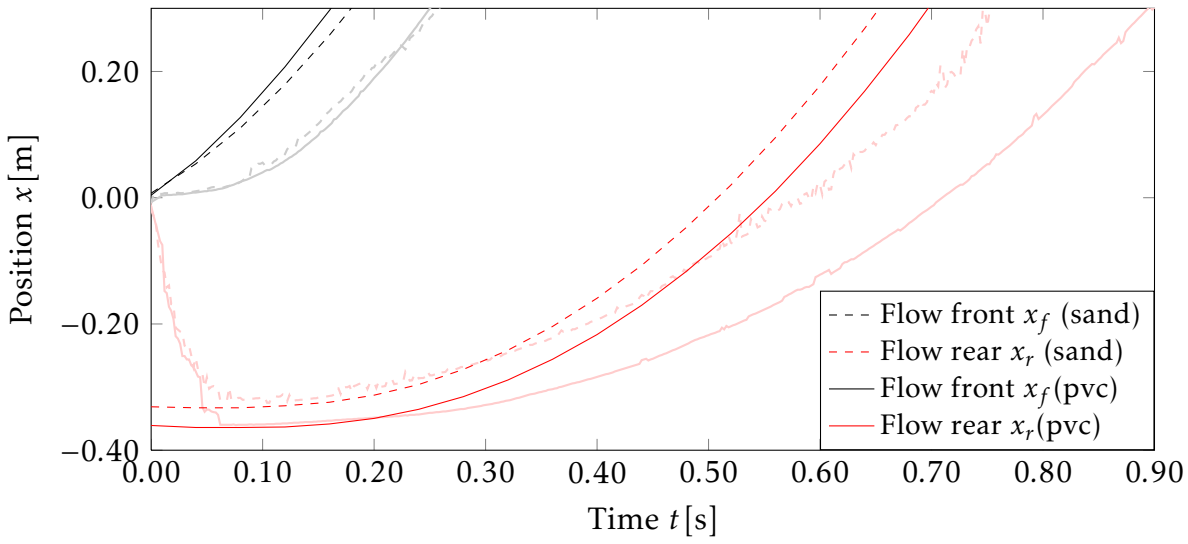

Figure 6.39 – Savage-Hutter simulations of the triangular initial deposit experiment: Flow front and rear position. Simulated temporal evolution of PVC and sand flow front and rear position for 50° inclination angle in comparison to the measured positions (depicted in light red and gray).

observed, gravity driven flow, the fluidization at the gate is accompanied by a slipping of the complete block (Fig. 6.21). In correlation with this observation, the simulated rear of the flow is first lagging the experimental one, but then moves faster than observed in the experiment towards the end of the experiment and thus reaches the end of the observed area earlier. The simulated front position of the flow moves faster than the experimental one throughout the experiment (Fig. 6.39). This observation is true for PVC and sand. Nevertheless, the qualitative differences between the two materials are well captured by the simulations.

Taken together, the simulations are well suited to predict the geometry of flows after the initiation phase and yield reasonable predictions for final depositions in case they occur. Additionally, they are capable of discriminating behavior of PVC and sand just by taking the internal and bottom sliding friction angle into account. On the other hand, the simulations fail to predict the dynamics occurring during the initiation of the flow and the time scales in which the experiment evolved and mean velocities are constantly overestimated.

6.2.3 Non-depth-averaged numerical simulations

The non-depth-averaged character of the simulations developed in this study using the OpenFOAM® software enables the simulation of all parameters described in the experimental section. As mentioned above, simple Coulomb-type friction was chosen as rheological model. For the bottom friction, preliminary simulations (data not shown) suggested that best agreements with observed velocity profiles were achieved when the bottom friction angle was assumed to be equal to the internal friction angle of the material. This condition is implemented in the simulation by setting the velocity to $u = 0$ at the bottom of the channel (stick condition).

6.2.3.1 Rectangular container

Due to the non-depth-averaged character of the simulations, the velocity profile and filling parameters of the simulated flow (Fig. 6.40) can be compared to the PIV results of the experiments (Fig. 6.11). The shape of the fluidized fraction and the time-scales are well captured for all three lower inclination angles (0°, 10° and 20°). Also the velocity profile is qualitatively well predicted but the simulated velocities are slightly lower than the observed ones. The influence of the inclination angle on the flow behavior is well captured by the simulation: the fluidized fraction as well as the velocities increase for higher inclination angles. For the highest inclination angle (30°), which causes the material to be completely fluidized during the experiment, the complete fluidization is not predicted by the simulation due to the assumed stick condition (Fig. 6.41).

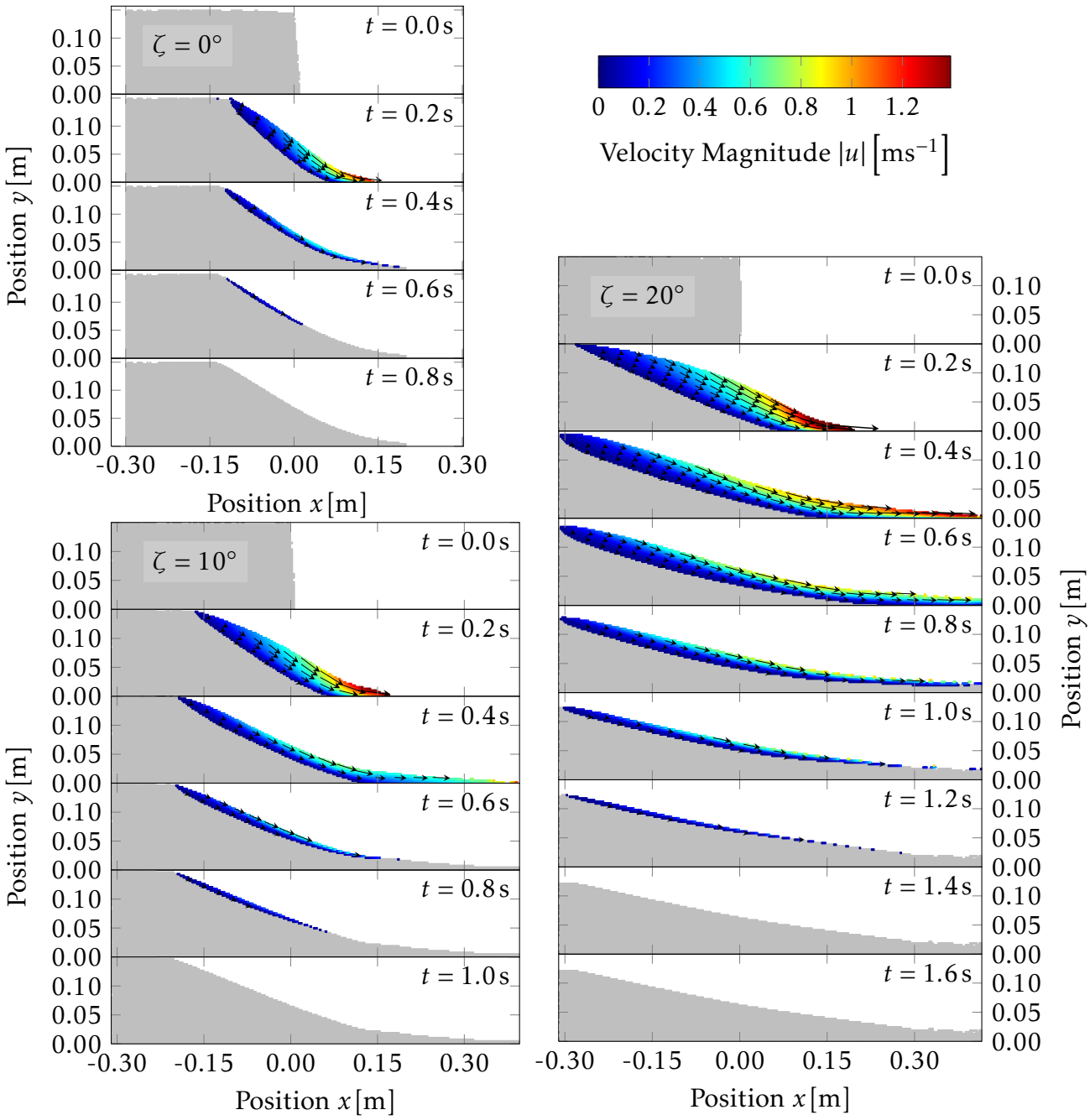

Figure 6.40 – OpenFOAM® simulations of draining of a rectangular container: Overview on velocity fields for small inclination angles. Overlay of simulated velocity fields with simulated shape of the granular flow of PVC particles during the draining of a rectangular container at 0°, 10° and 20° inclination angle. Velocities in single patches corresponding to the numerical grid are represented by a heat map (reaching from blue for the minimal velocity to red for the maximal velocity). Direction of the velocities are depicted by arrows, the length of the arrows corresponds to the magnitude. For a better overview, only arrows for each tenth patch in x-direction and every fourth patch in y-direction are shown.

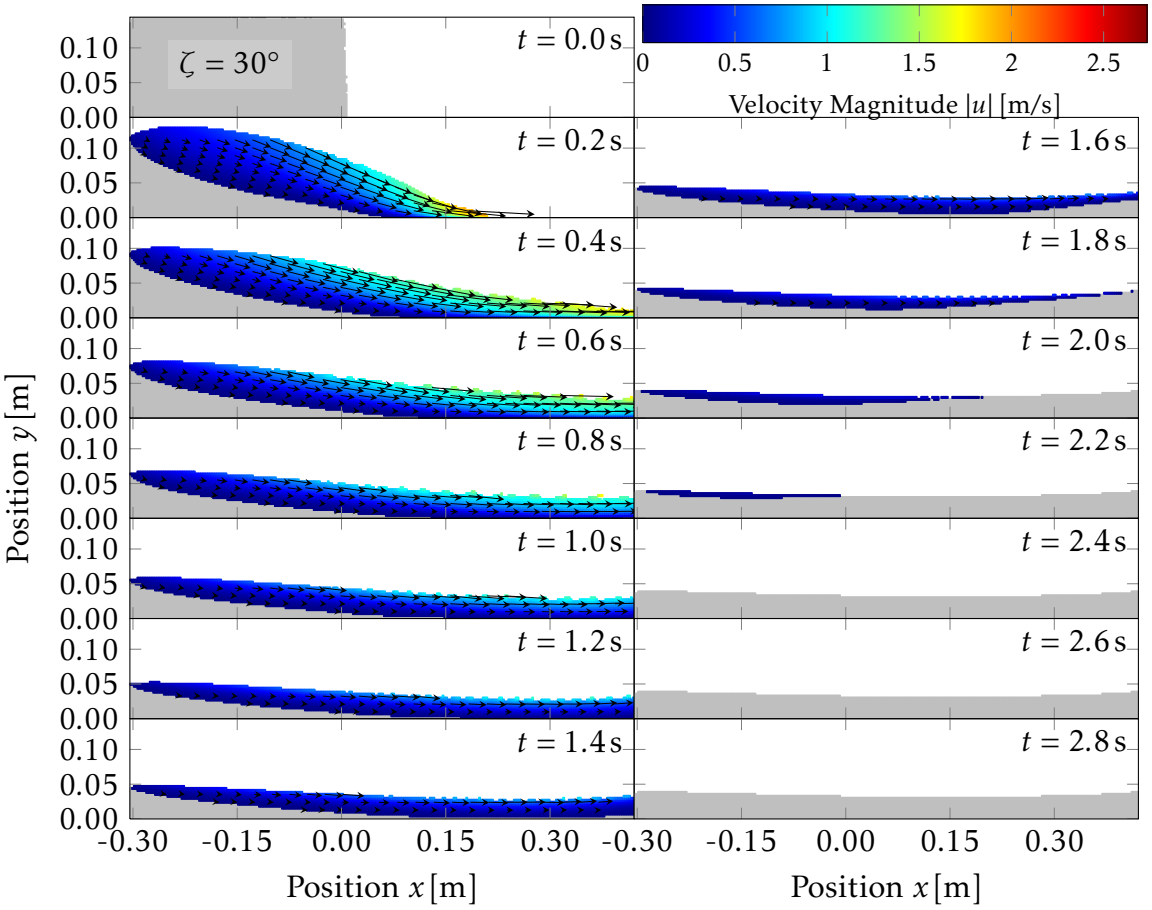

Figure 6.41 – OpenFOAM® simulations of draining of a rectangular container: Overview on velocity fields for 30° inclination angle. Overlay of simulated velocity fields with simulated shape of the granular flow of PVC particles during the draining of a rectangular container at 30° inclination angle. Velocities in single patches corresponding to the numerical grid are represented by a heat map (reaching from blue for the minimal velocity to red for the maximal velocity). Direction of the velocities are depicted by arrows, the length of the arrows corresponds to the magnitude. For a better overview, only arrows for each tenth patch in x-direction and every fourth patch in y-direction are shown.

Apart from this, especially the simulated initialization phase is in good agreement with the experimental data concerning both the shape of the fluidized fraction and the velocity profile. The temporal volume evolution during the initialization is best predicted for 20° and 30° inclination (Fig. 6.42). Here, the simulation predicts the observed flow both qualitatively and quantitatively. For 0° and 10°, the simulation slightly underestimates the volume as well as the total flow time and fails to predict the phase of constant flow volume. Despite these slight deviations from the measured events, the simulations presented here are clearly superior to the depth-averaged simulations, which are incapable of distinguishing between moving and resting phase and fail in the prediction of time-scales for this experiment. Additionally, in contrast to the depth-averaged model, the simulations with OpenFOAM® are well capable of predicting the initial area of mo-

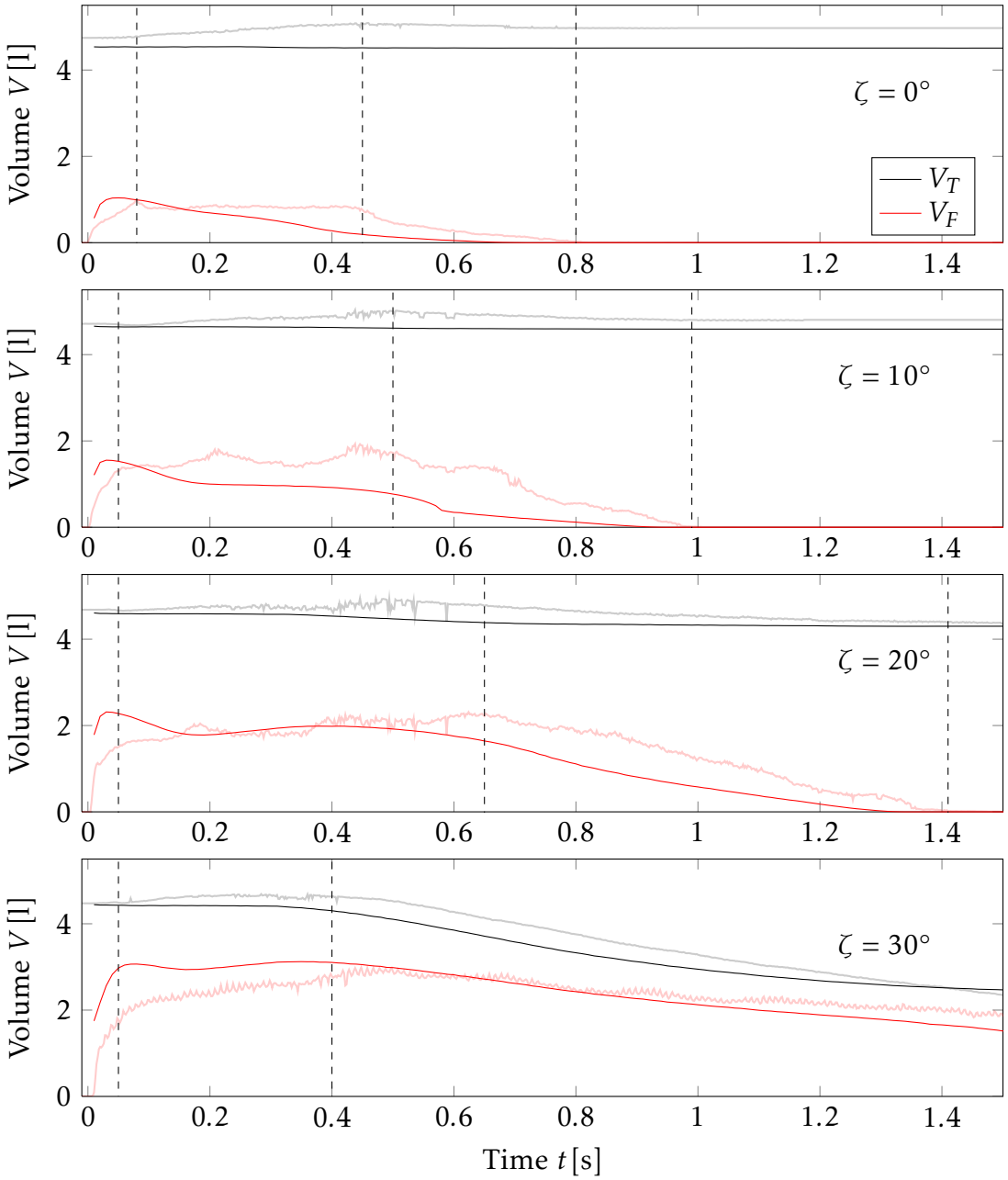

Figure 6.42 – OpenFOAM® simulations of draining of a rectangular container: Temporal evolution of flowing volume. Simulated temporal evolution of the flowing volume fraction (V_F) and the total volume (V_T) during the draining of a rectangular container filled with PVC particles at 0°, 10°, 20° and 30° inclination angle. Vertical dashed lines mark (from left to right) the initial fluidization phase, the constant outflow phase and the phase in which the mass comes to rest again (0°, 10° and 20°). The light red and gray lines represent the measured volume evolution.

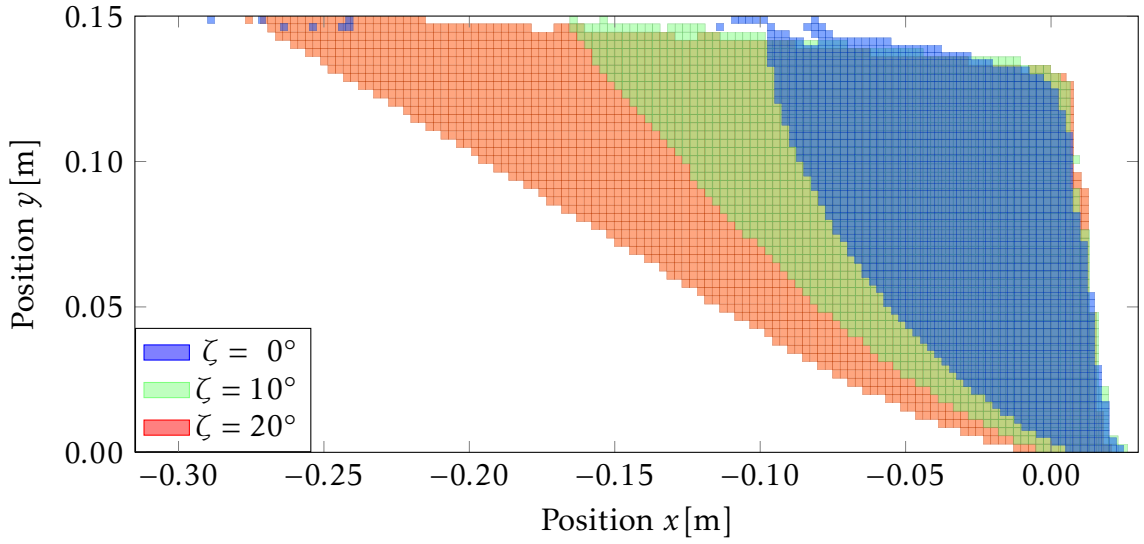

Figure 6.43 – OpenFOAM® simulations of draining of a rectangular container: Initial area of motion. Simulated outline of the initial mobilized fraction of PVC particles for 0° (blue), 10° (green) and 20° (red) inclination angle.

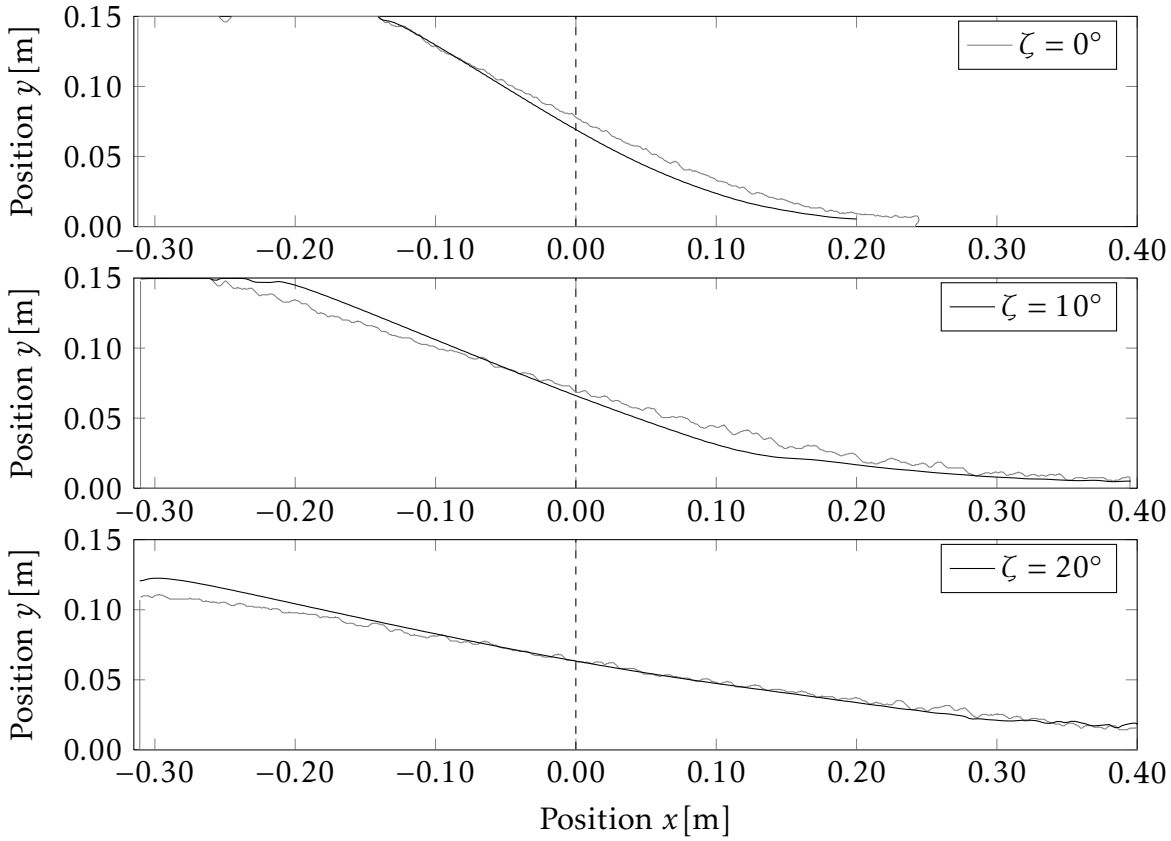

Figure 6.44 – OpenFOAM® simulations of draining of a rectangular container: Final deposit. Simulated shape of the final deposit in the starting zone of PVC flow for 0°, 10° and 20° inclination angle (black lines). Gray lines represent the measured outline. The vertical dashed black lines mark the position of the gate.

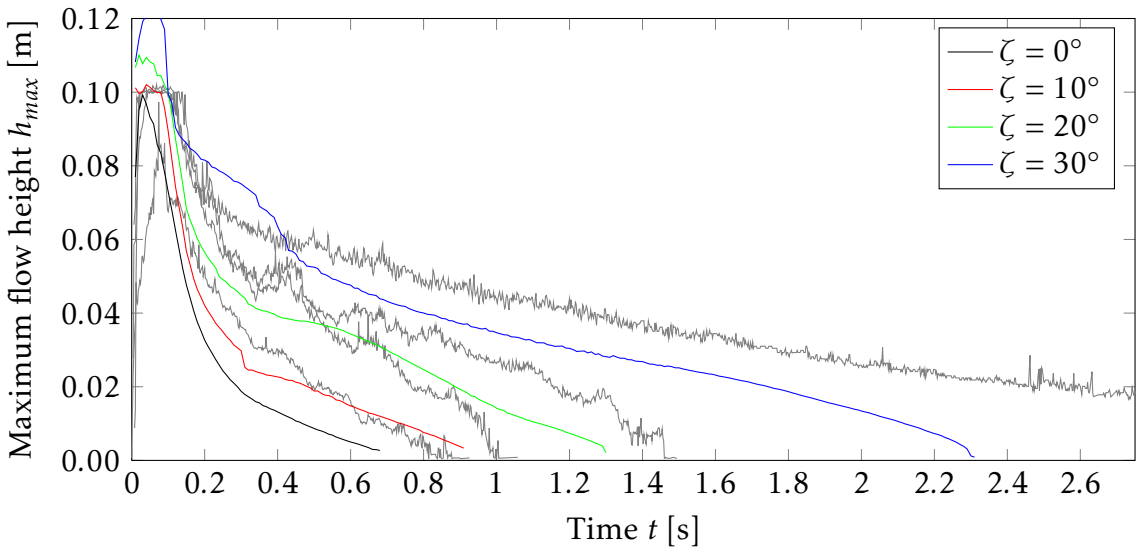

Figure 6.45 – OpenFOAM® simulations of draining of a rectangular container: Maximal flow height in the observed area. Simulated temporal evolution of the maximal flow height of PVC particles perpendicular to the solid-fluid interface for 0°, 10°, 20° and 30° inclination angle. Gray lines represent experimentally observed maximal flow heights.

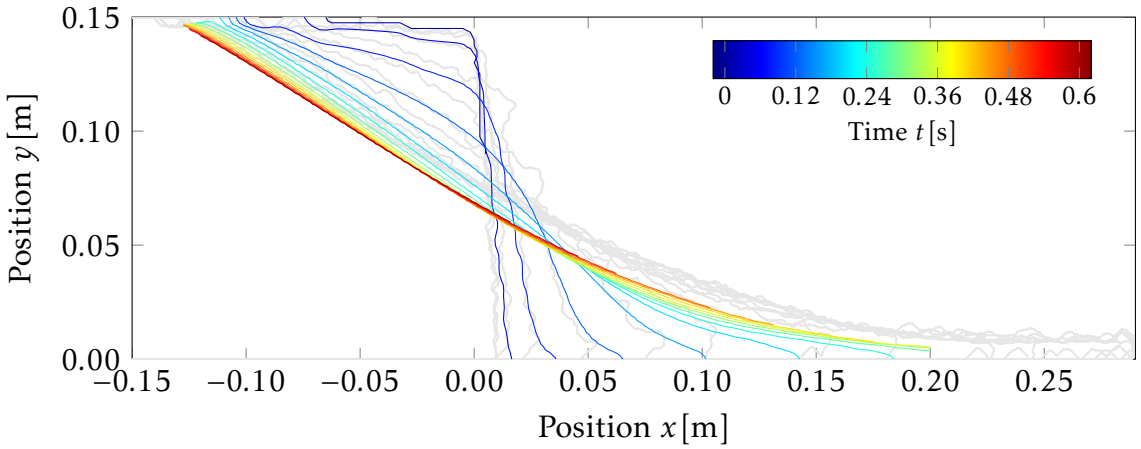

Figure 6.46 – OpenFOAM® simulations of draining of a rectangular container: Temporal evolution of free surface shape at 0° inclination angle. Simulated outline of the free surface during the granular flow of PVC particles at 0° inclination angle depicted for time steps of 0.04s. The light gray lines represent the experimentally observed shapes.

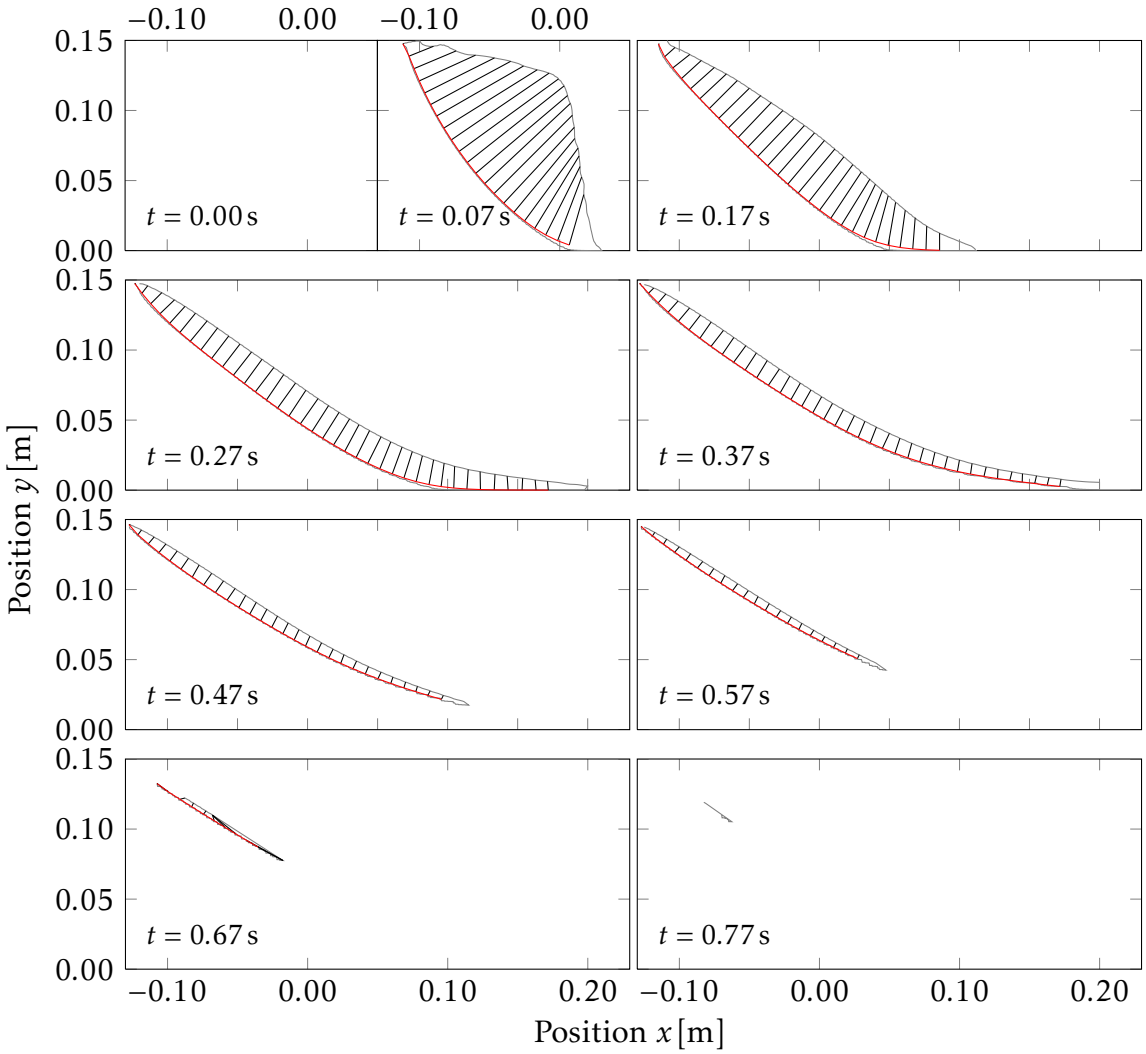

Figure 6.47 – OpenFOAM® simulations of draining of a rectangular container: Shape of fluidized area for 0° inclination angle. The fluidized area of the PVC flow (defined as $\alpha_1 > 0.5$ and $|u| > 0.01 m/s$) is outlined in gray. The solid-fluid interface (red line) is obtained by smoothing of the calculated interface with a running average. Flow heights (black lines) are determined as lines perpendicular to local linear fits to the solid-fluid interface.

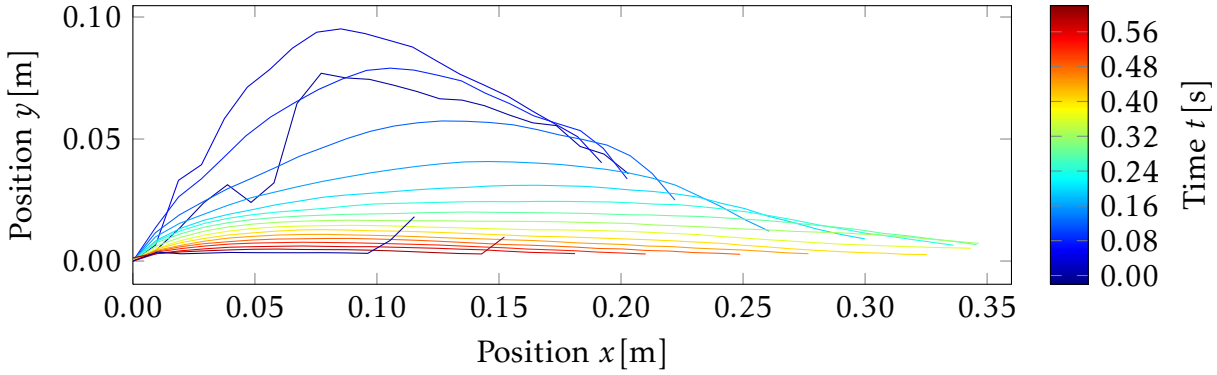

Figure 6.48 – OpenFOAM® simulations of draining of a rectangular container: Temporal evolution of flow height. Simulated temporal evolution of PVC flow height at 0° inclination angle perpendicular to the soilid-fluid interface.

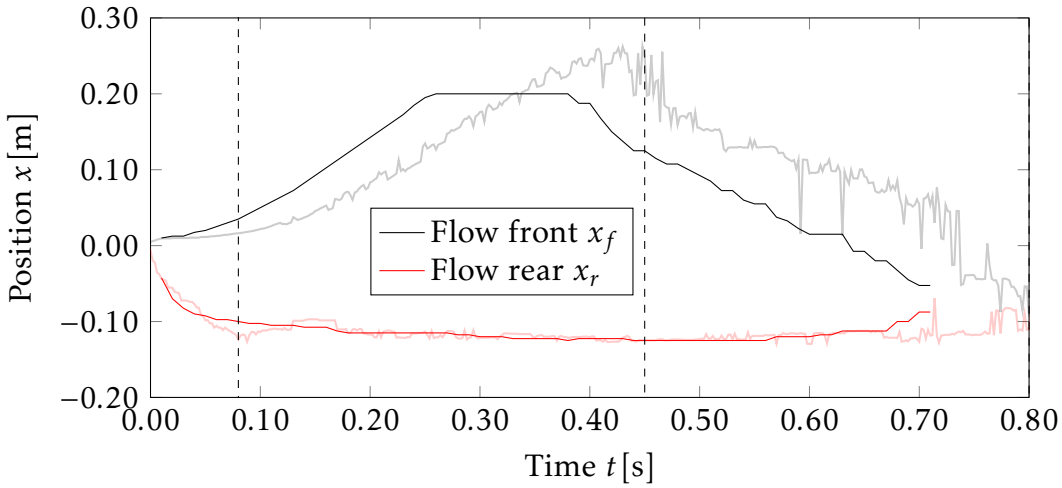

Figure 6.49 – OpenFOAM® simulations of draining of a rectangular container: Flow front and rear position. Simulated temporal evolution of PVC flow front and rear position for 0° inclination angle. Vertical dashed lines mark (from left to right) the initial fluidization phase, the constant outflow phase and the phase in which the mass comes to rest again during the experiment. Experimental data is depicted in light red and gray.

tion (Fig. 6.43). The triangular shape as well as the size increase of this area for higher inclination angles are in good agreement with the experimental observations. Quantitatively, the size of the mobilized fraction is well predicted for 10° and slightly overestimated or underestimated for 20° and 0°, respectively. The shape of the final deposition is well predicted for all inclination angles (Fig. 6.44) as it was already observed for the depth-averaged simulations (Fig. 6.31). Due to the possibility of distinguishing between fluidized and solid phase, the evolution of the maximum flow height can be depicted for the OpenFOAM® simulations (Fig. 6.45). Qualitatively, the evolution of this fluidized fraction is well predicted: the simulations display an exponentially decreasing maximal flow height. Quantitatively the flow height is underestimated by the simulations.

Concerning the shape evolution of the free surface for the 0° case, the simulation yields a good prediction of the first time-steps and is, as suggested by the good prediction of the initial area of motion, able to predict the shape conservation in the beginning. Nevertheless, the spreading of the flow occurs slightly in advance in the simulation (Fig. 6.46). In accordance with this observation, also the shape evolution of the fluidized fraction is well predicted by the simulation, although the height of the flowing fraction is slightly underestimated as described before (Figs. 6.47 and 6.48). Especially the shape and position of the solid-fluid interface are in good agreement with the experiment (Fig. 6.18).

Qualitatively, the spreading of the flow front position into the channel and its subsequent retraction are well predicted by the simulations (Fig. 6.49). Nevertheless, here

again a slight deviation in time scales is observed. As suggested by the good prediction of the solid- fluid interface, the rear position of the flow is exactly predicted by the simulation.

Taken together, the non-depth-averaged simulations with OpenFOAM® are clearly superior to the depth-averaged simulations because they are able to predict velocity profiles and thus right fluidized volumes and the initial area. Additionally, time-scales are better captured.

6.2.3.2 Triangular initial deposit

At the high inclination angle of 50° employed for the dam break with triangular initial deposit , the OpenFOAM® simulations correctly predict the fluidization of the complete material (Fig. 6.50). The velocity profile is also well predicted: the highest velocities are observed at the flow front and at the surface of the flow. A slight difference to the experiment is observed in the shape evolution of the material, which is simulated to spread out stronger than observed in the experiment. This is again a consequence of the stick condition.

The flowing volume evolution over time is qualitatively well described by the simulations but is slightly underestimated (Fig. 6.51). This is a consequence of the incompressibility assumption of the simulation, which does not allow volume increase due to dilatancy. Thus, also the outflow rates for both PVC and sand are underestimated by the simulation. Nevertheless, the tendency of a higher outflow rate for PVC is predicted correctly. Compared to the depth-averaged Savage-Hutter simulations, the initial fluidization is better described by the non-depth-averaged OpenFOAM® simulations. Non of the simulations correctly predicts the outflow rate in the range of the errors. The overestimation of the Savage-Hutter simulations ($1.85\,\mathrm{ls}^{-1}$ for PVC and $0.77\,\mathrm{ls}^{-1}$ for sand) and the underestimation of the OpenFOAM® simulations ($0.62\,\mathrm{ls}^{-1}$ for PVC and $1.43\,\mathrm{ls}^{-1}$ for sand) are in the same range, thus non of the simulations proves to be superior for this parameter.

As suggested by the velocity fields, the OpenFOAM® simulations yield a good prediction of the flow front position (Fig. 6.52), which is not the case for the depth-averaged simulations. The rear of the simulated flow lags behind the experimentally observed rear, again due to the stick condition. Again, it becomes clear that the tendency of a higher outflow rate for PVC is predicted correctly.

The simulated evolution of the free surface shape reveals a good agreement with the experimental data (Fig. 6.53): the shape preservation and the flow height are well predicted. In this, the OpenFOAM® simulations are superior to the depth-averaged simulations. However, they also fail to simulate the projection of material observed in the experiment.

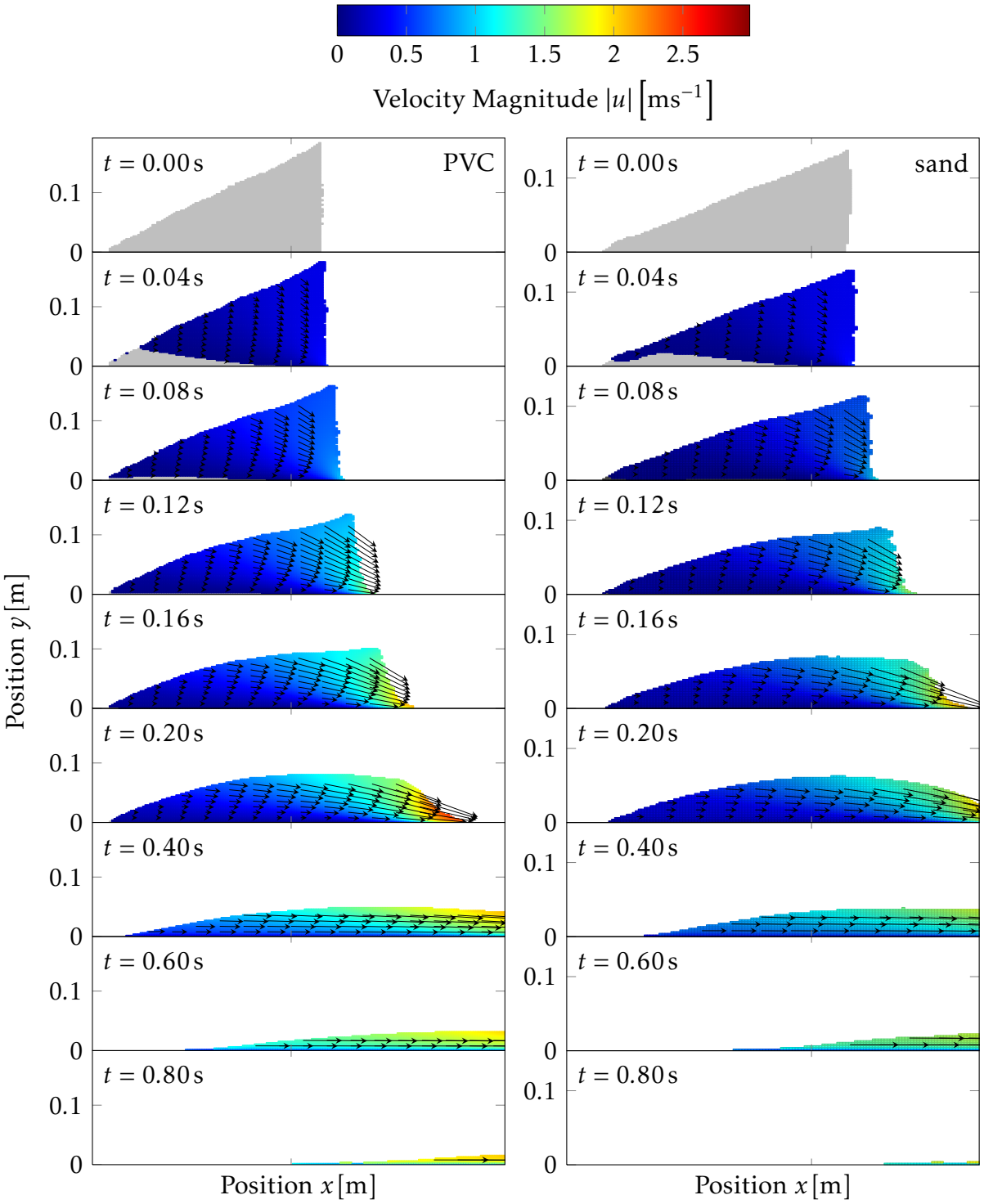

Figure 6.50 – OpenFOAM® simulations of the triangular initial deposit experiment: Overview on velocity fields. Overlay of simulated velocity fields with simulated shape of the granular flow of PVC (left panel) and sand (right panel) particles during the triangular initial deposit experiment at 50° inclination angle. Velocities in single patches corresponding to the numerical grid are represented by a heat map (reaching from blue for the minimal velocity to red for the maximal velocity). Direction of the velocities are depicted by arrows, the length of the arrows corresponds to the magnitude. For a better overview, only arrows for each tenth patch in x-direction and every fourth patch in y-direction are shown.

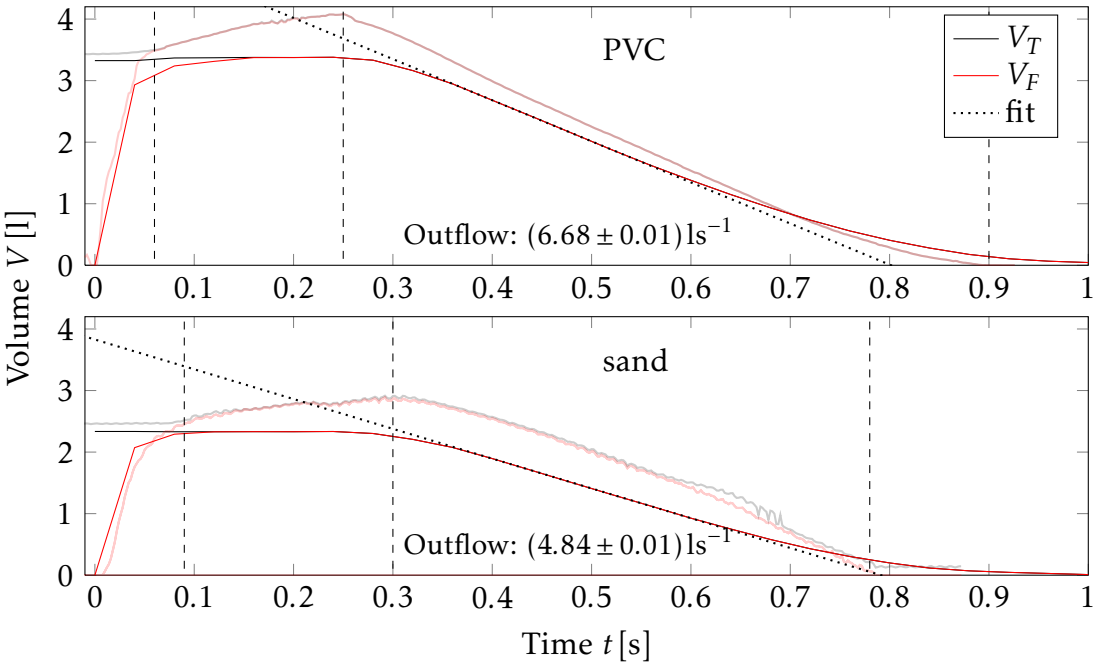

Figure 6.51 – OpenFOAM® simulations of the triangular initial deposit experiment: Temporal evolution of flowing volume. Simulated temporal evolution of the flowing volume fraction (V_F) and the total volume (V_T) during the triangular initial deposit experiment of PVC and sand particles at 50° inclination angle in comparison to the measured volume (depicted in light red and gray). Vertical dashed lines mark (from left to right) the initial fluidization phase, the constant outflow phase and the phase in which the mass leaves the observed area during the experiment. The outflow rate is calculated by a linear fit (black dotted line) to the curve in the constant outflow phase. The respective outflow rates for the simulated curves are given in the graphs.

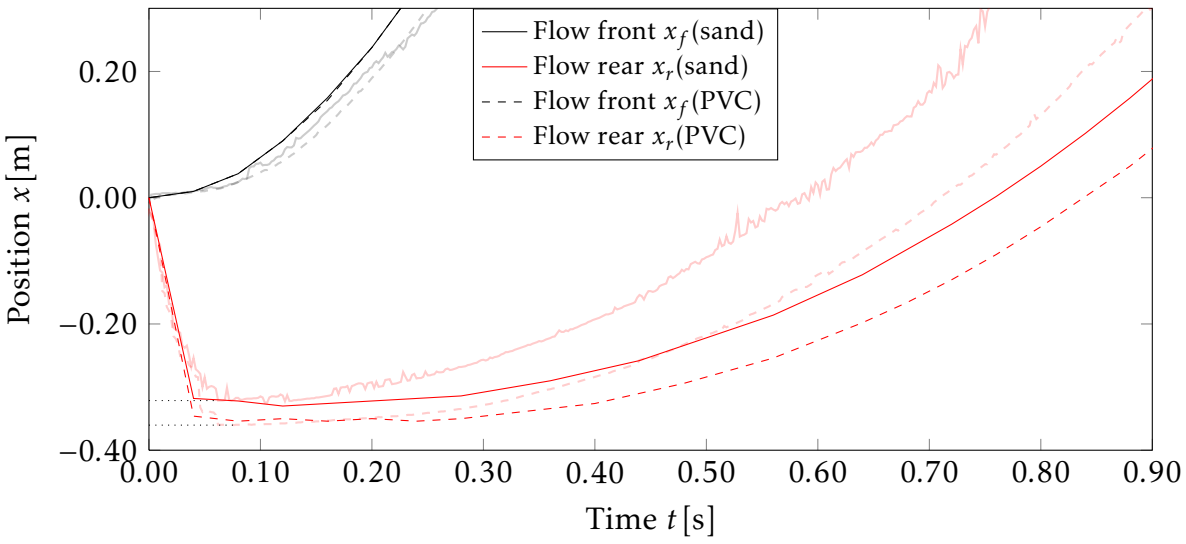

Figure 6.52 – OpenFOAM® simulations of the triangular initial deposit experiment: Flow front and rear position. Simulated temporal evolution of PVC and sand flow front and rear position for 50° inclination angle in comparison to the measured positions (depicted in light red and gray).

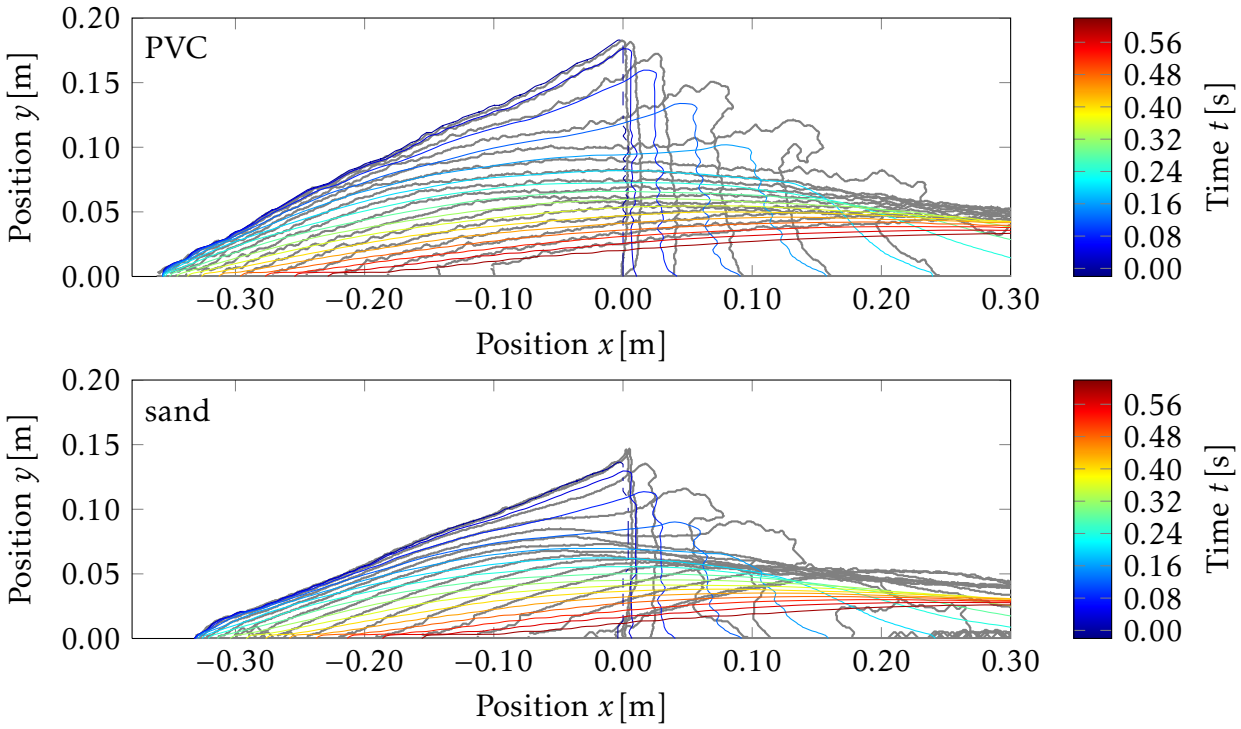

Figure 6.53 – OpenFOAM® simulations of the triangular initial deposit experiment: Temporal evolution of free surface shape. Outline of the free surface during the granular flow of PVC and sand particles at 50° inclination angle depicted for time steps of 0.04 s. Experimentally observed shapes are depicted in gray.

With the non-depth-averaged simulation, it is possible to predict velocity profiles with the OpenFOAM® simulations. The simulated profiles for both PVC and sand at the gate display a striking similarity to the measured profiles (Figs. 6.54 and 6.55). This is also reflected in a very accurate prediction of the strain rate and slip velocity evolution over time. The non-depth-averaged simulations further allow to compare simulated spatial velocity profiles over the complete observed area to the measured profiles (Figs. 6.56 and 6.57). As for the velocity profile at the gate position, a very good agreement between simulations and experiments are observed for PVC and sand. Both the mean velocities and the strain rates depicted by the variance are in good agreement between experiment and simulation.

In summary, the OpenFOAM® simulations are well capable of predicting the velocity profiles for the triangular initial deposit experiment. Strong deviations from the observed behavior are only observed in the flow volume due to the incompressibility assumption in the simulations.

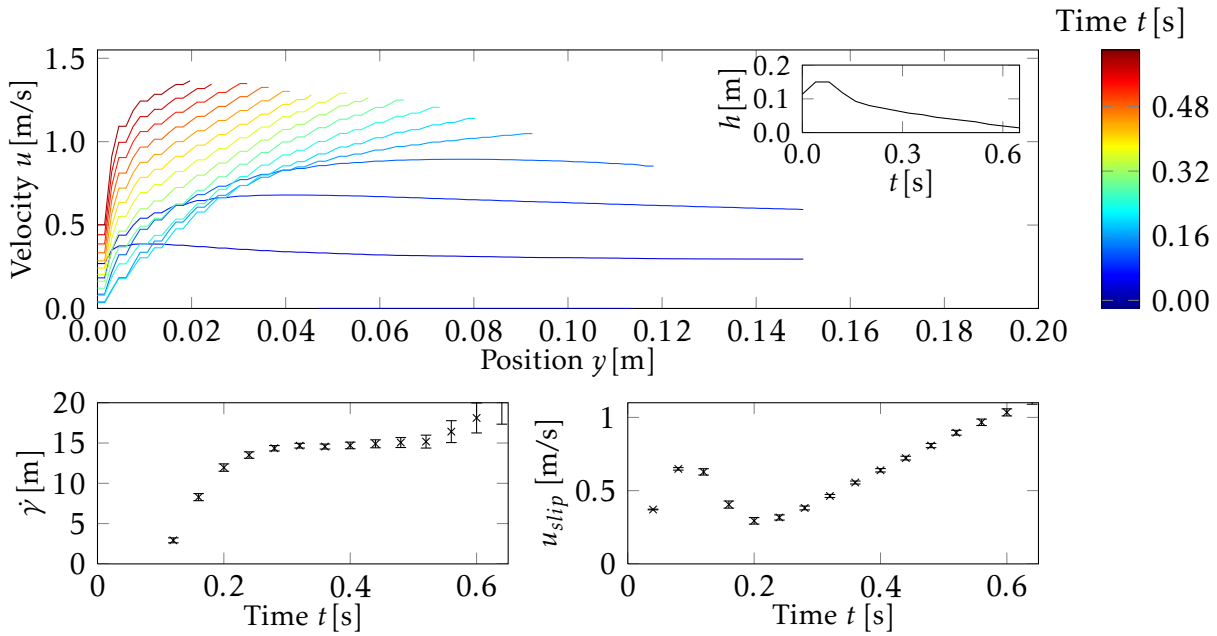

Figure 6.54 – OpenFOAM® simulations of the triangular initial deposit experiment: Velocity profiles at gate position ($x = 0$). Upper panel: Simulated y-direction dependent velocity profiles for the triangular initial deposit experiment experiment with PVC at the position of the gate ($x = 0$). Time steps are color coded as in Fig. 6.53. The included panel in the upper left corner depicts the height evolution of the simulated flow at the gate position. Lower left panel: Strain rate $\dot{\gamma}$ calculated from linear regression fitted to the velocity profiles. Lower right panel: Slip velocity u_{slip} calculated from linear regression fitted to the velocity profiles.

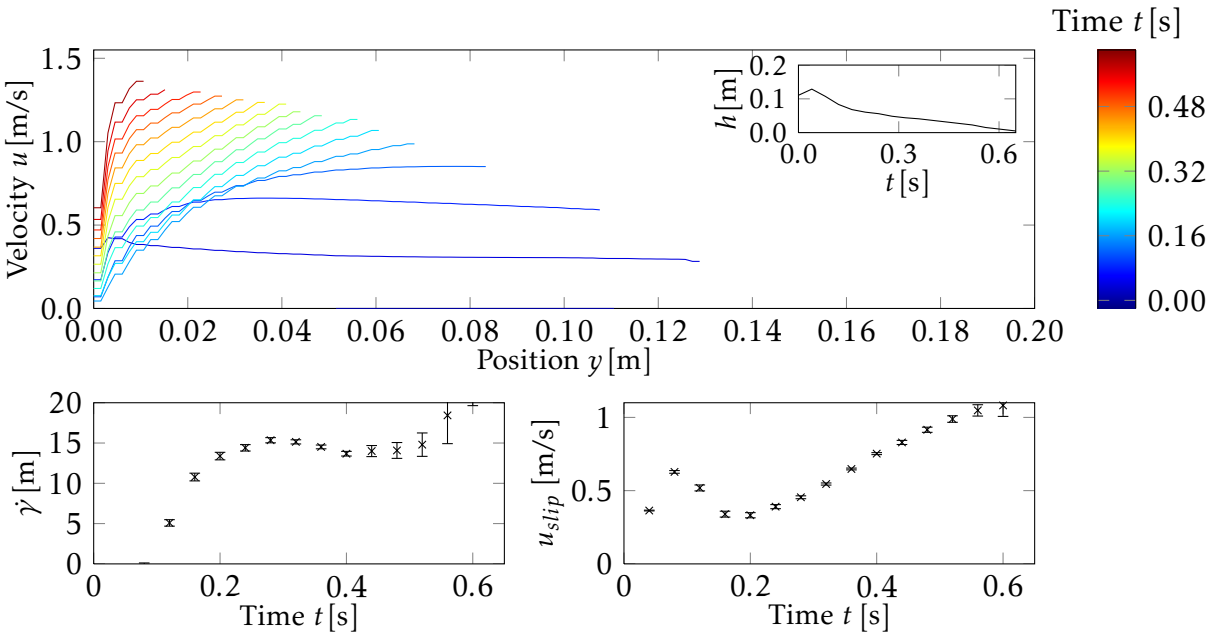

Figure 6.55 – OpenFOAM® simulations of the triangular initial deposit experiment: Velocity profiles at gate position ($x = 0$). Upper panel: Simulated y-direction dependent velocity profiles for the triangular initial deposit experiment experiment with sand at the position of the gate ($x = 0$). Time steps are color coded as in Fig. 6.53. The included panel in the upper left corner depicts the height evolution of the simulated flow at the gate position. Lower left panel: Strain rate $\dot{\gamma}$ calculated from linear regression fitted to the velocity profiles. Lower right panel: Slip velocity u_{slip} calculated from linear regression fitted to the velocity profiles.

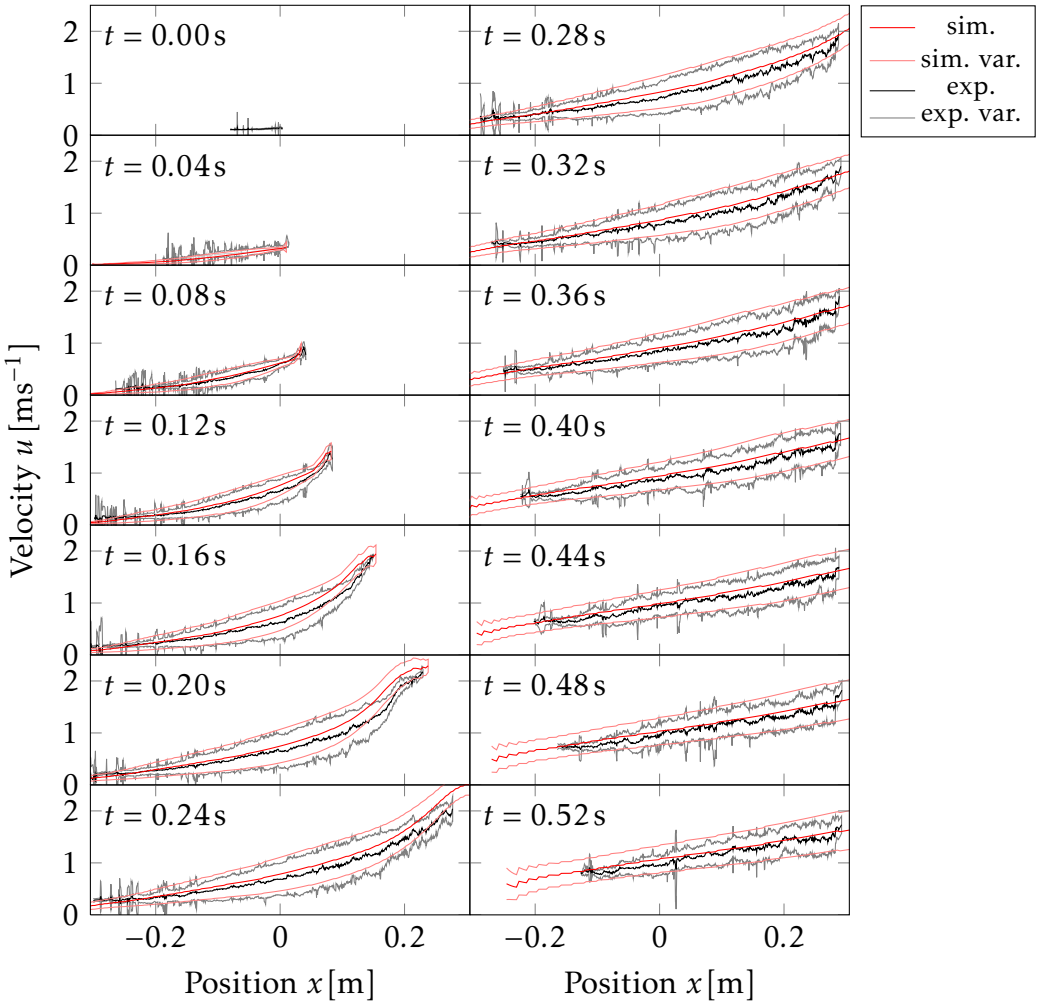

Figure 6.56 – OpenFOAM® simulations of the triangular initial deposit experiment: Temporal evolution of spatial velocity profiles for PVC. Simulated mean velocities over the complete observed area during the triangular initial deposit experiment with PVC are depicted by the red lines, light red lines indicate the variance. Experimentally measured mean velocities are depicted in black with gray variance lines.

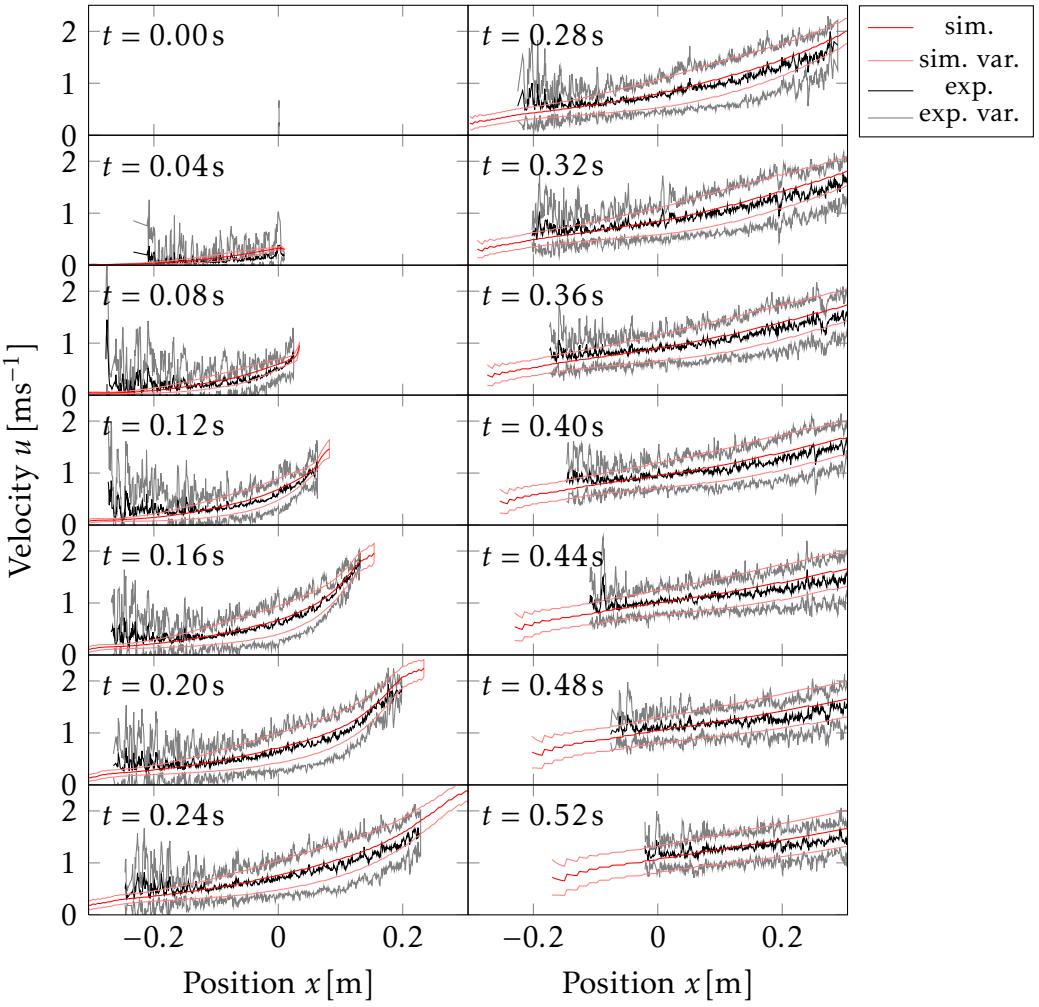

Figure 6.57 – OpenFOAM® simulations of the triangular initial deposit experiment: Temporal evolution of spatial velocity profiles for sand. Simulated mean velocities over the complete observed area during the triangular initial deposit experiment with sand are depicted by the red lines, light red lines indicate the variance. Experimentally measured mean velocities are depicted in black with gray variance lines.

6.3 Undisturbed bottom sliding and velocity profiles

To mimic events taking place during the undisturbed flow of a granular material down a slope, an undisturbed flow of a large volume of material down the channel is considered.

6.3.1 Experimental description

To consider steady-state conditions of an undisturbed flow, the draining of a reservoir filled with 30l of granular material (PVC and sand) at an inclination of $\zeta = 50°$ was recorded (Fig. 6.58). The orifice of the channel had a height of 0.15 m. Here, a clear difference for the two materials is visible: the flow height for sand is lower than for PVC. This observation can be explained by the higher internal friction of sand: it causes stronger energy dissipation through friction between particles during the silo draining and thus a slower emptying of the silo.

First, a sector in 0.55 m to 1.55 m distance to the gate is observed. In Figure 6.59, the height profile and the mean velocities for this area are displayed. The height monotonically decreases from $h(x = 0.6\,\mathrm{m}) = 3.1\,\mathrm{cm}$ to $h(x = 1.5\,\mathrm{m}) = 2.1\,\mathrm{cm}$ for PVC and from $h(x = 0.6\,\mathrm{m}) = 2.4\,\mathrm{cm}$ to $h(x = 1.5\,\mathrm{m}) = 1.6\,\mathrm{cm}$ for sand. Thus, although the sand particles form a thinner steady-state flow, the rate of height decrease is similar for both materials. While the flow height decreases, the mean velocity increases from $u_m(x = 0.6\,\mathrm{m}) = 2.2\,\mathrm{ms}^{-1}$ to $u_m(x = 1.5\,\mathrm{m}) = 3.5\,\mathrm{ms}^{-1}$ for PVC and $u_m(x = 0.6\,\mathrm{m}) = 1.9\,\mathrm{ms}^{-1}$ to a maximum value of $u_m(x = 1.5\,\mathrm{m}) = 2.4\,\mathrm{ms}^{-1}$ for sand. Despite these small differences in the mean values of the velocities for PVC and sand, their values are largely the same in the range of errors. The relatively large observed errors in the height profile can be explained by the diameter of the particles $d = 4\,\mathrm{mm}$ in the case of PVC: depending on the position of the particle at the moment of observation variations of about the radius length are observed. For the sand particles, the PIV recording is less smooth although the particles are smaller $d = 0.71 - 1.25\,\mathrm{mm}$. This can be explained by first the low contrast between the sand and the dark background compared to the high contrast between the background and the white PVC particles. Second, the height profile displays indeed stronger variation in the case of sand, as demonstrated by the detailed recordings of channel sections: due to the resolution limitation of the camera at an observed range of ($s_{m\to px} = 1m/1280px = 7.8125 \cdot 10^{-4}$m/px), no further detailed resolution of the height profile and velocity field are possible. Especially at $x = 1.5$m, the flow height of 2.1 cm is only displayed by 27 Pixels. Therefore, smaller ranges of the channel at ($x_1 = 0.5\,\mathrm{m}$, $x_2 = 1.0\,\mathrm{m}$, $x_3 = 1.5\,\mathrm{m}$) were recorded to enable the necessary high resolution to capture a detailed height and velocity profile of the steady-state flow. As mentioned above, sand displays much stronger variation in the height profile compared to PVC (Fig. 6.59). Apart

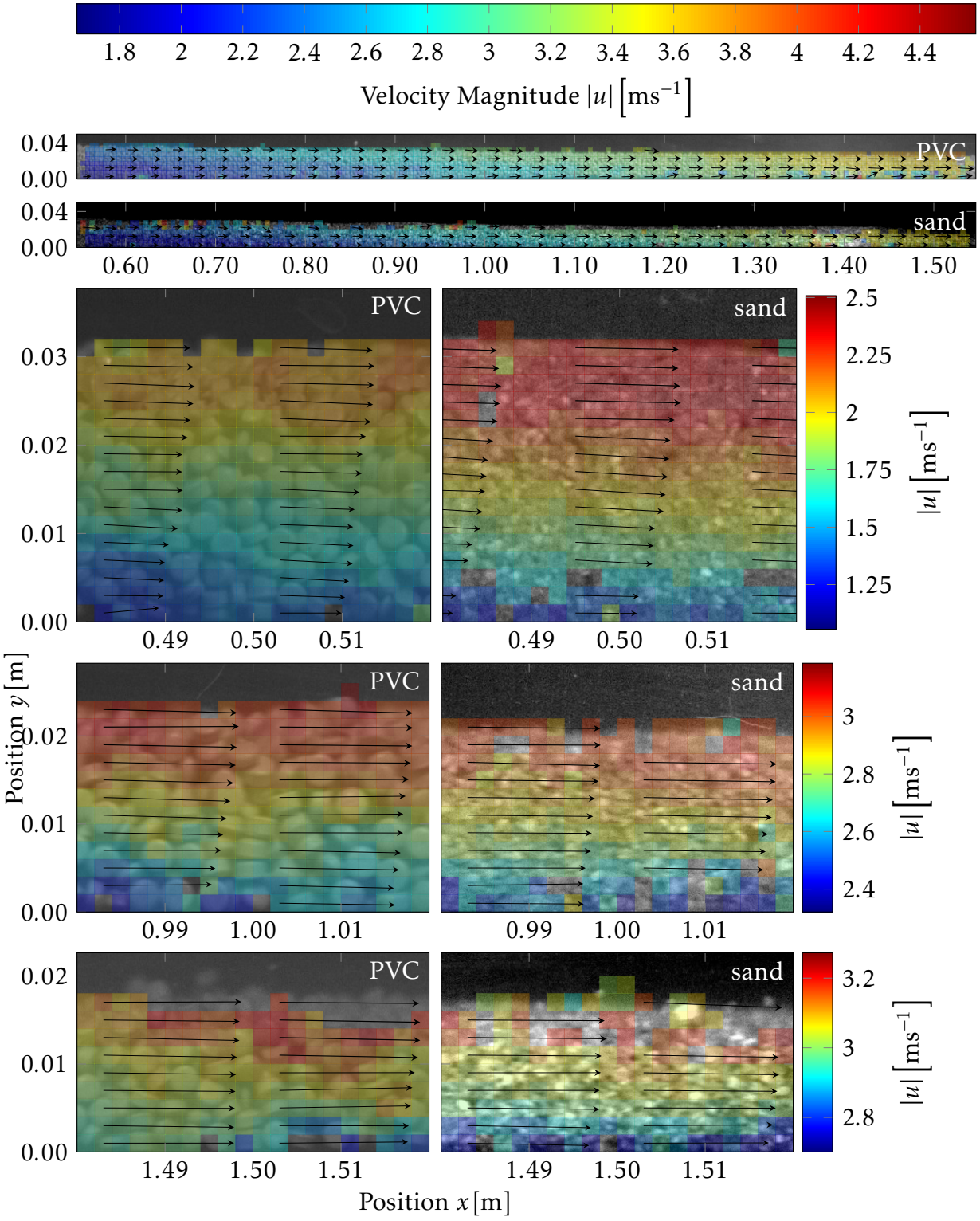

Figure 6.58 – Undisturbed flow: PIV measurements. Overlay of velocity fields measured by PIV with pictures of the granular flow of PVC and sand particles during an undisturbed flow at 50° inclination angle. The two upper panels display an overview on the observed area (1.0 m, starting at 0.5 m distance from the gate) for the two materials. The lower panels represent close up views at 0.5 m, 1m and 1.5 m distance from the gate. Magnitudes of mean velocities in 5 mm x 5 mm patches (upper two panels) and 2 mm x 2 mm patches (lower panels) are represented by a heat map (reaching from blue for the minimal velocity to red for the maximal velocity). Direction of the velocities are depicted by arrows, the length of the arrows corresponds to the magnitude. For a better overview, only arrows for each third patch in x-direction and every other patch in y-direction are shown.

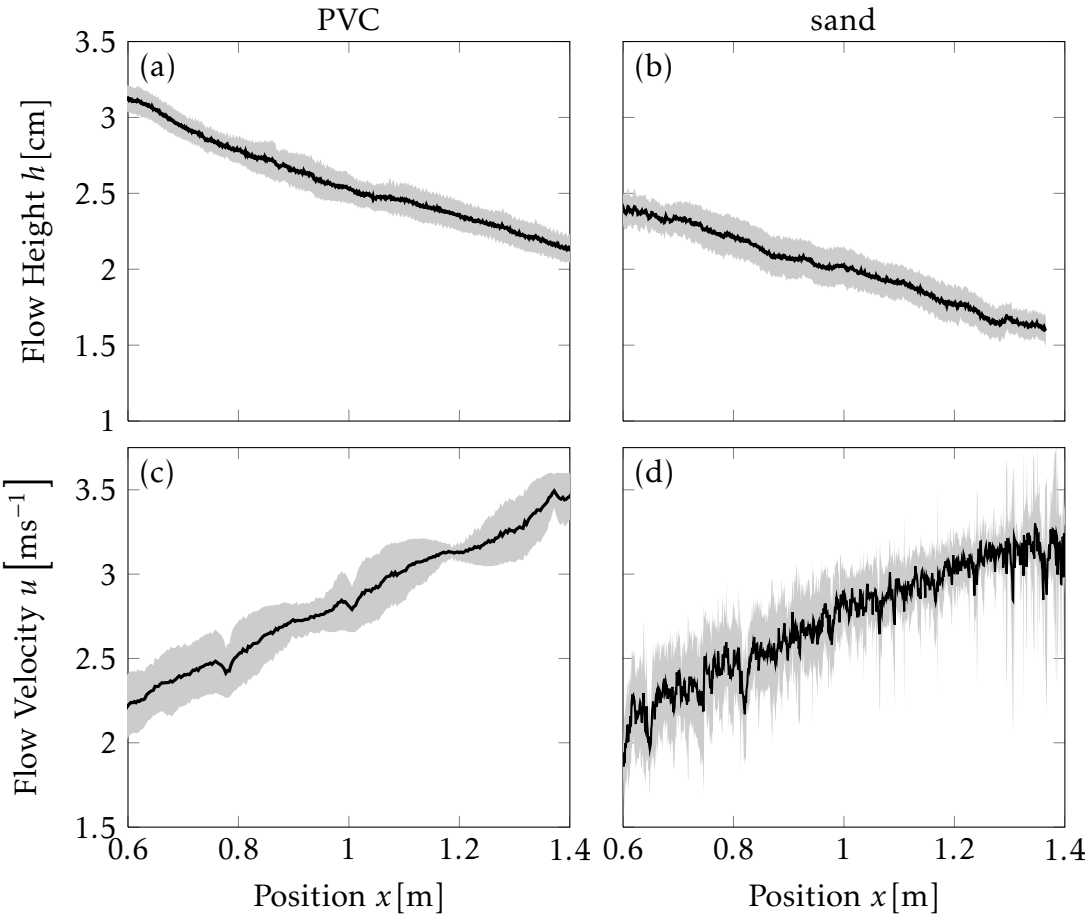

Figure 6.59 – Undisturbed flow: Height and velocity profiles. (a) and (b): Flow height distribution over the observed area for PVC (a) and sand (b). Depicted flow height represents the mean of 500 pictures (one second), error bands represent standard deviation from the mean. (c) and (d): Spatial mean velocity distribution over the observed area for PVC (c) and sand (d) in x-direction (u, parallel to channel). Depicted velocities are mean values of the mean velocities in 500 pictures (one second), error bands represent standard deviation from the mean.

from these variations, the detailed height profiles remain constant over the observed time at all three recorded locations, indicating that indeed a steady-state is observed (Fig. 6.60 (a)). At all three points in the channel a linear velocity profile, which is slightly increasing towards the top of the flow, is observed (Fig. 6.60). It becomes obvious that not only the mean velocities (Fig. 6.59) but also the spatial velocity profiles in y-direction for sand and PVC are the same in the range of the errors. The most important component determining the flow of the whole granular mass is the bottom sliding velocity, which increases from $1.5\,\mathrm{ms}^{-1}$ at 0.5 m to $3.3\,\mathrm{ms}^{-1}$ at 1.5 m (Fig. 6.60 (b)).

For that reason, the next experiment focuses on the slip velocity at the bottom of the channel. The same experiment as described before was recorded from the bottom of the channel at a range form $x = 0\,\mathrm{m}$ to $x = 1\,\mathrm{m}$ and the velocity was determined at

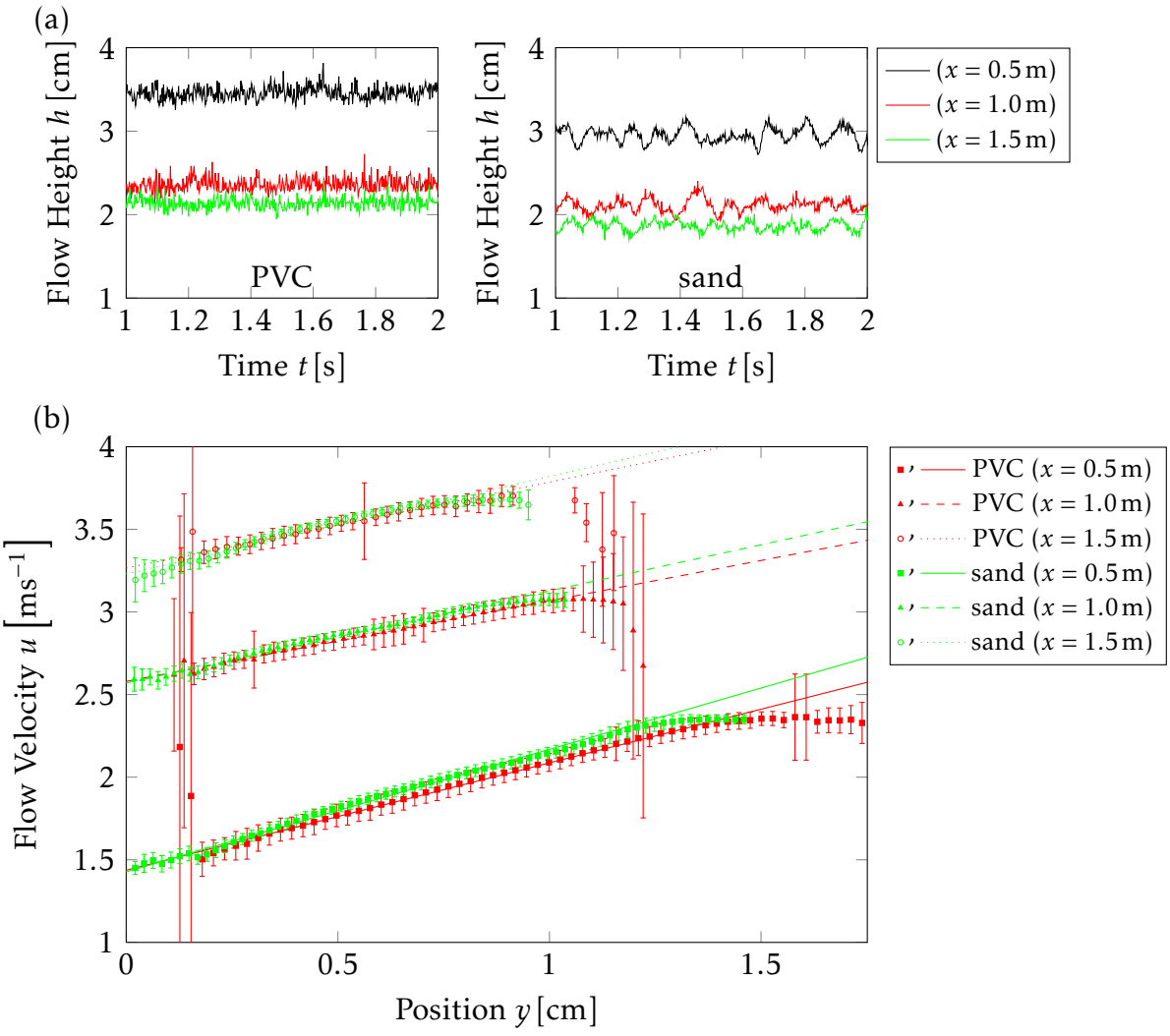

Figure 6.60 – Undisturbed flow: Temporal height evolution and velocity profiles. (a) Temporal flow height evolution at 0.5 m, 1 m and 1.5 m distance from the gate for PVC and sand. (b) Velocity profiles in y-direction (perpendicular to channel bottom) at 0.5 m, 1 m and 1.5 m distance from the gate for PVC and sand. Mean velocities recorded in 500 pictures (one second) are depicted with standard deviations. Straight lines represent a linear fit for each profile.

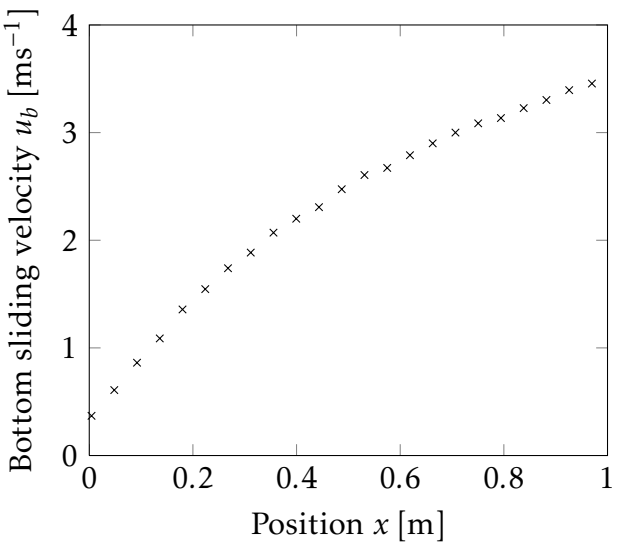

Figure 6.61 – Undisturbed flow: Bottom sliding velocity. The bottom sliding velocity of PVC particles was captured by recording a picture series from below the channel in the same set up as in Fig. 6.58 to 6.60 and applying the PIV method to the pictures. The respective calculated velocities at the middle of the channel bottom are depicted for positions from 0 to 1 m from the gate.

the middle of the channel (Fig. 6.61). This revealed an increasing bottom slip velocity over the observed area, while the acceleration is decreasing over this range, resulting in a square-root function shape of the velocity profile.

6.3.2 Analytical predictions using the Savage-Hutter model

For the simple case of an undisturbed steady-state flow, the Savage-Hutter type model equations can be solved analytically. For this purpose, exact analytical solution of the equations presented by Pudasaini (2011) are employed to compare the resulting calculated flow heights and velocities to the experiments. The equations require the flow height (h_0) and the flow velocity (u_0) at a certain channel position to predict the flow further down an inclined plane:

$$u = 2\sqrt{\frac{1}{3}(2sx - 2sx_0 + u_0^2 + 2\beta h_0)}\cos\left[\frac{\arccos\left\{-\beta h_0 u_0\left(\frac{3}{(2sx-2sx_0+u_0^2+2\beta h_0)}\right)^{\frac{3}{2}}\right\}}{3}\right] \tag{6.1}$$

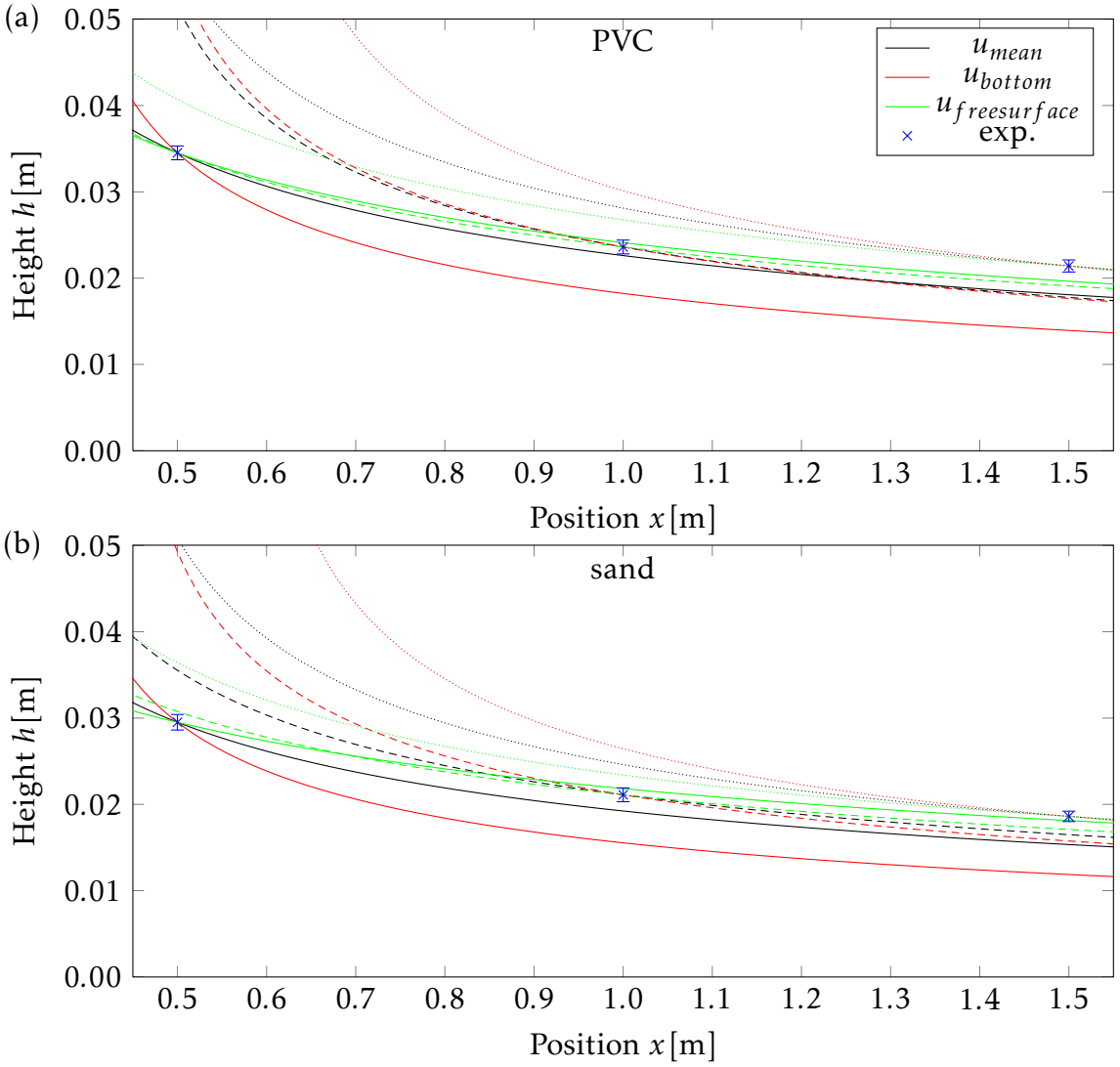

Figure 6.62 – Predictions for spatial undisturbed flow height evolution by analytic solutions of the Savage-Hutter model at distinct points of the undisturbed flow. Spatial height distributions over the area from 0.5 m to 1.5 m distance from the orifice for PVC and sand were calculated employing the measured flow velocities and heights (for detailed procedure see text). The measured flow heights are depicted in blue. Calculations were done for all three experimentally observed points (0.5 m (continuous lines), 1 m (dashed lines) and 1.5 m (dotted lines) distance from the orifice). Velocities employed for the calculation were the mean velocity (u_{mean}), the velocity at the free surface ($u_{freesurface}$) and the velocity at the bottom of the flow (u_{bottom}) at the respective point.

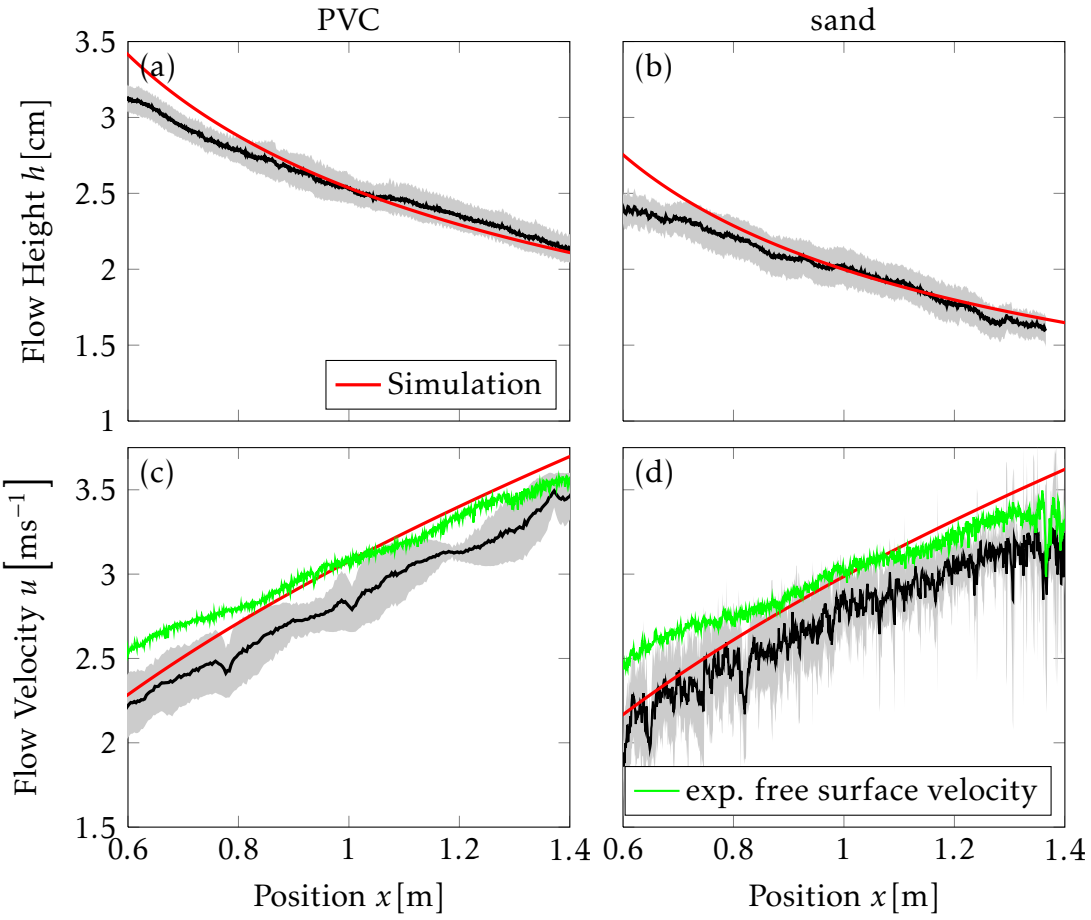

Figure 6.63 – Analytical predictions for spatial undisturbed flow height and velocity evolution by the Savage-Hutter model over 1.5 m undisturbed flow. (a) and (b): Calculated flow height distribution over the observed area for PVC (a) and sand (b) (red line). Experimental data from Fig. 6.59 is included for comparison (black line and gray error bands). (c) and (d): Calculated mean velocity distribution over the observed area for PVC (c) and sand (d) in x-direction (u, parallel to channel) (red line). Experimental data from Fig. 6.59 (black line and gray error bands) and the experimentally observed free surface velocity (green line) are included for comparison .

where u is the depth-averaged down-slope velocity. The material parameters ϕ and δ and the inclination angle ζ are included in this solution via the variable s:

$$s = (\sin\zeta - \tan\delta\cos\zeta) \tag{6.2}$$

and the so-called pressure parameter β, which depends on gravity and the earth pressure coefficient $k_{\text{act/pass}} = k_{\text{act/pas}}(\phi,\delta)$:

$$\beta = gK\cos\zeta. \tag{6.3}$$

The comparison of the Savage-Hutter simulations for the dam break scenarios at

$\zeta = 50°$ inclination angle with the experimental findings suggests that the simulated mean velocities rather agree with the free surface velocities than with the basal velocities (see section 6.2.2.2). For this reason, not only the experimentally observed bottom sliding velocity but also the free surface and mean velocities were considered for the analytical description of the undisturbed flow. By inserting the measured velocities and height values at one point of the channel in the equations presented above, the height evolution over the complete observed area can be determined ($h = u_0 h_0 / u$). A separate height evolution is calculated for each of the three considered points in the detailed measurements (at distances 0.5, 1 and 1.5 m from the gate) (Fig. 6.62). These height evolutions can now be evaluated according to their precision in predicting the correct flow height at the other two points. As suggested by the results of the dam break experiments, the free surface velocity at one point is suited best to predict the flow height at the other two points for both sand and PVC. In the case of PVC, the values calculated using the first two points precisely predict the respective other points, while a slight deviation is observed for the third point. For sand, the values of the first point allow a prediction of both other points in the range of the errors.

To evaluate the predictive power of the calculations over the complete observed area, height and velocity evolution for PVC and sand is concerned using the measured height and free surface velocity at 1 m distance as h_0 and u_0 (Fig. 6.63). Except for the first 20 cm, the calculations fits to the measured flow height in the whole observed area within the error range for both PVC and sand. A similar observation is made for the velocities: in the first 20 cm the calculated velocities rather represent the mean velocities, while they yield a good prediction for the free surface velocity in the other parts of the observed area.

Taken together, the results demonstrate that the height and velocity evolution of a simple, undisturbed steady-state flow can be described analytical solution for the Savage-Hutter type model. Nevertheless, precise predictions are only possible when taking the free surface velocity as input for the calculations.

6.3.3 Non-depth-averaged simulations

The non-depth-averaged simulations with OpenFOAM® allow to predict velocity profiles for the undisturbed flow in y-direction. For this purpose, the measured velocity profiles at 0.5 m distance from the gate where used as starting conditions to predict the profiles at 1 m and 1.5 m distance from the gate (Fig. 6.64). Here, it has to be noted that the simulated velocities are zero at the bottom due to employed stick condition. Apart from this difference to the experiment, the linear character of the velocity profiles is well predicted from a height of 0.7 cm on. Regarding the slope of the velocity profile, a very good agreement is observed between the experiment and the simulations at 1 m distance

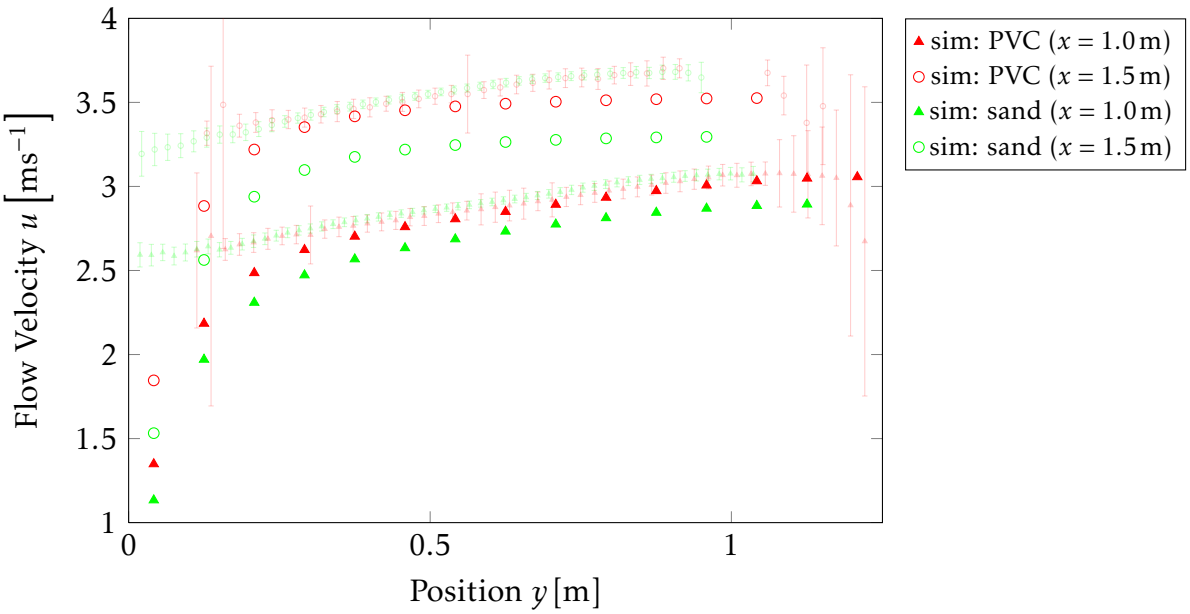

Figure 6.64 – OpenFOAM® simulations of undisturbed flow: Velocity profiles in y-direction. Simulated velocity profiles in y-direction (perpendicular to channel bottom) at 0.5 m, 1 m and 1.5 m distance from the gate for PVC and sand. For comparison the experimentally observed velocity profiles are included (light green and light red).

from the gate for both PVC and sand. At 1.5 m distance, the simulated profile displays a lower slope compared to the experiment. Concerning the amplitude of the velocity, the simulations for PVC at both positions are in good agreement with the measured profiles, while the velocity of sand is underestimated by the simulation. Thus, the simulation is not able to predict the material independent flow behavior observed for this experiment. This is likely caused by the stick condition, which assumes the bottom friction angle to be equal to the internal friction angle. The higher internal friction angle of sand thus has a stronger influence and decelerated the simulated flow to strong.

When concerning the broader view on the channel over one meter flow, the simulation well predicts both the flow height and the mean velocity for PVC and sand (Fig. 6.65). The velocity is slightly underestimated but within the variation band the measurements and simulations agree well. Differences in the broadness of the variation band can be either explained by the higher density of concerned points in the simulation or by the strong variation in the simulated velocity profiles caused by the stick condition.

Taken together, the simulation are able to predict velocity profiles in an undisturbed flow but with some inaccuracy due to the employed stick condition.

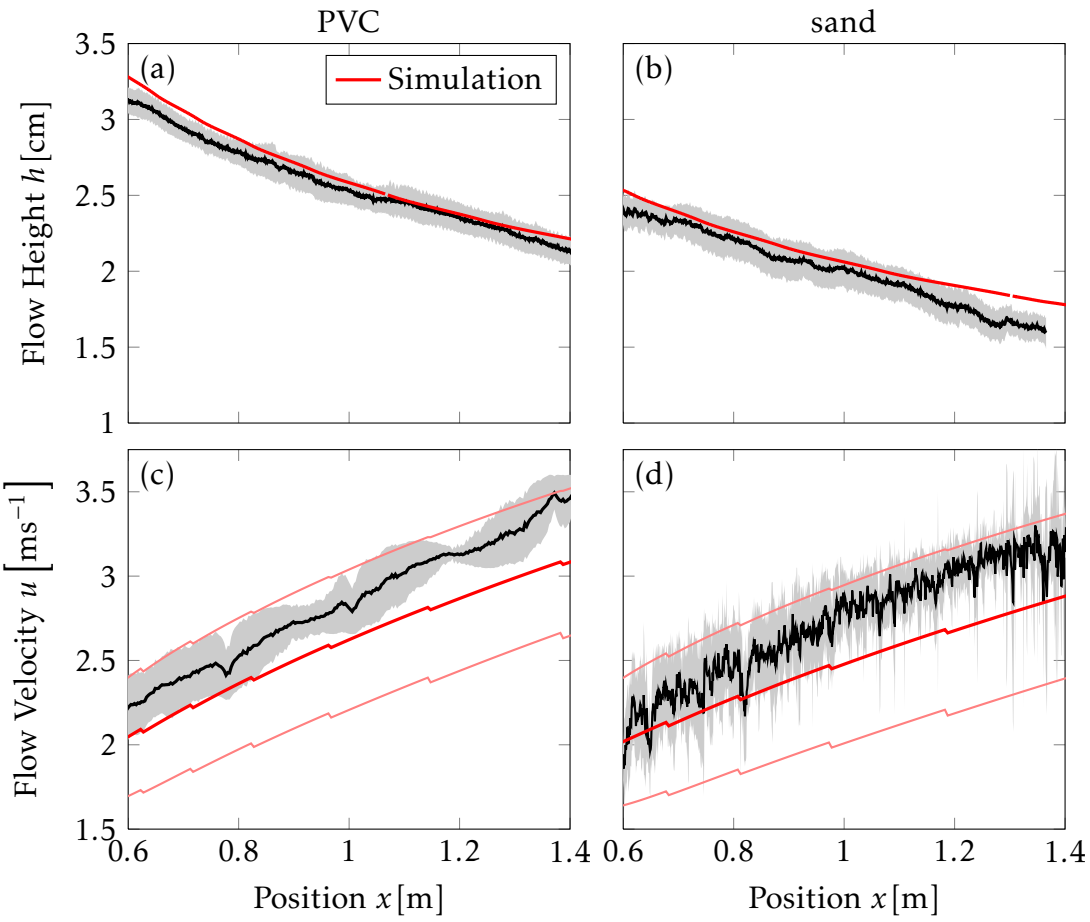

Figure 6.65 – OpenFOAM® simulations of undisturbed flow: Height and velocity profiles. (a) and (b): Simulated flow height distribution over the observed area for PVC (a) and sand (b) (red line). Experimental data from Fig. 6.59 is included for comparison (black line and gray error bands). (c) and (d): Simulated mean velocity distribution over the observed area for PVC and sand in x-direction (u, parallel to channel) (red line, light red lines represent standard deviation from the mean. Experimental data from Fig. 6.59 is included for comparison (black line and gray error bands).

6.4 Obstacle inside channel

As a first case of an obstacle encountered by the granular flow in the channel, an obstacle which can be completely overcome by the material is considered. Therefore, a flow at $\zeta = 50°$ as described in section 6.3 is slowed down by an obstacle decreasing the inclination to 5° on a section of 17 cm at a position of 76 cm down the channel (Fig. 6.66). With this experimental set-up, the granular flow is disturbed but not stopped, similar to the situation found when an avalanche flows over a protection construct built over a road along a mountain side.

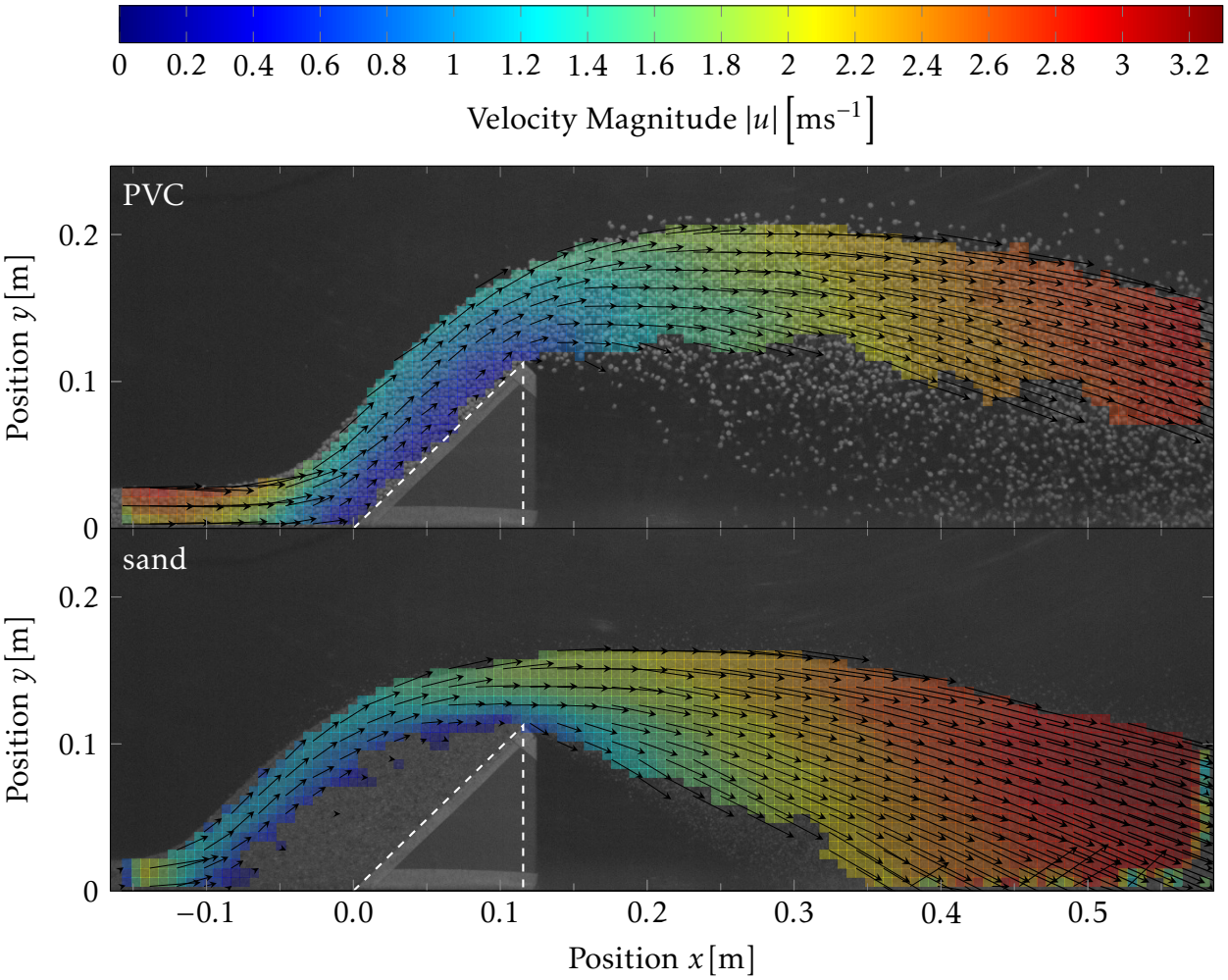

Figure 6.66 – Encountering of an obstacle: PIV measurements. Overlay of velocity fields measured by PIV with pictures of the granular flow of PVC and sand particles for a flow encountering an obstacle at 50° inclination angle. The obstacle surface (dashed white line) decreases the inclination to 5° for a path lenght of 17 cm starting at 76 cm distance from the orifice. Magnitudes of mean velocities in 5 mm x 5 mm patches are represented by a heat map (reaching from blue for the minimal velocity to red for the maximal velocity). Direction of the velocities are depicted by arrows, the length of the arrows corresponds to the magnitude. For a better overview, only arrows for each third patch in x-direction and every other patch in y-direction are shown. Note that in this section x-coordinates are 0 at the starting point of the obstacle.

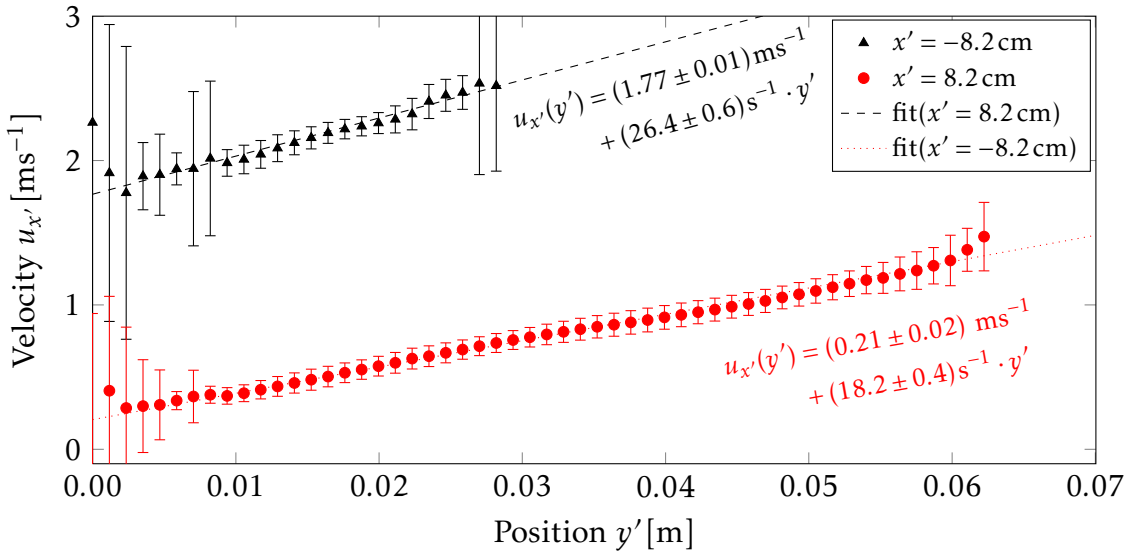

Figure 6.67 – Encountering of an obstacle: Velocity profiles for PVC. Spatial mean velocity distribution in y'-direction in front of the obstacle (black line, $x' = -8.2$ cm) and on the obstacle (red line, $x' = 8.2$ cm), where the x'-coordinate follows the bottom profile including the obstacle and y' is perpendicular to this profile. Depicted velocities are mean velocities in 630 pictures (one second), error bars represent standard deviation from the mean. Dashed and dotted lines and respective equations represent a linear fit to the measured values.

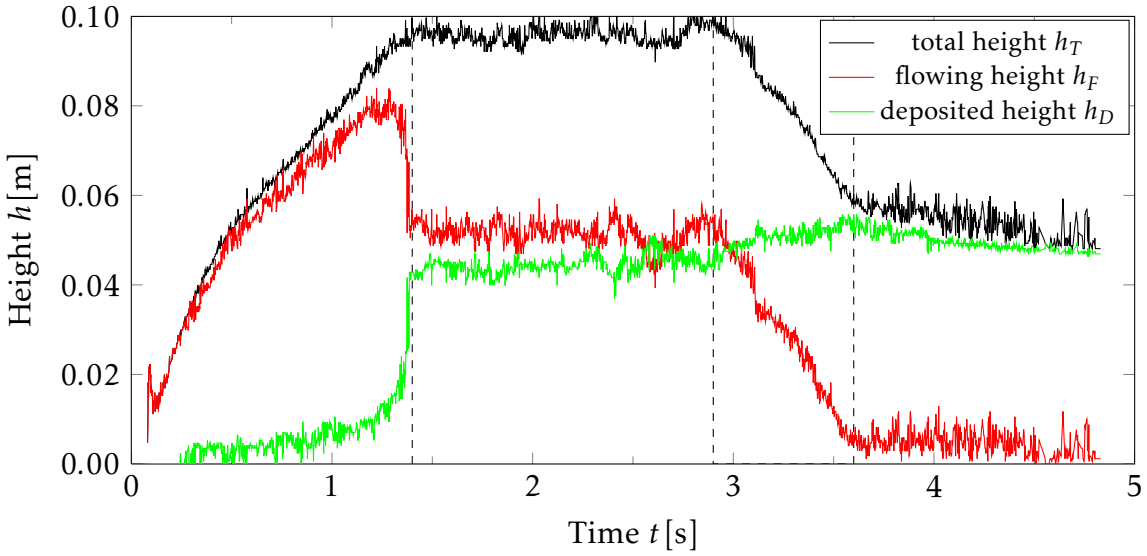

Figure 6.68 – Encountering of an obstacle: Temporal evolution of sand height profiles in front of the obstacle. Temporal height evolution of total material (black line), flowing fraction (red line) and deposited fraction (green line) at position $x' = -5$ cm.

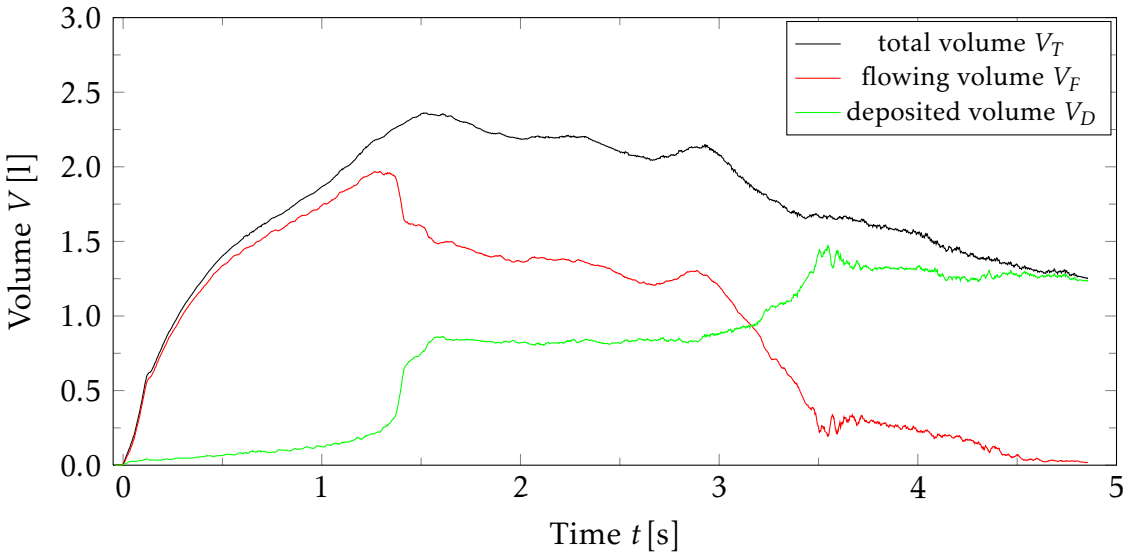

Figure 6.69 – Encountering of an obstacle: Temporal evolution of sand volumes. Temporal volume evolution of total material (black line), flowing fraction (red line) and deposited fraction (green line) in an area reaching from $x' = -16.5\,\text{cm}$ to the end of the obstacle.

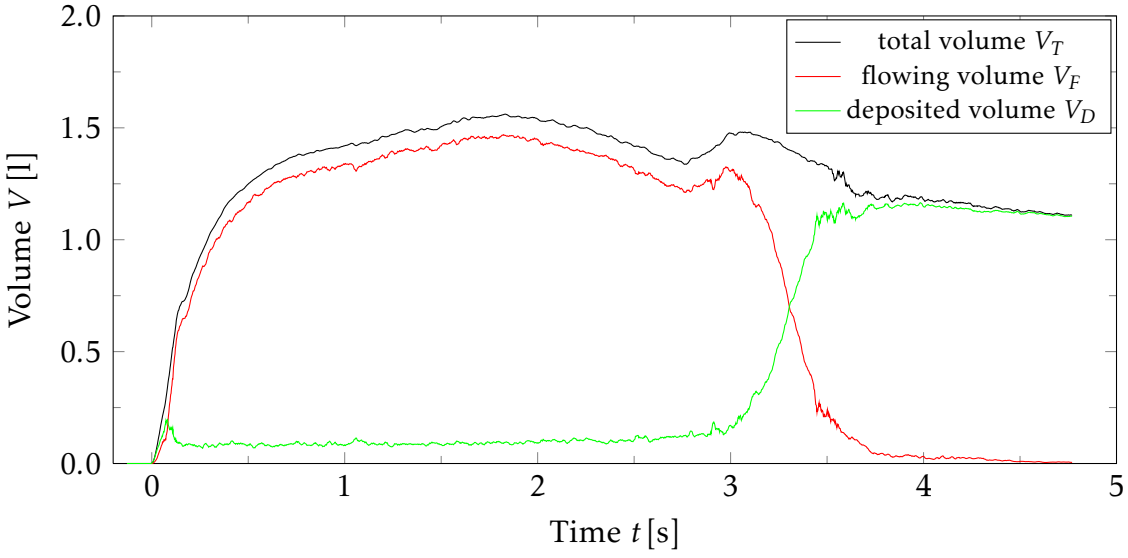

Figure 6.70 – Encountering of an obstacle: Temporal evolution of PVC volumes. Temporal volume evolution of total material (black line), flowing fraction (red line) and deposited fraction (green line) in an area reaching from $x' = -16.5\,\text{cm}$ to the end of the obstacle.

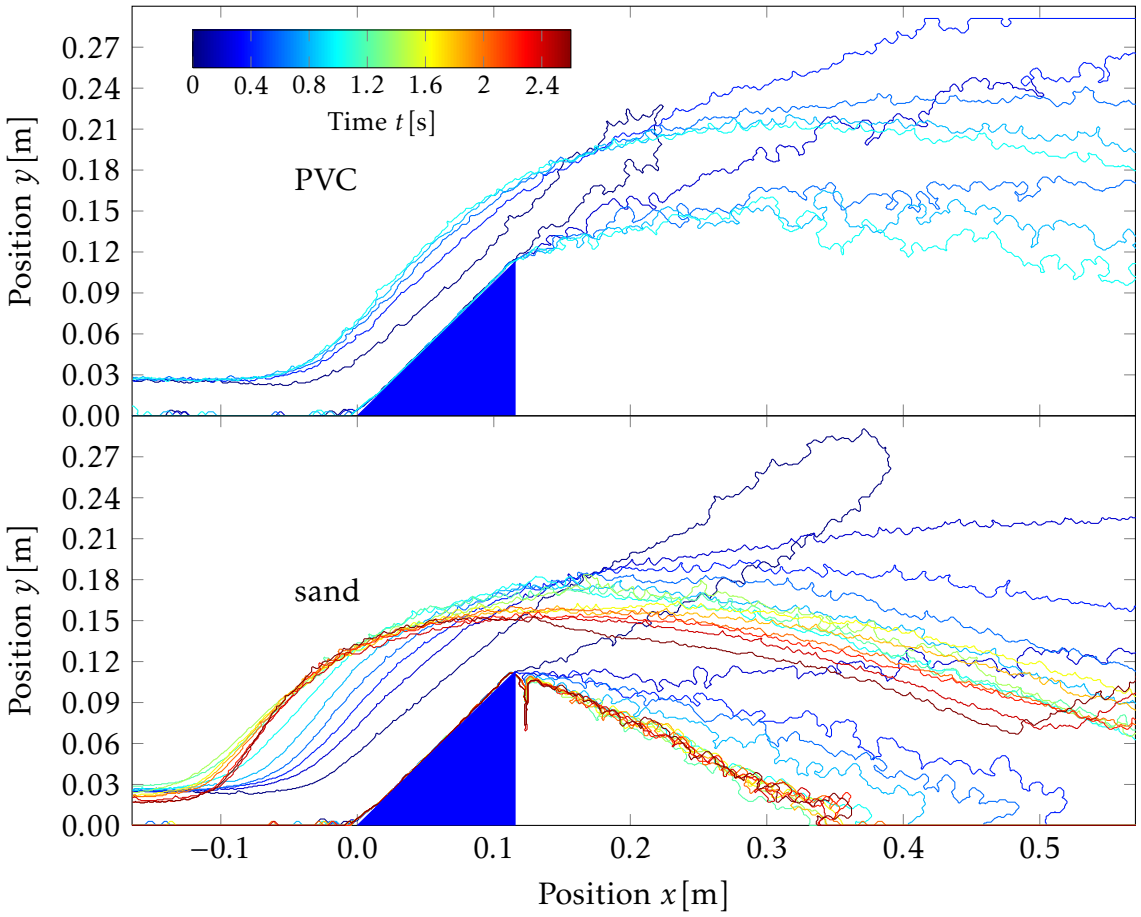

Figure 6.71 – Encountering of an obstacle: Temporal evolution of flow shape. Temporal evolution of the flow outline for PVC and sand during the first seconds of the experiment.

6.4.1 Experimental findings

Here, two clear differences between the behavior of PVC and sand are observed. First, the PVC flow is distracted stronger and returns to the channel bottom further down the channel compared to the sand flow. Second, while the PVC stays completely fluidized, a deposit is formed in front of the obstacle in the case of sand (Fig. 6.66). Due to this fact, different parameters have to be considered for the two cases.

For PVC, the velocity profile before the impact and during the flow over the obstacle can be considered (Fig. 6.67). As displayed in the PIV images (Fig. 6.66), the flow is slowed down when hitting the obstacle and thus the height increases. The spatial profile remains unchanged in linear form but with a higher strain rate on the obstacle ($(18.2 \pm 0.4)\mathrm{s}^{-1}$ before the obstacle and $(26.4 \pm 0.6)\mathrm{s}^{-1}$ on the obstacle). To describe the formation of the deposition in the case of sand, the height profile over time and its fluid and solid fraction at a position 5 cm in front of the obstacle ($x = -5\,\mathrm{cm}$) are considered (Fig. 6.68). Deposition of material occurs suddenly after about 1.5 s and remains almost constant for the rest of the considered time. For about 1.5 s a steady-state flow is es-

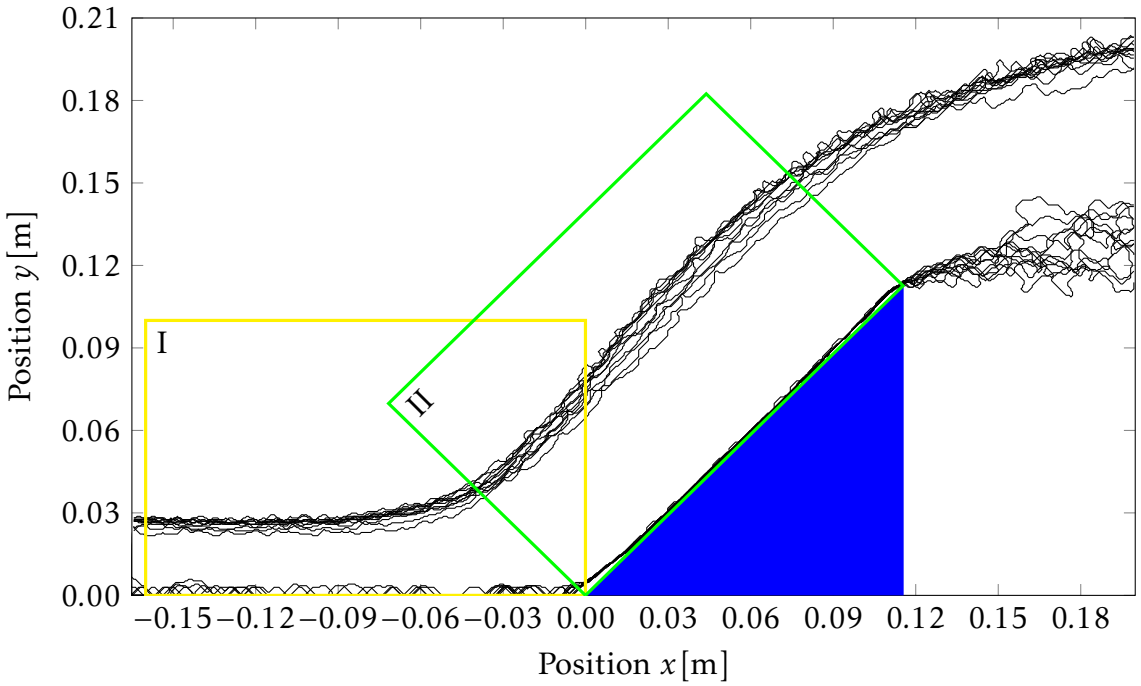

Figure 6.72 – Encountering of an obstacle: Flow geometry during steady state flow of PVC. Flow geometry in the observed area at several time points during the steady state flow phase of quasi constant flow height. The yellow and green boxes mark the areas which are considered in detail in Fig. 6.74.

tablished in which a constant height of the fluidized material is observed. To illustrate the evolution of the deposition, the evolution of the total volume and its fluid and solid fractions are considered for both PVC and sand (Figs. 6.69 and 6.70). For sand similar results as for the height evolution at one position are obtained. After 1.3 s the deposition is formed and remains constant over the steady-state flow phase. Towards the end of the experiment the deposited volume increases. This can be explained by the decrease in material flowing down the channel towards the end of the experiment, which leads to a decrease in pressure. The PVC graphic illustrates that a final deposition at the end of the experiment is formed suddenly after about 3 s and then remains constant after about 4 s, similar to the formation of the sand deposition during the flow.

Next, the geometry of the flow is further investigated. To analyze the events during the first time-steps after encountering the obstacle before the steady-state flow is reached, the flow geometry evolution over the entire observed area is considered for both PVC and sand (Fig. 6.71). In the first time steps, the flow is much thinner than in the steady-state period, resulting in a lower pressure at the bottom of the flow. This results in a reduced bottom friction and thus in stronger distraction of the material by the obstacle. This observation underpins the importance to consider initial processes in addition to steady-state flows, since the three dimensional space affected by the flow is larger during the first time-steps (the material “jumps” higher during the initial phase).

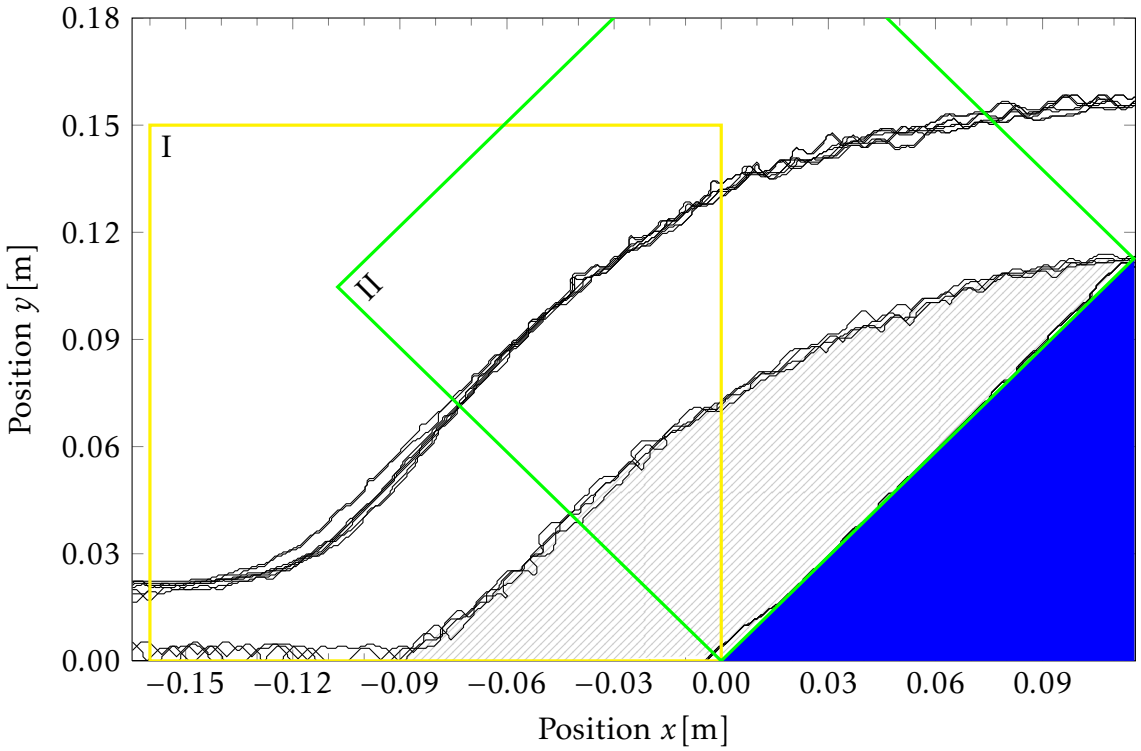

Figure 6.73 – Encountering of an obstacle: Flow geometry during steady state flow of sand. Flow geometry in the observed area at several time points during the steady state flow phase of quasi constant flow height. The yellow and green boxes mark the areas which are considered in detail in Fig. 6.75. The hatched area marks the deposit of sand in front of and on the obstacle.

The flow geometry during the steady-state flow (Figs. 6.72 and 6.73) reveals that no sharp shock front is formed. Considering the height profile of PVC measured perpendicular to the channel bottom (Fig. 6.74), a smooth increase in height towards the obstacle is observed. The increase starts 6 cm in front of the obstacle, marking the position at which the influence of the obstacle on the flow becomes evident. In contrast to that, the height profile perpendicular to the obstacle surface is almost constant over the complete surface.

Because of the deposition during the sand experiment, again the complete material and its solid and fluid fraction are considered for the height profiles perpendicular to the channel bottom and the obstacle surface (Fig. 6.75). Here, the flow thickness begins to increase at 12 cm upstream from the obstacle, indicating that the obstacle effects the sand flow much earlier in the channel than the PVC flow. Deposit formation starts at -9 cm and again a smooth increase in height both for the complete material and the deposit are observed. The height of the fluid fraction remains constant over the complete length of the obstacle, while the height of the deposition smoothly decreases starting at position $x' = 6$ cm (Fig. 6.75).

Calculation of the strain rate and slip velocity for PVC in the two areas (Fig.6.76)

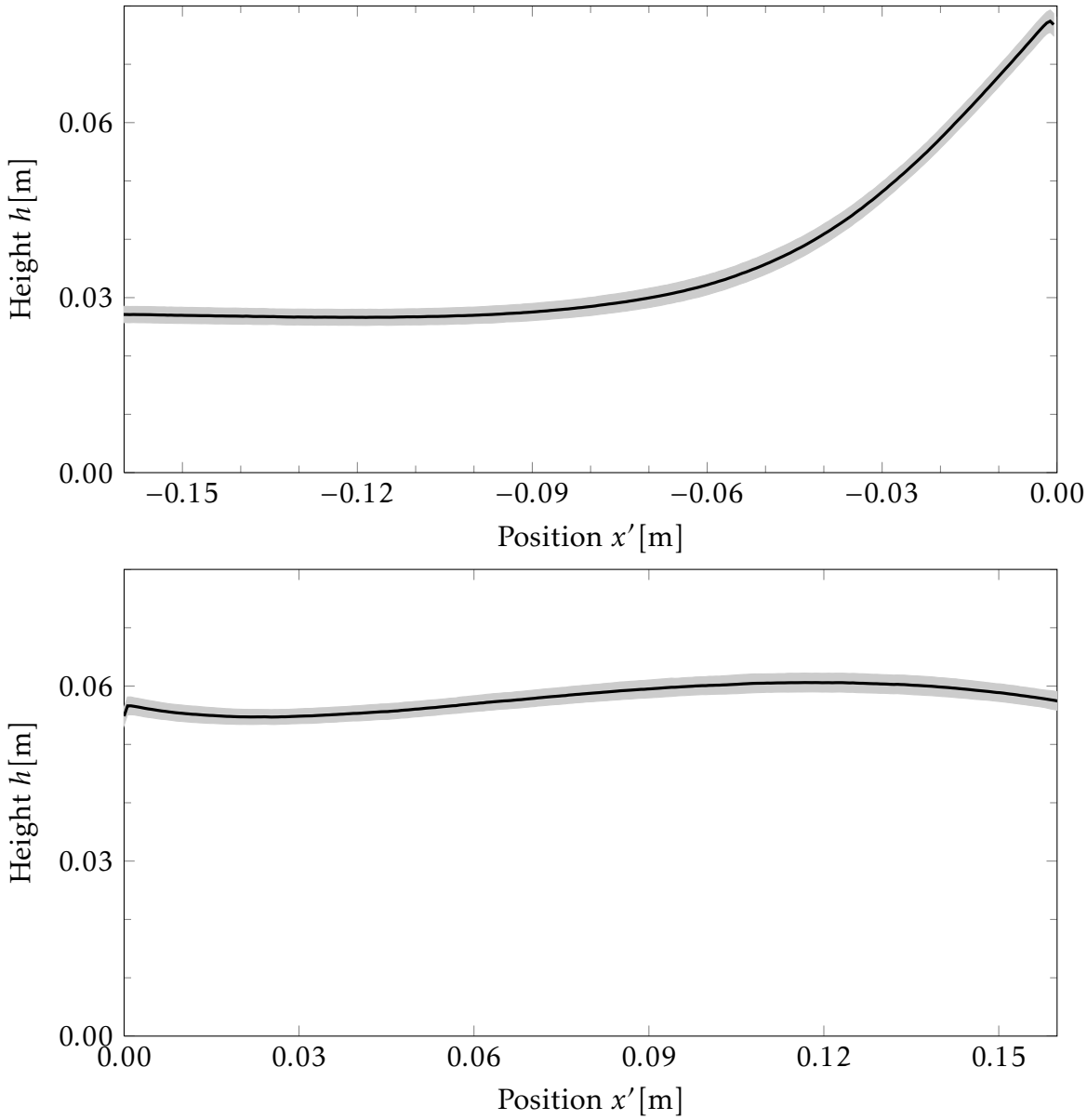

Figure 6.74 – Encountering of an obstacle: Flow height during steady state flow for PVC in areas I and II. Detailed view on the flow height profile in the two boxes indicated in Fig. 6.72. Upper panel depicts the height profile in front of the obstacle (yellow box in Fig. 6.72), lower panel corresponds to the green box. Depicted heights are mean values of 630 pictures (one second), error bands represent standard deviation from the mean.

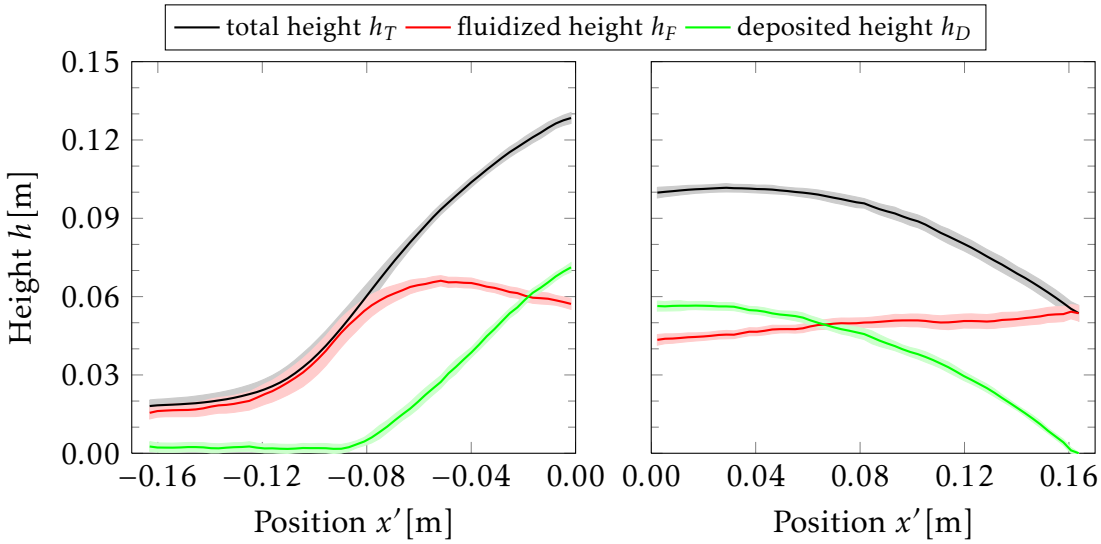

Figure 6.75 – Encountering of an obstacle: Flow height during steady state flow for sand in areas I and II. Detailed view on the flow height, deposit height and total material height in front of the obstacle (left panel, corresponding to yellow box in Fig. 6.73) and on the obstacle (right panel, corresponding to green box in Fig. 6.73) for the sand experiment. Depicted heights are mean values of 630 pictures (one second), error bands represent standard deviation from the mean.

reveals that although the height increases just from -6 cm on (Fig. 6.74), the decrease in slip velocity is already observed at -13 cm. As a consequence of the deceleration an increase in strain rate is visible at -13 cm as well. This suggests effects of the obstacle starting at about -13 cm. At -6 cm the decreasing velocity is no longer compensated by a higher strain rate but by the increase in flow height and the strain rate begins to decrease again. On the obstacle, the flow is slowly accelerated until it reaches velocity values as observed before influenced by the obstacle. The strain rate decreases steadily on the obstacle and reaches its initial value towards the end of the obstacle. Due to the deposit formation in the sand case, calculations of strain rates and slip velocities do not make sense here for sand.

6.4.2 Savage-Hutter simulations

For Savage-Hutter type models, curvature radii have to be higher than the flow height. With this restriction, a simulation of the abrupt change in inclination caused by the obstacle in the experiment is not possible. Therefore, simulations are performed using the F_B function described in section 3.2 and adding up the height of the obstacle to the bottom surface of the channel. Resulting flow heights and velocities predicted by this method are depicted in Figure 6.77. It becomes obvious, that the results are largely independent of the material and accordingly of the internal friction angle. Both height and velocity evolution differ only in their initial values, but stay the same relative to each other during

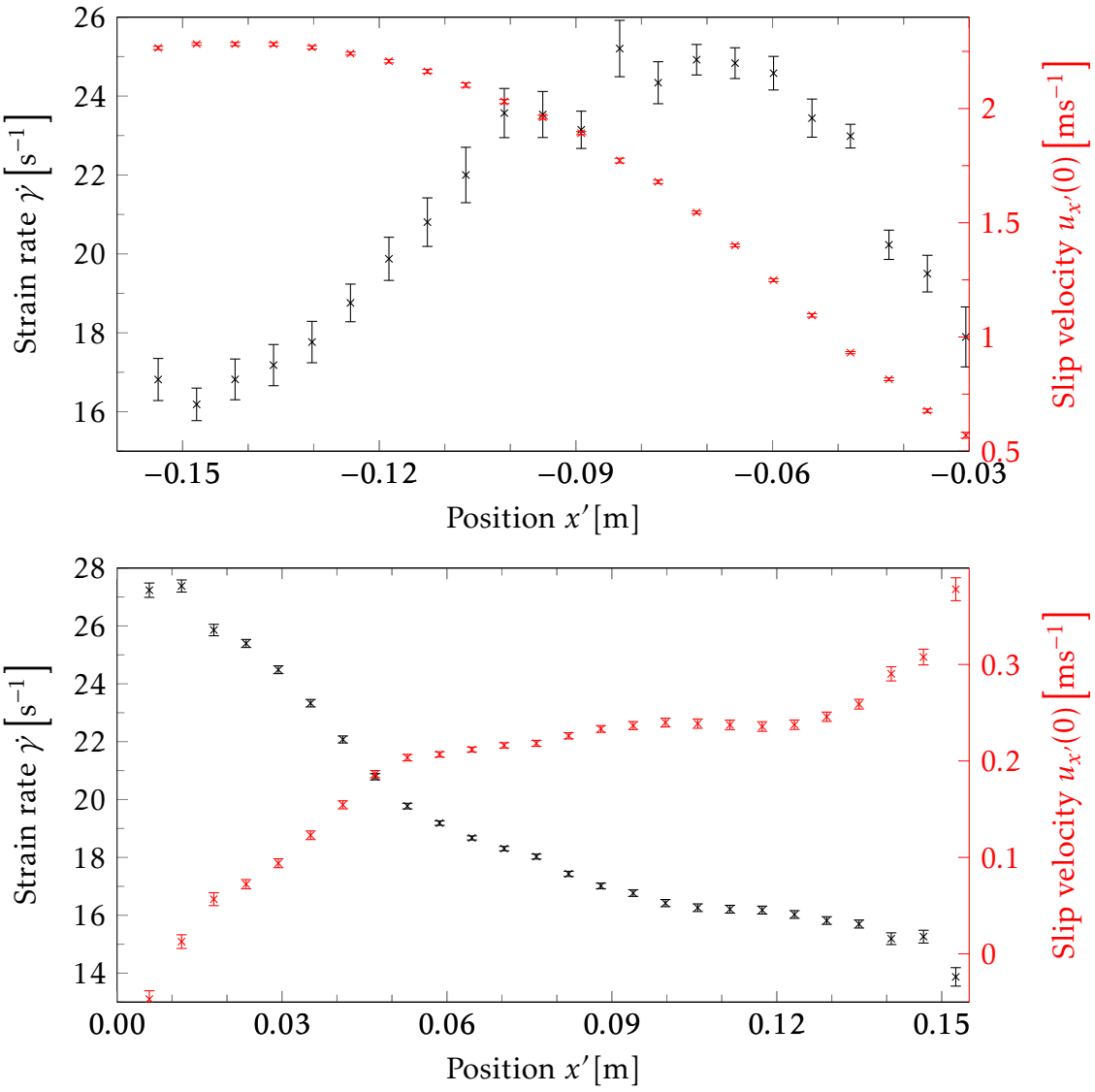

Figure 6.76 – Encountering of an obstacle: Strain rates and slip velocities for PVC in areas I and II. Strain rates and slip velocities in front of the obstacle (upper panel) and on the obstacle (lower panel). Strain rates and slip velocities are calculated from linear regression over the velocity profile at each position averaged over one second (630 frames). Error bars represent the standard deviation of the regression coefficients.

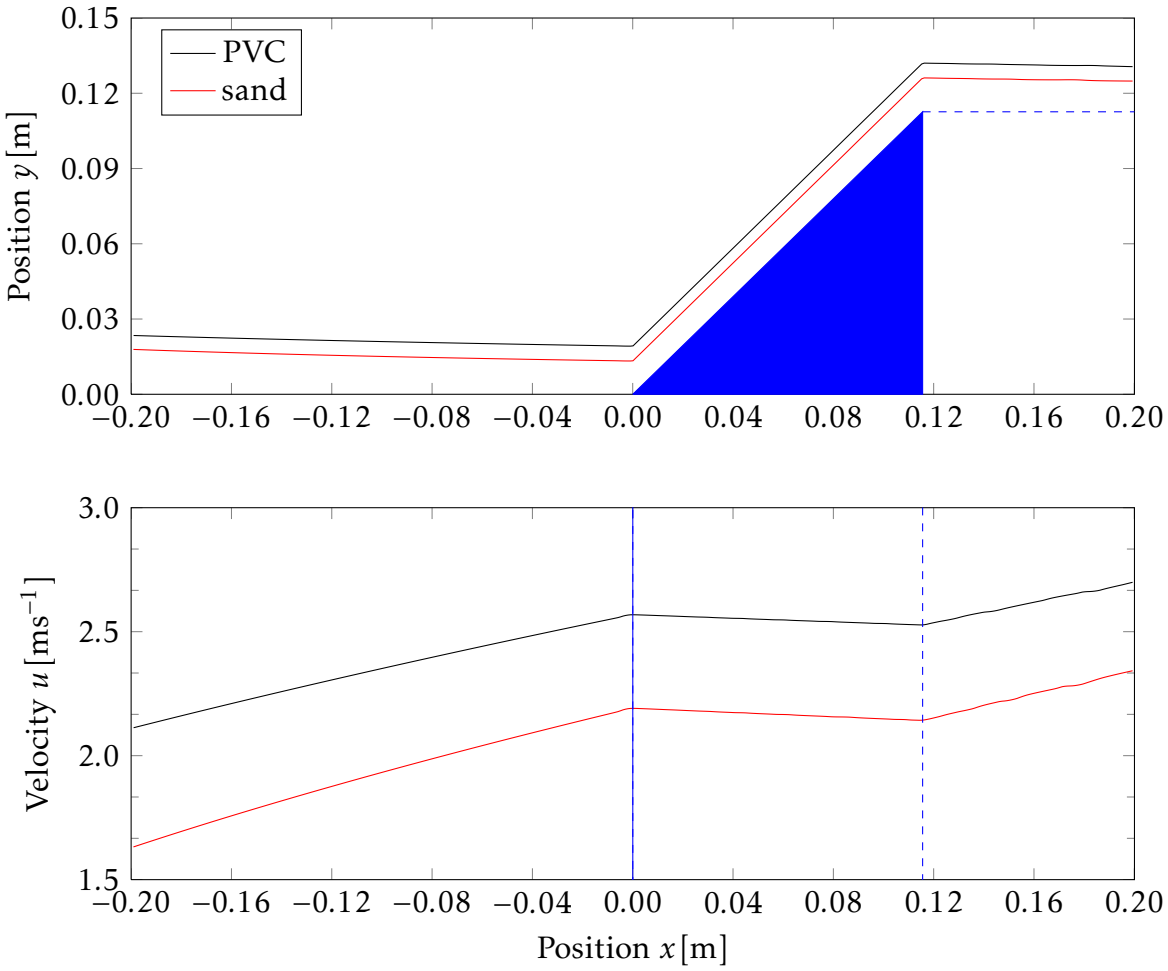

Figure 6.77 – Savage-Hutter simulations of obstacle inside channel: Flow heights and velocities. Savage-Hutter simulations were performed with the obstacle included in the height function of the bottom surface. Depicted are flow heights (upper panel) and flow velocities (lower panel) over the complete observed area.

the flow. This is in sharp contrast to the experimentally observed height and velocity evolutions, which strongly differed between sand and PVC due to the deposition of material in the case of sand. Additionally, the flow height is reduced when the simulated flow hits the obstacle, whereas the opposite effect is observed in the experiment. The initial velocity included in the simulations is again the free surface velocity. Thus, comparisons with the measured slip velocity might not be adequate. Nevertheless, both the measured slip velocity and the PIV measurements demonstrate that the flow is decelerated when approaching the obstacle, while the simulations predict an acceleration. Also the values of the velocity are about 10-fold overestimated by the simulation.

Taken together, the Savage-Hutter simulations are incapable of simulating the flow behavior over an obstacle of the shape employed here.

6.4.3 Non-depth-averaged simulations

Non-depth-averaged simulations for the interaction of the granular flow with an obstacle were performed in an area starting 20 cm before the obstacle and ending at the highest point of the obstacle. The area after the obstacle was excluded from the simulation due to the enormous change in density of the granular material. To simulate such situations, a variable density has to be included in the simulation, which is not topic to this work. The simulated velocity field and filling parameters (Fig. 6.78) reveal that the OpenFOAM® simulations are well capable to qualitatively predict the velocity fields for both sand and PVC observed in Figure 6.66. The deceleration of the flow in front of the obstacle and the resulting increase in flow height on the obstacle are well captured. Additionally, the simulations correctly predict the formation of a deposition on the obstacle for sand but not for PVC. Velocity fields in front and on the obstacle are qualitatively well captured: lowest velocities are observed at the bottom of the channel or the obstacle (deposition) and increase towards the surface. The simulation also correctly predicts that higher surface velocities are reached for PVC. Comparison of detailed velocity profiles in y-direction for PVC in front of and on the obstacle reveal that the shape of the velocity profile is well predicted in front of the obstacle, while the actual velocities area constantly underestimated by around $0.25\,\mathrm{ms}^{-1}$ (Fig. 6.79). The velocity profile on the obstacle is predicted to be more fluctuating than the actual observed profile but the simulated values vary around the actual values: they slightly underestimate the observed values close to the bottom of the channel and overestimate in higher layers (Fig. 6.79).

Figure 6.78 shows that the formation of a deposition in front of and on the obstacle for the sand flow is predicted correctly. Detailed considerations on the total, flowing fraction and deposition height over time reveal that the height of the flowing fraction is well predicted throughout the steady-state phase (Fig. 6.80). In contrast, the deposition formation and thus the total material height only reach the measured values at the end of the steady-state phase due to a failure of the simulation to predict sudden changes in flow height. Thus, the simulated formation of the deposition takes longer than the observed deposit formation but the resulting flow and material heights after 3 seconds of flow are correctly predicted, except for the height of the deposition, which is slightly underestimated. The same hold true for the respective volumes (Fig. 6.81).

The Volume evolution of the PVC experiment is well captured by the simulations, both quantitatively and qualitatively (Fig. 6.82). After one second, a steady-state is reached and the simulations were stopped at this point. The formation of a steady state flow can be visualized by the flow geometry evolution over time in the first part of the simulations (Fig. 6.83): after about 0.8 seconds the geometry of the PVC flow remains practically constant in shape. In contrast, the sand geometry only reaches a steady-state at 2.4 seconds.

Therefore, the simulations in this case were carried out for 3 seconds. The flow thickness and shape of PVC is very accurately predicted in front of the obstacle and on the first half of the obstacle. On the second half of the obstacle it is slightly underestimated (Figs. 6.84 and 6.85). The detailed view on the flow thickness demonstrates that especially the increase in flow height in front of the obstacle is well predicted.

In the case of sand, the deviations from the measured flow geometry deviates slightly more from the measured geometry (Fig. 6.86). As suggested by the height evolution at one position (Fig.6.80), the overall flow height is quite accurately predicted. Strong deviations from the measured flow height occur only at the position immediately in front of the obstacle, where the simulation is incapable of predicting the sudden increase in flow height and reaches the constant flow height on the obstacle earlier than the actually observed (Fig. 6.87), resulting also in an overestimation of the total flow height at this position. The formation of the deposition is well predicted in front of the obstacle. Correlated with the underestimated volume of the deposition (Fig. 6.81), the height of the deposition and thus the total flow height is underestimated on the obstacle (Fig. 6.87). As a consequence, the simulated deposition is thinner towards the end of the obstacle.

As suggested by the good prediction of the slope of the velocity profile in front of the obstacle for PVC (Fig. 6.79), the strain rate is accurately predicted in front of the obstacle until about $x = -8$cm in (Fig. 6.88 upper panel) and afterwards overestimated. The slip velocity is accurately predicted to decrease towards the obstacle, but is constantly underestimated as suggested by the velocity profile in Fig. 6.79. This underestimation of the slip velocity continues until $x = 11$cm (Fig. 6.88 lower panel).

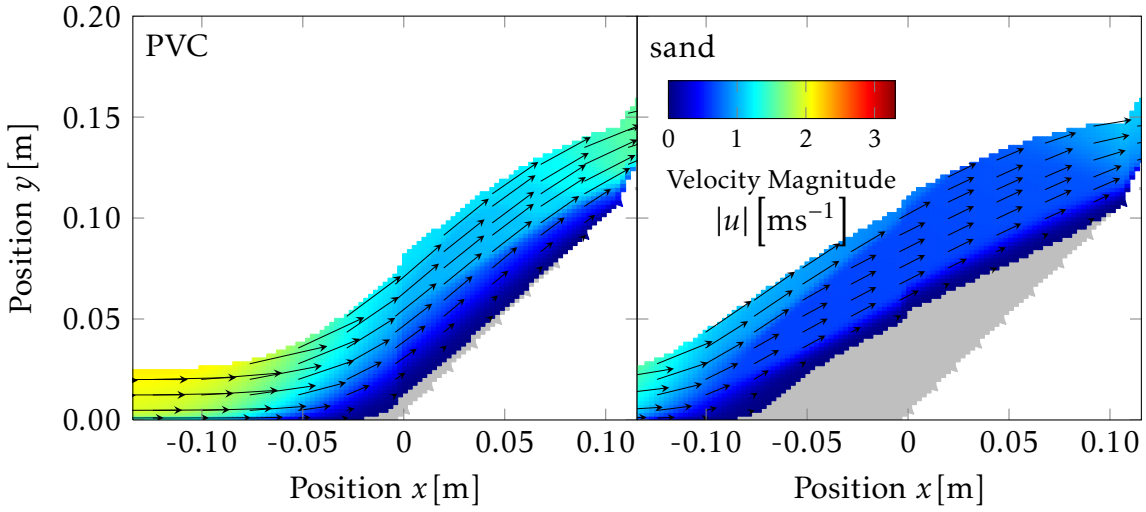

Figure 6.78 – OpenFOAM® simulations of obstacle inside channel: Overview on velocity fields. Overlay of simulated velocity fields with simulated shape during the flow encountering an obstacle inside the channel in a setup as described in Fig. 6.66. Velocities in single patches corresponding to the numerical grid are represented by a heat map (reaching from blue for the minimal velocity to red for the maximal velocity). Direction of the velocities are depicted by arrows, the length of the arrows corresponds to the magnitude. For a better overview, only arrows for each tenth patch in x-direction and every third patch in y-direction are shown. Gray areas represent deposited material.

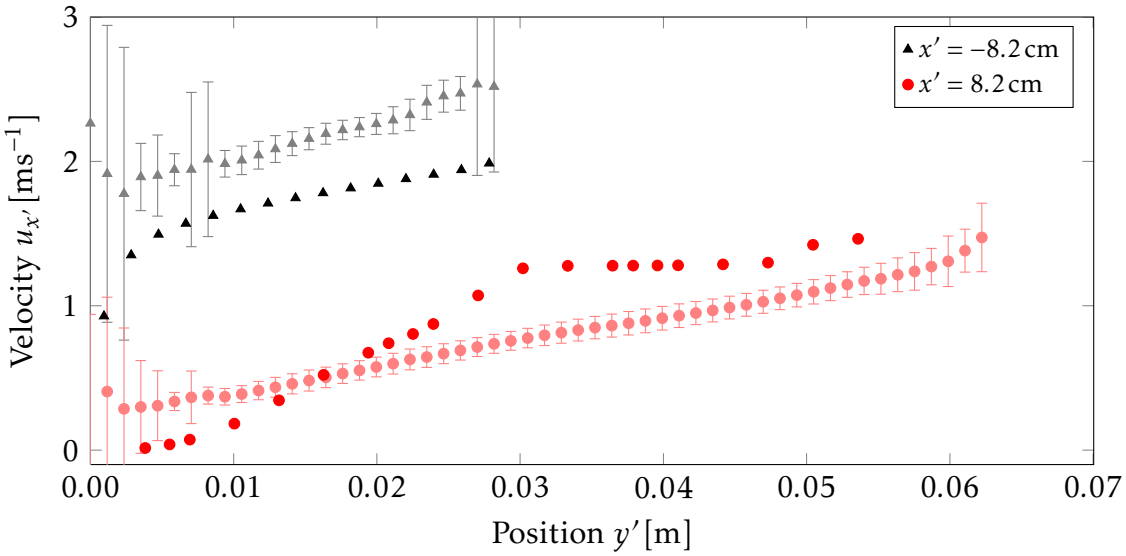

Figure 6.79 – OpenFOAM® simulations of obstacle inside channel: Velocity profiles in y'-direction for PVC. Simulated spatial mean velocity distribution in y'-direction in front of the obstacle (black line, $x' = -8.2\,\mathrm{cm}$) and on the obstacle (red line, $x' = 8.2\,\mathrm{cm}$). For comparison, experimental results from Fig. 6.67 are included in light red and gray.

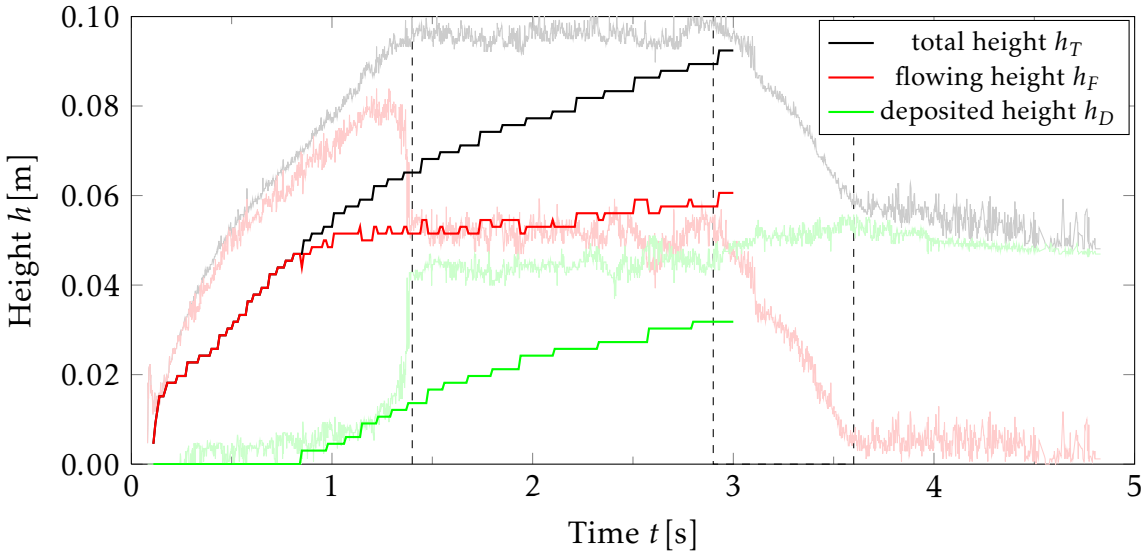

Figure 6.80 – OpenFOAM® simulations of obstacle inside channel: Temporal evolution of sand height profiles in front of the obstacle. Simulated temporal height evolution of total material (black line), flowing fraction (red line) and deposited fraction (green line) at position $x' = -5\,\text{cm}$. For comparison, experimental results from Fig. 6.68 are included in light colors.

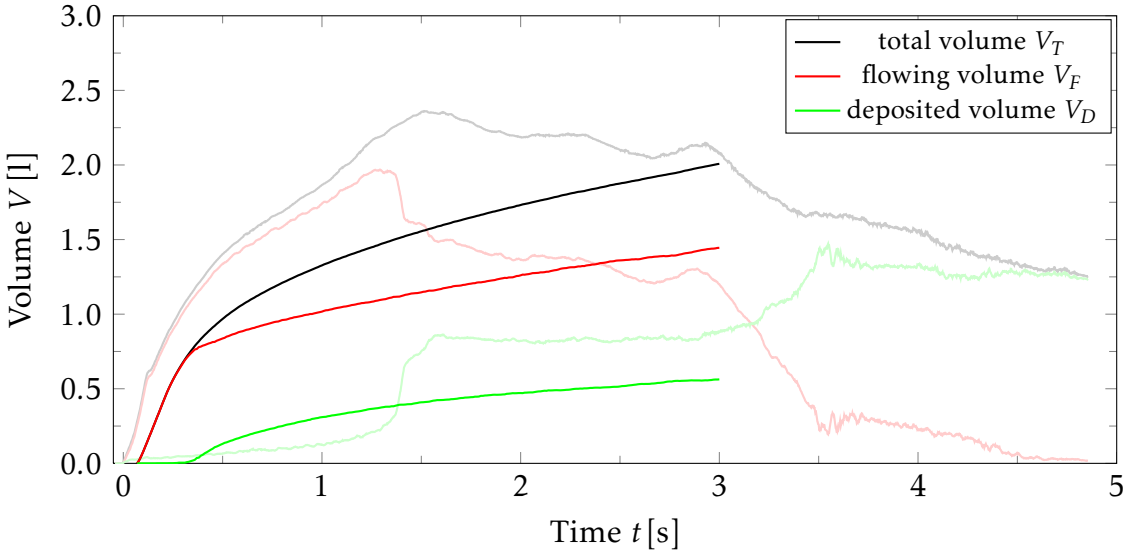

Figure 6.81 – OpenFOAM® simulations of obstacle inside channel: Temporal evolution of sand volumes. Simulated temporal volume evolution of total material (black line), flowing fraction (red line) and deposited fraction (green line) in an area reaching from $x' = -16.5\,\text{cm}$ to the end of the obstacle. For comparison, experimental results from Fig. 6.69 are included in light colors.

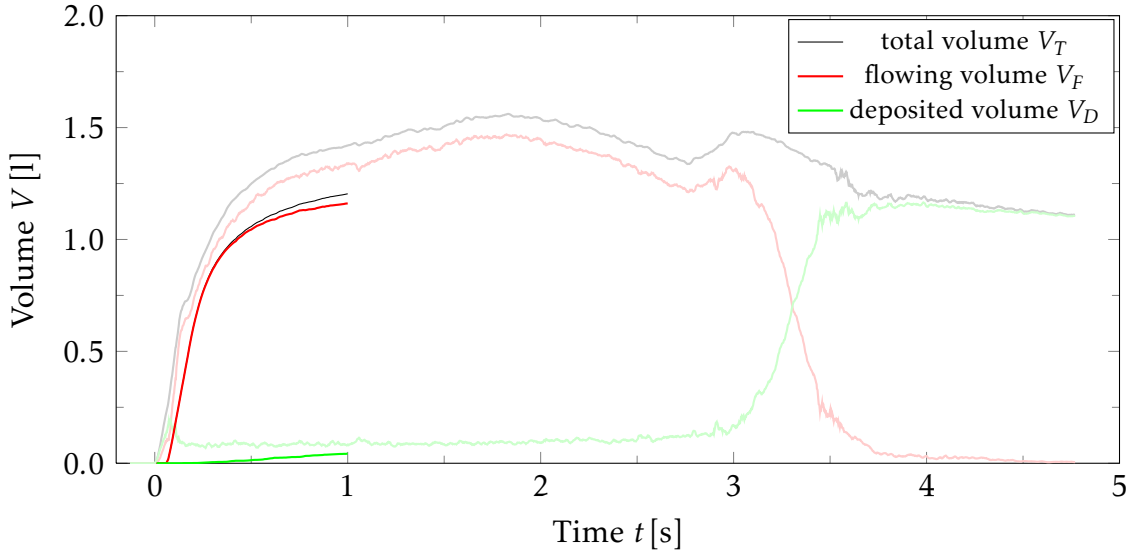

Figure 6.82 – OpenFOAM® simulations of obstacle inside channel: Temporal evolution of PVC volumes. Simulated temporal volume evolution of total material (black line), flowing fraction (red line) and deposited fraction (green line) in an area reaching from $x' = -16.5\,\mathrm{cm}$ to the end of the obstacle. For comparison, experimental results from Fig. 6.70 are included in light colors.

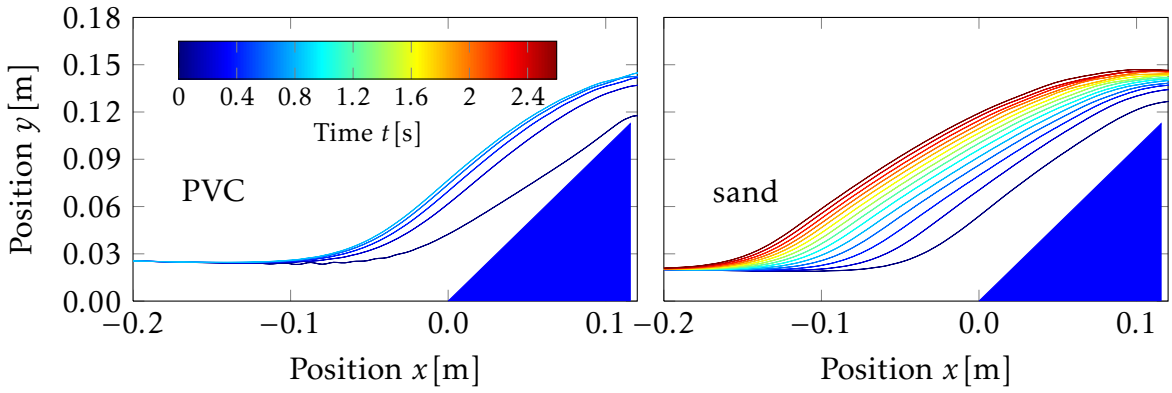

Figure 6.83 – OpenFOAM® simulations of obstacle inside channel: Temporal evolution of flow shape. Simulated temporal evolution of the flow outline for PVC and sand during the first seconds of the experiment.

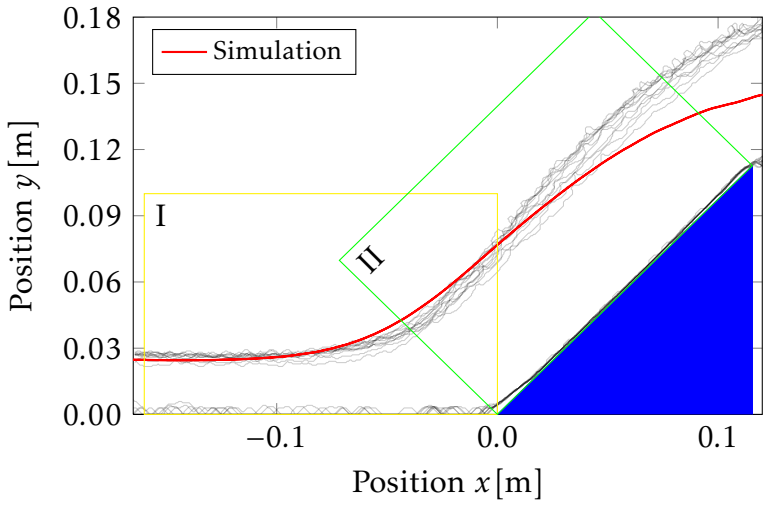

Figure 6.84 – OpenFOAM® simulations of obstacle inside channel: Flow geometry during steady state flow of PVC. Simulated flow geometry in the observed area after one second of simulation when a the steady state flow phase is reached (red line). The yellow and green boxes mark the areas which are considered in detail Fig. 6.85. For better comparison, experimental results from Fig. 6.72 are included in gray.

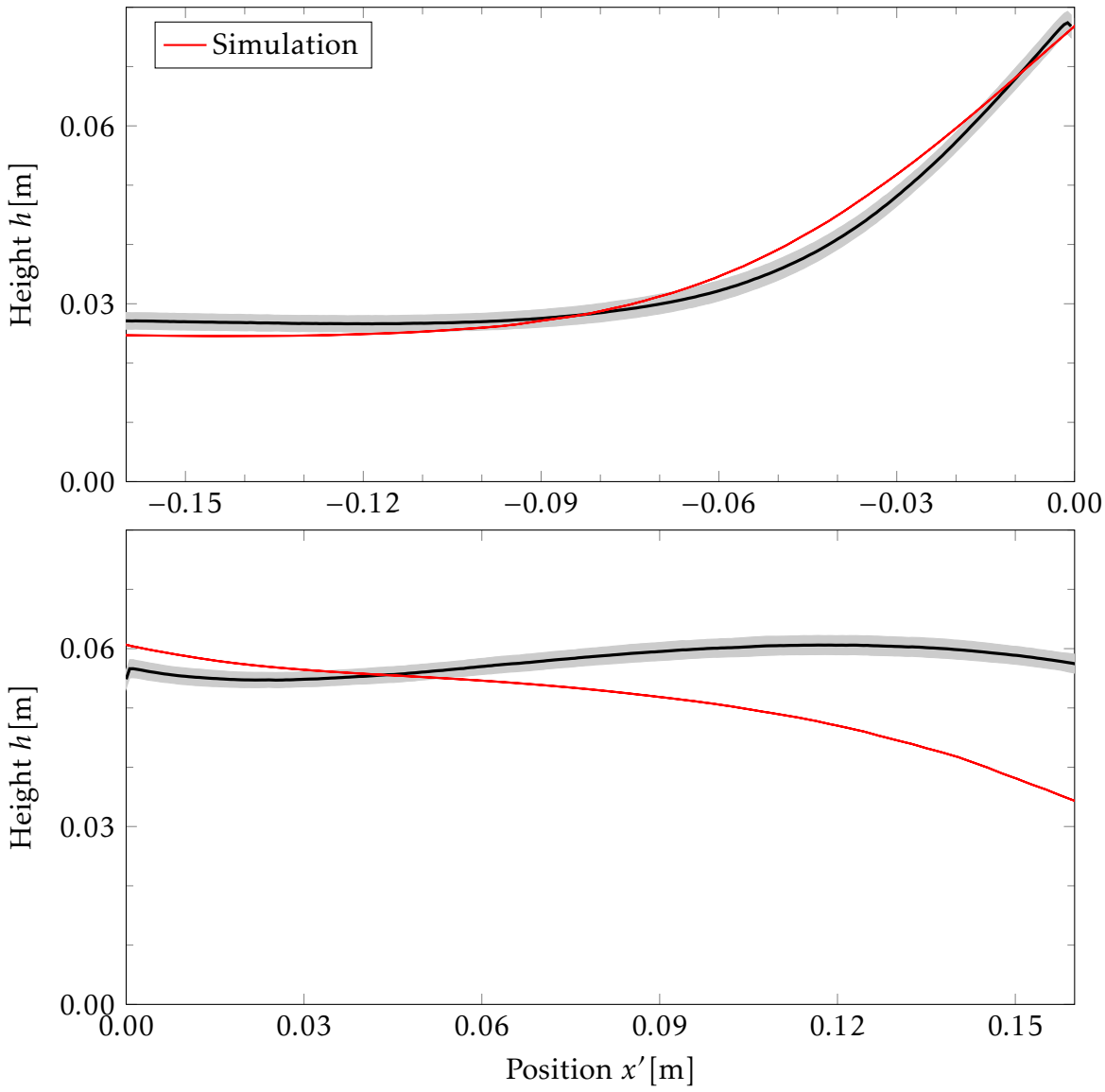

Figure 6.85 – OpenFOAM® simulations of obstacle inside channel: Flow height during steady state flow for PVC in areas I and II. Detailed view on the simulated flow height profile (red line) in the two boxes indicated in Fig, 6.84. Upper panel depicts the height profile in front of the obstacle (yellow box in Fig. 6.84), lower panel corresponds to the green box. For better comparison experimental results from Fig. 6.74 are included (black lines and gray error bands).

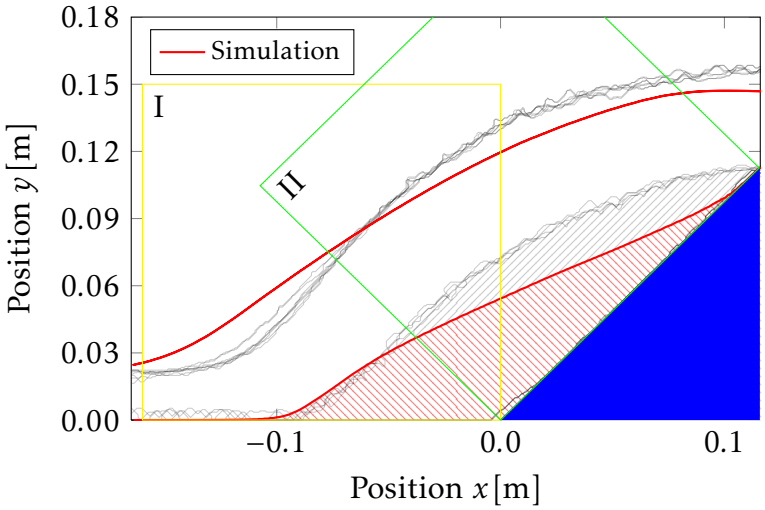

Figure 6.86 – OpenFOAM® simulations of obstacle inside channel: Flow geometry during steady state flow of sand. Simulated flow geometry in the observed area after three seconds of simulation when a the steady state flow phase is reached (red line). The hatched area marks the deposit of sand in front of and on the obstacle. For better comparison experimental results from Fig. 6.73 are included in gray.

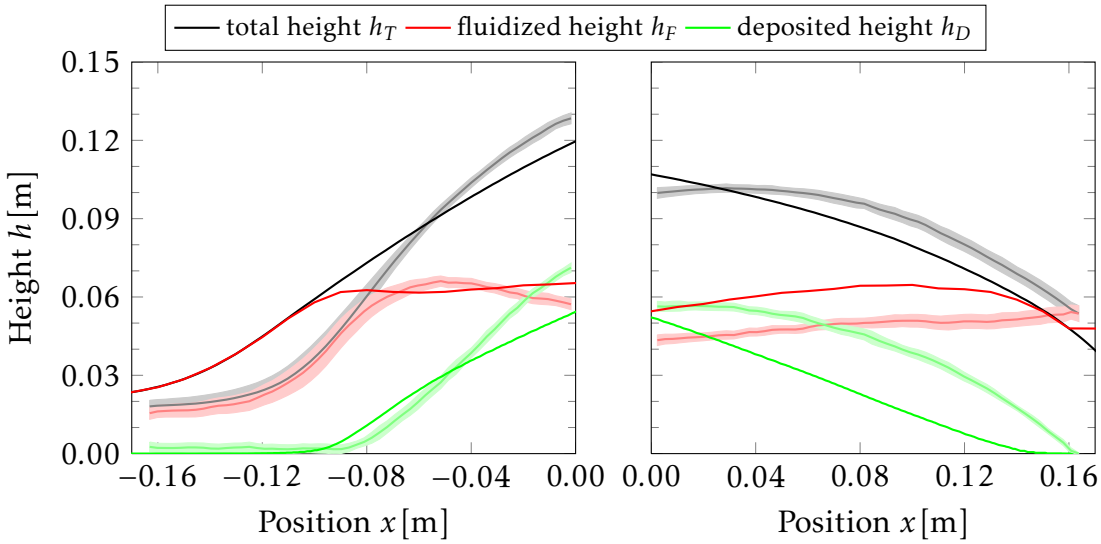

Figure 6.87 – OpenFOAM® simulations of obstacle inside channel: Flow height during steady state flow for sand in areas I and II. Detailed view on simulated flow height, deposit height and total material height in front of the obstacle (left panel, corresponding to yellow box in Fig. 6.86) and on the obstacle (right panel, corresponding to green box in Fig. 6.86) for the sand case. For better comparison, experimental results from Fig. 6.75 are included in light colors.

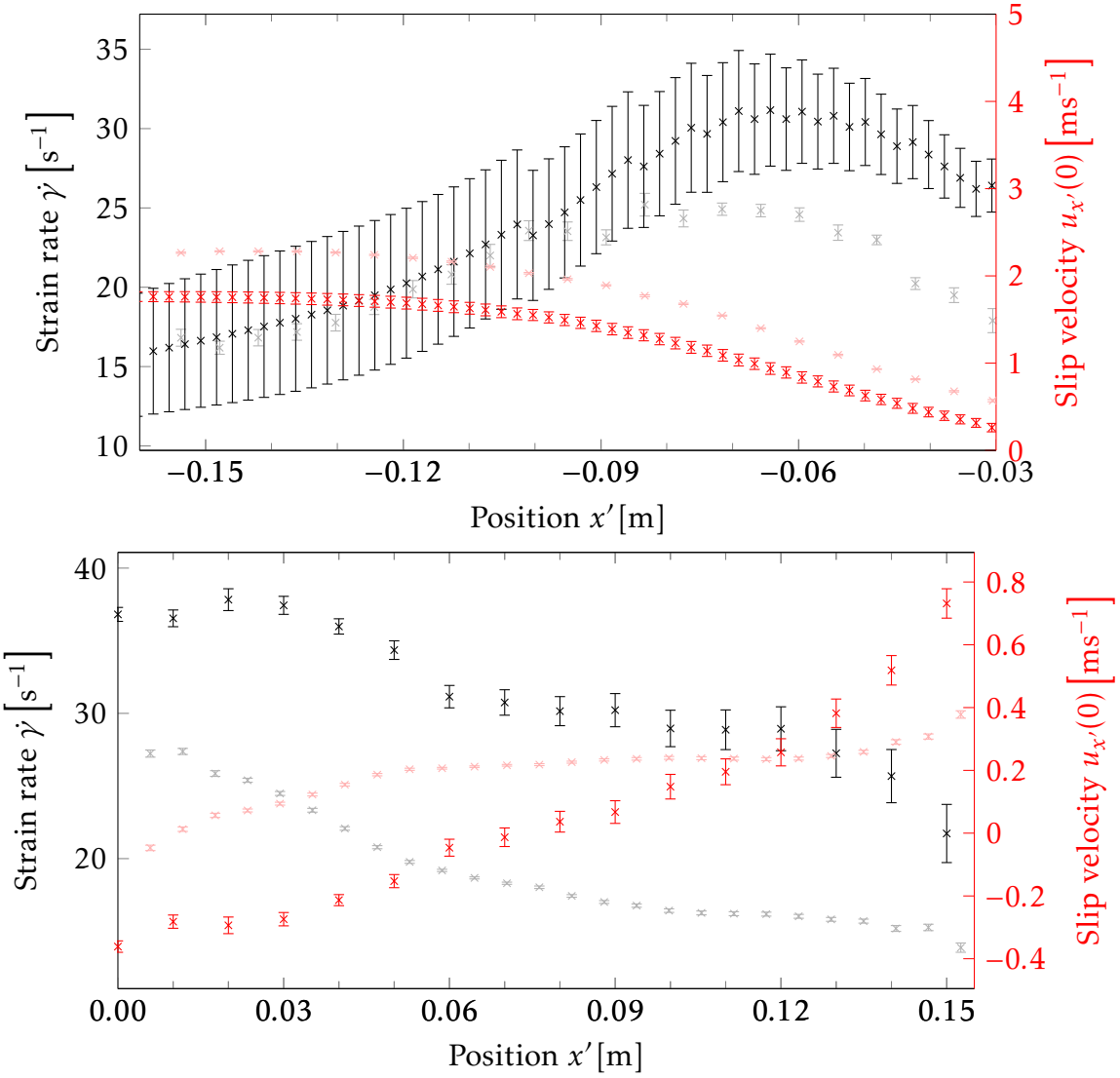

Figure 6.88 – OpenFOAM® simulations of obstacle inside channel: Strain rates and slip velocities for PVC. Strain rates and slip velocities in front of the obstacle (upper panel) and on the obstacle (lower panel) calculated by regression analysis from the simulated velocity profiles measured after one second. Error bars represent the standard deviation of the regression coefficients. For better comparison experimental results from Fig 6.76 are included in light colors.

6.5 Shock Formation at the end of a closed channel

Beside the observation of a granular material overflowing an obstacle, it is also important to be able to predict the behavior of the material when being completely stopped by an obstacle. This can be the case when an avalanche hits a defense structure, which are usually built perpendicular to the mountain slope, or the wall of a building. To mimic this situation, the channel can be closed by a perpendicular wall at the end. Such experiments have been performed before (Gray et al., 2003) and were also combined with PIV measurements and depth-averaged simulations (Pudasaini et al., 2007; Pudasaini and Kröner, 2008), but the spatial and temporal resolution of the PIV was relatively low. Therefore, in order to observe detailed flow evolutions and velocity fields with high temporal resolution during a shock formation for comparison with depth-averaged and non-depth-averaged simulations, such experiments were included in this work.

6.5.1 Experimental findings

Seven experiments were recorded under the following set-ups: PVC flows at 40° and 50° inclination angle and inflow heights of 5, 10 and 15 cm and an experiment with sand at 50° and 10 cm inflow height. Image sequences of the last 50 cm of the channel were recorded for each experiment and the volume of the granular material V_T and the volume of the fluidized fraction V_F was extracted from these images. The PIV measurements illustrate the abrupt deceleration of the flow (Fig. 6.89), resulting in the following shock formation and propagation in the upstream direction: first the material flows up the perpendicular wall until a maximum height is reached, then deposition starts at the lowest corner and the flow continues to overflow the deposit while constantly more material is deposited. This results in an S-shaped flowing fraction and causes the shock front to move in the upstream direction. Finally, a parabolic shaped deposition is formed. This shock formation is observed for all experiments.

In order to analyze and compare the flow behavior during these different experiments in more detail, graphics are scaled according to the volume influx. The temporal volume evolution is shown in Figs. 6.90 and 6.91. All experiments display a very similar volume evolution regardless of the inclination angle, inflow hight and material. Differences between the experiments are observed in the time scales: as expected, both an increase in inflow height and inclination angle cause the shock process to happen faster (Fig.6.90). Five phases of different flow behavior can be characterized: The first phase (I) is defined as the time between the opening of the silo gate and time $t = 0$ s when the front of the granular flow impacts the wall. In the following phase (II) the granular flow is redirected and moving up the perpendicular wall. No deposition occurs in this phase. The transition

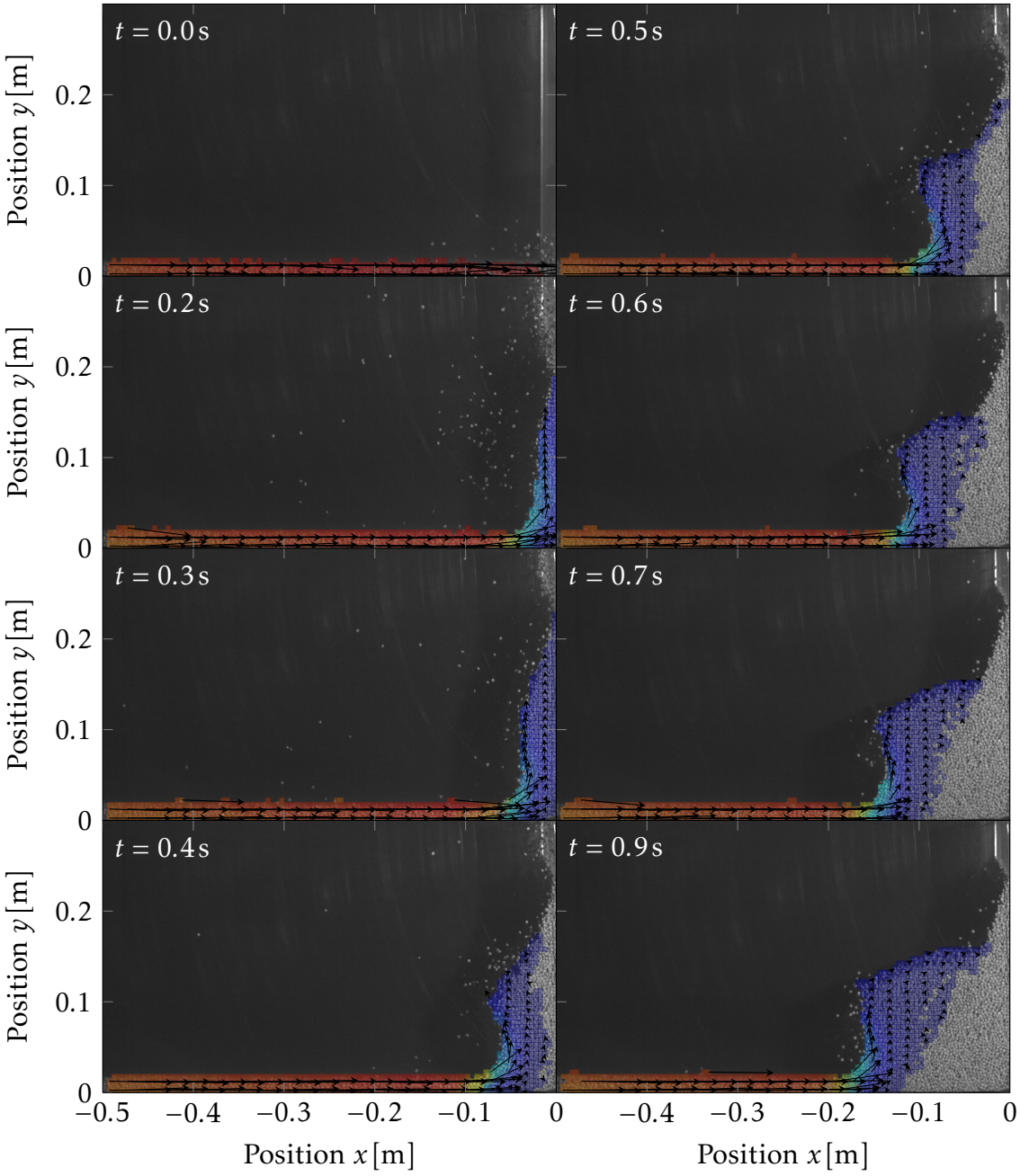

Figure 6.89 – Shock formation: PIV measurements. Overlay of velocity fields measured by PIV with pictures of the granular flow of PVC particles for a shock formation at the end of a closed channel at 50° inclination angle and 10 cm inflow height. Magnitudes of mean velocities in 5 mm x 5 mm patches are represented by a heat map (reaching from blue for the minimal velocity to red for the maximal velocity). Direction of the velocities are depicted by arrows, the length of the arrows corresponds to the magnitude. For a better overview, only arrows for each third patch in x-direction and every other patch in y-direction are shown. Note that in this section x coordinates are 0 at the wall at the end of the channel. Figure continued on next page.

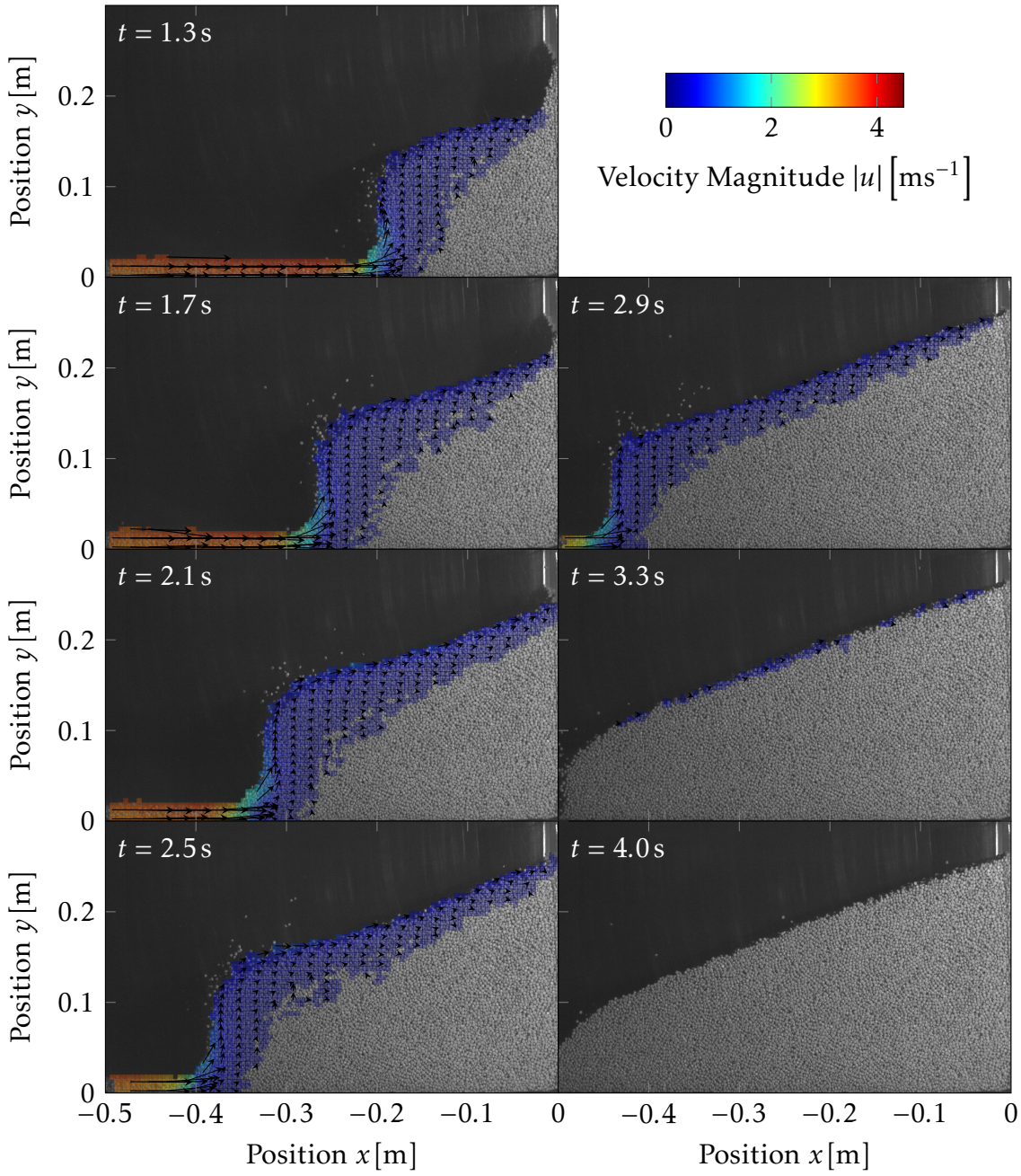

Figure 6.89 – Shock formation: PIV measurements.(cont.)

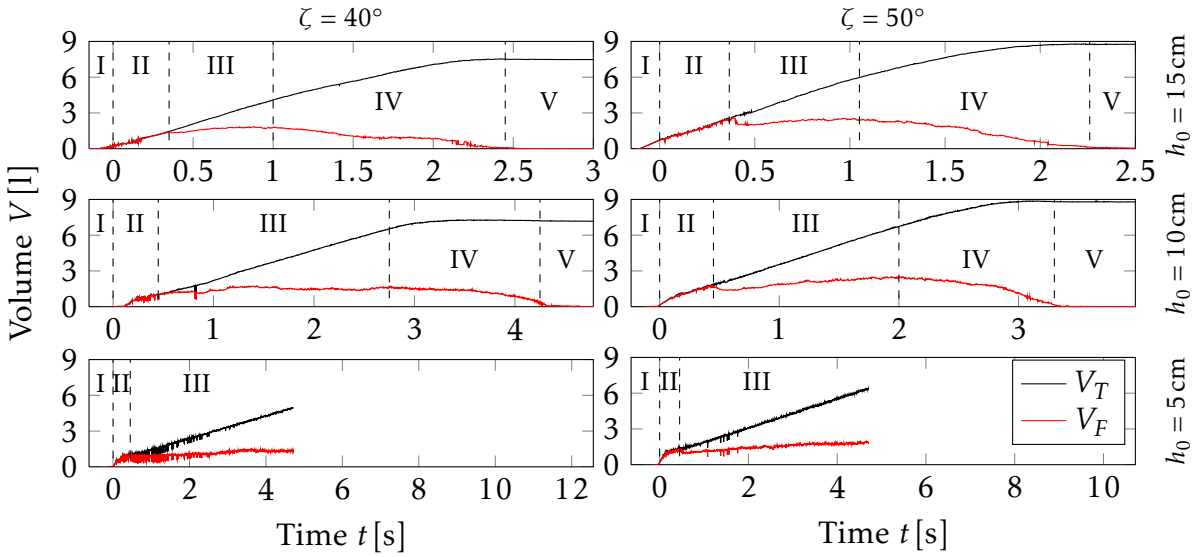

Figure 6.90 – Shock formation: Temporal volume evolution of PVC. Temporal evolution of total PVC volume (V_T) and flowing PVC volume (V_F) in the observed area (50 cm, starting at position $x = -50$ cm, corresponding to the area shown in Fig. 6.89) during the PVC flow for different inclination angles and inflow heights. Due to limitations in the maximal recording time, experiments for inflow height $h_0 = 5$ cm could not be recorded until the flow stopped. For description of flow phases (roman numerals) see text.

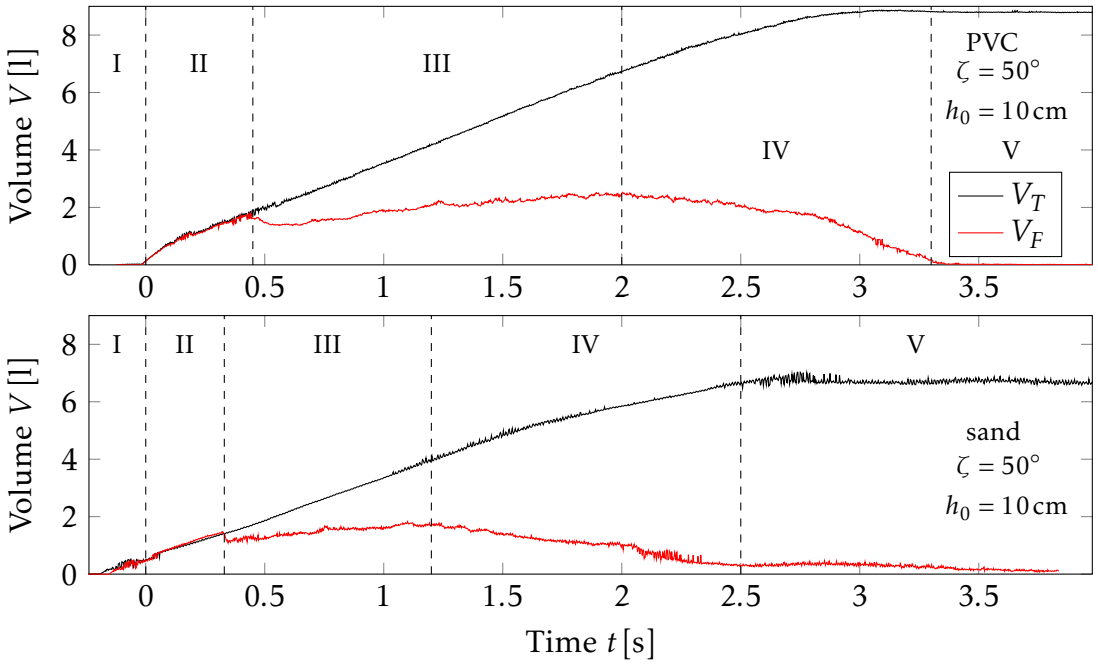

Figure 6.91 – Shock formation: Comparison of temporal volume evolution of PVC and sand. Temporal volume (total and flowing volume) evolution of PVC (upper panel) and sand (lower panel) at 50° inclination angle and 10 cm inflow height.

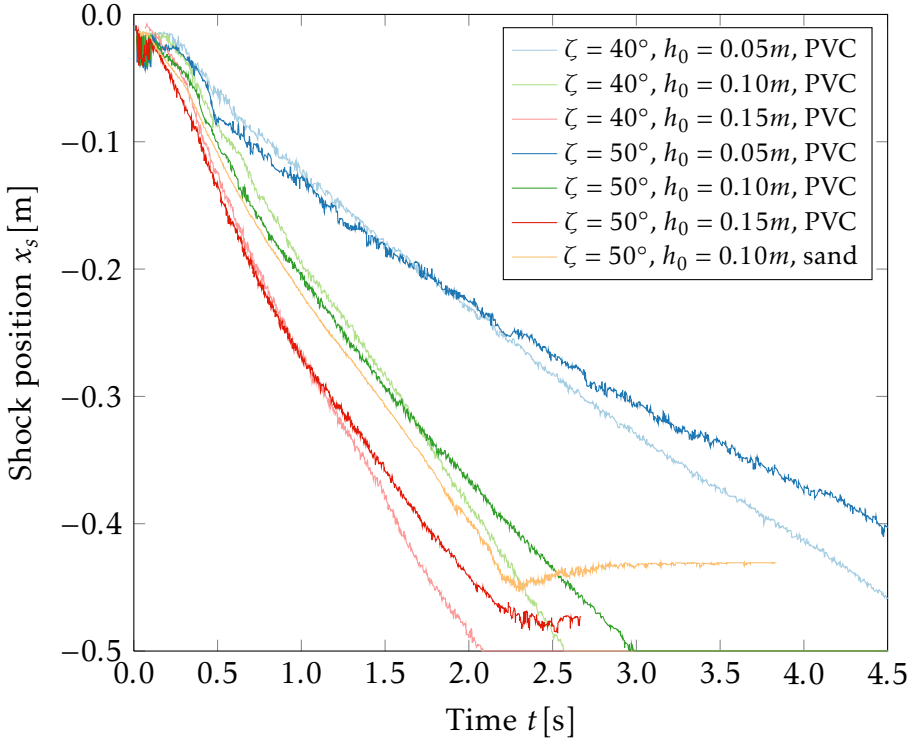

Figure 6.92 – Shock formation: Temporal evolution of shock front position. Time-depended movement of the shock front (position of strongest alteration in height, where height of the material increases abruptly due to formation of deposit) during experiments with PVC and sand at different inclination angles and inflow height.

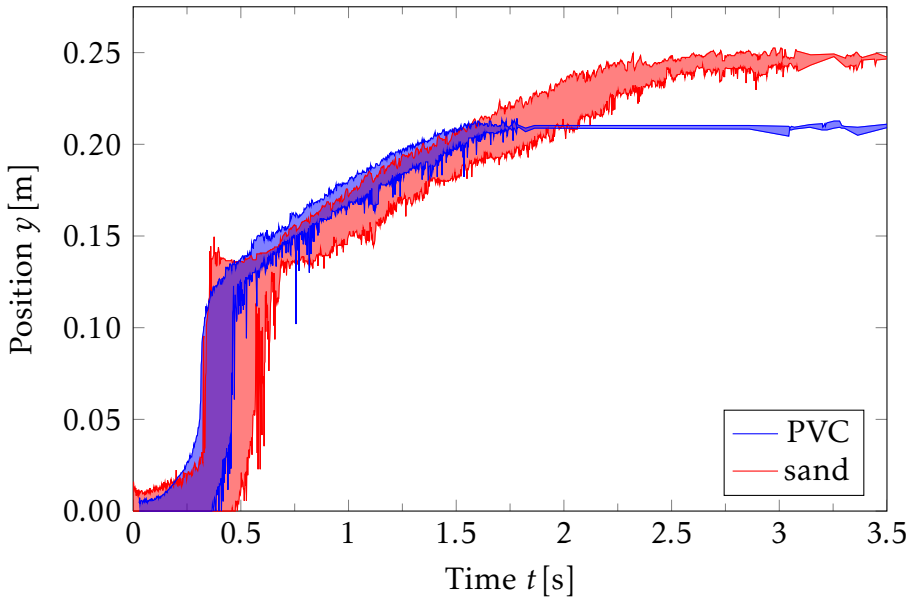

Figure 6.93 – Shock formation: Temporal height evolution at a fixed position. Temporal evolution of flow position in y-direction at a fixed position in the channel ($x = -5$ cm) at 50° inclination angle and 10 cm inflow height. The strong colored lines represent the solid-fluid and the fluid-air interface for the respective material, the lighter colored space in between indicates the complete flowing layer.

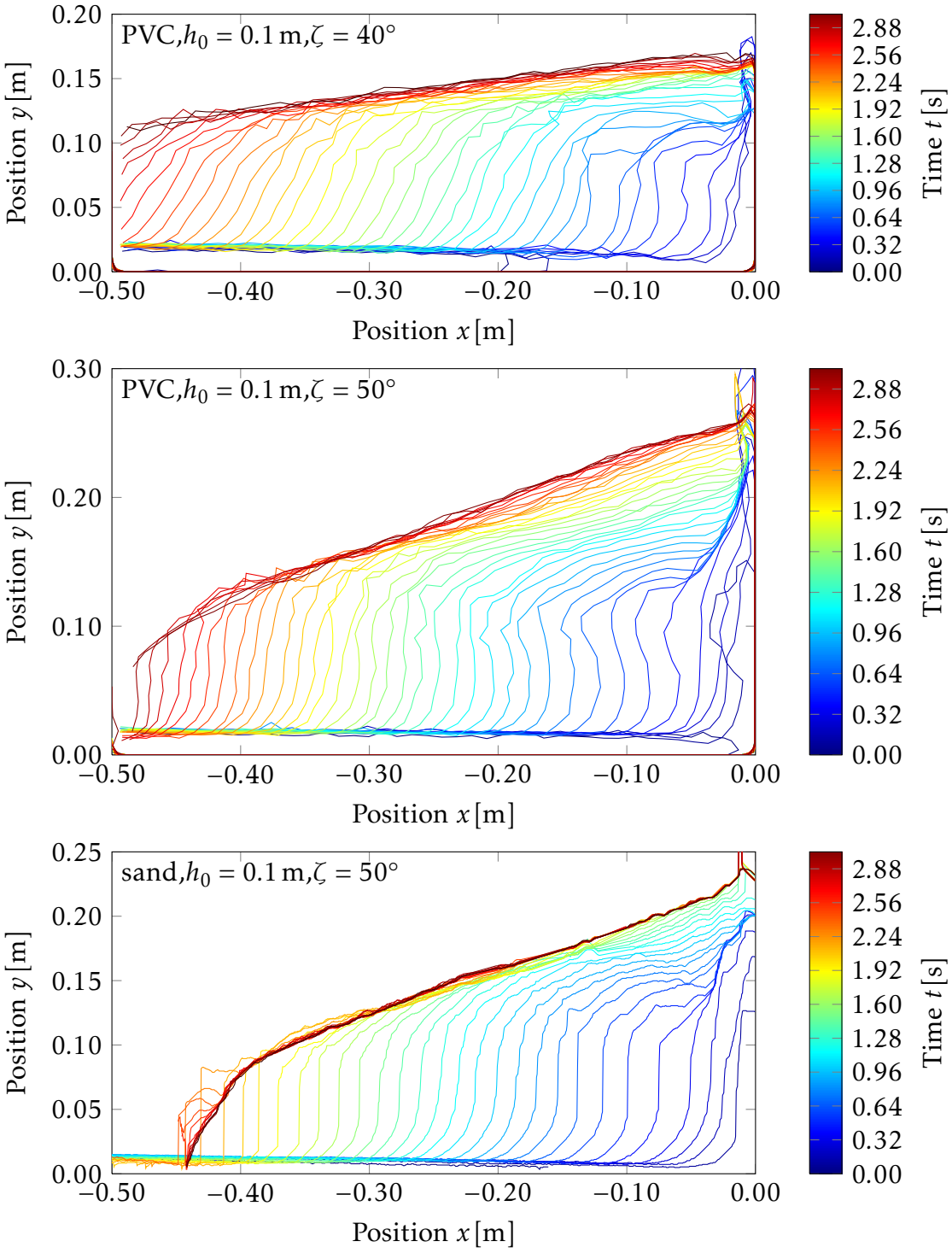

Figure 6.94 – Shock formation: Temporal evolution of flow geometry. Evolution of free surface geometry during the shock formation for different inclination angles (40° and 50° PVC, 50° sand) at a fixed inflow height of 10 cm. Differences in the volume of the final deposit for sand and PVC at 50° inclination angle and 10 cm inflow height can be explained by a slightly lower starting volume employed in the sand case.

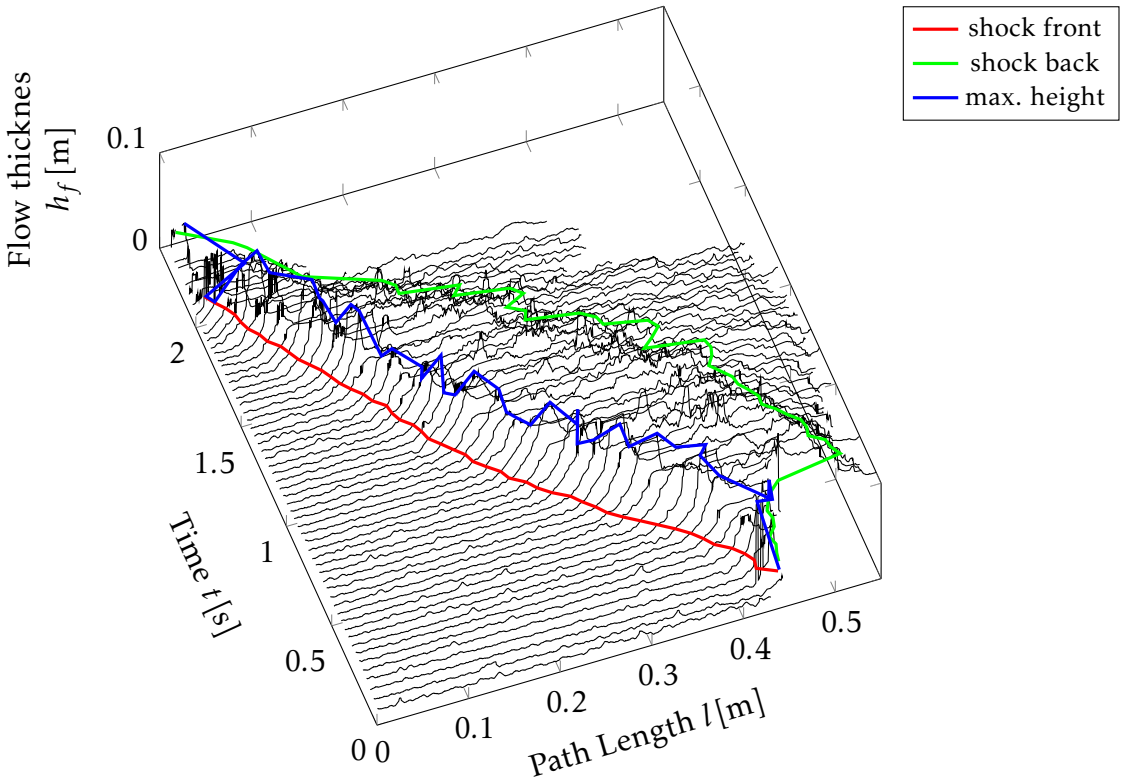

Figure 6.95 – Shock formation: Temporal and spatial evolution of flow thickness for PVC. Three-dimensional view on flow thickness distribution over the observed area at consecutive time-points during the shock formation for 50° inclination angle and 10 cm inflow height. Flow thickness is determined in a curvilinear coordinate system following the solid-fluid interface. Colored lines represent the shock front (red), the maximal flow height and the shock back (green).

to phase III is characterized by a stagnation of the flowing volume evolution, indicating that the first grains are deposited. Throughout phase III the volume of the fluidized fraction stays almost constant while the total volume increases linearly. Phase IV defines the time in which the fluidized fraction starts to decrease until the entire material is at rest. It should be noted here that the final volume is reached earlier than the end of phase IV and that the remaining fluidized fraction consists of local rearrangements until all grains are deposited at the beginning of phase V.

Another characteristic describing the flows is the temporal evolution of the shock position (Fig. 6.92). All shocks display a constant velocity, which decreases with increasing inflow heights and is more or less independent of the inclination angle and the material. Comparison of the temporal evolution of the deposit and height of the fluidized fraction for PVC and sand at a fixed position (Fig. 6.93) reveals that in accordance with the similar velocities, the shock reaches the position at a similar time for both materials and a sudden increase in flow height occurs, followed by a slower but constant increase for more than one second. The main differences between the two materials concern the

solid-fluid interface: it is formed earlier in the PVC experiment, meaning that deposition occurs earlier, resulting in a thinner fluidized layer for this material.

The shock can be further characterized by the geometry evolution of the deposit over time (Fig. 6.94). Comparing 40° and 50° inclination angle, an obvious difference in the shape of the steep shock front is observed: while for 50° inclination, angles of 90° and above between the channel floor and the shock front are observed for all time points, such steep slopes only occur during the very first time points for 40° inclination angle. Comparing the geometry of the sand experiment to the other two, it seems to take an intermediate position between the former shapes: the slope of the S-shape is steeper than for 40° PVC but not as steep as for the corresponding 50°.

To provide an accurate overview over the temporal and spatial evolution of the flow thickness, again the curvilinear coordinate system is employed (Fig. 6.95). With this, the way length the material passes over the deposit becomes directly visible (between the shock front (red line) and the shock back (green line)). The way length becomes longer during the first second of the flow and decreases again afterwards. The distance between the shock front and the point of highest flow thickness (red and blue lines) remains constant during the first second of the flow and then slowly decreases. This way of displaying also clearly indicates that after 0.5 seconds the flow no longer reaches the wall at the end of the channel but stops on the deposit.

6.5.2 Savage-Hutter simulations

As already observed previously (Pudasaini et al., 2007; Pudasaini and Kröner, 2008), the geometry evolution of the deposit over time for PVC and sand can be qualitatively well predicted by Savage-Hutter type simulations (Fig. 6.96): the height at the wall is correctly estimated for all three cases (40° PVC and 50° PVC and sand). The same holds true for the inclination of the deposit surface during all time-steps. This indicates that the simulation is capable of correctly predicting parameter dependent properties of the shock formation. Nevertheless, some characteristics are very similar between the three simulations whereas they differ in the experiment: the length of the deposit is well predicted for PVC and but overestimated for the sand experiment while the simulated inclination of the deposit at the shock front rather resembles the sand situation and is not as steep as the observed shape for PVC. The similar distances of the single curves of the deposit shape in the simulations and measurements suggest a good prediction of the shock front velocity. This observation is confirmed by the simulated position evolution of the shock front over time (Fig. 6.97). The simulated inclinations (the velocities) are very similar to the measured ones. The observed offset is caused by difficulties in accurately determining the zero time point for the shock in the experiment.

Taken together, the Savage-Hutter type simulations are, on the one hand, well suited

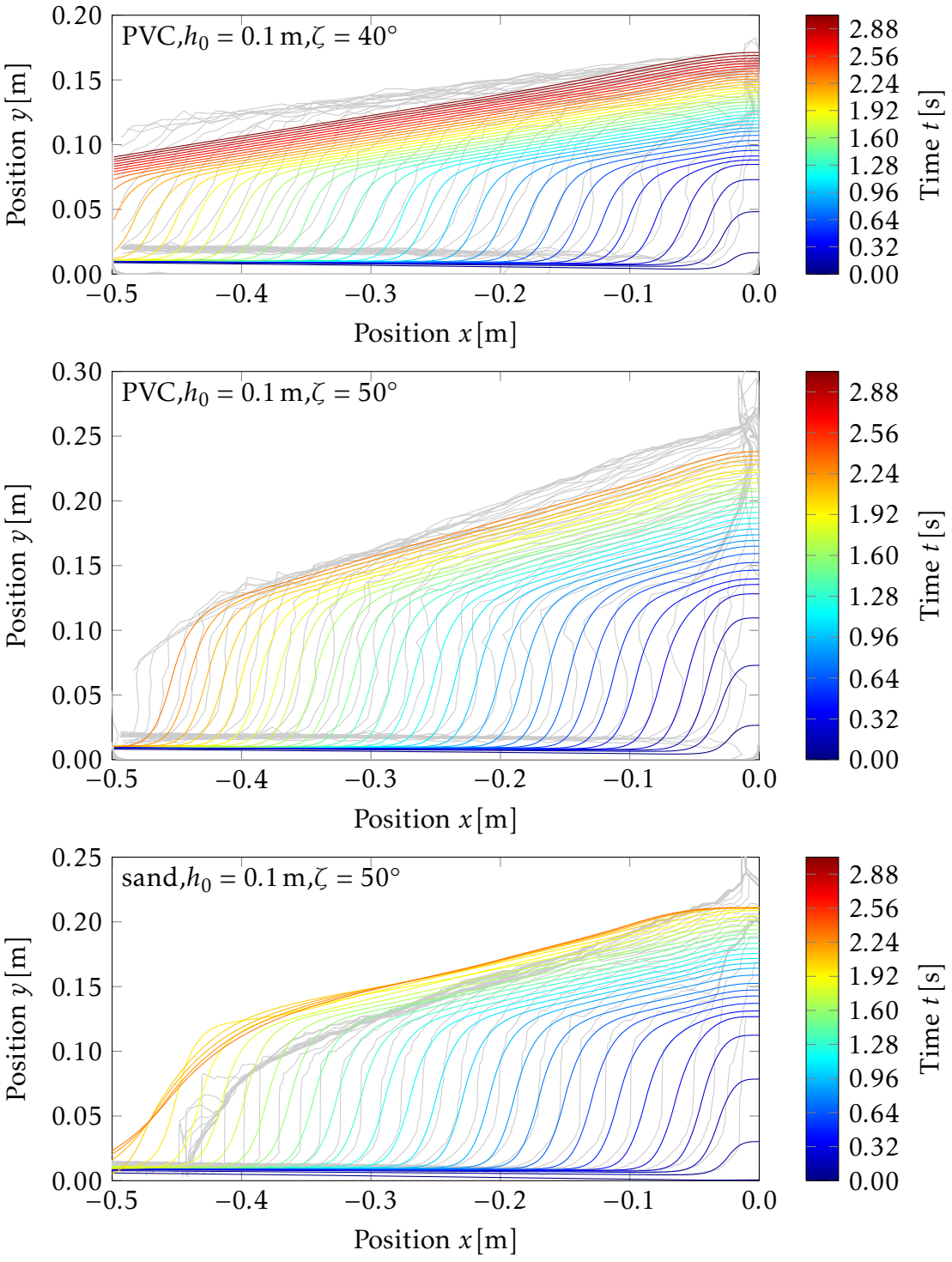

Figure 6.96 – Savage-Hutter simulations of shock formation: Temporal evolution of flow geometry. Simulated evolution of free surface geometry during the shock formation for different inclination angles (40° and 50° PVC, 50° sand) at a fixed inflow height of 10 cm. For comparison, experimental results are included in gray.

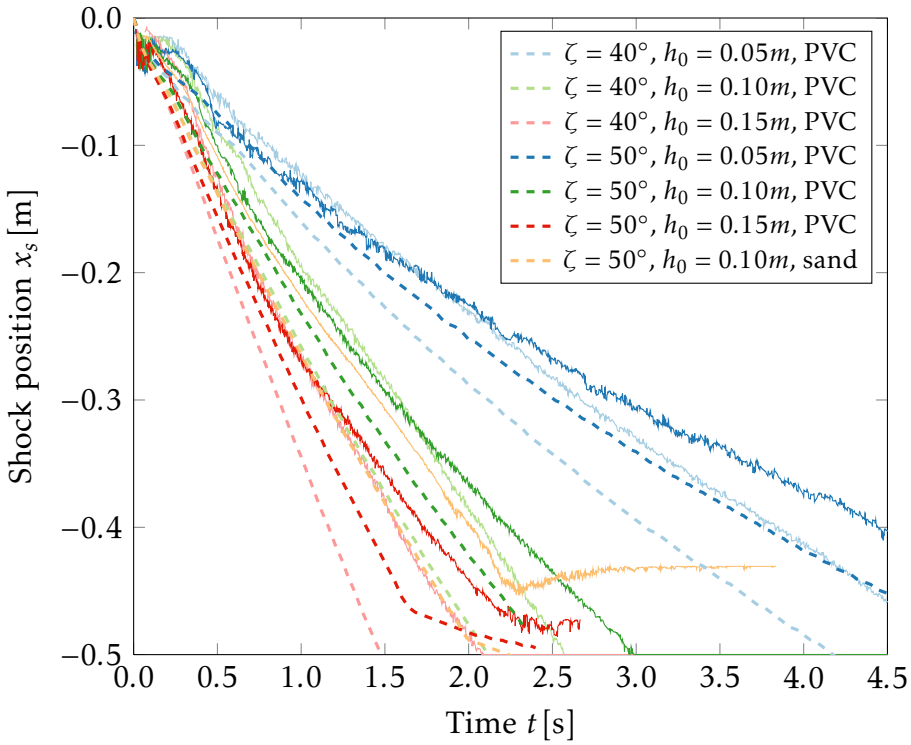

Figure 6.97 – Savage-Hutter simulations of shock formation: Temporal evolution of shock front position. Time-depended movement of the simulated shock front (interface between deposited material and flowing material) for PVC and sand at different inclination angles and inflow heights. For comparison, experimental data is included (continuous lines, same color code as for simulation).

for prediction of the shock front velocity and the impact height on the vertical wall. On the other hand, the simulations display some difficulties to precisely simulate differences in materials. All other variables considered in the experimental section can not be determined due to the depth-averaged character of the simulations.

6.5.3 Non-depth-averaged simulations

The velocity field and filling parameter of the OpenFOAM® simulations for the PVC shock set-up at 10 cm inflow height and 50° inclination angle (Fig. 6.98) reveals that the simulations are well capable to predict the flow behavior during shock formation: initially, the material is abruptly decelerated at the wall and is piled up at the wall with a much lower velocity until a height of above 20 cm. The formation of the deposition in the lowest corner is also correctly predicted. In the following time steps, the formation of the S-shaped flowing fraction which becomes broader with time is well captured by the simulation, however, the depth of the flowing fraction is underestimated in some time steps and overestimated in others. This fluctuation is explained later in the context of the flowing volume evolution. Towards the end of the flow, the simulation well predicts the

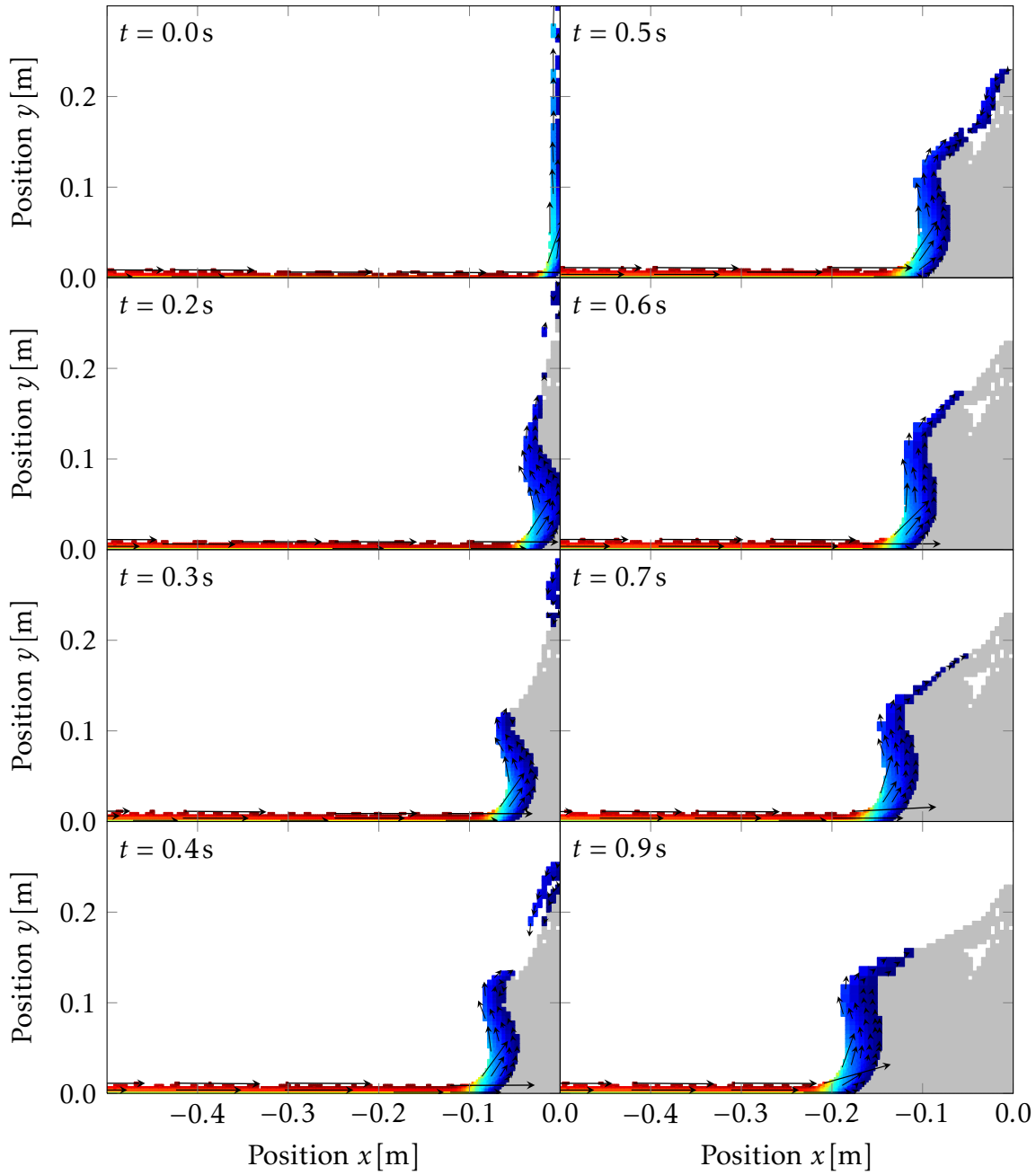

Figure 6.98 – OpenFOAM® simulations of shock formation: Overview on velocity fields. Overlay of simulated velocity fields with simulated shape during a shock formation at the end of a closed channel at 50° inclination angle and 10 cm inflow height. Velocities in single patches corresponding to the numerical grid are represented by a heat map (reaching from blue for the minimal velocity to red for the maximal velocity). Gray patches represent the deposit. Direction of the velocities are depicted by arrows, the length of the arrows corresponds to the magnitude. For a better overview, only arrows for each third patch in x-direction and every other patch in y-direction are shown. Figure continued on next page.

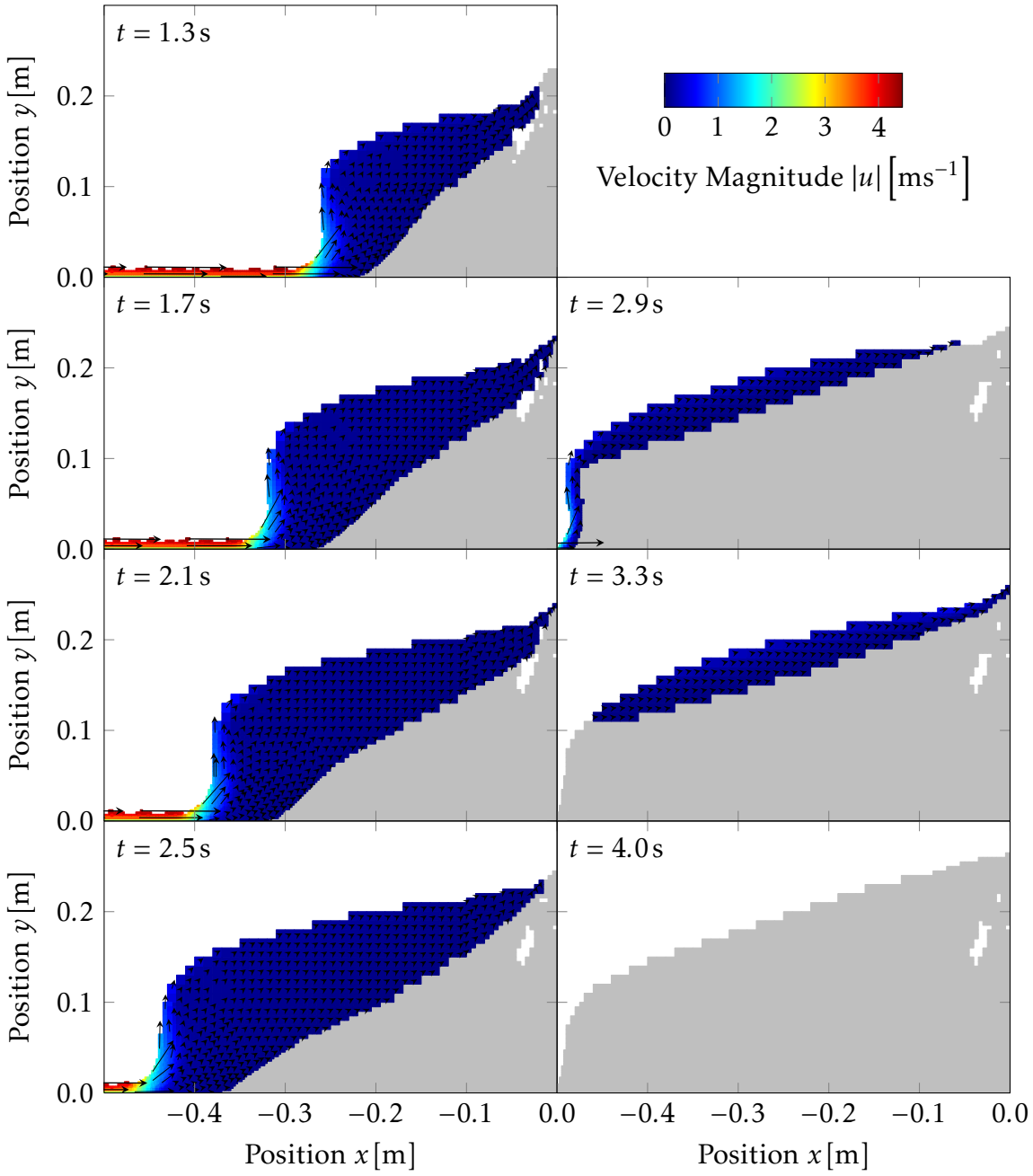

Figure 6.98 – OpenFOAM® simulations of shock formation: Overview of velocity fields.(cont.)

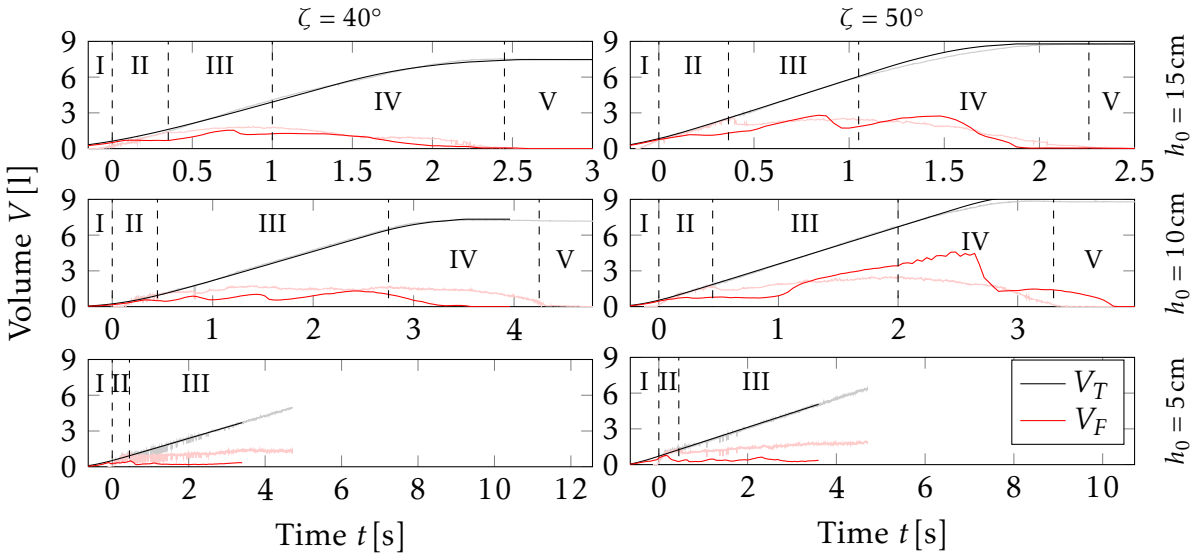

Figure 6.99 – OpenFOAM® simulations of shock formation: Temporal volume evolution of PVC. Simulated temporal evolution of total PVC volume (V_T) and flowing PVC volume (V_F) in the observed area (50 cm, starting at position $x = -50$ cm) during the PVC flow for different inclination angles and inflow heights. For better comparison experimental results from Fig 6.90 are included (gray and light red lines). The inflow volume in the simulation was set to be equal to the inflow volume observed in the experiments.

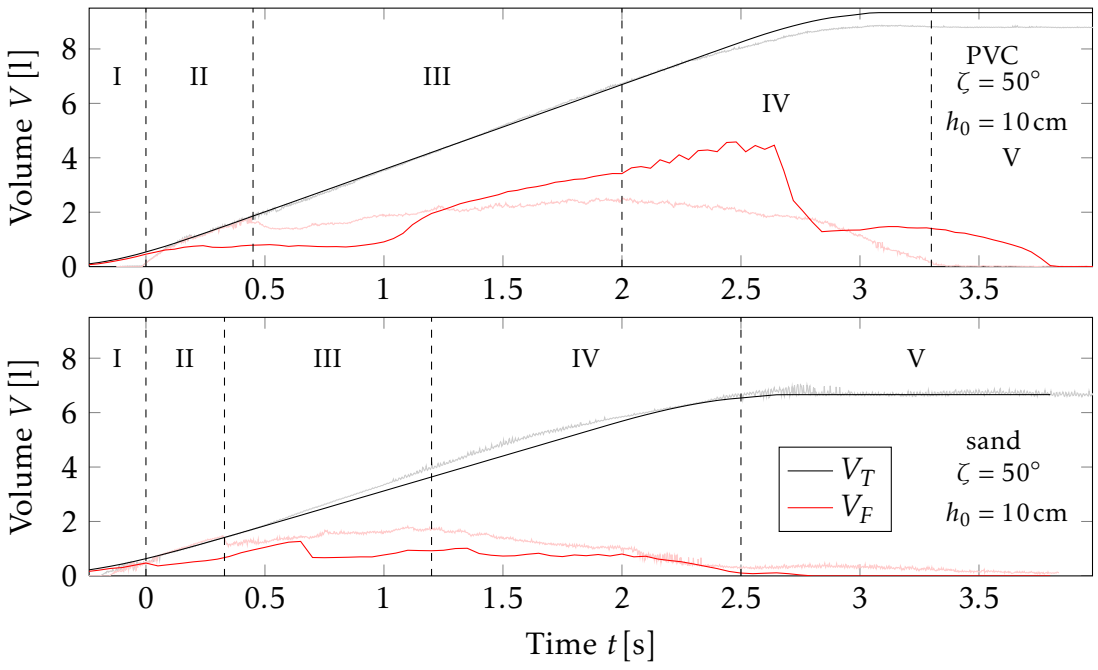

Figure 6.100 – OpenFOAM® simulations of shock formation: Comparison of temporal volume evolution of sand and PVC. Simulated temporal volume (total and flowing volume) evolution of PVC (upper panel) and sand (lower panel) at 50° inclination angle and 10 cm inflow height. For better comparison experimental results from Fig 6.91 are included (gray and light red lines).

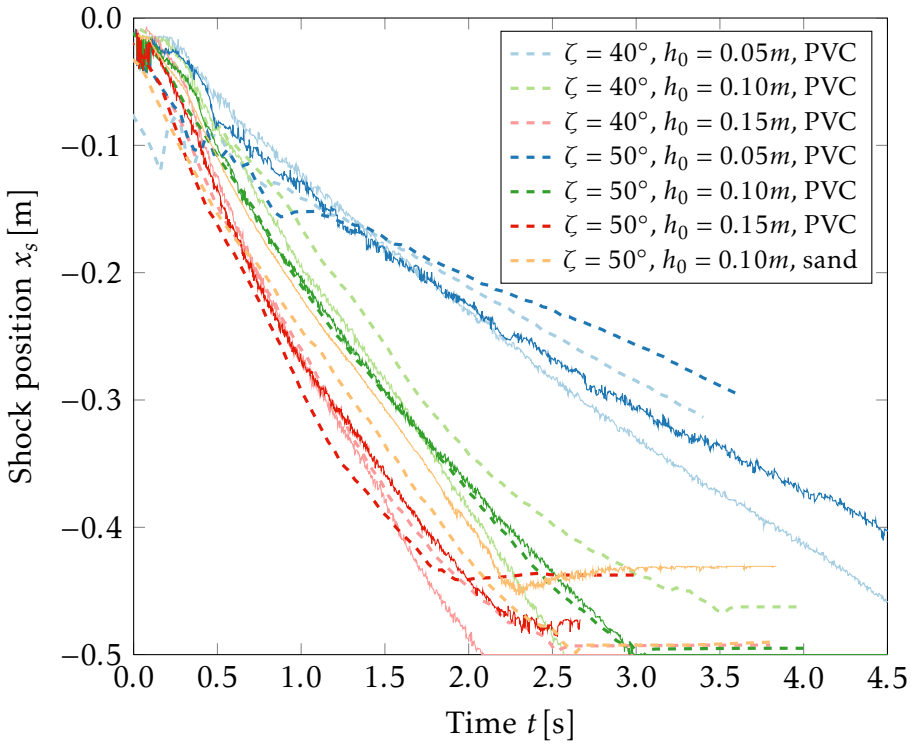

Figure 6.101 – OpenFOAM® simulations of shock formation: Temporal evolution of shock front position. Time-depended movement of the simulated shock front (interface between deposited material and flowing material) for PVC and sand at different inclination angles and inflow heights. For better comparison experimental results from Fig 6.92 are included (continuous lines, same color code as for simulation).

observed thinning of the flowing fraction and the formation of the parabolic shaped final deposition.

Analysis of the simulated flowing and total volume fraction for the different inflow height and inclination angles reveal that the simulation is overall well capable to predict the fraction of fluidized material for a given inflow volume (Fig. 6.99). However, the flowing volume in the case of 5 cm inflow height is underestimated for both inclination angles. The detailed evolutions of the flowing volumes for 10 and 15 cm inflow height show that the simulated flows are fluctuating. Compared to the experimentally observed volume evolution the simulated evolution displays a stronger variance and does not reach a continuous phase as seen in the experiment. These fluctuations can be explained by the way of determining volumes from the simulation results employed here: a cutoff in velocities needs to be specified during the evaluation of the simulation to describe the stop condition. Thus, the material seems to be deposited faster in the beginning (prior to the start of phase III in the experiment) but the estimated deposition becomes unstable afterwards and thus a larger fraction than in the experiment is considered to be fluidized towards the end of phase III. Nevertheless, the order of magnitude of the flowing fraction and the overall volume is well predicted for 10 and 15 cm inflow height. Especially in the

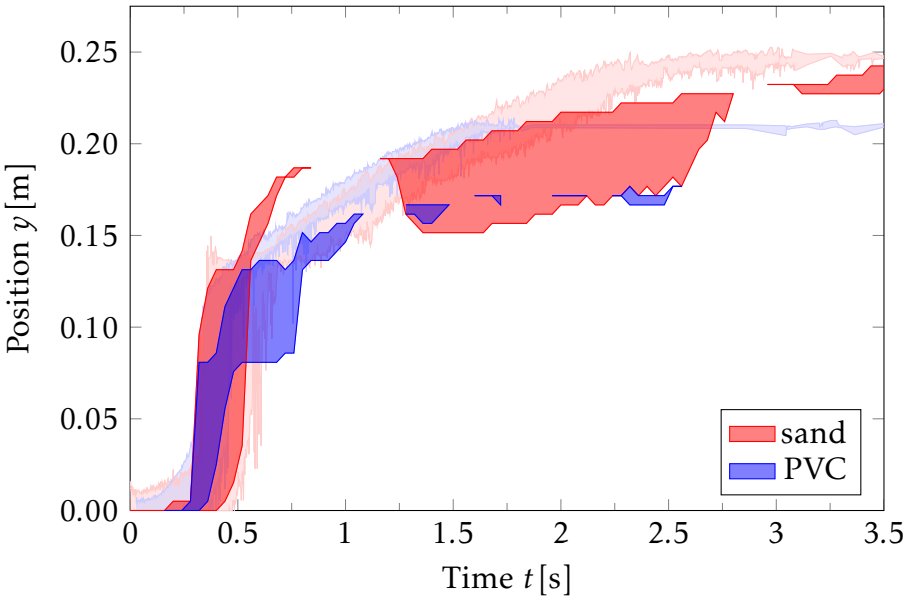

Figure 6.102 – OpenFOAM® simulations of shock formation: Temporal height evolution at a fixed position. Simulated temporal evolution of flow position in y-direction at a fixed position in the channel ($x = -5$ cm) at 50° inclination angle and 10 cm inflow height. The strong colored lines represent the solid-fluid and the fluid-air interface for the respective material, the lighter colored surface in between indicates the complete flowing layer. For better comparison experimental results from Fig 6.93 are included (semi-transparent).

case of 40° inclination angle and 15 cm inflow height, the predicted flow volume is very well predicted throughout the observed time.

Comparison of the simulations with sand and PVC at 10 cm inflow height and 50° inclination angle reveal that the simulation is well capable of capturing differences between the two materials: the simulated flowing volume for sand is smaller than that of PVC throughout the observed time as in the experiment (Fig. 6.100). In general, the evolution of the flowing volume for sand is reasonably well predicted but underestimated.

The evolution of the flow front position (Fig. 6.101) is on average equally well predicted as in the case of the Savage-Hutter simulations (Fig. 6.97). In the two cases with 5 cm inflow height, the velocity of the flow front is underestimated by the simulation, which is in agreement with the underestimation of the flowing fraction in those cases. In the case of 10 cm inflow height and 40° inclination angle the shock velocity (the inclination of the curve) is well predicted but a small offset in the beginning of the simulation causes some deviation from the observed curve. This can be explained by some artifacts occurring in the beginning of the simulation due to the VOF method. All other simulations show an accurate prediction of the experimentally observed flow front positions. Also the increase in slope for increasing inflow heights and the independence of the slopes towards inclination angles and material are correctly predicted.

Concerning the temporal evolution of the deposit and height of the fluidized fraction

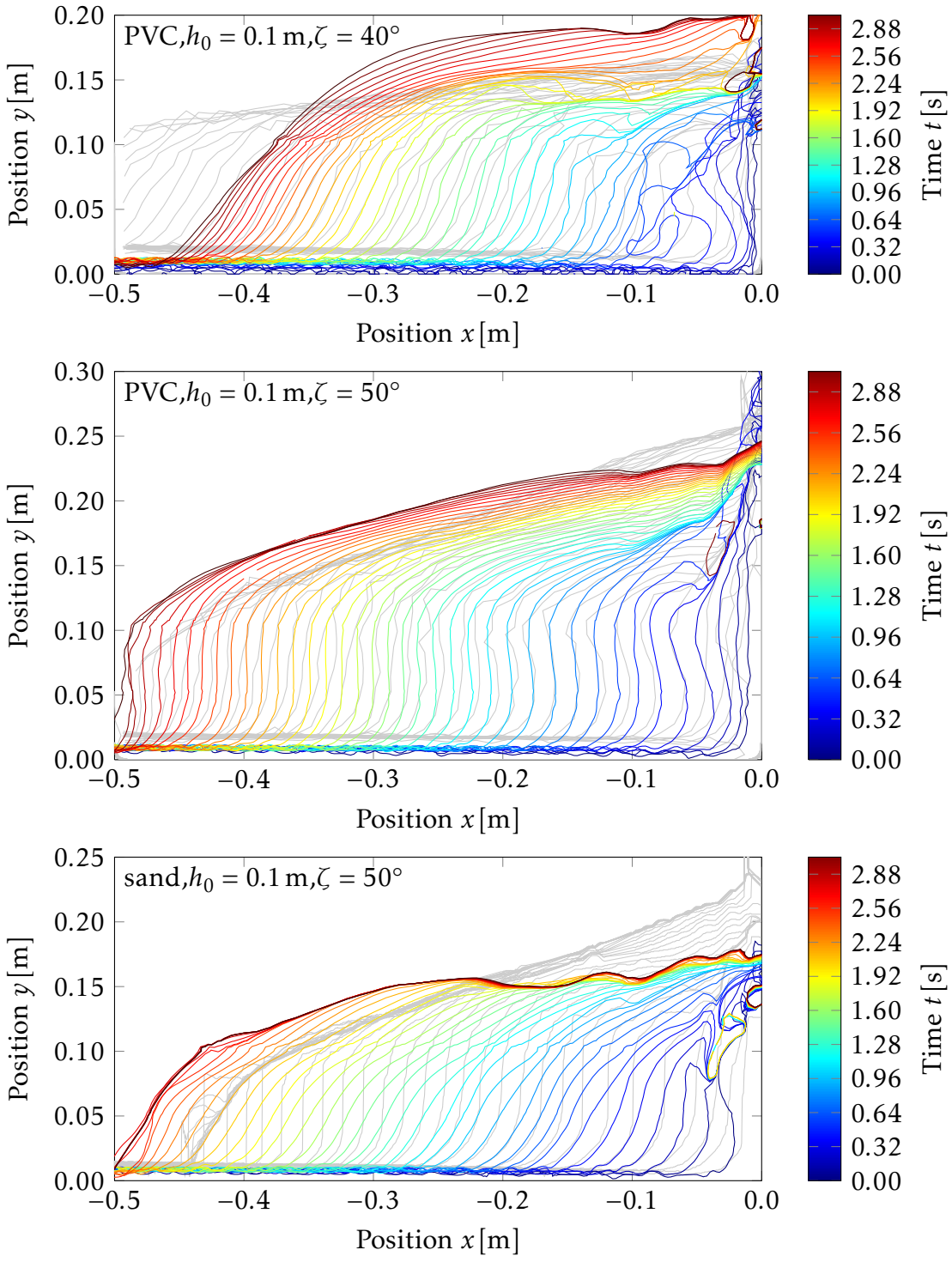

Figure 6.103 – OpenFOAM® simulations of shock formation: Temporal evolution of flow geometry. Simulated evolution of free surface geometry during the shock formation for different inclination angles (40° and 50° PVC, 50° sand) at a fixed inflow height of 10 cm. For better comparison experimental results from Fig 6.94 are included (gray lines).

for PVC and sand at a fixed position (Fig. 6.102), the simulation is well capable of predicting the steep increase of the inflow height and the width of the flowing fraction in the moment when the shock front passes the observed point. Afterwards, the discontinuity of the flowing fraction determined from the simulation becomes obvious again. The flow stops for about 0.2 to 0.4 seconds and is re-initiated later. The height of the flow is underestimated for both material. Nevertheless, the simulation correctly predicts the thinner fluidized layer for PVC in comparison to sand.

The geometry evolution of the deposit over time for 10 cm inflow height and 50° inclination angle with PVC material is very accurately predicted by the simulation, except for a slight deviation in the shape of the final deposit (Fig. 6.103). Especially the inclination of the deposit at the shock front is well predicted, the angles higher than 90° in the first time steps and the 90° turn of the flow in the later time steps is accurately captured (Fig 6.103). The deposit geometry of 10 cm inflow height and 40° inclination angle illustrates the problems caused by the VOF method during the first steps of the simulation: due to the lower inflow rate at 40° and the resulting thinner flow, the density values decrease below the threshold for cells to be assigned as granular material containing cells. This results in the formation of air bubbles and thus to a breaking wave formed at the shock front. The air inclusion also causes a decrease in material density and thus leads to formation of a higher and shorter deposit than experimentally observed. Nevertheless, the inclination of the shock front is well captured in the simulation indication that apart from the numerical artifacts caused during the initialization the simulation is well capable of predicting changes in flow geometry due to changes in inclination angle. In the case of sand at 10 cm inflow height and 50° inclination angle the final shape is globally well predicted, only the length of the deposit is slightly overestimated while the height close to the wall is underestimated. The inclination of the shock front is less steep than for the PVC simulation, which is in agreement with the observed slopes. However, the simulated decrease in shock front inclination from PVC to sand is stronger than the actual one.

Taken together, the OpenFOAM® simulations are capable of simulating a shock formation with a sudden deceleration of the flow velocity as the flow impacts a wall. Differences in material, inclination angle and inflow height are well captured. However, some numerical problems lead to quantitative inaccuracy in the prediction.

6.6 Wide channel

The experiments performed in the inclined PMMA channel and the respective simulations demonstrated that the OpenFOAM® simulations introduced in this study are well capable to predict important flow parameters such as the flow geometry and the velocity field inside the flow for all considered problems except for the shock set-up. Neverthe-

less, these considerations were restricted to two dimensions. The flow behavior along the channel width was assumed to be constant due to the narrow channel character of the chute and could be neglected. To predict natural hazardous granular flows, it is however also important to predict the spreading and behavior of the flow in this direction. To perform three-dimensional experiments for the validation of the OpenFOAM® predictions, a wider chute with variable obstacles was used (section 5.2.3). Similar experiments were already performed for the validation of Savage-Hutter type simulations in a three-dimensional set-up (e.g. in Gray et al. (2003), Chiou et al. (2005) and Tai et al. (1999a)). Therefore, no Savage-Hutter type simulations were performed for this experiment.

6.6.1 Experimental findings

The experimental set-up allows the observation of granular flow around obstacles in three dimensions. The recording of such tree-dimensional experiments requires an image capturing set-up that strongly differs from the set-up for the two-dimensional measurements (see section 5.5). The set-up employed in this study allows 3D reconstruction of the flow surface with only one camera. However, velocity fields can not be recorded with this system. Three experiments were performed monitoring the flow behavior of sand during a steady flow phase around obstacles (Fig. 6.104). First, a tetrahedron was placed in the flow with one edge facing the upstream direction. This set-up mimics structures which redirect hazardous granular flows as the dams protecting the village Flateyri, Iceland (section 1.2.6). The measured height profile (Fig. 6.104 (a)) displays the expected behavior: the flow is redirected to both sides of the tetrahedron, resulting in a large sheltered area behind the obstacle similar to the behavior of avalanches in Flateyri (Jóhannesson, 2001). At both sides of the tetrahedron and especially in the redirected flow behind the obstacle, the flow height increases up to 4-fold as compared to the undisturbed flow in front of the obstacle and a sharp edge between the flow and the sheltered area is formed. In contrast, the flow remains almost unchanged in front of the obstacle and no deposition is formed. It has to noted here that the flow height also increases on the sides of the tetrahedron, but this steep inclination could not be captured with the experimental set-up. The second obstacle considered was a cylinder (Fig. 6.104 (b)): it also redirects the flow, but the observed sheltered area behind the obstacle is much smaller than in the case of a tetrahedron. The redirected flow reaches heights similar to the tetrahedron case but the flow height continuously decreases towards the sheltered area and no sharp edge is formed. Additionally, the cylinder also disturbed the flow in front of it, resulting in an increased flow height in front of the cylinder. As a third experiment, the tetrahedron was placed inside the chute with one face directed to the upstream direction (Fig. 6.104 (c)). Compared to the other tetrahedron experiment, the sheltered area is much smaller. The flow height strongly increases in front of the obstacle and two large areas of increased

flow height are formed on the sides of the tetrahedron. As in the case of the cylinder, the flow height continuously decreases towards the sheltered area. This tetrahedron experiment mimics one part of a deflecting structure which is intended to catch the flow rather than to gently redirect it. Due to the large deceleration of the flow and due to the strong geometrical support of the obstacle, a deposit is formed in this experiment (Fig. 6.104 (d)).

6.6.2 Non-depth-averaged simulations

In the case of the tetrahedron with the edge facing the upstream direction, a very good agreement with the experimental findings is observed. The flow height is qualitatively well predicted (Fig. 6.105 (a)). There is almost no congestion in front of the obstacle and the flow is redirected to the sides resulting in a sheltered area as observed in the experiment. Also the sharp edge between the flow and the sheltered area is well predicted. Only a slight underestimation of the spreading of the flow occurs, leading to an overestimation of the flow height behind the obstacle. Similar results are obtained for the cylinder: the flow height distribution and the formation of the sheltered area are qualitatively well predicted (Fig.6.105 (b)). Quantitatively, the initial catching of the material in front of the obstacle is predicted to be too localized and too strong and is thus not redirected wide enough to the sides of the obstacle. Nevertheless, the sheltered area is predicted quite well. The angle of redirection for the second tetrahedron experiment is clearly underestimated as well as the surface of the congestion. Thus, the flow height behind the obstacle is strongly overestimated in a small area facing the sheltered area and underestimated at the sides if the tetrahedron (Fig. 6.105 (c)). This is similar to the problem observed for the two-dimensional shock experiment: the flow is suddenly decelerated and the high pressure gradients cause instabilities. Despite of this, also here the sheltered are is predicted correctly. Also the tendencies of the flow behavior compared to the first tetrahedron experiment are predicted well: the sheltered area is reduced compared to the tetrahedron with an edge the upstream direction and the formation of a final deposition is correctly predicted as well, although the height of the deposit is slightly overestimated (Fig. 6.105 (d)).

Taken together, these results demonstrate that the simulation method using OpenFOAM® with simple Coulomb sliding is well capable of predicting basic features of three-dimensional granular flow behavior, even with strong flow structure interactions and redirection of the flow by obstacles. Especially the sheltered areas, which are of great importance for risk assessment, are well captured. Concerning the quantitative differences it should be noted that the assumed initial velocities in the simulations are only roughly estimated from the experiments. Shock formation and sudden deceleration of the flow also cause some qualitative deviations from the observed flow behavior but sheltered ar-

eas can still be very accurately predicted for differently shaped obstacles.

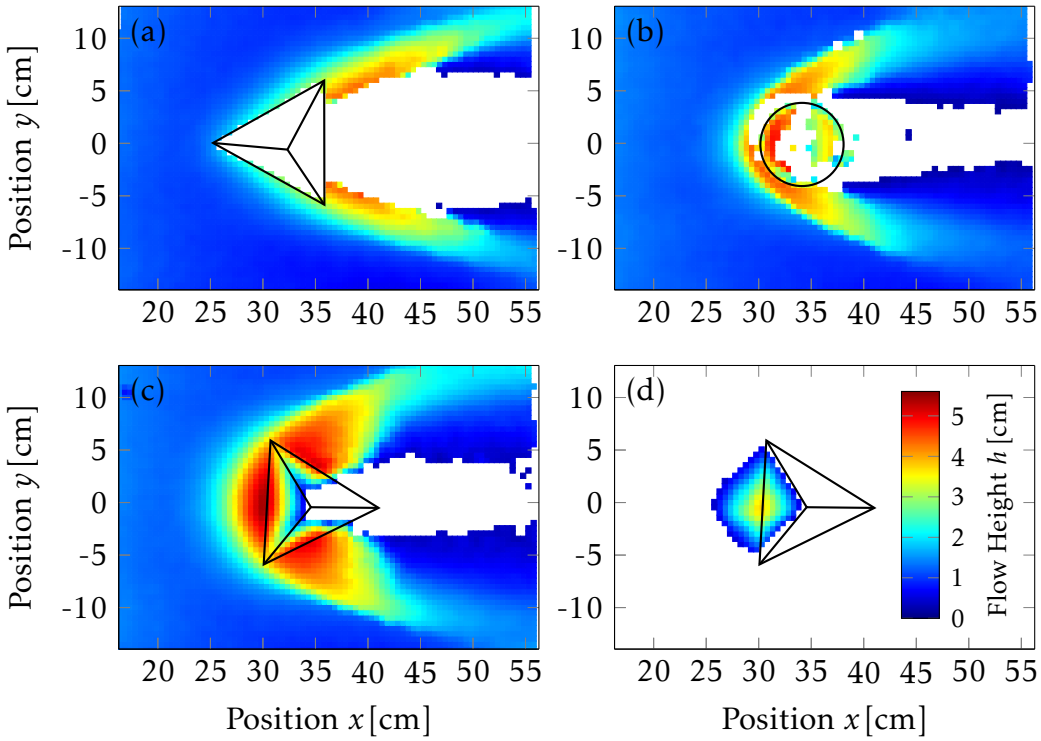

Figure 6.104 – Wide Channel: Experimental measurements. Flow thickness of a steady flows around obstacles (a-c). (d) depicts the final deposit of case (c), while no deposit is formed for cases (a) and (b). The flow thickness and deposit height on the obstacles is measured from the surface of the obstacle, not from the ground below the obstacle. Presence of material inside the obstacle in case (b) is due to the hollow character of the obstacles.

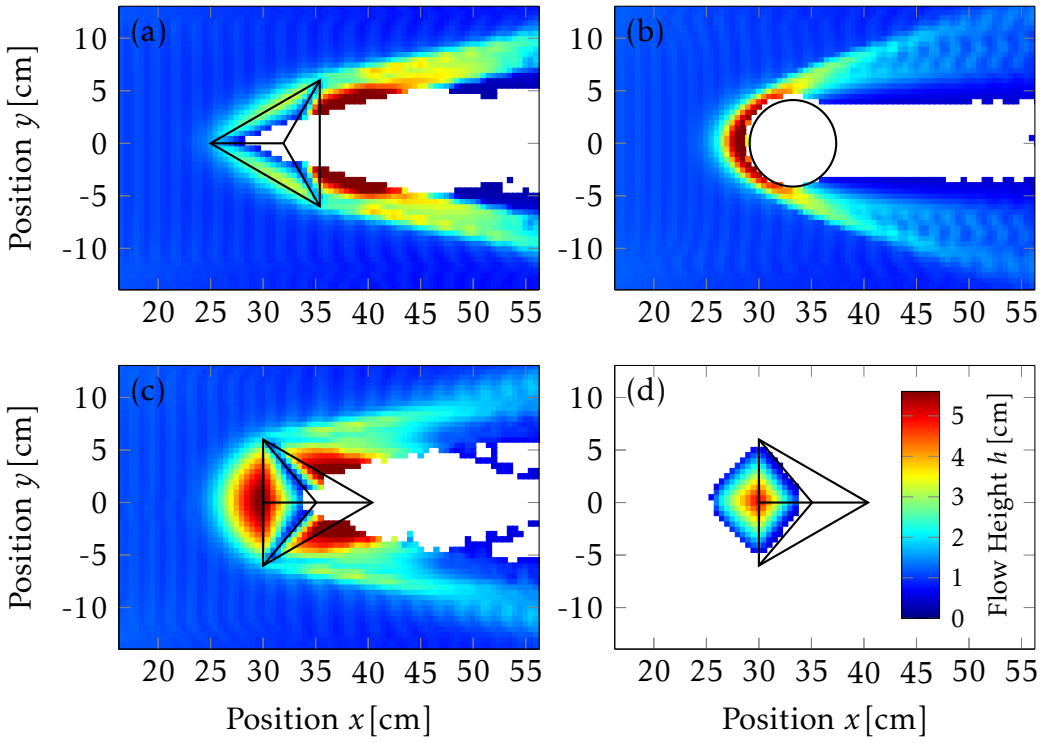

Figure 6.105 – Wide Channel: Numerical simulations with OpenFOAM® . Flow thickness of a steady flows around obstacles (a-c). (d) depicts the final deposit of case (c). Inflow boundary conditions: 1.5 cm inflow height at 1 m/s.

The previous chapter demonstrated that the non-depth-averaged simulations developed in this study are well capable of predicting the behavior of a granular flow in various laboratory experiments. Transferring the developed model and employed simulation technique to prediction of real case hazardous granular flows requires the following further pre-processing tools, tests and data: 1. the generation of a grid reflecting the topography of the considered site, which is at the same time suitable for the numerical scheme employed, 2. test simulations to demonstrate that the employed model can simulate granular flows on a complex topography and 3. detailed empirical data of hazardous granular flows for providing the initial and boundary conditions for the simulation (e.g., location, geometry and amount of the initial material) and information about the observed flow behavior, including the track taken by the flow, the run-out distance and deposition formation.

In this chapter, first a work flow to generate a grid suitable for the above described OpenFOAM® simulations from a real case topography is introduced. As a first validation of the mesh generation method in combination with non-depth-averaged OpenFOAM® simulations with the simple Coulomb model as introduced in the previous chapters, the procedure is then applied to simulate an experimentally observed three-dimensional channelized flow as described in Wieland et al. (1999). Then, a real case non-depth-averaged simulation using OpenFOAM® is analyzed in order to test the adaptability of the simulations to complex real topographies. The results of the simulation are furthermore compared to the available observed flow behavior.

As a real case hazardous granular flow to be simulated, an avalanche observed in the Swiss valley "In den Arelen" near Davos in 1968 was chosen (Christen et al., 2010b). The avalanche was a combined flow of snow mass from three release areas, which were channelized in a narrow valley and subsequently formed a three-armed deposit in a shallow run-out zone. As mentioned in Christen et al. (2010b), this event is well documented since it occurred in the vicinity of the SLF avalanche research station at Weissfluhjoch. From observed snow fall heights and weather conditions the initially involved snow mass could be extrapolated and the run-out zone as well as the damages caused by the avalanche were recorded in detail (Christen et al., 2010b). The avalanche is an example of dense dry snow avalanche without a powder or wet snow component and thus exactly the type of avalanche which can be described by the cohesionless granular flow simulation introduced in this study. Furthermore, the strong channelization resulted in large flow heights which require consideration of at least two dimensional events (Christen et al., 2010b). Additionally, large flow heights suggest strong influence of internal friction and

thus formation of a velocity profile through the flow depth which could not be captured by the so far employed state-of-the-art depth-averaged simulations and would be better characterized by non-depth-averaged three-dimensional simulations as suggested in this work.

7.1 Mesh generation and initialization

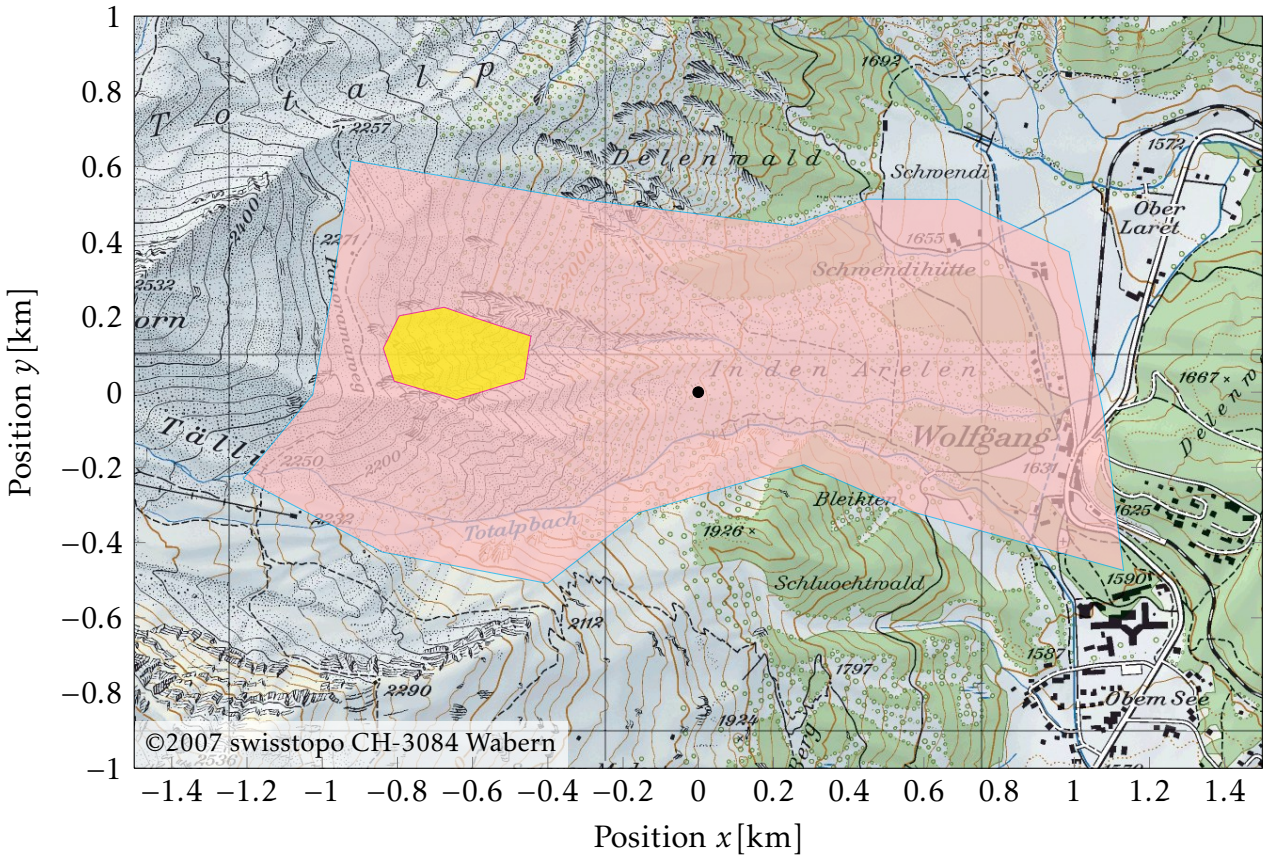

Figure 7.1 – Simulations of "In den Arelen" avalanche: Area of interest and initial filling. Overlay of topological map with area of interest employed for generation of topological mesh (pink area) and area of initial filling used in the simulations (yellow area). Map source: swisstopo, copyright: Bundesbehörden der Schweizerischen Eidgenossenschaft, 2007. `http://www.disclaimer.admin.ch`

Topological information for the area of interest was obtain from www.viewfinderpanoramas.org. This website offers surface height data of the Alps at 1 arc second resolution (digital elevation model (DEM)), which corresponds to a data point every 30 meters. The information is extracted by combination of satellite pictures and topological maps. More detailed terrain information is not freely available and can be purchased for single cases, which was not done for the test simulations performed here.

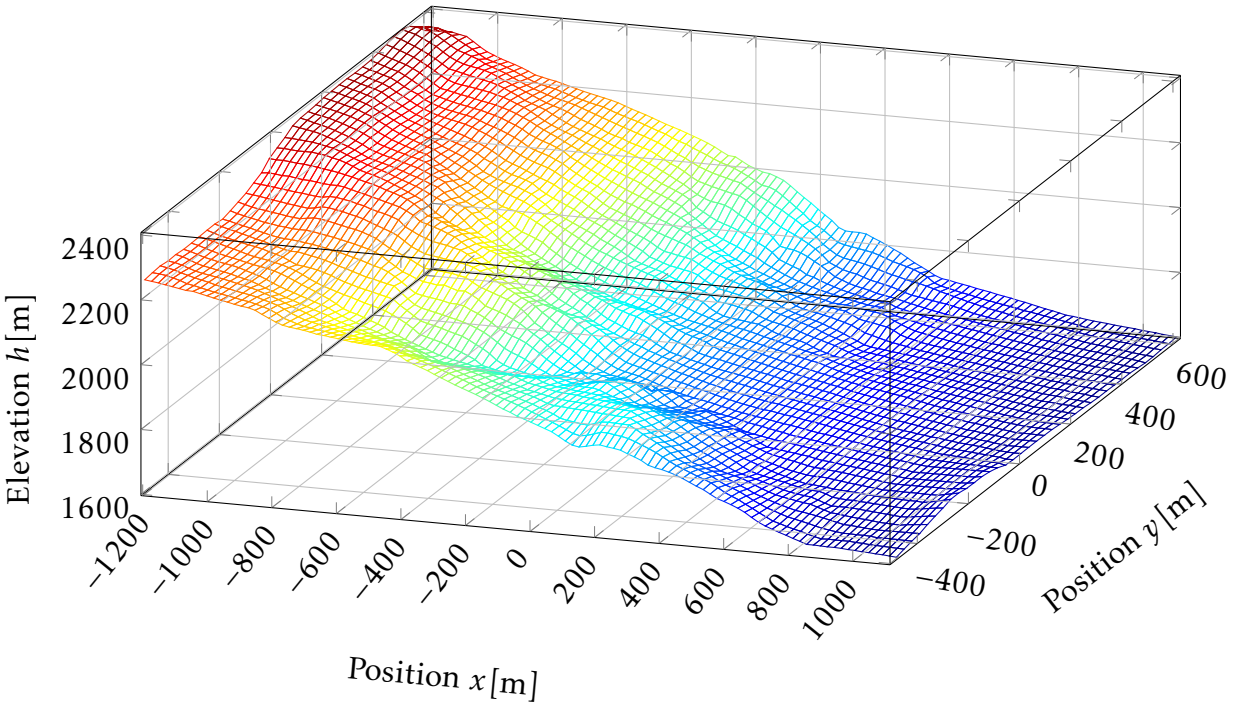

Figure 7.2 – Simulations of "In den Arelen" avalanche: DEM data. Representation of "In den Arelen" area topography in the boundary box of the area of interest extracted from DEM data with a resolution of 30 m. Colors correspond to elevation, reaching from blue for the lowest points in the area to red for the highest points.

From this website, tiles of 1° width covering the area of interest were obtained. To generate the three-dimensional contours of the area to be simulated, several steps and refinements are necessary: first, the area of interest (in this case the whole flank of the mountain) was sketched on a topological map as a polygon, pink area (Fig. 7.1). Via a series of custom scripts a rectangular boundary box was calculated from the coordinates of the area of interest and all DEM data points containing this area were extracted from the tiles and combined in one file (Fig. 7.2). The world geodetic coordinates (wgs) used in the databases are not handy to work with and where thus transformed into universal transverse Mercator coordinates (utm). To obtain smaller numbers for subsequent calculations, the origin of the utm coordinates was shifted to the middle of the area of interest. A three dimensional grid was generated from the DEM data by construction of parallelepipeds with a height of 50 m on top of each group of four points. This grid was then processed by the OpenFOAM® component BlockMeshDict for refinement of the grid cells (2 times in x/y-direction and 20 times in z-direction) and determination of the boundary surfaces of the previously created three-dimensional mesh. To save calculation time, this grid was trimmed to the area of interest in its original form (the polygon in Fig. 7.1) by deforming all cells overlapping with the boundary to this boundary: via a custom script, a series of triangles assembling in a 4 km high extruded polygon was generated on the

area of interest in the grid coordinates. These triangles and the grid were further processed using the OpenFOAM® component SnappyHexMesh to cut out the area of interest from the grid generated in the previous step (which contained the contours of the ground and the surface of the grid). By triangulation, the surfaces of all 6 boundaries (ground, top-surface and the four geographic directions) of the resulting grid were determined and kept for further processing.

To generate the final grid for the simulation, the same components and scripts as above were employed: first, a three-dimensional boundary box around the area of interest was created. This box was filled with a 10 m x 10 m x 10 m grid by BlockMeshDict. By combining this grid and the triangulated volume of interest in SnappyHexMesh, the cells overlapping with the boundary could be identified. These cell were then further refined depending on their position (up to 8 times at the bottom and 2 to 3 times at the sides and the surface). This refined grid was cut at the boundaries of the volume of interest and the cells overlapping with the boundary were deformed to match the boundary. This boundary cells were then further refined to introduce a boundary layer of small cells. Using the resulting grid, the non-depth-averaged OpenFOAM® simulation introduced in the previous chapters can be transferred to complex topographies.

7.1.1 Experimental verification of the proposed method

To validate the mesh generation method described in the previous section and to test the ability of the non-depth-averaged simulations with OpenFOAM® in combination with a complex grid, simulations for experiments described in Wieland et al. (1999) were performed. They introduced a channelized inclined chute which after 175 cm of constant inclination (40°) smoothly transits into a shallow run-out zone ending in a horizontal plane. The material used in the experiments was composed of rounded plastic beads (Vestolen) with a mean diameter of $d = 2 - 3.5\,\mathrm{mm}$, an internal friction angle of $\phi = 33°$ and a bottom friction angle of $\delta = 27°$. In agreement with the notation of Wieland et al. (1999) the experiment is hereafter referred to as V05. To initiate a flow, they placed a parabolic cap filled with the material inside the channel and released the material quickly by removing the cap. The resulting flow behavior was captured with a high speed camera and selected pictures showing the evolution of the flow at each quarter of a second are available in the publication. From these pictures, the outline of the flow during the different time steps is known and can be employed for comparisons with simulations. Additionally, Wieland et al. (1999) present a detailed height profile of the final deposit, which can be used for comparisons as well.

To include the channel topography of Wieland et al. (1999) into OpenFOAM®, artificial DEM data with a resolution of 1 cm x 1 cm was calculated from the provided curvi-

linear coordinates. The reference surface is described by:

$$\zeta = \begin{cases} \zeta_0 & \text{for } x < x_a \\ \zeta_0(x_b - x)/(x_b - x_a) & \text{for } x_a \le x \le x_b \\ 0 & \text{for } x_b < x \end{cases} \tag{7.1}$$

with $\zeta_0 = 40°$, $x_a = 175\,\text{cm}$ and $x_b = 215\,\text{cm}$. The superimposed bottom topography is defined by:

$$b = \begin{cases} \frac{y^2}{2R} & \text{for } x < x_a \\ \frac{y^2}{2R}\left\{3\left(\frac{x_b - x}{x_b - x_a}\right)^2 - 2\left(\frac{x_b - x}{x_b - x_a}\right)^3\right\} & \text{for } x_a \le x \le x_b \\ 0 & \text{for } x_b < x \end{cases} \tag{7.2}$$

with $R = 110\,\text{cm}$.

The initial free surface (the shape of the material in the cap) can be described by

$$s(x, y, 0) = (r^2 - x^2 - y^2)^{1/2} - (r - h_c) \tag{7.3}$$

with $h_c = 22\,\text{cm}$ and $r = 32\,\text{cm}$.

This data was then used to perform non-depth-averaged simulations with OpenFOAM® using the provided parameters for internal and bottom friction angle. The resulting prediction for the flow shape and height evolution over time is depicted in Figure 7.3. A good qualitative agreement with the experimental data is observed: first, the material stretches (mainly in the downslope direction) during the flow down the inclined part resulting in an "elliptic shape". When the material flows over the transition zone and enters the run-out zone, the flow front widens in transversal direction and a narrow languet is formed on the slope. Finally, all material enters the run-out zone and forms a "round deposit". Quantitative deviations from the experimental data are observed mainly at the flow front margin, mainly during the flow transition into the run-out zone. As a consequence, the frontal reach of the final deposit is not predicted to reach as far as the observed longitudinal run-out. However, the rear margin and the lateral extends of the flow and depositions are quite well simulated. Moreover, the final deposit height structure is well predicted by the simulations (Fig. 7.4): as observed in the experiment, the highest point is predicted to be closer to the chute side of the deposit, the simulated inclination of the deposit is similar to the observed inclination and steeper at the site facing the inclined channel. Also quantitatively a good agreement is observed with only a slight deviation from the highest observed value. Taken together, the results demonstrate the ability of the OpenFOAM® simulations introduced in this study to simulate flow behavior on topography included with the mesh generation method described in the previous section. This can be taken as a first hint that the OpenFOAM® simulations can be transferred to complex real topogra-

phies. This will be further examined in the next section for the real case avalanche “In den Arelen”.

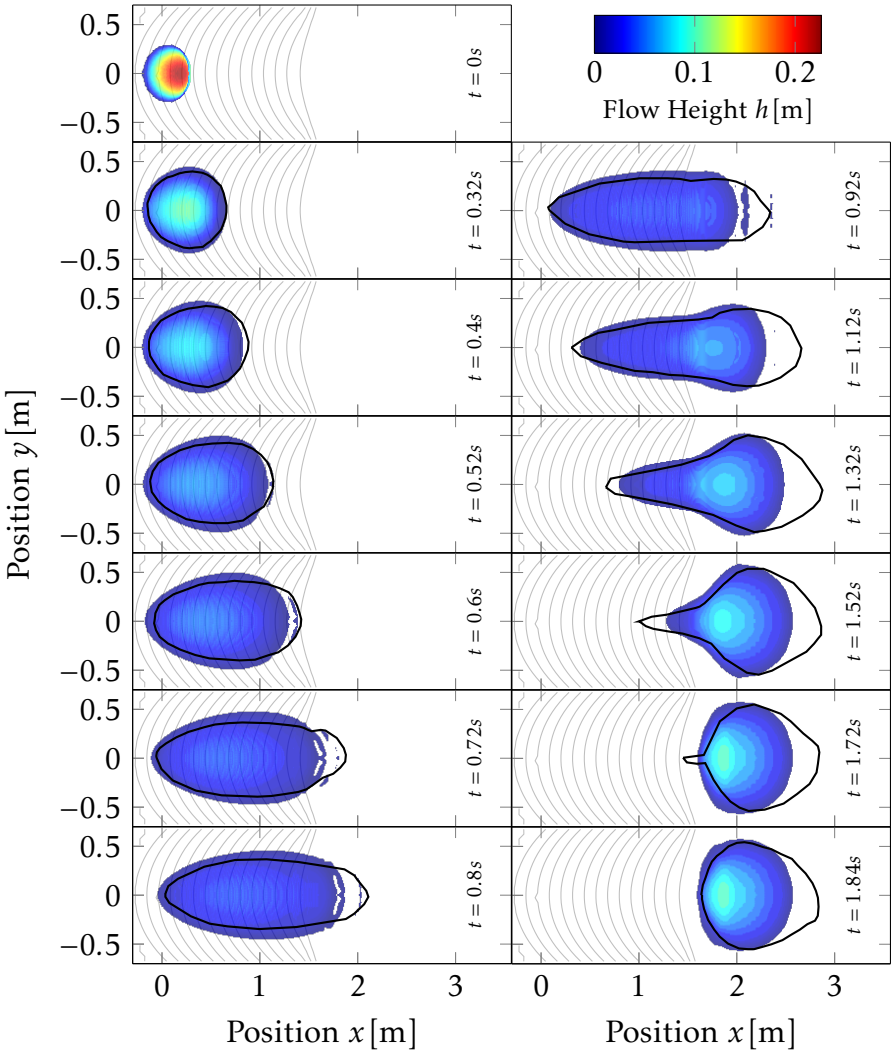

Figure 7.3 – Simulations of experiment V05 of Wieland et al. (1999): Temporal evolution of flow height. Simulated flow height for the experiment V05 of Wieland et al. (1999) as predicted by OpenFOAM®. Depicted are time steps as published by Wieland et al. (1999), the simulated flow height is represented by a heat map reaching from dark blue (lowest flow height) to dark red (highest flow height). Black lines represent the experimentally observed flow boundaries (Wieland et al. (1999)). Gray contour lines depict the channel topography.

7.2 Real mountain avalanche simulation: “In den Arelen”

To include the initial filling of material into the grid generated in section 7.1, a second polygon was selected in the area of interest (Fig. 7.1). The shape of this polygon was estimated from the initial area suggested in Christen et al. (2010b) considering the slope of the mountain side and including areas of 30° to 50° inclination. A custom script was employed to extract the coordinates of this polygon and to transform them into the grid

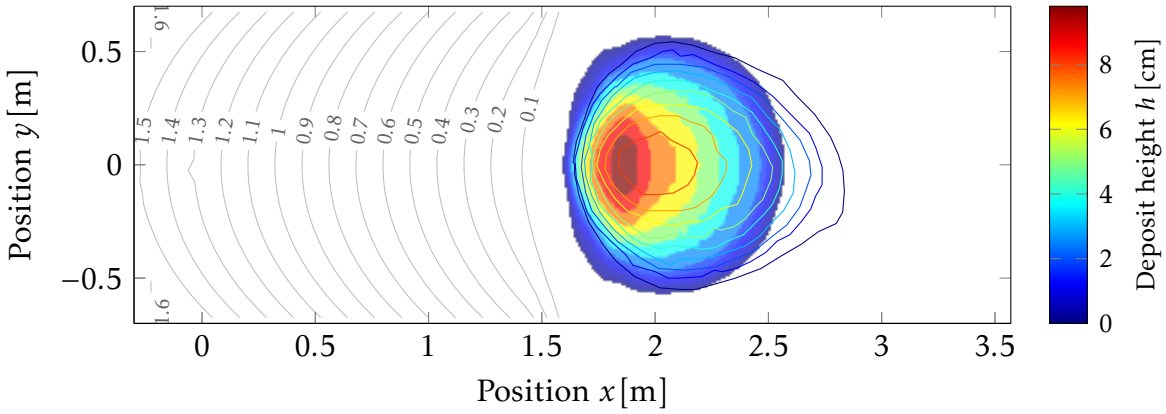

Figure 7.4 – Simulations of experiment V05 of Wieland et al. (1999): Final deposit. Outline and height of the final deposit predicted by OpenFOAM® for experiment V05 of Wieland et al. (1999). The height is represented by a heat map reaching from dark blue (low) to dark red (high). The contour lines of the experimental deposit are extracted from Wieland et al. (1999) and colored accordingly from dark blue (0 cm) to dark red (9 cm).

coordinates. The filling was performed by a custom program, which reads in the polygon coordinates. Afterwards, the closest point on the ground of the mesh is determined for each cell. Only cells for which the closest point was inside the polygon and which displayed a distance to the ground smaller or equal to the desired filling height (1.5 m in this case) the filling parameter α_1 was set to 1. In all other cases α_1 was set to 0. From this condition, an OpenFOAM® simulation was started using an internal friction angle of $\phi = 20°$ and a bottom friction angle of $\delta = 15°$. These values are rough estimates from the friction coefficients used in Christen et al. (2010b). Only the north western event of the avalanches was simulated.

The resulting simulations clearly demonstrate that the generated complex topography grid can be combined with the simple Coulomb simulation implemented in OpenFOAM® in this study (Fig. 7.5). No information about the exact track of the avalanche is available, but the simulated flow follows the expected track suggested by the topography. By considering the flow height over time (Fig. 7.5), the channelization of the avalanche is observed: the flow is strongly narrowed when it enters the gully-type valley (starting at $t = 8$s), leading to a rapidly increased flow height in the channelized part. Upon exiting the narrow valley and entering the more shallow run-out zone, the avalanche spreads out again and the flow height decreases (starting at $t = 32$s). A two armed final deposition is formed, where the norther arm reaches further downstream than the southern arm (Fig. 7.6). No data describing the on-track behavior of the avalanche is available, but the shape of the flow and the qualitative flow height distribution predicted in this work are in good agreement with a simulated prediction of the flow in Christen et al. (2010b). Concerning the recorded actual extent of the avalanche (Fig. 7.6, red line), most of the material is finally predicted to be deposited in this area and only a slight deviation occurs at the

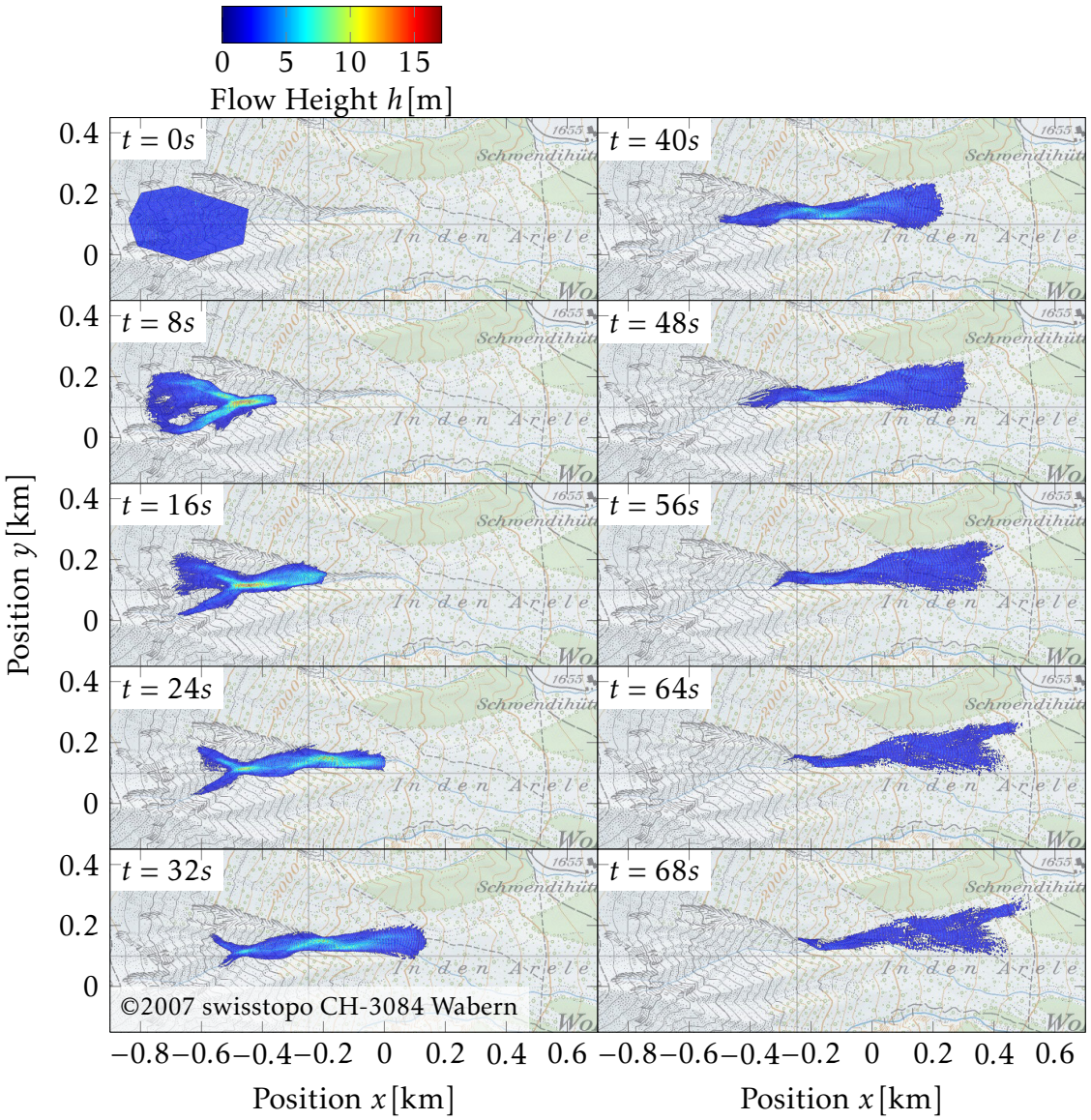

Figure 7.5 – Simulations of "In den Arelen" avalanche: Temporal evolution of flow height. Simulated flow height for the northern arm of the "In den Arelen" avalanche as predicted by OpenFOAM®. Depicted are time steps of 8 seconds, the flow height is represented by a heat map reaching from dark blue (lowest flow height) to dark red (highest flow height).

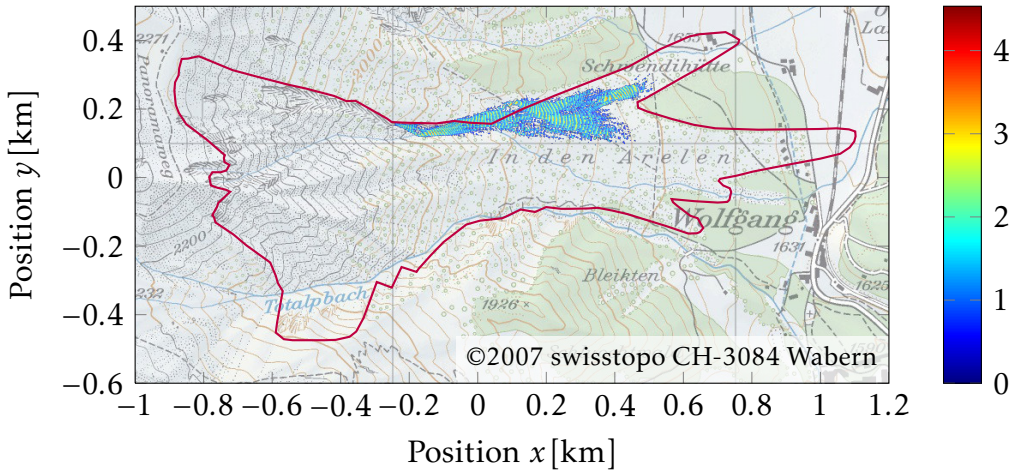

Figure 7.6 – Simulations of “In den Arelen” avalanche: Final deposit. Outline and height of the final deposit predicted by OpenFOAM® for the northern arm of the “In den Arelen” avalanche. The height is represented by a heat map reaching from dark blue (low) to dark red (high). The actually recorded outline of the avalanche extent (inundation) as described in Christen et al. (2010b) is depicted in red.

northern side. The extent of the run-out distance is underestimated by the simulation, probably due to deviations by the rough estimation of several parameters like the initial area, snow cover and the friction angles. The simulations performed here yield the full velocity profile during the complete flow of the avalanche. To illustrate the possibilities offered by this data, the surface velocity during the avalanche flow is depicted in Figure 7.7 as an example. No data was recorded for the velocities of the “In den Arelen” avalanche and no simulated data was published so far. Therefore, the result can only be evaluated based on expectations and on the physical correctness of the simulated flow behavior. As expected for a gravity driven flow, the surface velocity increases during the passage down the steep channel. When the avalanche enters the wide, open and more shallow run-out zone, the velocity decreases gradually until the deposition is formed. During the passage through the steep channel, predicted velocities are higher towards the middle of the flow, which could be explained by the friction encountered at the sides. Thus, the simulations yield physically reasonable predictions.

Taken together, the results demonstrate that the non-depth-averaged simulations employed in this study can be transferred to complex topographies of real case avalanches. Detailed evaluation of the predictive power will require further recording of real case avalanche data.

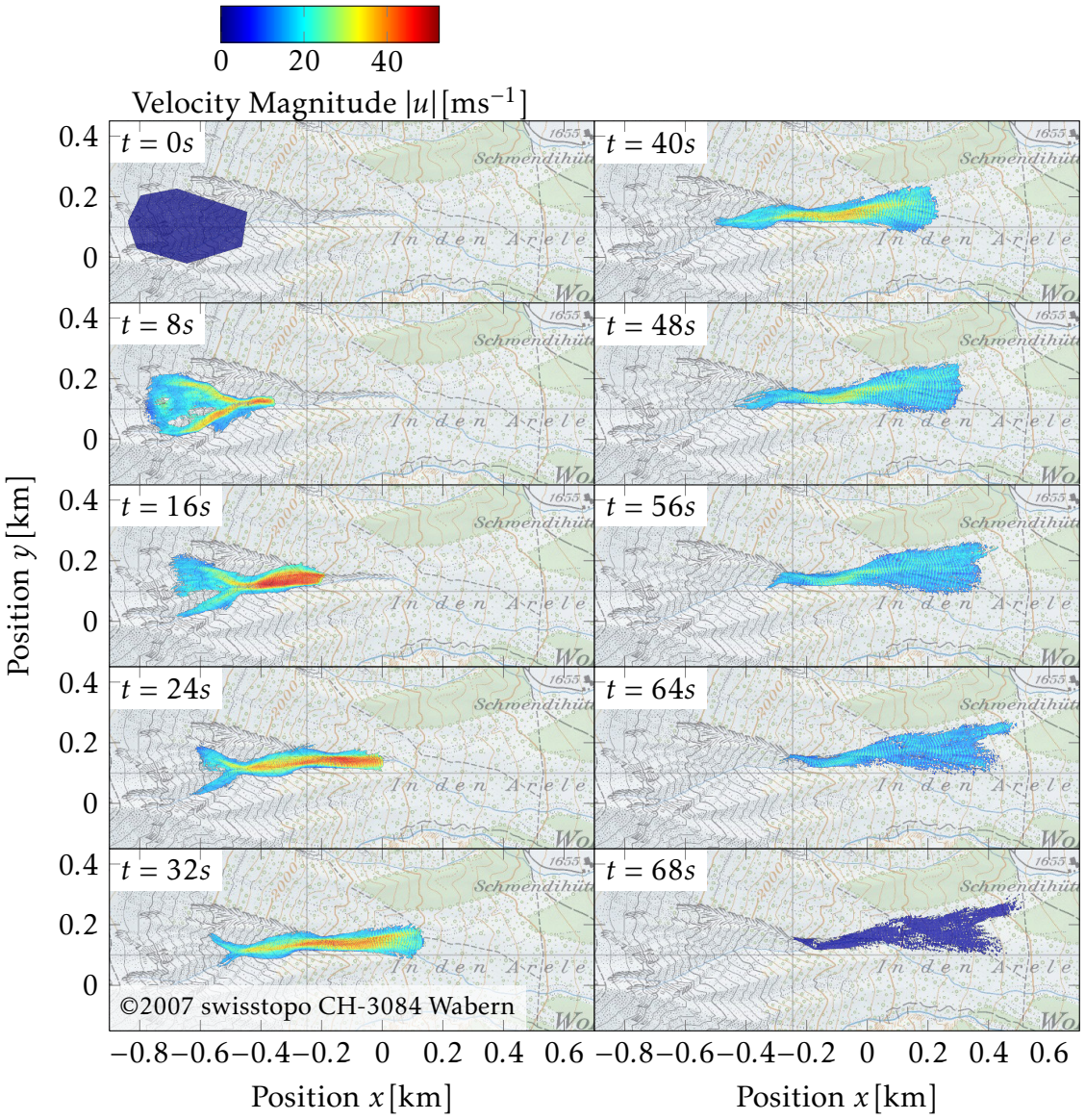

Figure 7.7 – Simulations of "In den Arelen" avalanche: Temporal evolution of surface velocity. Simulated surface velocity for the northern arm of the "In den Arelen" avalanche as predicted by OpenFOAM®. Depicted are time steps of 8 seconds, the surface velocity is represented by a heat map reaching from dark blue (resting fractions) to dark red (highest velocity).

8.1 Choice of the experiments

The experiments in this study were designed to, on the one hand, serve as models for various situations occurring during natural hazardous granular flows and should, on the other hand, yield experimentally observed flow variables and parameters for the comparison with numerical simulations. For this reason, they should allow observations of dynamic variables like velocity fields, flow height and parameters including volumes and solid-fluid interfaces. These are important quantities to understand the dynamics of granular flows and to later on calculate their destructive power by estimating the impact pressure on obstacles. To gain a better understanding of the behavior of granular flows, small scale experiments have been employed since the middle of the last century. Such experiments are still necessary for several reasons. First, in order to evaluate mutual dependencies of parameters, which can be varied separately in experiments while all other variables can be kept constant in controlled conditions. Second, because natural granular flows are hard to predict and thus often only their inundation area and final deposits are recorded, mapped or estimated but not the dynamics during the flow. Third, due to their dangerous character and their often huge dimensions, the above mentioned parameters are hard to determine for actual hazardous granular flows in nature.

8.1.1 Design of the channel and imaging system

As formulated in the aim of this study, the experimental set-up should be able to capture detailed velocity profiles in the flow direction and in the flow depth occurring during a granular flow. Transparent PMMA channels as employed in this study are widely used in the field of granular flow dynamics as they allow capturing of images which mimic a cross-section of a granular flow (Faug et al., 2002). In combination with the customized granular PIV software created in this study, detailed velocity profiles can be captured. In this context, it has to be noted that this PIV software will be made publicly available after the completion of this study. Thus, it could reduce the cost of the experimental set-up by thousands of Euro, which are usually required for an equivalent PIV system. The design of the channel was chosen in a way that allows recording over the complete time of most experiments with a typical high-speed camera available at that moment. For this reason, the length of the channel and the size of the silo were designed to perform experiments with a duration of around 4 seconds. At 4 seconds duration, the employed camera allows capturing images with a rate of 500 pictures per second. This speed was necessary for the

PIV technology for rapid granular flows. Thus, the experiment was designed to facilitate maximal recording of information concerning both temporal and spatial resolution and duration of the experiments.

Nevertheless, the analysis of the recorded experiments and the comparison with the simulation data also revealed some limitations of the experimental set-up, which should be taken into account for further designs. One problem caused by limited volume of the silo is that the amount of material which could be discharged in this time span was not high enough to allow completely constant discharge rates when the orifice was higher than 10 cm. Thus, the inflow of the material was slightly variable in these cases (for example in Fig. 6.90 where the volume increase is lowering towards the end of the experiment). Such small deviations from a constant flow rate could be avoided by a longer recording time and a larger silo of the channel. On the other hand, this would cause the cost for a high-speed camera to increase immensely and might not be necessary since the experiments in this work show that a steady-state flow is establish also with the silo size employed here. One point to consider is the adjustment of the camera and the channel. In order to only record the first layer of the flow and no fractions of the flow surface, the camera has to be very accurately adjusted. The present set-up did not allow a precise adjustment of the camera to the optimal height and angle for image capturing. The adjustment was performed manually and resulted in some errors in the estimation of the flow height when the material/air boarder was automatically captured. These errors had to be manually corrected in this work.

Another often observed source of differences between data and simulations is the influence of the side walls in channel experiments. Substantial influence of the side walls can lead to elevated angles of repose as seen for the rotating box experiment in this work (section 6.1.3). However, good agreements between experimental data and simulations was observed for both Savage-Hutter and OpenFOAM® simulations when the actual inclination angles were employed. Thus, the effects of the side walls seem to be negligible in the set-up employed here. Even more important than the effect of the side walls is the effect of the channel bottom. Two scenarios are possible here: the bottom can either be of the same smooth material as the channel walls or can be coated with the particles used in the experiments or other rough materials (Lube et al., 2011). In this work, the first possibility was chosen to allow capturing of the flow velocity from beneath the channel as presented in Figure 6.61. This procedure could be criticized because natural granular flows may occur on a ground which is similar to or composed of the granular material, e.g. mud flows sliding over ground made of the same soil or snow avalanches which sliding over a similar snow cover. However, also scenarios with a more smooth sliding surface occur frequently. One example are slab avalanches formed by the abrupt breaking of a weak layer. Such weak layers can be formed when fresh snow deposed on smooth, dense,

maybe partially molten and re-frozen smooth layers of old snow (Schweizer et al., 2003).

8.1.2 Choice of material

The two materials employed in the study represent the two fields which are mainly interested in rapid granular flow behavior: industrial processes (PVC) and hazardous granular flows like landslides (sand). Furthermore, the two materials differ in important characteristics like grain size and internal friction angle. A potential limitation of PVC particles is the presence of electrostatic forces inside the material during the flow. However, electrostatic forces can be assumed to be much smaller in sand. The fact that differences between the two material can be simulated by only considering their respective density and angle of repose rules out the possibility that electrostatic forces dominate the PVC flows. Thus, once a simulation has proven to be able to simulate the flow of both materials, it is very likely to be suited for other cohesionless materials as well. Such materials could be other plastics granulates, grains or pills in industrial processes and dry rock-soil mixtures often found in landslides. Many simulations, including the Savage-Hutter and Pudasaini-Hutter type of simulations focus on the simulation of snow avalanches, which cause huge damage in central Europe each year (see section 1.2.5.3). Especially, the highly destructive dry dense flow avalanches can be considered as cohesionless granular flows as described by the models employed in this study.

8.1.3 Experimental design

The high flexibility of the channel (large silo, adjustable outflow height, inclusion of obstacles, removable wall at the end) allow to perform experiments resembling all tree steps of an avalanche flow (initiation, steady-state flow and deposition) as well as the interaction with obstacles.

The performed dam break experiments allowed a detailed observation of the inception of a granular flow. In combination with the PIV measurements, it was possible to reconstruct the temporal succession of the fluidization events in the granular material. The dam break experiments with rectangular initial deposit were designed as such to function as models for the cases of mobilization and fluidization possible in nature: either a complete mobilization and fluidization and sliding of the complete mass down the slope (at 30° inclination and higher), or a partial mobilization and fluidization with a fraction of the material sliding down the slope (20°) or fluidization of a fraction which quickly comes to rest again close to the area of initialization and thus only causes local rearrangements (0° and 10° inclination). The triangular initial deposit experiment is an example for a fast mobilization and fluidization of a complete mass of granular material measured at higher slopes where, for example, snow avalanches often occur. Thus, in

combination, the performed inception experiments can serve as a model for a wide range of inception processes which can occur in hazardous granular flows in nature and are thus a good model to test simulation of these events for there predictive power. Here, it has to be noted that although the dam break experiments mimic the inception of a granular flow, these experiments do not focus on how and when a granular flow is initiated. The experiments are always designed in a way that requires them to initiate a granular flow as soon as the gate is opened since the free surface was raised above the critical angle of repose. Experiments on the criteria for initiation of granular flows require different experimental designs and were not the topic of this work.

The observations on the undisturbed flow were designed to mimic a steady state granular flow. For this experiment the size of the silo was crucial, as it allowed an almost constant inflow into the channel for several seconds. The experiment allowed to gain insight into velocity profiles both in flow direction and through the depth of the flow. This also allowed to test the predictive power of simulations on the height and velocity evolution of a granular flow at different locations on the slope. Furthermore, the experiment describes the ground state of the flow, which was then disturbed by the introduction of the obstacle. The obstacle is a model for a structure which suddenly disturbs, decelerates and redirects a granular flow. Especially for hazardous granular flows in nature it is important to predict the behavior of the flow in such cases. Such obstacles can be defense structured build for protection against granular flows like galleries over roads or trees, houses and other infrastructure components which are exposed to the flow. To calculate the risk of destruction and to built effective defense structures, the forces affecting the structures should be predicted. Therefore, the obstacle experiment can serve as a model to test the predictive power of simulations in such situations. In this special case, the two dimensional character of the channel is on the one hand limiting the information which can be obtained. Only the influence on the flow before and on the obstacle can be observed. No horizontal redirection of the flow can be observed. However, on the other hand, the observed experiment can be considered as a section through the events happening when an avalanche hits a long defense structure like a gallery build over a road. Usually, such structures are designed to span the complete risk area. Thus, the obstacle experiment is a very effective model for such cases.

Due to time limitations, it was not analyzed how the flow would reconstitute after the obstacle. Such experiments would be very useful to predict the efficiency of defense structures and are thus one potential further application for the experimental set-up introduced here.

The experiment on a shock formation at the end of the closed channel is in many ways similar to the obstacle experiment but still mimics a different situation: here, the obstacle in the way of the granular flow cannot be overcome by the flow, which causes the flow

to stop completely and form a shock front. This causes the formation of a large deposit and thus models one possible case of complete deposition of a granular flow. Again, the effective forces are of special interest here, since such situations occur during the impact of hazardous granular flows on infra structure elements.

Taken together, the performed experiments can serve as models for several aspects and stages of granular flow behavior and are thus well suited to test simulations for predictions of granular flow dynamics. The only exception not considered here are run-out zones in which the granular flow comes to rest without encountering an obstacle. This behavior is only mimicked in a minimal way in the dam break experiments with local rearrangement. Experiments with run-out zones after a rapid granular flow down the complete slope of the channel would require additional components for the experimental set-up and were not performed due to time limitations. Such experiments were for example described with low time resolution by Pudasaini et al. (2005a). Run-out experiments with the high resolution PIV set-up of this study are subject to further research.

8.1.4 Consequences of experimental results for further experiments and simulations of granular flows

The PIV measurements employed in this study revealed that the assumption of the granular material sliding down a slope as a block is not correct for the materials used in this study. The assumption of a block-like sliding behavior is a central aspect of depth-averaged simulations and models. The experiments reveal that a more detailed, non-depth-averaged description is needed to predict the actual velocity profile. The shape of the velocity profile measured in this study for the undisturbed flow is a linear one as it was described for similar experimental set-ups before (Ancey, 2001a). Thus, the experiments confirm the necessity of non-depth-averaged models for precise velocity prediction inside a granular flow.

The detailed PIV measurements and resulting strain rates and slip velocities for PVC during the obstacle experiment (Fig. 6.76) revealed that although a height increase of the flow just becomes obvious at -6 cm, a beginning increase in strain rate is already visible at -14 cm. This emphasizes the importance of strain rate observations and thus the necessity to record velocity profiles as facilitated by the PIV measurement technique established in this work. The flow geometry during the initiation of the obstacle experiment demonstrates the necessity to observe also pre-steady state events: the room occupied by the granular material (and thus the area affected by the flow) is larger during this initiation phase (Fig. 6.71). The obstacle experiment revealed also the necessity to employ different materials in such model experiments. While the PVC material could almost completely overcome the obstacle, a large deposition was formed by the sand. Additionally, the sand

flow is not distracted as far as the PVC flow. This demonstrates that also small differences in material parameters like density and internal friction angle of a granular material can cause dramatic differences when encountering an obstacle or defense structures. The differences also underpin the importance of correct capturing of material differences by simulations for risk assessment.

8.1.5 Three-dimensional experiments

The three-dimensional experiments in the wide channel allow to mimic the lateral spreading of a granular flow and thus complement the channel experiments which could not describe this part of a granular flow. Due to the employed set-up and the three-dimensional character of the experiments, velocity profiles inside the material could not be determined. Thus, only the flow height was measured for comparison with simulations. The main purpose of these experiments was to validate the simulations in three-dimensional cases, assuming that if the simulations predicted correct velocity profiles in the narrow channel and predict correct flow height in the wide channel one could infer that also here the velocity profiles would be predicted reasonably well. As mentioned in section 6.6.1, the experiments mimic situations which also occur during the impact of rapid granular flows on defense structures. The small scale experiment displayed the same behavior for the granular material as observed for snow avalanches when encountering huge defense structures of similar shape (Fig. 6.104 and Jóhannesson (2001)).

8.2 Achievements and limitations of the Savage-Hutter simulations

In terms of calculation power and time, depth-averaged simulations like the ones of the Savage-Hutter model are greatly advantageous compared to non-depth-averaged simulations as introduced here. Depth-averaged simulations can be run in a fraction of the time needed for non-depth-averaged simulations and do not require parallelization. They actually have minimal hardware requirements. Nevertheless, these simulations fail to precisely simulate important aspects of granular flows like velocity profiles along the flow depth and some interactions with obstacles as demonstrated in this work. In order to optimize predictive accuracy and computational resources, it is therefore necessary to evaluate which problems can be simulated with depth-averaged models and which ones require non-depth-averaged simulations. The results of this study regarding this question are summarized in Table 8.1. The Savage-Hutter simulations proved again, as shown by various publications (e.g., Hutter et al. (1995), for a review see Hutter et al. (2005)) well capable of predicting free surface shape evolutions and final deposits. Especially for

the undisturbed steady-state flow very good results are obtained. Here, a simple analytical solution (Pudasaini, 2011) was employed, highlighting the predictive power of the Savage-Hutter model even without the necessity of simulations for such simple cases.

8.3 Achivements, improvements to established models and limitations of OpenFOAM® simulations

As mentioned above, classical depth-averaged models do not predict velocity fields along the flow depth and cannot predict geometries involving a solid-liquid interface. The non-depth-averaged simulations employed in this study are able to overcome these limitations and yield highly resolved velocity fields and are able to predict solid-fluid interfaces for the channel experiments. The simulations also yield good predictions of the flow height in the three-dimensional experiments in the wider channel, for the flow shape and deposition height in the three dimensional channelized flow described by Wieland et al. (1999) and physically reasonable results in the real case avalanche simulation. In combination these results suggest that the OpenFOAM® simulations using a simple Coulomb model are capable of simulating real case hazardous granular flows in nature and will thus allow the prediction of velocity fields in such cases. Knowledge on velocity fields is very important for the estimation of the impact pressure and thus for the forces which are applied to infrastructure elements, buildings and defense structures.

Beside these obvious advantages over the depth-averaged models, the simulations in this work also revealed some cases where the OpenFOAM® simulations outperformed the classical depth-averaged simulations in predicting parameters which could be simulated by the Savage-Hutter model in theory (Tab. 8.1). The most obvious example is the obstacle experiment in the channel: the Savage-Hutter simulations completely fail to simulate

Table 8.1 ***(facing page)*** **– Summary of simulation capabilities.** Summary of simulation capabilities of the depth-averaged Savage-Hutter type simulations and the non-depth-averaged simulations with a simple Coulomb model implemented into OpenFOAM® in this study. Each row represents a variables tested in one of the comparisons between experimental data obtained from the PMMA channel experiment and simulations in this study. The capability of the simulations to predict the experimentally observed results is judged according to the qualitative and quantitative agreement. Additionally, the ability of the simulations to correctly predict the material influence, i.e. the differences observed between PVC and sand, and the influence of variations in the channel inclination is displayed. The capability is depicted by a color code, where green indicates good agreement between experiment and simulation, yellow indicates good agreement only in some cases which are specified in the respective cell of the table. Light red indicates low or no agreement with the experiment and red marks variables which cannot be determined due to the depth-averaged character of the Savage-Hutter type simulations. Gray marks not tested variables and white fields indicate not applicable.

		Savage-Hutter				OpenFoam			
		qualitative	quantitative	material influence	inclination influence	qualitative	quantitative	material influence	inclination influence
Rectangular container	Temporal evolution of flowing volume					only steeper inclination angles	only steeper inclination angles		
	Initial area						only 10° inclination		
	Final deposition								
	Temporal evolution of maximal flow height								
	Free surface shape evolution	only after flow flattening							
	Shape of flowing fraction/fluid solid interface								
	Height evolution perpendicular to fluid-liquid interface								
	Flow front and rear position						only rear position		
Triangular initial deposit	Free surface shape evolution	only after flow flattening							
	Temporal evolution of volume	only at later stages							
	Flow front and rear position						only front position		
	Velocity profile at gate								
	strain rate								
	slip velocity								
	spatial velocity over complete area		only surface velocity						
Undisturbed	Height profile over channel								
	Velocity profile over channel								
	Velocity profiles in y-direction						only PVC		
Obstacle inside channel	Velocity profiles in y-direction								
	Temporal evolution of flow height in front of obstacle								
	Temporal evolution of volumes						only PVC		
	Flow geometry and height during steady-state flow						only PVC until middle of obstacle		
	Strain rate					only PVC in front of obstacle			
	Slip velocity					only PVC in front of obstacle			
Shock formation	Temporal volume evolution						only some inflow heights		
	Temporal evolution of shock position						not for 5cm inflow height		
	Temporal evolution of deposition and flow height					only during first time-steps			
	Shape evolution of deposit (overall)		only PVC 50° inclination				only PVC 50° inclination		
	Inclination angle of deposit at shock front					only PVC			

this situation, although they were shown to be capable of simulating encountering of obstacles in real three-dimensional cases ((Pudasaini and Hutter, 2007; Cui and Gray, 2013)). Furthermore, resulting from the simplified treatment of the hydrostatic pressure, the Savage-Hutter model overestimates velocities in pressure dominated situations. This leads to a failure of the model to accurately predict the temporal evolution of flow behavior in such cases (e.g., temporal volume evolution and flow front and rear position in the case of the triangular initial deposit experiment).

8.3.1 Choice of rheological model and associated experiments

The rotating box set-up in combination with the PIV measurements in a rotating system introduced in this study allows determination of the best suited rheological model for the description of a material with a simple and easy to handle set-up. The square shape of the box causes a quasi-steady state flow with periodic disturbance and thus allows the observation of the materials response to such disturbances. This experiment allowed to characterize the employed granular material as plastic material. In combination with pilot simulations, it was further clarified that a pressure component is needed to describe the behavior of the material. As mentioned above, previously used models for the description of pressure influenced plastic flow behavior require hard to determine material parameters (section 6.1.2). For this reason, these models are not easy to transfer to other materials. Therefore, this study tested a simple Coulomb model which only requires the internal friction angle and the density of the material as input, which is a great advantage. These parameters are easy to determine for each given material. Thus, once a simulation has proven to correctly predict the material influence, the results can be easily transferred to other materials by adjusting the density and internal friction angle. The pilot simulation with the simple Coulomb model revealed that the model is indeed well suited to predict the flow behavior but only when higher internal friction angles than the measured ones are used. As suggested in section 6.1.3, this might be caused by the influence of the side walls (Savage, 1979; Hutter et al., 1995; Jop et al., 2005), which are probably very strong due to the thin layer of particles considered. The simulations of the experiment in the 10 cm wide channel and in the wide channel revealed that here the actual internal friction angles yield more accurate results. Furthermore, it could be shown that the influence of the material on the outcome of experiments could (with few exceptions) be well captured by the OpenFOAM® simulations with the simple Coulomb model. This suggest that the behavior of a granular material can be well predicted using a simple Coulomb model with only the internal friction angle and the material density as input parameters and will likely be transferable to other cohesionless materials. The good agreement between the OpenFOAM® simulations and the channelized flow experiment with Vestolen particles performed by Wieland et al. (1999) and the qualitatively

well predicted real case avalanche simulation in comparison to other simulations (Christen et al., 2010b) and the physically reasonable results for the velocity profiles seem to confirm this observation.

8.3.2 Limitations

The OpenFOAM® simulations with a simple Coulomb model introduced in this study yield a good agreement for most of the experimental set-ups tested, especially when qualitative agreement is considered (Tab. 8.1). Nevertheless, when quantitatively compared to the experiments, some deviations in the predictions occur. These deviations can be explained by several limitations of the OpenFOAM® simulations as well as of the experimental procedure. One limitation introduced by the experimental procedure is that the inflow could not be accurately determined in all cases due to the limited observed area and the slight fluctuations in the inflow rate. Also the initial flow height was difficult to determine due to the adjustment of the camera (see above). The inflow rate and the flow height were necessary parameters which had to be set in the case of the obstacle and shock experiments and small variations in the parameters used to the actual parameters might cause some of the deviation of the simulations from the experimental observation.

8.3.2.1 Problems caused by employed model

Beside the rheological model, also the model for the bottom friction has to be chosen for a fluid dynamics simulation as employed here. The bottom friction in the OpenFOAM® simulations was described as Coulomb-type friction as well in this study. This requires a bottom sliding angle to be set. As mentioned in section 6.2.3, the bottom sliding angle was set to be equal to the internal friction angle in this study by applying a stick condition. Nevertheless, the measured bottom sliding angle for sand and PVC on PMMA is lower than their internal friction angles (around 22° compared to 32° and 37° internal friction for PVC and sand, respectively). However, the results of the simulations yield the better predictions for the behavior of sand and PVC with the stick condition than with the actual measured bottom friction angle (data not shown). This indicates a stronger effective bottom friction in the PMMA channel experiments than measured. Bottom friction angles in this study were determined by filling a cylinder (without bottom) with the respective material, placing it in the channel and measuring the inclination which is necessary to make this cylinder start to slide down the channel. In this set-up, no rearrangements between the particles occur. The stronger effective bottom sliding friction and thus the higher bottom sliding angles suggested by the simulations might be caused by the high velocities of the particles and their strong shearing during the actual experiment. This might lead to some turbulent effects in the lowest layer, to canting between

the particles or to electrostatic forces between the particles. Another possible explanation would be the influence of the side walls. Further experiments have to clarify the exact cause for this observation. The hypothesis that the higher effective bottom friction is caused by the effects of the high velocities is enhanced by the observations during the dam break experiments. For high inclination angles, which cause high sliding velocities, the stick condition yields good predictions, whereas for medium inclination angles like (30°) the effective bottom sliding angles is below the internal friction angle. Therefore, the material is completely fluidized in the experiment but does not completely leave the channel in the simulations, as expected for inclinations below the assumed bottom sliding angle.

8.3.2.2 Problems caused by the simulation method

Some deviations between the experiments and the simulations can be explained by the VOF method. This method can cause artifacts observed at the fluid-air interface. At the interface, the filling parameter α_1 is employed to describe the composition of air and granular material in the interface cells. In these cells, the parameters of both materials are combined according to their abundance. This can cause the granular material to be less viscous in these boundary cells. In most of the cases, the fluid-air interface is only composed of one layer of cells and thus no strong influence on the flow behavior is observed. However, in cases of rapid filling changes (at the side walls of the rotating box (Fig. 6.7)) or when very thin layers of granular flow are observed (shortly before the impact in the shock experiments), artifacts like inclusion of air patches or breaking waves can occur.

Additionally, no sudden changes in pressure and flow height (for example at obstacle deposit formation) can be simulated. This problem has already been described by Jop et al. (2006). Since the model employed here can be understood as a simplification of the model introduced by Jop et al. (2006), it is not surprising to observe similar limitations. Addressing these problems will be subject to future research.

8.3.3 Application to complex topographies

As described in the previous sections, the OpenFOAM® simulations with simple Coulomb model introduced in this study are well suitable for non-depth-averaged simulations of rapid granular flows but require some improvements to reach the accuracy desired for predictions of real granular flows in hazard prevention. Nevertheless, prior to further investigations and research, it had to be ensured that the non-depth-averaged simulations introduced in this study are transferable to real case hazardous granular flows and that they can be performed on complex topographies. For this reason, the pilot simulations on

the channelized three dimensional flow experiments described by Wieland et al. (1999) and on the real case dry dense snow slab avalanche "In den Arelen" were performed (see chapter 7). In this chapter, a combination of programs and tools developed in this study with existing tools of OpenFOAM® was introduced to apply non-depth-averaged simulations using simple Coulomb friction to complex topographies. This technique allows inclusion of the actual, three-dimensional mountain topographies into the numerical simulations, which can be employed at any resolution provided a accurate map source is available. The simulations for the channelized three-dimensional flow experiments described by Wieland et al. (1999) demonstrated that the computational tools are well suitable for the introduction of three dimensional topographies into OpenFOAM® simulations. In this first pilot simulations, good agreements with experimentally observed results were obtained. The observable quantitative deviations might be explained by the preliminary character of the simulations like the coarse grid. The stick condition was not employed here since no influence of the side wall is expected.

Despite the fact that this pilot simulations demonstrated the transferability of the OpenFOAM® simulations to three dimensional topographies, it also demonstrates that the OpenFOAM® simulations are likely to yield good predictions for run-out zone, which is not tested in the channel experiments in this study.

Also the simulations performed on the complex real topography of the "In den Arelen" avalanche were only a rough estimate, since several parameters could not be determined exactly (like the initial area and mass and the bottom and internal friction angles of the material) and the mesh employed was coarse due to the 30 m resolution limit for public available data for the concerned area. Because of time limitations, the simulations were only performed once with one combination of ϕ and δ estimated from the friction coefficients used in Christen et al. (2010b). Despite these limitations, the qualitative flow behavior could be well captured and channelization of the flow and spreading of the material in the run-out zone was well predicted. Additionally, the simulated velocities yielded physically reasonable data. Together, these results demonstrate that the non-depth-averaged OpenFOAM® simulations with a simple Coulomb rheology performed in this study can be transferred to complex topographies. These simulations enable capturing of the full three-dimensional behavior of a hazardous granular flow including velocity and pressure fields. Especially when the refinements of the simulations described in the previous section will be included, further real case simulations can be performed and compared to actually observed flow behaviors. Validation of these simulations and particularly of the velocity fields and pressures will require further investigations on real case hazardous granular flows as suggested in the next chapter.

In this study, a series of experiments was performed to study the behavior of granular material sliding down inclined channels. Experiments were designed to serve as models for various situations occurring during hazardous granular flows in nature. In combination with the PIV system develop in this study, the experiments allow a detailed view on the velocity fields during a granular flow of PVC and sand particles. These observations revealed strong shearing results inside the granular material leading to steep velocity gradients inside the material especially during encountering of obstacles and shock formation. Thus, the experiments emphasized the necessity of non-depth-averaged simulations to correctly predict the events during a granular flow. A novel type of non-depth-averaged simulations employing simple Coulomb sliding as rheological model in fluid dynamics continuum mechanics numerical simulations was introduced and could be shown to be well suitable to predict the observed experimental events. In its predictive power, the model proved clearly superior to classical depth-averaged simulations with regards to the parameters which can be simulated and to the quantitative and qualitative agreement with the experiments. Nevertheless, the depth-averaged simulations performed in this study for comparison with the new model displayed a good agreement with the experiments concerning final deposits, free surface shape evolutions and undisturbed steady-state flows. Therefore, the results of this study can on the one hand serve as a guide when to employ the less resource intensive depth-averaged simulations and on the other hand supplies a non-depth-averaged model to be used in situations and for parameters where depth-averaged models fail. The type of non-depth-averaged simulations introduced in this study can be further extended in future to yield even more precise predictions. One possible extension would be the introduction of a variable density. This would enable the simulation of air uptake by the granular material and thus the prediction of volume increase as observed after the obstacle experiment in this study. In this case, the obstacle causes the material to spread and results in a decrease in density. Such situation would be important to simulate as the space occupied and thus the space effected by a hazardous granular flow increases upon volume increase. Another possible extension would be to allow the formation of shear bands in the granular material. This would enable the prediction of sudden deceleration of several layers of material and thus enhance the ability of the simulation to accurately predict fast deposition processes as observed during the shock formation or the obstacle inside the channel for sand.

Furthermore, additional experiments could be performed to test the predictive power of the non-depth-averaged model in run-out zones and to monitor the influence of obstacle inclinations on the granular flow. These experiments can be performed in the channel

designed for this study and are planned for the future.

Apart from this, the channel designed in this experiment and the PIV system can also be used to analyze the behavior of other granular flows like cohesive flows (e.g. wet granular material) and colloidal mixtures (e.g. mud/water mixtures). These experiments would mimic hazardous granular flows of the mud flow type.

An extension for both the experiment and the simulations would be the analysis of erosion and deposition at the channel bottom, thus monitoring if the granular flow can take up or loose material during the flow. This could be tested by introducing a second granular material with a higher internal and bottom friction angle. The channel could be filled with this material and the granular flow would be triggered to flow on top of this material. The PIV system developed in this work would then allow to observe erosion and deposition of the material. A simple way to perform such an experiment would be to include a compacted layer of slightly wet sand in the channel and let dry sand slip over this layer. This experiment would mimic for example the flow of a large dry dense slab avalanche triggered due to breaking of a weak layer. In such cases, the avalanche travels over a more compact older snow layer and can take up parts of this layer during the flow. The OpenFOAM® software used in this study would allow to include a third material (in addition to air and the first material) into the filling parameter α_1 Rusche (2002). Thus, erosion and deposition could be easily included in the model employed in this study. Erosion and thus entrainment of the granular flow with more snow mass might be one of the phenomena which would yield better results for the run-out behavior of real case avalanches, as the results of chapter 7 revealed an underestimation of the final deposit predicted by the OpenFOAM® simulations. Another application for mixtures of materials would be to monitor segregation events. They could be investigated in the channel by using mixtures of granular material varying in size and density. Such events can for example be important when large rocks, pieces of buildings or trees are transported by a hazardous granular flow.

Also the wide channel experiment introduced in this study could be employed for further investigations. One possibility would be the combination of various obstacle which can be freely placed in the channel. Another option would be the introduction of deformable obstacles or obstacles which can be removed by the granular flow and are transported along with the flow like trees in real case scenarios. OpenFOAM® offers various options for simulations of flows modifying the grid structure during the flow or to incorporate obstacles Rusche (2002). Thus, also deformation and displacement events could be included in the model introduced in this study. To obtain velocity information from the wide channel experiment, a PIV system using a second high speed camera and tracer particles could be included.

One great advantage of the simulations introduced in this study is that the velocity

and pressure field is predicted for every point of the granular flow. This allows the calculation of the impact pressure, which is of great importance for the destructive power of a granular flow in nature. However, only the velocities were measured in this study and the correctness of the calculated impact pressures could not be validated. Therefore, this parameter was not included in the simulation results. Future experiments should therefore include means for the measurement of the impact pressure. Possible solutions which could be included in the existing experimental set up are a scale instead of the wall at the end of the channel to measure the global impact pressure as introduced in (Faug et al., 2011; Moriguchi et al., 2009) or the usage of tracer particles measuring the a spatial pressure field as employed in large scale snow experiments.

The results in chapter 7 demonstrate that the model can be transferred to real scale hazardous natural granular flows and yields good qualitative predictions. Nevertheless, validation and further refinement of the model for snow avalanches and other natural granular flows would require more empirical data on the events taking place during the granular flow. So far, most reports only describe the final deposit of an avalanche and estimate the starting zone and material involved from the final situation. To overcome this problem, several research groups in alpine regions established observation areas in avalanche prone regions and install sensors for determination of velocities at places where avalanches are likely to pass by (e.g. in "Vallée de la Sionne", `http://www.slf.ch/ueber/organisation/warnung_praevention/projekte/vallee_de_la_sionne/index_EN`, 15.03.2013). However, these measurements are usually limited to single places inside the avalanches and broad spatial information is still lacking. It will be a challenging task in future research to install measurement instruments for monitoring of velocity fields inside real avalanches with fine spatial resolution. Additionally, detailed investigation on the internal and bottom sliding angles of different snow types (or soil types in the case of landslides) on different grounds would be necessary.

Taken together, the novel non-depth-averaged model build in this study by observing the performed experiments will serve as a basis for the development of a prediction model for real scale hazardous granular flows and is thus an important step towards the correct prediction of granular flow behavior for risk assessment in endangered regions.

C. Ancey. Dry granular flows down an inclined channel: Experimental investigations on the frictional-collisional regime. *Physical Review E*, 65(1):011304, 2001a.

C. Ancey. Snow avalanches. *Geomorphological Fluid Mechanics*, 319–338, 2001b.

C. Ancey. Are there dragon-kings events (ie genuine outliers) among extreme avalanches? *The European Physical Journal Special Topics*, 205(1):117–129, 2012.

C. Ancey and S. Cochard. The dam-break problem for Herschel-Bulkley viscoplastic fluids down steep flumes. *Journal of Non-Newtonian Fluid Mechanics*, 158(1-3):18 – 35, 2009.

C. Ancey, N. Andreini, and G. Epely-Chauvin. Viscoplastic dambreak waves: Review of simple computational approaches and comparison with experiments. *Advances in Water Resources*, 48:79–91, 2012.

R. Aris. *Vectors, tensors, and the basic equations of fluid mechanics*. Dover Pubns, 1989.

R. Artoni, A. C. Santomaso, F. Gabrieli, D. Tono, and S. Cola. Collapse of quasi-two-dimensional wet granular columns. *Physical Review E*, 87:032205, 2013.

R. A. Bagnold. Experiments on a gravity-free dispersion of large solid spheres in a newtonian fluid under shear. *Proceedings of the Royal Society of London. Series A. Mathematical and Physical Sciences*, 225(1160):49–63, 1954.

N. J. Balmforth and R. R. Kerswell. Granular collapse in two dimensions. *Journal of Fluid Mechanics*, 538:399–428, 2005.

H. Z. Barakat and J. A. Clark. Analytical and experimental study of the transient laminar natural convection flows in partially filled liquid containers. *Proc 3rd Int Heat Transfer Conf*, 2:152, 1966.

M. Barbolini and D. Issler. Avalanche test sites and research equipment in Europe: an updated overview. *Final-Report Deliverable D*, 8, 2006.

M. Barbolini, F. Cappabianca, and R. Sailer. Empirical estimate of vulnerability relations for use in snow avalanche risk assessment. *Risk Analysis IV*, 533–542, 2004.

M. Barbolini, A. Biancardi, L. Natale, and M. Pagliardi. A low cost system for the estimation of concentration and velocity profiles in rapid dry granular flows. *Cold Regions Science and Technology*, 43(1):49–61, 2005.

P. Bartelt, L. B. Salm, and U. Gruberl. Calculating dense-snow avalanche runout using a Voellmy fluid model with active/passive longitudinal straining. *Journal of Glaciology*, 45(150):242–254, 1999.

P. Bebi, D. Kulakowski, and C. Rixen. Snow avalanche disturbances in forest ecosystems – State of research and implications for management. *Forest Ecology and Management*, 257(9):1883–1892, 2009.

E. C. Bingham. *An investigation of the laws of plastic flow*, volume 13. Govt. Print. Off., 1917.

R. B. Bird, R. C. Armstrong, and O. Hassager. *Dynamics of polymeric liquids. Vol. 1: Fluid mechanics*. John Wiley and Sons Inc., New York, NY, 1987.

F. Bouchut, E. Fernández-Nieto, A. Mangeney, and P.-Y. Lagrée. On new erosion models of savage-hutter type for avalanches. *Acta Mechanica*, 199:181–208, 2008.

E. Bovet, B. Chiaia, and L. Preziosi. A new model for snow avalanche dynamics based on non-Newtonian fluids. *Meccanica*, 45(6):753–765, 2010.

G. Bradski. The OpenCV Library. *Dr. Dobb's Journal of Software Tools*, 2000.

E. A. Bryant. *Natural Hazards-Threat, Disaster, Effect, Response*. Cambridge University Press, Melbourne, 1991.

O. Buser and H. Frutiger. Über maximale Auslaufstrecken von Lawinen und die Bestimmung der Reibungswerte μ und ϵ. *Internationales Symposion INTERPRAEVENT*, 3: 125–134, 1980.

J. Canny. A computational approach to edge detection. *Pattern Analysis and Machine Intelligence, IEEE Transactions on*, PAMI-8(6):679 –698, 1986.

R.-H. Chen, K. J. Kuo, Y.-N. Chen, and C.-W. Ku. Model tests for studying the failure mechanism of dry granular soil slopes. *Engineering Geology*, 119(1-2):51 – 63, 2011.

M.-C. Chiou, Y. Wang, and K. Hutter. Influence of obstacles on rapid granular flows. *Acta Mechanica*, 175:105–122, 2005.

A. J. Chorin. Numerical solution of the Navier-Stokes equations. *Mathematics of Computation*, 22(104):745–762, 1968.

M. Christen, J. Kowalski, and P. Bartelt. RAMMS: Numerical simulation of dense snow avalanches in three-dimensional terrain. *Cold Regions Science and Technology*, 63(1): 1–14, 2010a.

M. Christen, P. Bartelt, and U. Gruber. AVAL-1D: An avalanche dynamics program for the practice. In *International Congress Interpraevent*, 715–725, 2002.

M. Christen, P. Bartelt, and J. Kowalski. Back calculation of the in den arelen avalanche with RAMMS: interpretation of model results. *Annals of Glaciology*, 51(54):161–168, 2010b.

M. Christen, Y. Bühler, P. Bartelt, R. Leine, J. Glover, A. Schweizer, C. Graf, B. W. McArdell, W. Gerber, Y. Deubelbeiss, T. Feistl, and A. Volkwein. Integral hazard management using a unified software environment. In *Proceedings of 12th Congress Interprevent*, 77–86, 2012.

C. A. Coulomb. In memories de mathematique et de physique. *Academic Royal des Sciences par diver sans*, 7:343–382, 1773.

R. Courant, K. Friedrichs, and H. Lewy. Über die partiellen Differenzengleichungen der mathematischen Physik. *Mathematische Annalen*, 100(1):32–74, 1928.

R. Courant, E. Isaacson, and M. Rees. On the solution of nonlinear hyperbolic differential equations by finite differences. *Communications on Pure and Applied Mathematics*, 5(3): 243–255, 1952.

G. B. Crosta, H. Chen, and C. F. Lee. Replay of the 1987 Val Pola landslide, Italian alps. *Geomorphology*, 60(1-2):127 – 146, 2004.

X. Cui and J. M. N. T. Gray. Gravity-driven granular free-surface flow around a circular cylinder. *Journal of Fluid Mechanics*, 720:314–337, 2013.

J. Cuzzi, R. Clark, G. Filacchione, R. French, R. Johnson, E. Marouf, and L. Spilker. Ring particle composition and size distribution. In *Saturn from Cassini-Huygens*, 459–509. Springer, 2009.

A. Daerr and S. Douady. Two types of avalanche behaviour in granular media. *Nature*, 399(6733):241–243, 1999.

F. V. De Blasio. *Introduction to the Physics of Landslides: Lecture Notes on the Dynamics of Mass Wasting*. Springer Verlag, 2011.

A. J. C. B. de Saint-Venant. Théorie du mouvement non permanent des eaux, avec application aux crues des rivières et à l'introduction des marées dans leurs lits. *Comptes Rendus des séances de l'Académie des Sciences*, 73:237–240, 1871.

S. J. de Vet, B. Yohannes, K. M. Hill, and J. R. de Bruyn. Collapse of a rectangular well in a quasi-two-dimensional granular bed. *Physical Review E*, 82:041304, 2010.

R. P. Denlinger and R. M. Iverson. Flow of variably fluidized granular masses across three-dimensional terrain: 2. Numerical predictions and experimental tests. *Journal of Geophysical Research*, 106(B1):553–566, 2001.

Y. Deubelbeiss and C. Graf. Two different starting conditions in numerical debris flow models–Case study at Dorfbach, Randa (Valais, Switzerland). *GRAF, C.(Red.) Mattertal–ein Tal in Bewegung. Publikation zur Jahrestagung der Schweizerischen Geomorphologischen Gesellschaft*, 29:125–138, 2013.

E. E. Doyle, H. E. Huppert, G. Lube, H. M. Mader, and R. S. J. Sparks. Static and flowing regions in granular collapses down channels: Insights from a sedimenting shallow water model. *Physics of Fluids*, 19(10):106601, 2007.

R. O. Duda and P. E. Hart. Use of the Hough transformation to detect lines and curves in pictures. *Communications of the ACM*, 15(1):11–15, 1972.

J. Duran. *Sands, powders, and grains*. Springer New York, 2000.

W. Eckart, J. M. N. T. Gray, and K. Hutter. Particle Image Velocimetry (PIV) for granular avalanches on inclined planes. In K. Hutter and N. Kirchner, editors, *Dynamic Response of Granular and Porous Materials under Large and Catastrophic Deformations*, volume 11 of *Lecture Notes in Applied and Computational Mechanics*, 195–218. Springer Berlin Heidelberg, 2003.

N. Eckert, E. Parent, M. Naaim, and D. Richard. Bayesian stochastic modelling for avalanche predetermination: from a general system framework to return period computations. *Stochastic Environmental Research and Risk Assessment*, 22(2):185–206, 2008.

D. Ertaş and T. C. Halsey. Granular gravitational collapse and chute flow. *EPL (Europhysics Letters)*, 60(6):931, 2002.

C. Fang, Y. Wang, and K. Hutter. A unified evolution equation for the Cauchy stress tensor of an isotropic elasto-visco-plastic material. *Continuum Mechanics and Thermodynamics*, 19(7):423–440, 2008.

T. Faug, P. Lachamp, and M. Naaim. Experimental investigation on steady granular flows interacting with an obstacle down an inclined channel: study of the dead zone upstream from the obstacle. Application to interaction between dense snow avalanches and defence structures. *Natural Hazards and Earth System Science*, 2(3/4):187–191, 2002.

T. Faug, P. Caccamo, and B. Chanut. Equation for the force experienced by a wall overflowed by a granular avalanche: Experimental verification. *Physical Review E*, 84: 051301, 2011.

J. H. Ferziger and M. Peri. *Computational Methods for Fluid Dynamics*. Springer, 1999.

J.-T. Fischer, J. Kowalski, and S. P. Pudasaini. Topographic curvature effects in applied avalanche modeling. *Cold Regions Science and Technology*, 74:21–30, 2012.

Y. Forterre and O. Pouliquen. Flows of dense granular media. *Annual Review of Fluid Mechanics*, 40:1–24, 2008.

P. Francis. *Volcanoes. A planetary perspective.* Clarendon Press, Oxford (UK), 1993.

P. J. García Nieto, J. J. del Coz Díaz, D. Castro-Fresno, and F. Ballester Muñoz. Numerical simulation of the performance of a snow fence with airfoil snow plates by FVM. *Journal of computational and applied mathematics*, 234(4):1200–1210, 2010.

GDR MIDI. On dense granular flows. *The European Physical Journal E - Soft Matter*, 14 (4):341–365, 2004.

R. A. Gentry, R. E. Martin, and B. J. Daly. An Eulerian differencing method for unsteady compressible flow problems. *Journal of Computational Physics*, 1(1):87 – 118, 1966.

I. Goldhirsch, S. H. Noskowicz, and O. Bar-Lev. Theory of granular gases: some recent results and some open problems. *Journal of Physics: Condensed Matter*, 17(24):S2591, 2005.

G. H. Golub and C. F. Van Loan. *Matrix computations*, volume 3. Johns Hopkins Univ Pr, 1996.

M. Granig and S. Oberndorfer. Entwicklung und Kalibrierung des Fliess- und Staublawinenmodells SAMOS-AT, development and calibration of the dense and powder snow avalanche model SAMOS-AT. In *Proceedings of 8th Congress Interprevent, Vol.2*, 493–504, 2008.

F. Gray. Pulse code communication, 1953.

J. M. N. T. Gray. Granular flow in partially filled slowly rotating drums. *Journal of Fluid Mechanics*, 441(4):1–29, 2001.

J. M. N. T. Gray and X. Cui. Weak, strong and detached oblique shocks in gravity-driven granular free-surface flows. *Journal of Fluid Mechanics*, 579:113–136, 2007.

J. M. N. T. Gray and K. Hutter. Physik granularer Lawinen. *Physikalische Blätter*, 54(1): 37–44, 1998.

J. M. N. T. Gray, M. Wieland, and K. Hutter. Gravity-driven free surface flow of granular avalanches over complex basal topography. *Proceedings of the Royal Society of London. Series A: Mathematical, Physical and Engineering Sciences*, 455(1985):1841–1874, 1999.

J. M. N. T. Gray, Y.-C. Tai, and S. Noelle. Shock waves, dead zones and particle-free regions in rapid granular free-surface flows. *Journal of Fluid Mechanics*, 491:161–181, 2003.

R. Greve, T. Koch, and K. Hutter. Unconfined flow of granular avalanches along a partly curved surface. I. Theory. *Proceedings of the Royal Society of London. Series A: Mathematical and Physical Sciences*, 445(1924):399–413, 1994.

R. Greve and K. Hutter. Motion of a granular avalanche in a convex and concave curved chute: Experiments and theoretical predictions. *Philosophical Transactions of the Royal Society of London. Series A: Physical and Engineering Sciences*, 342(1666):573–600, 1993.

R. Grochowski, P. Walzel, M. Rouijaa, C. A. Kruelle, and I. Rehberg. Reversing granular flow on a vibratory conveyor. *Applied Physics Letters*, 84:1019, 2004.

C. Harbitz. A survey of computational models for snow avalanche motion. *NGI report*, 581:220–1, 1998.

F. H. Harlow and J. E. Welch. Numerical calculation of time-dependent viscous incompressible flow of fluid with free surface. *Physics of Fluids*, 8(12):2182, 1965.

A. Harten. High resolution schemes for hyperbolic conservation laws. *Journal of Computational Physics*, 49(3):357–393, 1983.

R. L. Hermanns and M. R. Strecker. Structural and lithological controls on large Quaternary rock avalanches (sturzstroms) in arid northwestern Argentina. *Geological Society of America Bulletin*, 111(6):934–948, 1999.

W. H. Herschel and R. Bulkley. Konsistenzmessungen von Gummi-Benzollösungen. *Colloid & Polymer Science*, 39(4):291–300, 1926.

M. R. Hestenes and E. Stiefel. Methods of conjugate gradients for solving linear systems. *Journal of Research of the National Bureau of Standards*, 49(6), 1952.

L. M. Highland and P. Bobrowsky. The landslide handbook–A guide to understanding landslides. *USGS Circular*, 1325:129, 2008.

C. Hirsch. *Numerical computation of internal and external flows: fundamentals of computational fluid dynamics*, volume 1. Butterworth-Heinemann, 2007.

C. W. Hirt and B. D. Nichols. Volume of fluid (VOF) method for the dynamics of free boundaries. *Journal of Computational Physics*, 39(1):201–225, 1981.

C. W. Hirt, A. A. Amsden, and J. L. Cook. An arbitrary Lagrangian-Eulerian computing method for all flow speeds. *Journal of Computational Physics*, 14(3):227–253, 1974.

A. J. Hogg. Two-dimensional granular slumps down slopes. *Physics of Fluids*, 19(9): 093301, 2007.

A. J. Hogg and D. Pritchard. The effects of hydraulic resistance on dam-break and other shallow inertial flows. *Journal of Fluid Mechanics*, 501:179–212, 2004.

E. J. Hopfinger. Snow avalanche motion and related phenomena. *Annual Review of Fluid Mechanics*, 15(1):47–76, 1983.

P. V. C. Hough. Machine analysis of bubble chamber pictures. In *International Conference on High Energy Accelerators and Instrumentation*, volume 73, 1959.

L. Huilin, H. Yurong, and D. Gidaspow. Hydrodynamic modelling of binary mixture in a gas bubbling fluidized bed using the kinetic theory of granular flow. *Chemical Engineering Science*, 58(7):1197–1205, 2003.

O. Hungr, S. G. Evans, M. J. Bovis, and J. N. Hutchinson. A review of the classification of landslides of the flow type. *Environmental & Engineering Geoscience*, 7(3):221–238, 2001.

K. Hutter and R. Greve. Two-dimensional similarity solutions for finite-mass granular avalanches with Coulomb- and viscous-type frictional resistance. *Journal of Glaciology*, 39:357–372, 1993.

K. Hutter, M. Siegel, S. Savage, and Y. Nohguchi. Two-dimensional spreading of a granular avalanche down an inclined plane Part I. theory. *Acta Mechanica*, 100:37–68, 1993.

K. Hutter, T. Koch, C. Plüss, and S. Savage. The dynamics of avalanches of granular materials from initiation to runout. Part II. Experiments. *Acta Mechanica*, 109:127–165, 1995.

K. Hutter, Y. Wang, and S. P. Pudasaini. The Savage-Hutter avalanche model: how far can it be pushed? *Philosophical Transactions of the Royal Society A: Mathematical, Physical and Engineering Sciences*, 363(1832):1507, 2005.

K. Hutter and K. Jöhnk. *Continuum methods of physical modeling: continuum mechanics, dimensional analysis, turbulence*. Springer Verlag, 2004.

K. Hutter and T. Koch. Motion of a granular avalanche in an exponentially curved chute: Experiments and theoretical predictions. *Philosophical Transactions: Physical Sciences and Engineering*, 334(1633):93–138, 1991.

R. I. Issa. Solution of the implicitly discretised fluid flow equations by operator-splitting. *Journal of Computational Physics*, 62(1):40–65, 1986.

D. Issler. Experimental information on the dynamics of dry-snow avalanches. *Dynamic Response of Granular and Porous Materials Under Large and Catastrophic Deformations*, 11:109, 2003.

J. D. Iversen and K. R. Rasmussen. The effect of surface slope on saltation threshold. *Sedimentology*, 41(4):721–728, 1994.

R. M. Iverson and R. P. Denlinger. Flow of variably fluidized granular masses across three-dimensional terrain: 1. Coulomb mixture theory. *Journal of Geophysical Research*, 106(B1):537–552, 2001.

D. A. H. Jacobs. Preconditioned conjugate gradient methods for solving systems of algebraic equations. Central electricity research laboratories report. Technical report, RD/L, 1980.

H. M. Jaeger, C.-h. Liu, and S. R. Nagel. Relaxation at the angle of repose. *Physical Review Letters*, 62:40–43, 1989.

H. M. Jaeger, S. R. Nagel, and R. P. Behringer. Granular solids, liquids, and gases. *Reviews of Modern Physics*, 68:1259–1273, 1996.

B. Jähne. *Digital Image Processing, 5th revised and extended edition*. Measurement Science and Technology, 2002.

B. Jamieson, T. Geldsetzer, and C. Stethem. Forecasting for deep slab avalanches. *Cold Regions Science and Technology*, 33(2-3):275–290, 2001.

B. Jamieson, S. Margreth, and A. Jones. Application and limitations of dynamic models for snow avalanche hazard mapping. In *Proceedings of the ISSW*, 730–739, 2008.

R. J. Janda, A. S. Daag, P. J. Delos Reyes, C. G. Newhall, T. C. Pierson, R. S. Punongbayan, K. S. Rodolfo, R. U. Solidum, and J. V. Umbal. Assessment and response to lahar hazard around Mount Pinatubo, 1991 to 1993. *Fire and Mud, Eruptions and Lahars of Mount Pinatubo, Philippines. PHIVOLCS Press, Quezon City, and University of Washington Press, Seattle*, 107–139, 1996.

H. Jasak. *Error analysis and estimation in the Finite Volume method with applications to fluid flows*. PhD thesis, Imperial College, University of London, 1996.

G. S. Jiang and E. Tadmor. Nonoscillatory central schemes for multidimensional hyperbolic conservation laws. *SIAM Journal on Scientific Computing*, 19(6):1892–1917, 1998.

T. Jóhannesson. Run-up of two avalanches on the deflecting dams at Flateyri, northwestern Iceland. *Annals of Glaciology*, 32(1):350–354, 2001.

T. Jóhannesson and K. M. Hákonardóttir. *Remarks on the design of avalanche braking mounds based on experiments in 3, 6, 9 and 34 m long chutes*. Veðurstofa Íslands, 2003.

P. Jop, Y. Forterre, and O. Pouliqen. Crucial role of sidewalls in granular surface flows: consequences for the rheology. *Journal of Fluid Mechanics*, 541:167–192, 2005.

P. Jop, Y. Forterre, and O. Pouliquen. A constitutive law for dense granular flows. *Nature*, 441(7094):727–730, 2006.

C. Josserand, P.-Y. Lagrée, D. Lhuillier, S. Popinet, P. Ray, and L. Staron. The spreading of a granular column from a Bingham point of view. *AIP Conference Proceedings*, 1145(1): 631–634, 2009.

V. F. Jung. Der Culmannsche und der Mohrsche Kreis. *Österreichisches Ingenieur-Archiv*, 1:408, 1947.

R. D. Keane and R. J. Adrian. Theory of cross-correlation analysis of PIV images. *Applied Scientific Research*, 49(3):191–215, 1992.

M. A. Kern, F. Tiefenbacher, and J. N. McElwaine. The rheology of snow in large chute flows. *Cold Regions Science and Technology*, 39(2-3):181 – 192, 2004.

R. R. Kerswell. Dam break with Coulomb friction: A model for granular slumping? *Physics of Fluids*, 17(5):057101, 2005.

T. Koch, R. Greve, and K. Hutter. Unconfined flow of granular avalanches along a partly curved surface. II. experiments and numerical computations. *Proceedings: Mathematical and Physical Sciences*, 445(1924):415–435, 1994.

H. J. Körner. Reichweite und Geschwindigkeit von Bergstürzen und Fließschneelawinen. *Rock Mechanics and Rock Engineering*, 8:225–256, 1976.

D. Krengel, S. Strobl, A. Sack, M. Heckel, and T. Pöschel. Pattern formation in a horizontally shaken granular submonolayer. *Granular Matter*, 1–11, 2013.

H. D. Kutzbach and R. Scherer. Internal friction of cereal grain-review. *Landtechnik*, 6: 213–219, 1977.

L. Lacaze and R. R. Kerswell. Axisymmetric granular collapse: A transient 3d flow test of viscoplasticity. *Physical Review Letters*, 102:108305, 2009.

L. Lacaze, J. C. Phillips, and R. R. Kerswell. Planar collapse of a granular column: Experiments and discrete element simulations. *Physics of Fluids*, 20(6):063302, 2008.

P.-Y. Lagrée, L. Staron, and S. Popinet. The granular column collapse as a continuum: validity of a two-dimensional Navier-Stokes model with a $\mu(I)$-rheology. *Journal of Fluid Mechanics*, 686:378–408, 2011.

E. Lajeunesse, A. Mangeney-Castelnau, and J. P. Vilotte. Spreading of a granular mass on a horizontal plane. *Physics of Fluids*, 16(7):2371–2381, 2004.

E. Lajeunesse, J. B. Monnier, and G. M. Homsy. Granular slumping on a horizontal surface. *Physics of Fluids*, 17(10):103302, 2005.

T. W. Lambe and R. V. Whitman. *Soil mechanics*. John Wiley, New York, 1969.

L. D. Landau and E. M. Lifšic. *Course of Theoretical Physics: Fluid mechanics*. Bd. 6. Pergamon Press, 1975.

D. Lanman and G. Taubin. Build your own 3D scanner: 3D photograhy for beginners. In *SIGGRAPH '09: ACM SIGGRAPH 2009 courses*, 1–87, New York, NY, USA, 2009. ACM.

E. Larrieu, L. Staron, and E. J. Hinch. Raining into shallow water as a description of the collapse of a column of grains. *Journal of Fluid Mechanics*, 554:259–270, 2006.

L. Lê and E. B. Pitman. A model for granular flows over an erodible surface. *Siam journal on applied mathematics*, 70(5):1407–1427, 2009.

F. Legros. The mobility of long-runout landslides. *Engineering Geology*, 63(3):301–331, 2002.

G. Lube, H. E. Huppert, R. S. J. Sparks, and M. A. Hallworth. Axisymmetric collapses of granular columns. *Journal of Fluid Mechanics*, 508:175–199, 2004.

G. Lube, H. E. Huppert, R. S. J. Sparks, and A. Freundt. Collapses of two-dimensional granular columns. *Physical Review E*, 72:041301, 2005.

G. Lube, H. E. Huppert, R. S. J. Sparks, and A. Freundt. Static and flowing regions in granular collapses down channels. *Physics of Fluids*, 19(4):043301, 2007.

G. Lube, H. E. Huppert, R. S. J. Sparks, and A. Freundt. Granular column collapses down rough, inclined channels. *Journal of Fluid Mechanics*, 675:347–368, 2011.

H. Ludwieg and W. Tillmann. *Investigations of the wall-shearing stress in turbulent boundary layers*. National Advisory Committee for Aeronautics Washington, 1950.

F. Maeno, A. J. Hogg, R. S. J. Sparks, and G. P. Matson. Unconfined slumping of a granular mass on a slope. *Physics of Fluids*, 25(2):023302, 2013.

M. Maggioni, M. Freppaz, E. Ceaglio, D. Godone, D. Viglietti, E. Zanini, M. Barbero, F. Barpi, M. B. Brunetto, E. Bovet, B. Chiaia, V. De Biagi, B. Frigo, and O. Pallara. A new experimental snow avalanche test site at Seehore peak in Aosta Valley (nw Italian Alps)–Part i: Conception and logistics. *Cold Regions Science and Technology*, 2012.

S. Margreth. Defense structures in avalanche starting zones. Technical guideline as an aid to enforcement. Environment in Practice 0704, Federal Office for the Environment, Bern; WSL Swiss Federal Institute for Snow and Avalanche Research SLF, Davos., 2007.

W. J. McGuire. Volcano instability: a review of contemporary themes. *Geological Society, London, Special Publications*, 110(1):1–23, 1996.

C. Mériaux. Two dimensional fall of granular columns controlled by slow horizontal withdrawal of a retaining wall. *Physics of Fluids*, 18(9):093301, 2006.

C. Mériaux and T. Triantafillou. Scaling the final deposits of dry cohesive granular columns after collapse and quasi-static fall. *Physics of Fluids*, 20(3):033301, 2008.

M. Meunier, C. Ancey, and J.-M. Taillandier. Fitting avalanche-dynamics models with documented events from the Col du Lautaret site (France) using the conceptual approach. *Cold Regions Science and Technology*, 39(1):55 – 66, 2004.

N. Mitarai and H. Nakanishi. Granular flow: Dry and wet. *The European Physical Journal Special Topics*, 204(1):5–17, 2012.

R. Molina, E. Muntan, L. Andreu, G. R. Furdada, P. Oller, E. Gutierrez, P. Martinez, and J. M. Vilaplana. Using vegetation to characterize the avalanche of Canal del Roc Roig, Vall de Núria, eastern Pyrenees, Spain. *Annals of Glaciology*, 38(1):159–165, 2004.

S. Moriguchi, R. Borja, A. Yashima, and K. Sawada. Estimating the impact force generated by granular flow on a rigid obstruction. *Acta Geotechnica*, 4:57–71, 2009.

S. Muzaferija. *Adaptive finite volume method for flow prediction using unstructured meshes and multigrid approach*. PhD thesis, University of London UK, 1994.

Nabla Ltd. FOAM – The Complete Guide., 2001.

Q.-H. Nguyen and N.-D. Nguyen. Incompressible non-Newtonian fluid flows. *CONTINUUM MECHANICS*, 47, 2012.

H. Norem, F. Irgens, and B. Schieldrop. A continuum model for calculating snow avalanche velocities. *IAHS (International Association of Hydrological Sciences) Publication*, 162:363–379, 1987.

C. Nöthiger, H. Elsasser, M. Bründl, and W. Ammann. Indirekte Auswirkungen von Naturgefahren auf den Tourismus–Das Beispiel des Lawinenwinters 1999 in der Schweiz. *Geogr. Helv*, 2:91–108, 2002.

J. M. Ottino and D. V. Khakhar. Mixing and segregation of granular materials. *Annual Review of Fluid Mechanics*, 32:55–91, 2000.

S. Patankar. Numerical heat and mass transfer. *Tylor & Francis*, 1980.

M. Peric, R. Kessler, and G. Scheuerer. Comparison of finite-volume numerical methods with staggered and colocated grids. *Computers & Fluids*, 16(4):389–403, 1988.

R. Perla, T. T. Cheng, and D. M. McClung. A two-parameter model of snow-avalanche motion. *Journal of Glaciology*, 26:197–207, 1980.

T. C. Pierson, R. J. Janda, J. C. Thouret, and C. A. Borrero. Perturbation and melting of snow and ice by the 13 november 1985 eruption of Nevado del Ruiz, Colombia, and consequent mobilization, flow and deposition of lahars. *Journal of Volcanology and Geothermal Research*, 41(1-4):17–66, 1990.

E. B. Pitman and L. Le. A two-fluid model for avalanche and debris flows. *Philosophical Transactions of the Royal Society A: Mathematical, Physical and Engineering Sciences*, 363 (1832):1573–1601, 2005.

O. Pouliquen. Scaling laws in granular flows down rough inclined planes. *Physics of Fluids*, 11(3):542–548, 1999.

O. Pouliquen and Y. Forterre. Friction law for dense granular flows: application to the motion of a mass down a rough inclined plane. *Journal of Fluid Mechanics*, 453:133–151, 2002.

O. Pouliquen, C. Cassar, P. Jop, Y. Forterre, and M. Nicolas. Flow of dense granular material: towards simple constitutive laws. *Journal of Statistical Mechanics: Theory and Experiment*, 2006(07):P07020, 2006.

S. P. Pudasaini. Some exact solutions for debris and avalanche flows. *Physics of Fluids*, 23: 043301, 2011.

S. P. Pudasaini and K. Hutter. *Avalanche dynamics: dynamics of rapid flows of dense granular avalanches*. Springer Verlag, 2007.

S. P. Pudasaini and C. Kröner. Shock waves in rapid flows of dense granular materials: Theoretical predictions and experimental results. *Physical Review E*, 78(4):041308, 2008.

S. P. Pudasaini, S. S. Hsiau, Y. Wang, and K. Hutter. Velocity measurements in dry granular avalanches using particle image velocimetry technique and comparison with theoretical predictions. *Physics of Fluids*, 17:093301, 2005a.

S. P. Pudasaini, Y. Wang, and K. Hutter. Modelling debris flows down general channels. *Natural Hazards and Earth System Science*, 5(6):799–819, 2005b.

S. P. Pudasaini, Y. Wang, and K. Hutter. Rapid motions of free-surface avalanches down curved and twisted channels and their numerical simulation. *Philosophical Transactions of the Royal Society A: Mathematical, Physical and Engineering Sciences*, 363(1832):1551, 2005c.

S. P. Pudasaini, K. Hutter, S. S. Hsiau, S. C. Tai, Y. Wang, and R. Katzenbach. Rapid flow of dry granular materials down inclined chutes impinging on rigid walls. *Physics of Fluids*, 19:053302, 2007.

S. P. Pudasaini, Y. Wang, L. T. Sheng, S. S. Hsiau, K. Hutter, and R. Katzenbach. Avalanching granular flows down curved and twisted channels: Theoretical and experimental results. *Physics of Fluids*, 20:073302, 2008.

S. P. Pudasaini. A general two-phase debris flow model. *Journal of Geophysical Research: Earth Surface (2003–2012)*, 117(F3), 2012.

S. P. Pudasaini and S. A. Miller. The hypermobility of huge landslides and avalanches. *Engineering Geology*, 2013.

W. J. M. Rankine. On the stability of loose earth. *Philosophical Transactions of the Royal Society of London*, 9–27, 1857.

O. Reynolds. On the dilatancy of media composed of rigid particles in contact. *Philosophical Magazine Series 5*, 50, 1885.

O. Reynolds. An experimental investigation of the circumstances which determine whether the motion of water shall be direct or sinuous, and of the law of resistance in parallel channels. *Proceedings of the Royal Society of London*, 35(224-226):84–99, 1883.

O. Reynolds. *On an inversion of ideas as to the structure of the universe:(The Rede lecture, June 10, 1902)*. University press, 1903.

C. Rhie and W. Chow. A numerical study of the turbulent flow past an isolated airfoil with trailing edge separation. In *Fluid Dynamics and Co-located Conferences*. American Institute of Aeronautics and Astronautics, 1982.

O. Roche, M. Attali, A. Mangeney, and A. Lucas. On the run-out distance of geophysical gravitational flows: Insight from fluidized granular collapse experiments. *Earth and Planetary Science Letters*, 311(3-4):375 – 385, 2011.

L. Rondon, O. Pouliquen, and P. Aussillous. Granular collapse in a fluid: Role of the initial volume fraction. *Physics of Fluids*, 23(7):073301, 2011.

A. Rosato, K. J. Strandburg, F. Prinz, and R. H. Swendsen. Why the brazil nuts are on top: Size segregation of particulate matter by shaking. *Physical Review Letters*, 58(10): 1038–1040, 1987.

H. Rusche. *Computational fluid dynamics of dispersed two-phase flows at high phase fractions*. PhD thesis, Imperial College, London, 2002.

B. Salm. Contribution to avalanche dynamics. *IAHS AISH Publ*, 69:199–214, 1966.

B. Salm. A short and personal history of snow avalanche dynamics. *Cold Regions Science and Technology*, 39(2):83–92, 2004.

B. Salm, A. Burkard, and H. Gubler. Berechnung von Fliesslawinen, eine Anleitung für Praktiker mit Beispielen, 1990.

P. Sampl. SamosAT–Modelltheorie und Numerik. *AVL List GmbH, Graz*, 2007.

S. Sauermoser. Avalanche hazard mapping – 30 years experience in Austria. In *Proceedings of the 2006 International Snow Science Workshop, Telluride, Colorado, ISSW USA, Colorado, USA*, 314–321, 2006.

S. B. Savage and K. Hutter. The motion of a finite mass of granular material down a rough incline. *Journal of Fluid Mechanics*, 199:177–215, 1989.

S. B. Savage and K. Hutter. The dynamics of avalanches of granular materials from initiation to runout. Part I: Analysis. *Acta Mechanica*, 86:201–223, 1991.

S. B. Savage. Gravity flow of cohesionless granular materials in chutes and channels. *Journal of Fluid Mechanics*, 92(01):53–96, 1979.

U. Schumann, B. Weinzierl, O. Reitebuch, H. Schlager, A. Minikin, C. Forster, R. Baumann, T. Sailer, K. Graf, H. Mannstein, and others. Airborne observations of the Eyjafjalla volcano ash cloud over Europe during air space closure in April and May 2010. *Atmos. Chem. Phys*, 11(5):2245–2279, 2011.

J. Schweizer and J. Seiler. Der Lawinenniedergang in Evoléne vom 21. Februar 1999 unter besonderer Berücksichtigung der Auswirkungen des Gerichtsverfahrens auf die Arbeit der Lawinendienste. Technical report, Eidg. Institut für Schnee- und Lawinenforschung SLF, 2007.

J. Schweizer, J. Bruce Jamieson, and M. Schneebeli. Snow avalanche formation. *Reviews of Geophysics*, 41(4):1016–, 2003.

K. M. Scott, J. W. Vallance, and P. T. Pringle. Sedimentology, behavior, and hazards of debris flows at Mount Rainer, Washington. *US. Geol. survey prof. paper/Dep. of the interior*, 1992.

S. Siavoshi and A. Kudrolli. Failure of a granular step. *Physical Review E*, 71:051302, 2005.

D. Sornette, A. Helmstetter, J. V. Andersen, S. Gluzman, J. R. Grasso, and V. Pisarenko. Towards landslide predictions: two case studies. *Physica A: Statistical Mechanics and its Applications*, 338(3):605–632, 2004.

B. Sovilla and P. Bartelt. Observations and modelling of snow avalanche entrainment. *Natural Hazards and Earth System Science*, 2(3/4):169–179, 2002.

L. Staron and E. Hinch. The spreading of a granular mass: role of grain properties and initial conditions. *Granular Matter*, 9:205–217, 2007.

J. J. Stoker. The formation of breakers and bores the theory of nonlinear wave propagation in shallow water and open channels. *Communications on Pure and Applied Mathematics*, 1(1):1–87, 1948.

Y. Tai and C. Kuo. A new model of granular flows over general topography with erosion and deposition. *Acta Mechanica*, 199:71–96, 2008.

Y.-C. Tai, Y. Wang, J. M. N. T. Gray, and K. Hutter. Methods of similitude in granular avalanche flows. In K. Hutter, Y. Wang, and H. Beer, editors, *Advances in Cold-Region Thermal Engineering and Sciences*, volume 533 of *Lecture Notes in Physics*, 415–428. Springer Berlin / Heidelberg, 1999a.

Y.-C. Tai, Y. Wang, J. M. N. T. Gray, and K. Hutter. Methods of similitude in granular avalanche flows. In *Advances in Cold-Region Thermal Engineering and Sciences*, 415–428. Springer, 1999b.

Y.-C. Tai, K. Hutter, and J. M. N. T. Gray. Dense granular avalanches: mathematical description and experimental validation. In *Geomorphological Fluid Mechanics*, 339–366. Springer, 2001.

Y.-C. Tai, C.-Y. Kuo, and W.-H. Hui. An alternative depth-integrated formulation for granular avalanches over temporally varying topography with small curvature. *Geophysical & Astrophysical Fluid Dynamics*, 1–34, 2012.

T. Theodoropoulos. *Prediction of three-dimensional engine flow on unstructured meshes*. PhD thesis, Imperial College, University of London, 1990.

E. L. Thompson and H. E. Huppert. Granular column collapses: further experimental results. *Journal of Fluid Mechanics*, 575:177–186, 2007.

M. Trepanier and S. V. Franklin. Column collapse of granular rods. *Physical Review E*, 82: 011308, 2010.

G. Tryggvason, B. Bunner, O. Ebrat, and W. Tauber. Computations of multiphase flows by a finite difference/front tracking method. I. Multi-fluid flows. *LECTURE SERIES-VON KARMAN INSTITUTE FOR FLUID DYNAMICS*, 7–7, 1998.

B. Turnbull and J. N. McElwaine. A comparison of powder-snow avalanches at Vallee de la Sionne, Switzerland, with plume theories. *Journal of Glaciology*, 53(180):30–40, 2007.

S. O. Unverdi and G. Tryggvason. A front-tracking method for viscous, incompressible, multi-fluid flows. *Journal of Computational Physics*, 100(1):25–37, 1992.

H. A. Van der Vorst. Bi-CGSTAB: A fast and smoothly converging variant of Bi-CG for the solution of nonsymmetric linear systems. *SIAM Journal on scientific and Statistical Computing*, 13:631, 1992.

D. J. Varnes. Slope movement types and processes. *Transportation Research Board Special Report*, (176):11–33, 1978.

H. K. Versteeg and W. Malalasekera. *An introduction to computational fluid dynamics: the finite volume method*. Prentice Hall, 2007.

A. Voellmy. Über die Zerstorungskraft von Lawinen. *Schweizerische Bauzeitung*, 159–165, 212–217, 246–249, 280–285, 1955.

Y. Wang, K. Hutter, and S. P. Pudasaini. The Savage-Hutter theory: A system of partial differential equations for avalanche flows of snow, debris, and mud. *ZAMM - Journal of Applied Mathematics and Mechanics / Zeitschrift für Angewandte Mathematik und Mechanik*, 84(8):507–527, 2004.

H. Weller. A code independent notation for finite volume algorithm. Technical report, Nabla Ltd., 2002.

H. G. Weller, G. Tabor, H. Jasak, and C. Fureby. A tensorial approach to computational continuum mechanics using object orientated techniques. *Computers in Physics*, 12(6): 620 – 631, 1998.

M. Wieland, J. M. N. T. Gray, and K. Hutter. Channelized free-surface flow of cohesionless granular avalanches in a chute with shallow lateral curvature. *Journal of Fluid Mechanics*, 392:73–100, 1999.

C. Wilhelm, T. Wiesinger, M. Bründl, and W. J. Ammann. The avalanche winter 1999 in Switzerland-an overview. In *Proceedings International Snow Science Workshop, Big Sky, Montana, USA, 1-6 October 2000*, 487–494, 2001.

R. Zenit. Computer simulations of the collapse of a granular column. *Physics of Fluids*, 17(3):031703, 2005.

D. Zhang and G. Wang. Study of the 1920 Haiyuan earthquake-induced landslides in loess (China). *Engineering Geology*, 94(1-2):76–88, 2007.

A.1 Common parameters

A.1.1 Physical parameters and transport properties

Air phase:
- **Transport model:** Newtonian
- **Viscosity:** $\nu = 1.48 \cdot 10^{-5}\,\mathrm{m^2 s^{-1}}$
- **Density:** $\rho = 1\,\mathrm{kgm^{-3}}$

PVC phase:
- **Transport model:** Coulomb
- **Viscosity:** $\mu = \tan(32°)$
- **Density:** $\rho = 936.17\,\mathrm{kgm^{-3}}$

sand phase:
- **Transport model:** Coulomb
- **Viscosity:** $\mu = \tan(37°)$
- **Density:** $\rho = 1626.67\,\mathrm{kgm^{-3}}$

Magnitude of gravitation: $g = 9.81\,ms{-}2$

A.1.2 Numerical parameters employed in OpenFOAM® simulations

A.1.2.1 Numerical schemes

ddtSchemes: Euler
gradSchemes: Gauss linear
divSchemes: **div(rho*phi,U):** Gauss limitedLinearV 1
- **div(phi,alpha):** Gauss vanLeer
- **div(phirb,alpha):** Gauss interfaceCompression
- **div(phi,p_rgh):** Gauss upwind

laplacianSchemes: gauss linear corrected
interpolationSchemes: linear
snGradSchemes: corrected
fluxRequired: p||p_rgh,pcorr,alpha1

A.1.2.2 Finite volume solution: fvSolution

Listing A.1 – fvSolution

```
solvers
{
    pcorr
    {
        solver          PCG;
        preconditioner  DIC;
        tolerance       1e-15;
        relTol          0;
    }

    "(p_rgh|p)"
    {
        solver          PCG;
        preconditioner  DIC;
        tolerance       1e-15;
        relTol          1e-7;
    }

    pFinal
    {
        solver          PCG;
        preconditioner  DIC;
        tolerance       1e-15;
        relTol          0;
    }

    U
    {
        solver          PBiCG;
        preconditioner  DILU;
        tolerance       1e-15;
        relTol          0;
    }
}

PISO
{
    momentumPredictor no;
    nCorrectors       9;
    nNonOrthogonalCorrectors 3;
    nAlphaCorr        1;
    nAlphaSubCycles   2;
    cAlpha            1;
}
```

A.1.2.3 Control parameters: controlDict

Listing A.2 – controlDict

```
maxCo           0.05;
maxAlphaCo      0.05;
maxDeltaT       1;
```

A.1.2.4 Numerical limits for calculated effective viscosity

nuMin $1 \cdot 10^{-15}$ Pas

nuMax $1 \cdot 10^{2}$ Pas

A.1.2.5 Boundary conditions

Wall

U: fixedValue(0 0 0)

p_rgh: buoyantPressure

alpha1: zeroGradient

Atmosphere

U: pressureInletOutletVelocity

p_rgh: totalPressure

alpha1: zeroGradient

Inflow

U: fixedValue

p_rgh: fixedFluxPressure

alpha1: fixedValue

Outflow

U: zeroGradient

p_rgh: zeroGradient

alpha1: zeroGradient

Wall with Coulomb friction

U: coulombSlip

p_rgh: buoyantPressure

alpha1: zeroGradient

A.2 Special parameters for Rotating Box

A.2.1 Mesh

Mesh bounding box in m: (0, 0) (0.2, 0.2)

Cell size in mm: 4 x 4

Number of cells: 50x50=2500

A.2.2 Initial and boundary conditions

A.2.2.1 Boundary conditions:

Wall: (0, 0) (0.2,0) (0.2,0.2) (0,0.2) (0,0)

A.2.2.2 Initial filling:

$\alpha 1_1$((0,0)x(0.2,0.11)) = 1

A.2.3 Physical parameters

Rotating periode: $T = 6.9274369s$

Transport properties:

Transport model: Coulomb

Viscosity: $\mu = \tan(54°)$

Density: $\rho = 1855\,\mathrm{kgm}^{-3}$

A.3 Special parameters for dam breaks

A.3.1 Mesh

0° **rectangular:**

Mesh bounding box: (-0.3,0) (0.2,0.15)

Cell size in mm: 2.5 x 2.5

Number of cells: 200x60=12000

10° **rectangular:**

Mesh bounding box in m: (-0.3102186311787072,0) (0.39545627376425850,0.17)

Cell size in mm:

Region I: (-0.3102186311787072,0) (0,0.17)

Cell size in mm: 2.58515525982256 x 2.833333333333334

Region II: (0,0) (0.39545627376425850,0.17)

Cell size in mm: 3.295468948035488 x 2.833333333333334

Number of cells: $2 \cdot (120x60) = 14400$

20° **rectangular:**

Mesh bounding box: (-0.3107547169811321,0) (0.41549056603773590,0.17)

Cell size in mm:

Region I: (-0.3107547169811321,0)(0,0.17)

Cell size in mm: 2.589622641509434 x 2.833333333333334

Region II: (0,0) (0.4154905660377359,0.17)

Cell size in mm: 2.596816037735849 x 2.833333333333334

Number of cells 120x60 + 160x60 = 16800

30° **rectangular:**

Mesh bounding box: (-0.3044256120527307,0) (0.4210263653483993,0.17)

Cell size in mm:

Region I: (-0.3044256120527307,0)x(0,0.17)

Cell size in mm: 2.536880100439423 x 2.83333333

Region II: (0,0) (0.4210263653483993,0.17)

Cell size in mm: 2.631414783427496 x 2.83333333

Number of cells: 120x60+160x60=16800

50° **triangular:**

Mesh bounding box: (-0.4,0) (0.4,0.19)

Cell size in mm:

variable: 200 x 75 cells, y-simple grading 1.25

Number of cells: 200x75=15000

A.3.2 Initial and boundary conditions

A.3.2.1 Boundary conditions:

Wall rectangular: (0,ymax) (xmin,ymax) (xmin,ymin) (xmax,ymin)
Wall triangular: (xmin,ymin) (xmax,ymin)
Atmosphere patches rectangular: (0,ymax) (xmax,ymax) (xmax,ymin)
Atmosphere patches triangular: (xmin,ymin) (xmin,ymax) (xmax,ymax) (xmax,ymin)

A.3.2.2 Initial filling:

Using polyFillAlpha extracted from experimental images (to many points to list here).

A.3.3 Physical parameters

Material rectangular: PVC
Material triangular: PVC and sand
Gravity

$0°$**:** $\mathbf{g} = (g \cdot \sin(0°), -g \cdot \cos(0°))$
$10°$**:** $\mathbf{g} = (g \cdot \sin(10°), -g \cdot \cos(10°))$
$20°$**:** $\mathbf{g} = (g \cdot \sin(20°), -g \cdot \cos(20°))$
$30°$**:** $\mathbf{g} = (g \cdot \sin(30°), -g \cdot \cos(30°))$
$50°$**:** $\mathbf{g} = (g \cdot \sin(50°), -g \cdot \cos(50°))$

A.4 Special parameters for undisturbed flow

A.4.1 Mesh

Mesh bounding box: (0.5,0) (2.25,0.1)
Cell size in mm:
Region I: (0.5,0) (2,0.1)
Cell size in mm: 5 x 1.666666666666667
Region II: (2,0)(2.25,0.1)
Cell size in mm: 5 x 1.666666666666667
Number of cells: 300x60+50x60=21000

A.4.2 Initial and boundary conditions

A.4.2.1 Boundary conditions:

Wall: (0.5,0) (2,0)

Atmosphere patches: (0.5,0.1) (2.25,0.1)
Outflow patches: (2,0) (2.25,0) (2.25,0.1)
Inlet patches: (0.5,0) (0.5,0.1)
Inlet velocity: if(y<0.0296m) (1.455838m/s+34.030481/s·y,0), else (0,0)
Inlet α_1: if(y<0.0296m) 1, else 0

A.4.3 Physical parameters

Material: sand or PVC
Gravity: $\mathbf{g} = (g \cdot \sin(50°), -g \cdot \cos(50°))$

A.5 Special parameters for obstacle inside channel

A.5.1 Mesh and boundary conditions

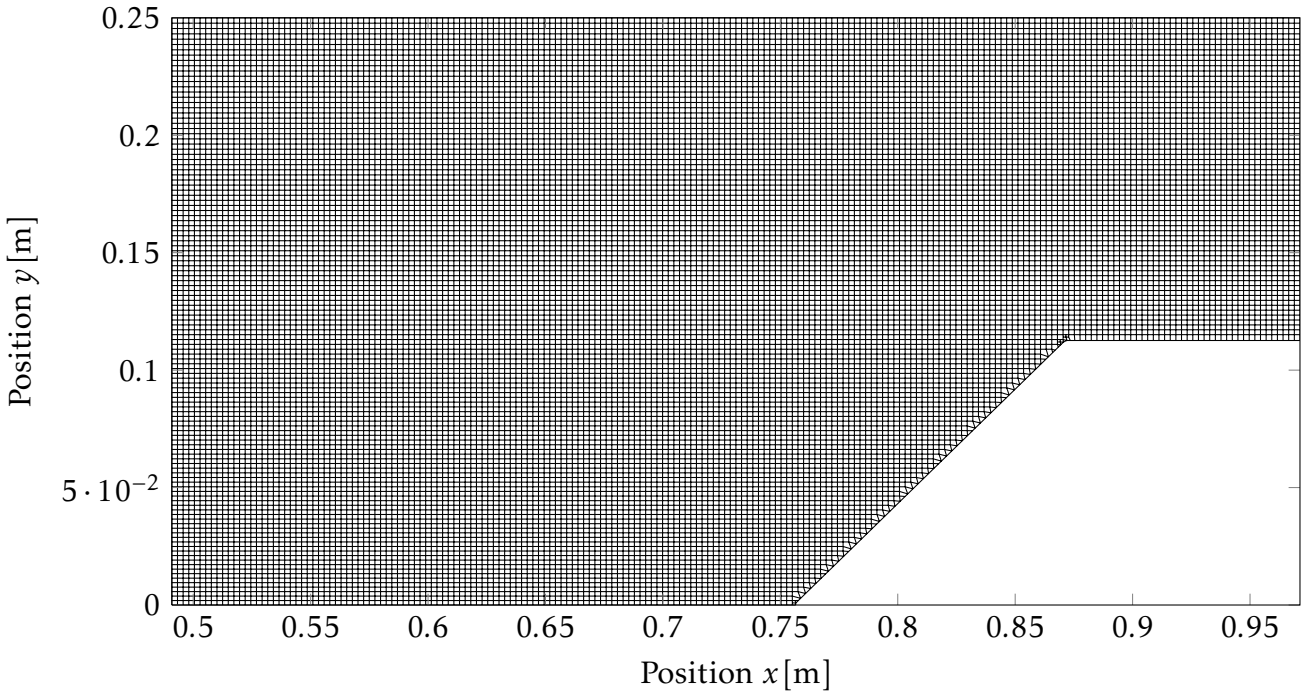

Number of cells: 20250 (20242 hexahedra and 8 polyhedra)
Overall domain bounding box: (0.490904 0) (0.971269 0.25)
Obstacle geometry: (0.755721 0) (0.871269 0.112615) (0.871269 0)

A.5.2 Physical parameters

Material: sand or PVC
Gravity: $\mathbf{g} = (g \cdot \sin(50°), -g \cdot \cos(50°))$

A.6 Special parameters for shock formation

A.6.1 Mesh

Overall domain bounding box: (-2 0) (0 0.5)

Cell size mm:

Region 0: (-2,0.1) (-0.5,0.5): 10 x 10

Region 1: (-2,0.05) (-0.5,0.1) and (-0.5,0.05) (0,0.5): 5 x 5

Region 2: (-2,0) (0,0.05) : 2.5 x 2.5

Cells: 29200 (28571 hexahedra and 629 polyhedra)

A.6.2 Initial and Boundary Conditions

Wall: (-2,0) (0,0) (0,0.5)

Athmosphere: (-2,0.5) (0,0.5)

Inflow: (-2,0) (-2,0.5)

A.6.3 Physical Parameters

Material: sand or pvc

Gravity:

40°: $\mathbf{g}_{40} = (g \cdot \sin(40°), -g \cdot \cos(40°))$

50°: $\mathbf{g}_{50} = (g \cdot \sin(50°), -g \cdot \cos(50°))$

A.7 Special parameters for wide channel

A.7.1 Mesh

Overall domain bounding box: (0 -0.1475 0) (0.59 0.1475 0.12)

Initial cell size mm: 2.5 x 2.5 x 2.5

Cells (cylinder): 1317600 (1315776 hexahedra and 1824 prism)

Cells (prism): 1362707 (1356273 hexahedra, 979 prisms, 37 tet wedges and 5418 polyhedra)

Cells (rotated prism): 1362370 (1356342 hexahedra, 581 prisms, 33 tet wedges and 5414 polyhedra)

A.7.2 Physical parameters

Material: PVC

Gravity: $\mathbf{g} = (g \cdot \sin(45°), -g \cdot \cos(45°))$

B Excerpts of major functions added to OpenFOAM®

Listing B.1 – Calculation of effective viscosity: calcNu

```
Foam::tmp<Foam::volScalarField>
Foam::viscosityModels::Coulomb::calcNu() const
{
    dimensionedScalar tone("tone", dimTime, 1.0);
    dimensionedScalar rtone("rtone", dimless/dimTime, 1.0);
    tmp<volScalarField> sr(strainRate());

    const volScalarField& pp=U_.db().lookupObject<volScalarField>("p");

    volScalarField nu__=muS_/(max(sr(), dimensionedScalar("VSMALL",
dimless/dimTime, VSMALL)))*pp/rhoS_;

Info << "Nu:" <<min(nu__).value()<<"␣->␣"<<max(nu__).value()<<endl;
Info << "p:" <<min(pp).value()<<"␣->␣"<<max(pp).value()<<endl;
Info << "sr:" <<min(sr()).value()<<"␣->␣"<<max(sr()).value()<<endl;

    return
    (
        min
        (
            max(nu__,nuMin_),nuMax_
        )
    );
}
```

Listing B.2 – Calculation of bottom sliding velocity: coulombSlip

```
template<class Type>
void coulombSlipNewFvPatchField<Type>::evaluate(const Pstream::commsTypes)
{
    if (!this->updated())
    {
        this->updateCoeffs();
    }

    vectorField nHat = this->patch().nf();

    scalarField deltaCoeffs_ = this->patch().deltaCoeffs();
    const volVectorField& U =
this->db().objectRegistry::lookupObject<volVectorField>("U");
    const volScalarField& alpha1 =
```

```
15 this->db().objectRegistry::lookupObject<volScalarField>("alpha1");
16     const volScalarField& mu =
17 this->db().objectRegistry::lookupObject<volScalarField>("mu");
18     const volScalarField& p =
19 this->db().objectRegistry::lookupObject<volScalarField>("p");
20     label patchi=this->patch().index();
21
22     forAll(this->patch(), facei)
23     {
24       label celli = this->patch().faceCells()[facei];
25       if(alpha1.boundaryField()[patchi][facei]>=0.5){
26        valueFraction_[facei]=
27                                 min(1,
28                                     max(0,
29                                         tanDe_[facei]/deltaCoeffs_[facei]
30                                         *p.boundaryField()[patchi][facei]
31                                         /max(VSMALL,
32                                           mu.boundaryField()[patchi][facei]
33                                           *mag(-nHat[facei]^(nHat[facei]^U.
                                                 internalField()[celli]))
34                                         )
35                                     )
36                                 );
37       }
38       else{
39        valueFraction_[facei]=1.0;
40       }
41     }
42     //Info << valueFraction_<<endl;
43     Field<Type>::operator=
44     (
45         (1.0-valueFraction_)*transform(I - sqr(nHat),
46 this->patchInternalField())
47     );
48
49     transformFvPatchField<Type>::evaluate();
50 }
```

Acknowledments

I would like to thank ...

Dr. Shiva P. Pudasaini for the opportunity to work on this interesting project and for the helpful discussion.

Prof. Stephen A. Miller for the opportunity to do my PhD in his group, for providing the high speed camera system and for the helpful discussion and comments to my project.

Prof. Nikolaus Froitzheim for being my second examiner.

Prof. Andreas Kemna and **Prof. Carsten Burstedde** for being members of my thesis committee.

Dr. Andreas Dreist for great IT support which was an essential component to make this work possible and for being such a patient listener and support.

Dirk Handwerk for his help during the construction of the channel.

Lisa Takacs for help in administrative questions.

Holger Weber for the fun in the old office, all the nice discussions and for sharing the ups and downs of the PhD life.

Granulat 2000 for providing the PVC particles.

Everybody in the Geodynamics / Geophysics group for the nice atmosphere.

The open source community, especially the developers of Debian, TORQUE/Maui, LaTeX, pgfplots, xmgrace and TikZ. Without those great projects this work would have been impossible.

Julia Engelhorn for her patience, her support and for always being there for me.

My Parents for their love and for all the support.